DIGITAL ACCESS TO SCHOLARSHIP AT HARVARD
DASH.HARVARD.EDU

HARVARD LIBRARY
Office for Scholarly Communication

All-Optical Neurophysiology in the 1-Photon Regime

Permanent link
http://nrs.harvard.edu/urn-3:HUL.InstRepos:40050055

Terms of Use
This article was downloaded from Harvard University's DASH repository, and is made available under the terms and conditions applicable to Other Posted Material, as set forth at http://nrs.harvard.edu/urn-3:HUL.InstRepos:dash.current.terms-of-use#LAA

Share Your Story

The Harvard community has made this article openly available.
Please share how this access benefits you. Submit a story .

Accessibility

All-Optical Neurophysiology in the 1-Photon Regime

A dissertation presented

by

Samouil Leon Farhi

to

The Committee on Higher Degrees in Chemical Biology

in partial fulfillment of the requirements

for the degree of

Doctor of Philosophy

in the subject of

Chemical Biology

Harvard University

Cambridge, Massachusetts

April, 2018

© 2018, Samouil Leon Farhi

All rights reserved

All-Optical Neurophysiology in the 1-Photon Regime

Abstract

Simultaneous optical recording and optical stimulation of neuronal activity could enable faster and more comprehensive investigation of neuronal function but is hampered by underdeveloped tools. Pairs of molecular transducers between light and neuronal function are necessary to enable independent perturbation and measurement of the system. These molecular tools must be further complemented by optical systems and light delivery protocols to minimize cross-talk between color channels and between cells. Here I present three all-optical neurophysiology (AON) systems. Each combines a red-shifted fluorescent reporter of voltage or calcium combined with spectrally orthogonal blue-shifted channelrhodopsins to enable independent control and readout of neuronal function in different contexts.

AON was first shown with a near-infrared fluorescent microbial rhodopsin-based voltage sensor. This system, Optopatch, can initiate and monitor synaptic inputs, action potential propagation, and neuronal excitability in cultured rodent neurons and human induced pluripotent stem-cell derived neurons over large fields of view.

A subsequent iteration used FlicR1, a bright and fast red-fluorescent voltage indicator. FlicR1's brightness is compatible with imaging voltage over larger areas of cultured brain slices, but the indicator is challenging to pair with channelrhodopsins in a crosstalk free manner.

Finally, we identified a channelrhodopsin blue-shifted enough to be combined with existing red-shifted calcium indicators. We developed a form of structured illumination microscopy based on Hadamard matrices which enables calcium based AON in thousands of cells in parallel in acute brain slices. We used this system to map pharmacological perturbations of excitability and synaptic connections on millimeter-length scales across brain slices.

Table of contents

List of figures

List of tables

Author list

The author for Chapter 1 is S. L Farhi.

The authors for Chapter 2 are D.R. Hochbaum, Y. Zhao, S.L. Farhi, N. Klapoetke, C.A. Werkley, V. Kapoor, P. Zou, J.M. Kralj, D. Maclaurin, N. Smedemark-Marguiles, J. Saulnier, G.L. Boulting, C. Straub, Y.K. Cho, M. Melkonian, G.K. Wong, D.J. Harrison, V.N. Murthy, B.L. Sabatini, E.S. Boyden, R.E. Campbell, and A.E. Cohen.

The authors for Chapter 3 are A.S. Abdelfattah, S.L. Farhi, Y. Zhao, D. Brinks, P. Zou, A. Ruangkittisakul, J. Platisa, V. Pieribone, K. Ballanyi, A.E. Cohen, and R.E. Campbell.

The authors for Chapter 4 are S.L. Farhi, V. Parot, A. Grama, M. Yamagata, A. . Abdelfattah, Y. Adam, S. Lou, J.J. Kim, R.E. Campbell, D.D. Cox, and A.E. Cohen.

The author for Chapter 5 is S.L. Farhi.

Appendix 1 is the result of two collaborations. The authors of the *Drosophila melanogaster* work were S.L. Farhi, S. Rayshubskiy, A.E. Cohen, and R. Wilson. The authors of the adrenal cortex imaging were S.L. Farhi, N.A. Guagliardo, A.E. Cohen, M.P. Beenhakker, and P.Q. Barrett.

The author of Appendix 2 is S.L. Farhi.

Detailed descriptions of author contributions in collaborative projects can be found at the end of each chapter.

Acknowledgements

This dissertation, like any other, required a lot of time, a lot of failure, and a lot of work; but, most of all, it required the support of a lot of people. With the last, the work has been lightened; the impact of the failures muted; and the years spent have been among the most enjoyable of my life.

When I came to grad school, all I knew is that I wanted to work on something cool. I had heard of "voltage" but didn't really know what it was. I didn't know how to work with living things and I certainly didn't know how to build a microscope. Adam took me into the lab despite my naïveté and let me run around in the scientific playground that he built. I'm forever grateful for that first opportunity, as well as for the subsequent years of mentorship, encouragement, rich discussion, clear thought, good humor, and collegiality.

I've been fortunate to overlap with many amazing students and postdocs in the Cohen Lab—Daniel Hochbaum, Veena Venkatachalam, Joel Kralj, Dougal Maclaurin, Shan Lou, Miao-Ping Chien, Daan Brinks, Hongkang Zhang, Peng Zou, Stefano Baccoardo, Kit Werley, Jennifer Hou, Min Ju Shon, Jeehae Park, Linlin Fan, Harry McNamara, Vicente Parot, He Tian, Yoav Adam, Urs Boehm, Simon Kheifets, Zheng Shi, Shane Nichols, Benjamin Gmeiner, JJ Kim, Eli Weinstein, Liz Wood, and Hao Wu—and to work with several excellent technicians—Tony Shen, Nik Smedemark-Marguiles, Vedha Nathan, Melinda Lee, Katherine Williams, and Shahin Begum. I'm especially indebted to Daniel for sharing his entire skill set with me as I learned what it was to do a project for the first time; to Kit for his never-ending patience explaining optics; to Yoav for being a constant sounding board for neuroscience; and to Vicente for our years working together on calcium imaging with Hadamard. Beyond our lab, our collaborators in the University of Alberta, Ahmed Abdelfattah, Yongxin Zhao, and Robert Campbell have played an integral part of every project I've worked on. I'm also thankful for the intellectual feedback from many members of the Harvard neuroscience

community, especially Bernardo Sabatini, Gary Yellen, Susan Dymecki, Xiaowei Zhuang, Josh Sanes, and Rachel Wilson.

The key to getting this work done was to make sure life continued outside of the microscope room. I'm grateful to my wonderful friends for helping that happen; to my roommates Justin, Su, and Alix who have filled our house with laughter, games, and bread, even when all of our experiments were going nowhere; to Vini and Tim, who've been on same path with me from the very beginning of undergrad in Berkeley; and to the always reliable lake house group: Angela, Leigh, Liv, Charlene, Hubert, Andrew, Aly, Jasmine, Kelsey, Sam, Wes, Harriet, Ayano and Rob.

Most importantly, I'm thankful to my family. To my grandparents, who have been an understanding sounding board an ocean away in Bulgaria. To Boris, Raina, and Anna, who have been a second family in America. And above all, to my parents—my mother Anelia and my father Leon—who, knowingly or unknowingly, started teaching me how to do science right around when I could talk and have supported this path my whole life.

1 Introduction

1.1 Advantages of light-based recordings

Mammalian brains store and process information through millions of electrically active interconnected neurons. The electrical activity arises from sequential opening and closing of ligand- or voltage-gated ion channels. For most of the 20th century, this activity was investigated by electrophysiological methods. Electrodes placed near neurons (extracellular), or making electrical contact with their contents (intracellular), can detect transmembrane currents and depolarizations. Additionally, cell activity may be perturbed by directly manipulating cellular voltage or current, allowing scientists to query input-output properties of molecules, cells, synaptic pairs, and even entire networks. Because of this power, concentrated efforts focused on improving the performance of electrophysiological recordings. Extracellular measurements have steadily increased in sensitivity and in number of simultaneously recorded cells *in vivo*[1]. The improvement in intracellular techniques has been equally impressive, with sensitivity increasing to enable single ion channel current recordings, and stability increasing to the point of allow recording from individual dendrites within live animals[2].

Despite the enormous advantages of electrophysiology, and its long history of development, it still suffers from notable drawbacks: certain structures are too fine for electrode access[3]; electrical properties of cells are known to vary over space, which is not detected with a single point measurement[4]; and intracellular electrodes are known to disturb the cell's internal signaling by dialyzing cell contents[5]. The limitations are even more dramatic when considering throughput. In general, one electrode yields signal from one cell. Due to the large size of electrodes, hard limits exist on the number of cells that may be queried simultaneously without destroying the tissue—currently 700 with extracellular electrodes[6] and roughly a dozen with intracellular electrodes[7–9]. Heroic intracellular recording efforts in the

Blue Brain Project have measured 14,000 cells from brain slices, over a 10 year project[10]. These numbers are dwarfed by the number of neurons in a brain: roughly 80 million in a mouse[11], and >80 billion in a human[12].

Alternative methods are required. One tempting possibility has been to use light to interface with neural tissue rather than electrodes. Light can be applied to a sample with nearly arbitrary spatial and temporal profiles, allowing for rapid interaction with specific neurons without the disturbance of an electrode. Replacing electrodes with light brings its own list of challenges, however. For neural activity to be read out, the electrical signals in a neuron must be converted to an optical signal with high fidelity. Similarly, for perturbation, light must be transduced into neural activity with high temporal precision. Both processes must not perturb the native function of the cell except when desired. Methods to address both points have been developed over the past 50 years and are becoming widespread across neuroscience. An unresolved challenge has been to perform the recording and perturbation simultaneously without crosstalk, and without changing the underlying biology of the neural circuit. The result would be a system for all-optical neurophysiology (AON). Such a system would enable much higher throughput measurements than traditional electrophysiology and would allow neuroscientists to design new experiments to probe the function of large collections of neurons working together.

In this chapter, I will overview the parallel developments in optical recording and optical actuation of neural activity, as well as the early efforts towards AON. The bulk of the thesis will focus on three projects I have undertaken to perform AON in cultured neurons, organotypic brain slices, and ultimately acute brain slices. I'll conclude with a review of the field as it stands today, and where it may expand in the future. Throughout, I will emphasize both the molecular tools as well as the equally important developments in optics which have that have made these breakthroughs possible.

1.2 Optical recording of neuronal activity

Optical measurements of neuronal activity were first performed almost 50 years ago, with the discovery that the birefringence of a squid giant axon reflects the underlying transmembrane potential[13]. Unfortunately, these signals are miniscule, requiring thousands of trials to be averaged for detection. Contrast reagents are thus required to enhance the signal to single trial levels.

A neuronal action potential is generated by the opening and closing of voltage-gated sodium and potassium channels. In many neurons, the firing of an action potential is also coupled to the flow of calcium ions into the cell through voltage-gated calcium channels. Since the cellular sodium and potassium concentrations are minimally affected by an action potential, the options for optical detection are to either measure the membrane potential directly, or to detect calcium transients as a proxy for neural firing. The first efforts were with small molecule probes, which expanded later to include genetically encoded sensors.

1.2.1 Small-molecule probes

The earliest category of optical contrast reagents for detecting neuronal activity were small molecule voltage sensitive dyes (VSDs). Dozens of variants have been developed, which can be separated by their mechanism of voltage sensitivity[14,15]. The oldest category, including the ANEPPS[16–18], ANNINE[18–20], and RH[21,22] series of dyes, functions by an electrochromic shift, where changes in the high transmembrane electric field ($\sim 10^7$ V/m) induce a molecular Stark effect and associated color change in chromophores in the plasma membrane. These dyes benefit from fast response kinetics but face a tradeoff between sensitivity and photon count. The second large category of dyes bypasses this problem by relying on a voltage dependent redistribution of chromophores, either between the extracellular environment and membrane or between leaflets of the plasma membrane, which is then detected either as a solvatochromic shift or via a Förster Resonance Energy Transfer (FRET) mechanism[23,24]. These dyes offer larger sensitivities but are slow and add a large capacitative load to the cell[25].

The most recent and best performing category of VSDs functions by an intramolecular photoinduced electron transfer (PeT) quenching mechanism[26–29]. Since PeT involves movement of a charged particle, it is sensitive to transmembrane voltage, allowing for bright, fast, and sensitive VSDs with minimal capacitative loading.

Even the best performing VSDs ultimately run into a major obstacle: they stain cell membranes non-specifically. In brain tissue, membranes of axons, dendrites, and glia are tightly packed and intertwined, making it difficult to assign VSD signal to individual cells. Even VSDs compatible with two-photon (2P) imaging don't solve the problem except in preparations with high neuronal spatial organization, such as the hippocampus or cerebellum[30,31]. The solution for tissue measurements has been to label individual cells by electrode-based loading methods, ceding many of the advantages compared to conventional electrophysiology[32]. Efforts to target VSDs to defined cell types or cellular subcompartments via genetic methods are underway (see Chapter 5), but in the meantime this challenge remains. As a result, VSD applications lagged behind calcium-sensing dyes, which detect cytosolic signals and are therefore more readily separable between cells.

Early efforts identified calcium-responsive fluorescent dyes which were non-specific for Ca^{2+} ions[33,34]. This changed with the introduction of the BAPTA calcium chelator in 1980 by Roger Tsien[35]. BAPTA was highly specific for calcium over other relevant metal ions, and, importantly, could serve as a PeT donor into a range of fluorescent scaffolds. In these dyes, the PeT efficiency is modulated by calcium binding as opposed to transmembrane voltage. This approach has proven to be generalizable and has yielded dyes of varying colors with large response, high brightness, and fast kinetics, including widely used molecules such as Quin2 (ref. 35), Fura-2 (ref. 36), Fluo-4 (ref. 37), and Oregon Green BAPTA. Because of this rapid and successful probe development, calcium dyes were poised to be first to take advantage of advances in imaging technology, including high speed cameras[38], confocal microscopy[39], and crucially, 2P microscopy[40]. With 2P imaging and acetoxymethyl ester caged calcium indicators

it was possible to image multiple cells in intact tissue samples with single cell resolution, offering the first high-throughput measurements of neuronal function[41,42].

1.2.2 Genetically encoded calcium indicators (GECIs)

As technology for genetic perturbation of neurons, such as viral transfection[43], BAC-transgenics[44], and knock-in mice[45] became available, interest in genetically encoded reporters of neuronal function grew[46]. By far the most successful approach has been genetically encoded calcium indicators (GECIs). In addition to enabling more precise biological questions by labeling genetically defined cell types, GECIs yield higher quality imaging than small molecule calcium sensors by removing background signals from neuropil, glia, and blood vessels.

Protein based calcium sensing had been demonstrated with aequorin in 1962 by Osamu Shimomura in the same paper that first reported green fluorescent protein (GFP)[47,48]. However, aequorin was a reaction-based sensor, complicating its use[49,50]. Roger Tsien's lab introduced modern GECIs with Cameleon[51] in 1997 and Camgaroo[52] in 1999. In Cameleon, calcium modulates a calmodulin (CaM)-M13 interaction, increasing intramolecular FRET between enhanced cyan and yellow fluorescent proteins (ECFP and EYFP). In Camgaroo, calcium binding to CaM modulates closes the barrel of a cyclically permuted EGFP (cpGFP), increasing its brightness. Both scaffolds have been the focus of extensive engineering efforts since, especially around the calcium binding domains and linkers. The cyclically permuted strategy has proven more popular, yielding the GCaMP6 family of proteins, which provide similar performance to Oregon Green BAPTA, with genetic targeting[53]. More recent efforts have targeted red shifted GECIs (RGECIs) which would enable imaging deeper into the cortex in *in vivo* preps as well as multichannel applications.

1.2.3 Genetically encoded voltage indicators (GEVIs)

Despite the success of GECIs in tracking neuronal activity, calcium imaging does not capture the full range of neurophysiological phenotypes. Specifically, calcium does not accurately represent action potential timing and is not sensitive to subthreshold events.

Genetically encoded voltage indicators (GEVIs) could thus give a fuller picture. With the benefit of genetic targeting, GEVIs may also avoid the nonspecific staining problem of VSDs to be more generally useful in intact preparations with multiple labeled cells. Unfortunately, development of GEVIs has proven difficult due to the more stringent requirements of voltage imaging relative to calcium imaging. Voltage signals are much faster than calcium signals, requiring faster sensors and correspondingly faster imaging frame rates. In the resulting low photon count regime, sensors must offer a brightness and sensitivity sufficient to exceed the shot noise floor. GEVIs must be embedded in the cell's plasma membrane to function, a property which does not easily translate between model systems and which complicates the protein engineering process.

The first GEVIs were based on insertions of GFP into voltage-sensitive ion channels—the Shaker potassium channel for FlaSh, Kv1.4 for Flare, Kv2.1 for VSFP1, and NaV1.4 for SPARC[54–57]. All three proteins based on ion channels showed slow kinetics, low sensitivities, and poor localization to mammalian membranes[56]. Instead attention turned to the voltage sensing domain from the *Ciona intestinalis* voltage-sensitive phosphatase (*Ci*-VSP) as a method to impart voltage sensitivity. Fusions of *Ci*-VSP with FRET pairs or single FPs yielded the VSFP2.x[58–60], VSFP3.x[60,61], VSFP-CR[62], VSFP-cpFP[63,64], Mermaid[65,66], and Butterfly[67,68] lines. Each of these proteins offered incremental performance improvements but measurements of single action potentials still had low signal-to-noise ratios, making these proteins more suitable for population wide "optical electroencephalography (EEG)" measurements[67,69].

GEVI engineering took a dramatic step forward in 2011 when the Cohen lab discovered that some microbial rhodopsins showed weak fluorescence with a large voltage sensitivity, and demonstrated their function in bacteria[70] and in mammalian neurons[71]. Nearly simultaneously, a serendipitous mutation in a *Ci*-VSP-based GEVI yielded ArcLight[72], with a nearly 10-fold improved sensitivity compared to earlier proteins based on this scaffold. These

papers reinvigorated GEVI engineering efforts, with subsequent work yielding a variety of GEVIs with dramatically improved performance (see Chapters 2, 3, and 5). GEVI imaging thus promises to be the next frontier of high content activity measurements.

1.3 Optical stimulation of neuronal activity

While optical recording of neural activity was being developed, a separate community of scientists was developing methods for optical control of neuronal firing. Once again, chemical methods preceded biological methods, with the development of photocaged neuroactive small molecules[73]. Of these, caged glutamate has been particularly widely applied, as ultraviolet (UV) or 2P illumination could uncage sufficient glutamate to mimic an excitatory synaptic input. Glutamate uncaging was not a general tool for driving arbitrary activity patterns as the caged molecule could be depleted and it was frequently challenging to uncage enough glutamate to drive a cell to fire[74]. As with small molecule dyes for optical recording, nonspecificity limited the utility of glutamate uncaging for examining multiple cells with single-cell precision[74]. Hybrid approaches for photoactivation of ion channels with azo-benzene small molecule mediators are effective at driving activity but do so with poor temporal resolution[75].

The key discovery came in 2005, when Boyden *et al.* showed that the light-sensitive cation channel, Channelrhodopsin-2 (ChR2) from the alga *Chlamydomonas reinhardtii* could be heterologously expressed in mammalian neurons[76]. When exposed to brief flashes of blue light (470 nm), ChR2 opens a cation-selective pore in the cell membrane, allowing positive ions to flow inside the cell. The resulting photocurrents could depolarize neurons past their threshold potential and elicit an action potential. Thus, custom activity patterns could be dictated by appropriate timing of the blue light, rather than by traditional electrical stimulation. ChR2 rapidly superseded previous genetically encoded methods for optically invoking neuronal activity[75,77] since it was a single component system and able to acquire its retinal chromophore *in situ*. Soon after this paper, techniques to stimulate neuronal activity with light via genetically

encoded proteins were termed optogenetics. ChR2 thus represented the first generally useful alternative to electrode-based stimulation.

The discovery of ChR2 spurred a burst of tool development to identify improved optogenetic actuators. Engineering of the original ChR2 scaffold yielded proteins with increased photocurrent[78,79], decreased desensitization to blue light[80], and faster kinetics[81–83], allowing for more precise control of neural activity. In parallel, other microbial rhodopsins were identified in nature, expanding the optogenetic palette to include rhodopsins activated by yellow and red light[84–87]. These efforts also yielded inhibitory rhodopsins able to depress neural activity, first based around proton[88] or chloride[89–91] pumps, and, more recently, around chloride[92–96] and potassium[97] channels. Progress on the molecular tools provided an impetus for development of more robust gene-delivery and light-delivery systems to neural tissue. The combination of these molecular, genetic, and optical tools has become a standard, broadly applicable tool for neuroscience, and has been extensively reviewed since[98,99].

1.4 All-optical neurophysiology

As large steps were made in both optical recording and optical stimulation, they were accompanied by efforts to combine both fields. Rapid progress was made to combine calcium imaging with glutamate-uncaging[100], or VSD measurements with optogenetics[101]. 2P glutamate uncaging combined with 2P calcium imaging has proven especially useful on short length scales, especially in the investigation of low numbers of individual synapses[102]. Applications stimulating action potentials at cell soma suffered from poor temporal resolution and temporal complexity[103]. Several VSDs spectrally orthogonal to ChR2 were developed, but measurements combined with optogenetics have been most useful in culture[28] and in cardiac cells[104], where cell segmentation is less challenging. In neuronal tissue, non-specific staining has limited them to reading out field-averaged responses to stimulation[105,106].

Combining genetically encoded indicators with optogenetics was challenging since almost all optical reporters are based on GFP, whose excitation wavelength overlaps with the

absorption spectrum of all available ChRs[86]. ChRs also tend to elicit an effect with lower levels of blue light then those necessary for imaging. Imaging activity would therefore cause severe perturbations to the system of interest. Efforts made to combine GFP-based reporters with ChR stimulation involved expressing the reporter and actuator in disjoint cells to prevent optical crosstalk, which allowed investigation of synaptic connectivity in limited applications[107]. Generalizable methods, however, remained elusive.

In the next chapters I will present three approaches to AON with genetically encoded reporters and actuators. In Chapter 2, I describe all-optical electrophysiology with microbial rhodopsins, the first to achieve single-cell, single-spike, crosstalk-free measurements with genetically encoded tools. In Chapter 3, I describe efforts to extend this approach to a different, brighter GEVI, with the hope of achieving larger field of view measurements in tissue. Finally, in Chapter 4, I describe ultra-widefield measurements of thousands of cells in parallel in intact tissue, made possible by calcium based all-optical measurements and a new microscopy technique.

2 All-optical electrophysiology with microbial rhodopsins

2.1 Background

To disentangle the complex interactions underlying neural dynamics, one would like to visualize membrane voltage across spatial scales, from single dendritic spines to large numbers of interacting neurons, while delivering spatially and temporally precise stimuli[108,109]. Optical methods for simultaneous perturbation and measurement of membrane potential could achieve this goal[110]. Ideally, the stimulation and recording should be confined to genetically specified cells. Genetic targeting is particularly important in intact tissue where closely spaced cells often perform distinct functions, but is also valuable *in vitro*, for characterizing heterogeneous cultures that arise during stem cell differentiation to neurons[111], or while studying neurons co-cultured with other cell types. As reviewed in Chapter 1, a variety of approaches have been developed for optical stimulation or recording of neural function, but there remains a need for sensitive, fast, and spectrally orthogonal tools for genetically targeted simultaneous optical perturbation and measurement of membrane voltage.

In this chapter we introduce variants of a near infrared archaerhodopsin-based voltage indicator and a blue light gated channelrhodopsin actuator which individually show greatly improved performance relative to existing optogenetic tools and which together constitute a tool for all-optical electrophysiology. First, we characterize the optical and electrophysiological properties of the indicator, the actuator, and the co-expressed pair (Optopatch) and compare against published tools. Second, we use Optopatch to probe neuronal excitation across spatial and temporal scales: from single dendritic spines to fields containing dozens of neurons measured in parallel, and from microsecond delays associated with action potential propagation to days-long changes in excitability. Third, we apply Optopatch to study excitability in human induced pluripotent stem cell (hiPSC)-derived neurons. These

measurements revealed the first evidence for homeostatic plasticity of intrinsic excitability in hiPSC-derived neurons. Fourth, we apply Optopatch in tissue. In organotypic brain slice, Optopatch initiates and reports action potentials and subthreshold dynamics with higher signal-to-noise ratios, better photostability, and better time resolution than ArcLight, a recently introduced GFP-based GEVI[72].

2.2 Results

2.2.1 Directed evolution of an Arch-based voltage indicator

We previously showed that Archaerhodopsin 3 (Arch) functions as a fast and sensitive voltage indicator[71]. Arch has the furthest red-shifted spectrum of any GEVI, giving it the unique property of little spectral overlap with channelrhodopsin actuators and GFP-based reporters. Thus it is natural to pair Arch-based indicators with optogenetic actuators for crosstalk-free all-optical electrophysiology.

However, wild-type Arch has undesirable reporter attributes: it is very dim, and the brightness is a nonlinear function of illumination intensity[112]. Further, illumination for imaging generates a hyperpolarizing photocurrent, which partially suppressed neural firing. The mutant Arch(D95N) does not pump, but its step response was dominated by a 41 ms time constant, too slow to resolve action potential (AP) waveforms. Other non-pumping mutants improved speed relative to Arch(D95N) but did not reach the speed of wild-type Arch and did not address the low brightness[113].

We sought to repair these defects in engineered mutants of Arch. To accommodate the multiple selection criteria, we adopted a hierarchical screen (**Figure 1a**). Five rounds of brightness screening in *E. coli* and random mutagenesis on a library of $>10^4$ Arch mutants resulted in a brighter Arch variant, containing 5 point-mutations (Methods 2.5.1). Further site-directed mutagenesis at known key residues improved voltage sensitivity and speed (**Figure 1**), while addition of an endoplasmic reticulum export motif and a trafficking sequence improved trafficking. The two most promising mutants were named QuasArs (Quality

superior to Arch). QuasAr1 comprised mutations P60S, T80S, D95H, D106H, F161V and QuasAr2 comprised QuasAr1(H95Q). Both proteins had fluorescence excitation maxima at 590 nm and emission maxima at 715 nm (**Figure 2a**). The fluorescence quantum yields of solubilized QuasAr1 and 2 were 19- and 10-fold enhanced, respectively, relative to the non-pumping voltage indicator Arch(D95N) (**Table 1**). All fluorescence microscopy of QuasArs used 640 nm excitation.

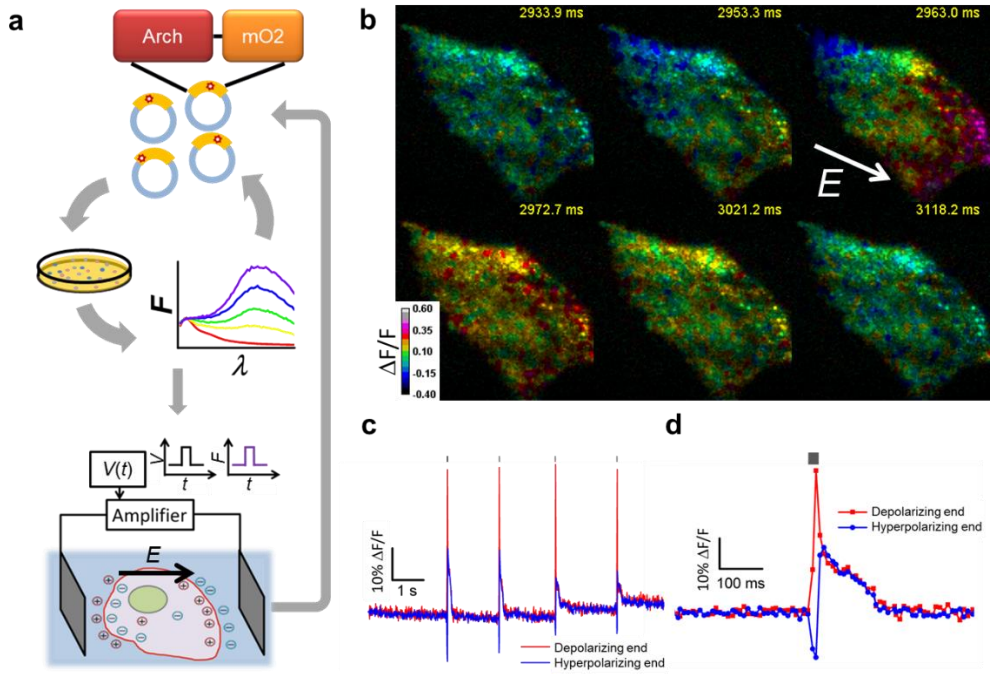

Figure 1. Hierarchical screen for Arch mutants with increased brightness, speed, and sensitivity.

a) Hierarchical screen to select improved Arch mutants. Five rounds of random mutagenesis and screening for brightness were performed in E. coli. The brightest mutants were subjected to targeted mutagenesis and screening for speed and voltage sensitivity in HeLa cells via induced transient voltage (ITV, bottom). V(t) represents the pulse generator and high-voltage amplifier. **b**) Frames of fluorescence response (ΔF/F) from a movie of a HeLa cell expressing QuasAr1 while being stimulated withca an electrical pulse (20 ms, 50 V/cm). The arrow labeled 'E' indicates the direction of the electric field. **c**) Fluorescence of the cell poles during the ITV experiment shown in (b). Gray marks above the fluorescence traces indicate timing and duration of the ITV pulses. **d**) Expanded view of one fluorescence intensity peak from (c).

Table 1. Quantum yields of Arch variants measured in solubilized protein.

	Quantum yield (QY)	QY relative to Arch D95N
Arch	N/A*	N/A*
Arch D95N	4×10^{-4}	1.0
QuasAr1	8×10^{-3}	19
QuasAr2	4×10^{-3}	10
Arch D95H/D106H	2×10^{-3}	4.2
Arch D95H/D106H/P60S	5×10^{-3}	12
Arch D95H/D106H/F161V	5×10^{-3}	13

Fluorescence emission spectra were recorded with excitation at 600 nm. Due to the low light intensities used to determine QYs, fluorescence from Arch (*) was not detected above baseline.

We compared the fluorescence, voltage sensitivity, and speed of the QuasArs to wild-type Arch in HEK cells, using epifluorescence microscopy and whole-cell patch clamp electrophysiology. Under low intensity illumination (500 mW/cm^2), QuasAr1 was 15-fold brighter than wild-type Arch, and QuasAr2 was 3.3-fold brighter (**Figure 2b**). Neither mutant showed the optical nonlinearity seen in the wild-type protein, implying that fluorescence was a 1-photon process with the voltage-sensitive transition occurring from the ground state. At high intensity (>100 W/cm^2) QuasAr1 was 2.5-fold brighter than wild-type Arch, while the brightness of QuasAr2 and of wild-type Arch were comparable.

Fluorescence of Arch, QuasAr1, and QuasAr2 increased nearly linearly with membrane voltage between -100 mV and +50 mV (**Figure 2c**). Sensitivities were ($\Delta F/F$ per 100 mV): 32 ± 3% for QuasAr1 (n = 5 cells; all statistics are mean ± s.e.m. unless specified) and 90 ± 2% for QuasAr2 (n = 6 cells). The sensitivity of QuasAr2 is a substantial improvement over both Arch (40% per 100 mV) and Arch(D95N) (60% per 100 mV).

Steps in membrane voltage (-70 mV to +30 mV) induced rapid fluorescence responses in both mutants, which we quantified on a fast photomultiplier (**Figure 2d**). At room temperature (23 °C) QuasAr1 had a step response time constant of 0.053 ± 0.002 ms (n = 6 cells), close to the 0.05 ms time resolution of the electronics and substantially faster than the 0.6 ms step response of wild-type Arch[112]. QuasAr2 had a bi-exponential step response

with time constants of 1.2 ± 0.1 ms (68%) and 11.8 ± 1.5 ms (32%) (n = 6 cells). At 34 °C, the apparent speed of QuasAr1 remained at the 0.05 ms resolution of the electronics, and the time constants of QuasAr2 decreased to 0.30 ± 0.05 ms (62%) and 3.2 ± 0.4 ms (38%) (n = 7 cells). Both mutants had similar response times on rising and falling edges (**Table 2**).

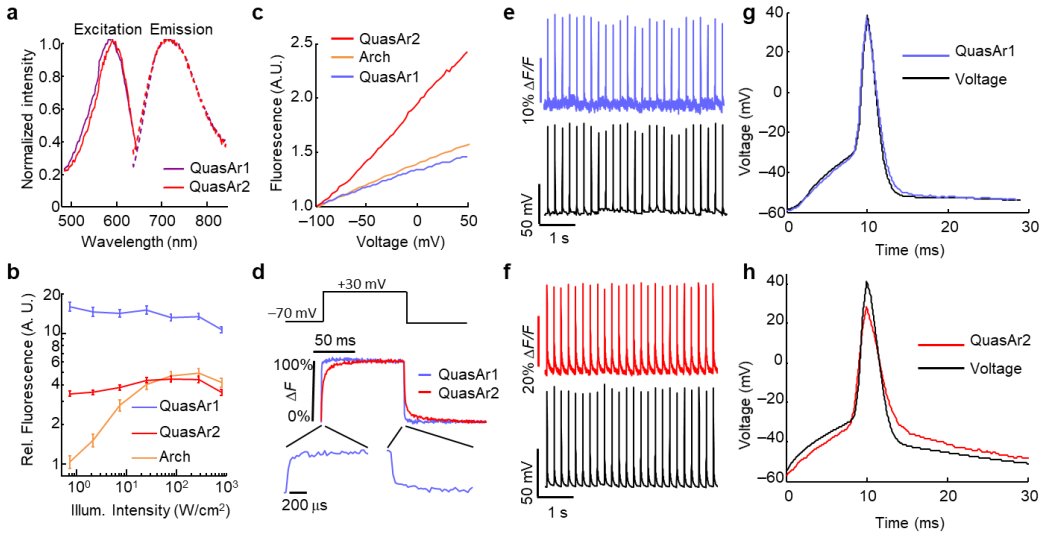

Figure 2. Non-pumping Arch-derived voltage indicators with improved speed, sensitivity, and brightness.

a) Excitation and emission spectra of QuasAr1 and QuasAr2. Arch was too dim to measure in a fluorimeter. Emission spectra were recorded with λ_{exc} = 600 nm. Excitation spectra were measured with λ_{em} = 750 nm. **b**) Fluorescence of Arch mutants fused to eGFP and expressed in HEK cells, as a function of illumination intensity. The plot shows Arch fluorescence normalized by 640 nm illumination intensity and by eGFP fluorescence (488 nm exc., 525-575 nm em.) to control for cell-to-cell variations in expression. A linear fluorophore (i.e. brightness proportional to illumination intensity) would appear as a horizontal line. Error bars represent s.e.m. (n = 7 cells for each mutant). **c**) Fluorescence vs. membrane voltage for Arch, QuasAr1, and QuasAr2 expressed in HEK cells. **d**) Fluorescence responses to a step in membrane voltage from -70 to +30 mV. **e**) Simultaneous optical and electrical recording of APs in a rat hippocampal neuron expressing QuasAr1. Frame rate 1 kHz. **g**) Overlay of mean optically and electrically recorded AP waveforms. Frame rate 2 kHz. **f,h**) Same as (**e**), (**g**) in neurons expressing QuasAr2. Data in (**b-h**) acquired on a 128 x 128 pixel EMCCD camera.

Table 2. Spectroscopic and kinetic properties of Arch mutants and ArcLight.

	Brightness (λ_{exc} = 640 nm)		τ_{up} (ms) -70 to +30 mV			τ_{down} (ms) +30 to -70 mV)			ΔF/F per 100 mV
	0.7 W/cm^2	800 W/cm^2	τ_1	τ_2	%τ_1	τ_1	τ_2	%τ_1	
23 ˚C									
Arch(WT)	1	4.0	0.6	NA	NA	0.25	1.9	67	40%
QuasAr1	15.2	10.3	0.05	3.2	94	0.07	1.9	88	33%
QuasAr2	3.4	4.4	1.2	11.8	68	1.0	15.9	80	90%
ArcLight A242			17.4	123	39	68	121	24	-32%
34 ˚C									
QuasAr2			0.3	3.2	62	0.3	4	73	
ArcLight A242			12	72	78	21.5	NA	100	

Brightness, response speed, and sensitivity were measured in HEK293 cells. Brightness and voltage sensitivity were comparable at 34 °C and 23 °C.

We expressed QuasArs in cultured rat hippocampal neurons, evoked APs via current injection from a patch pipette and recorded the fluorescence responses from the soma and proximal dendrites (1 kHz frame rate, **Figure 2e-h**, Methods 2.5.8.2). Single APs produced fluorescence transients with amplitude $\Delta F/F = 21 \pm 2\%$ for QuasAr1 ($n = 11$ cells) and $\Delta F/F = 48 \pm 3\%$ for QuasAr2 ($n = 24$ cells). Signal-to-noise ratios (SNRs) for single APs increased with illumination intensity. For QuasAr1, SNR values were 21 ± 2 (300 W/cm^2, $n = 6$ cells) and 32 ± 4 (800 W/cm^2, $n = 6$ cells). For QuasAr2, SNR values were 41 ± 4 (300 W/cm^2, $n = 12$ cells) and 70 ± 8 (800 W/cm^2, $n = 12$ cells). These SNRs correspond to equivalent electrical noise levels of 3.0 to 4.3 mV (800 to 300 W/cm^2) for QuasAr1, or 1.5 to 2.2 mV (800 to 300 W/cm^2) for QuasAr2.

QuasAr1 did not introduce detectable broadening in the optically recorded AP waveform, acquired at a 2 kHz frame rate (**Figure 2e,g**). At room temperature, QuasAr2 broadened the optically recorded AP by 650 ± 150 ms relative to the simultaneously recorded electrical waveform at 70% maximum depolarization ($n = 5$ cells; mean ± s.d.) (**Figure 2g**). At 34 °C, QuasAr2 broadened the optically recorded AP by 180 ± 120 ms ($n = 5$ cells; mean ± s.d). Both probes reported AP peak times with <100 μs jitter relative to simultaneously acquired patch clamp recordings (Methods 2.5.8.3). Neither QuasAr1 nor QuasAr2 generated detectable photocurrent under red light (tested up to 900 W/cm^2) or blue light (**Figure 3a**).

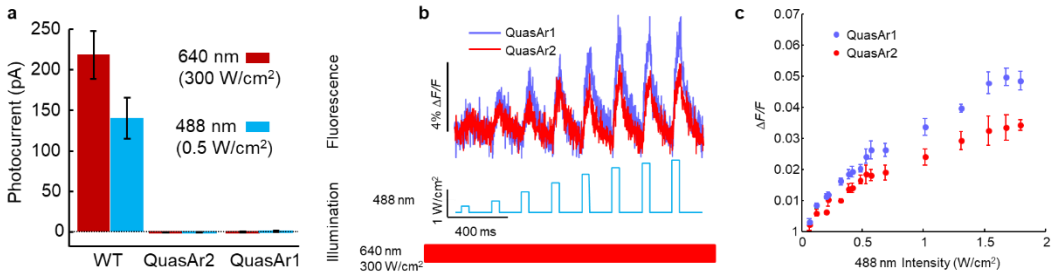

Figure 3. Quantification of optical and electrical crosstalk of QuasArs.

a) In cultured rat hippocampal neurons, wild-type Arch generated photocurrents of 220 ± 30 pA (n = 6 cells) under red illumination (1 s, 640 nm, 300 W/cm^2) and 140 ± 25 pA under blue light (1 s, 488 nm, 500 mW/cm^2). Steady state photocurrents were calculated by averaging the current over the last 0.25 seconds of light exposure and subtracting the holding current (cells held at -65 mV) in the dark. These currents hyperpolarized cells by 25 ± 4 mV and 19 ± 3 mV, respectively. Neither QuasAr1 (n = 9 cells) nor QuasAr2 (n = 7 cells) generated detectable photocurrents under either illumination condition, nor under red illumination at up to 900 W/cm^2. **b**) Effect of blue illumination on QuasAr fluorescence. HEK293T cells expressing QuasAr1 or QuasAr2 were exposed to continuous excitation at 640 nm (300 W/cm^2) and pulses of illumination at 488 nm (50 ms, 5 Hz). The intensity of the blue pulses increased from 0.06 to 1.8 W/cm^2. **c**) Quantification of crosstalk. Illumination with blue light at maximum intensity used to excite CheRiff (0.2 W/cm^2) increased QuasAr1 fluorescence by 1.1% and QuasAr2 fluorescence by 0.6%. Initiation of precisely timed APs with existing channelrhodopsins required whole-cell illumination at 0.5 to 2 W/cm^2 (ref. 114). Blue illumination at 1 W/cm^2 increased QuasAr1 fluorescence by 3.4% and QuasAr2 fluorescence by 2.4%, unacceptably high levels of optical crosstalk. Error bars represent s.e.m. for n = 5 cells for each QuasAr. Quantification is given in **Table 4**.

Photostability is a concern with any voltage indicator, so we quantified the stability of QuasArs under continuous illumination at standard imaging intensity (300 W/cm^2). Photobleaching time constants were 440 s for QuasAr1 and 1020 s for QuasAr2. We further tested for red light-induced phototoxicity using QuasAr2 as the readout. Under continuous illumination at 300 W/cm^2, QuasAr2 reported APs with 100% fidelity for the 30 min duration of the experiment, with no detectable change in AP width or waveform (**Figure 4**).

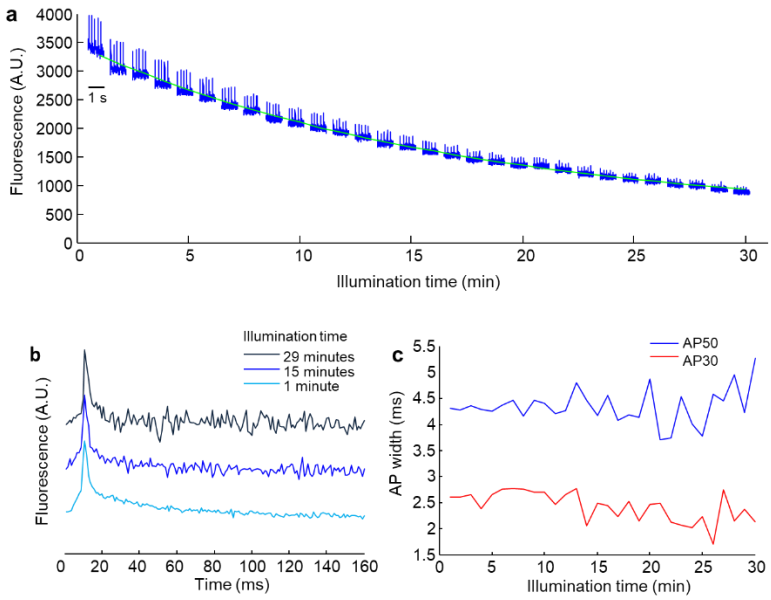

Figure 4. Photobleaching of QuasAr2 and test for red light induced phototoxicity.

a) Fluorescence traces from a neuron expressing QuasAr2 and CheRiff (Optopatch2, described below), with APs induced via blue light activation of the CheRiff. Optogenetic stimulation was preferable to manual patch clamp due to the poor stability of patch connections over long-term measurements. The cell was illuminated for 30 minutes continuously at 640 nm, 300 W/cm^2 and probed at 60 s intervals with blue light to induce a burst of APs (5 pulses of 10 ms, 5 Hz, 20 mW/cm^2). The cell fired APs with 100% fidelity over the recording period, though the signal-to-noise ratio decreased as the QuasAr2 fluorescence dropped. **b**) Fluorescence traces of APs at the beginning, middle, and end of the recording in (a). Each trace in (b) is an average of the 5 APs elicited during that time point. **c**) AP widths measured at 30% and 50% recovery from peak fluorescence deviation. APs did not show a detectable change in width over the 30-minute recording.

We compared the QuasArs to ArcLight A242 (ref. 72). Photophysical comparisons were performed in HEK cells (**Table 2**), and action potential comparisons were performed in matched neuronal cultures. ArcLight can be imaged with ~30-fold lower illumination intensity than is required for the QuasArs, facilitating measurements on readily available microscope systems. However, the QuasArs reported action potentials with 7- to 16-fold larger fractional fluorescence changes, 3 to 8-fold higher SNR, 30 to 1000-fold higher temporal resolution, and 6 to 15-fold greater photostability (**Figure 5**).

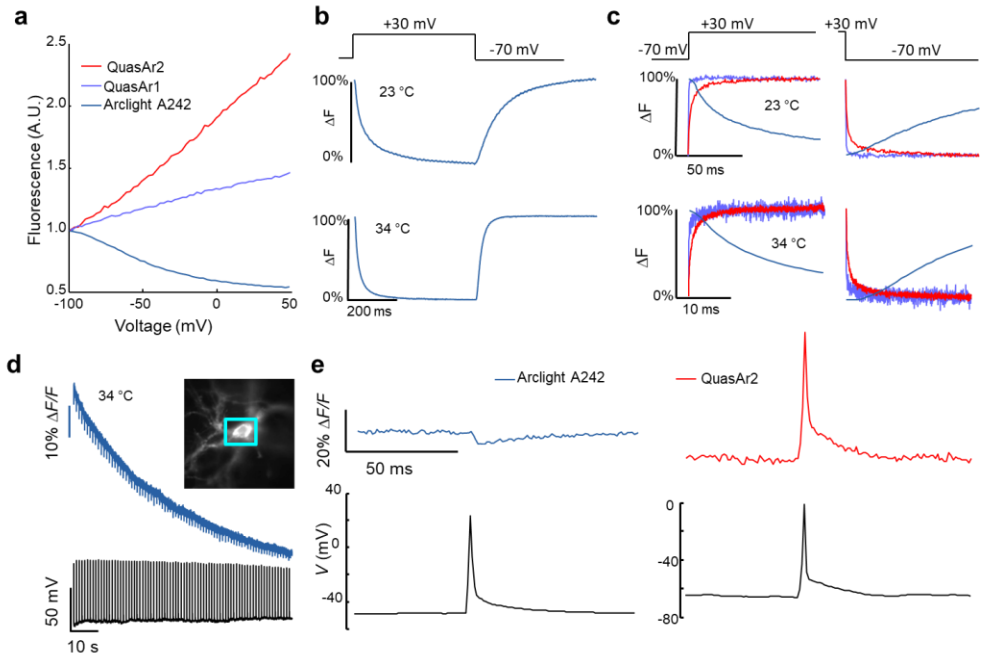

Figure 5. Comparison of voltage-indicating properties of QuasArs and ArcLight A242 in culture.

a) Fluorescence as a function of membrane voltage in HEK293T cells. ArcLight showed voltage sensitivity of -32 ± 3% ΔF/F per 100 mV (n = 7 cells), comparable in magnitude to QuasAr1 and 2.8-fold smaller than QuasAr2. **b**) Response of ArcLight to steps in membrane voltage. ArcLight showed bi-exponential kinetics in response to rising or falling voltage steps (**Table 2**). Mean half-response times were 42 ± 8 ms and 76 ± 5 ms on rising and falling edges at 23 °C (n = 6 cells) and 11 ± 1 and 17 ± 2 ms on rising and falling edges at 34 °C (n = 7 cells). **c**) Step responses of ArcLight and QuasArs overlaid on the same time axis at 23 °C (top) and 34 °C (bottom). **d**) Continuous illumination of a neuron expressing ArcLight (488 nm, 10 W/cm^2) led to photobleaching with a time constant of 70 s. Inset: Low-magnification image of the neuron. Cyan box shows field of view used for high-speed (1 kHz frame rate) movies of fluorescence dynamics. Fluorescence was calculated using the same pixel weighting algorithm used for QuasAr data (Methods 2.5.8.2). **e**) Single-trial fluorescence response of ArcLight (blue) and QuasAr2 (red) to a single AP (black), recorded at 34 °C and a 1 kHz frame rate. ArcLight reported action potentials with an amplitude of ΔF/F = -2.7 ± 0.5% (n = 5 cells) and a single-trial signal-to-noise ratio (SNR) of 8.8 ± 1.6 (488 nm, 10 W/cm^2). ArcLight distorted the AP waveforms to have a width of 14.5 ± 3.0 ms at 70% maximal fluorescence deviation, compared to the true width of 1.3 ± 0.1 ms simultaneously recorded with a patch pipette. QuasAr2 reported APs at 34 °C and 23 °C with comparable single-trial SNR (SNR at 34 °C: 41 ± 3, 300 W/cm^2, n = 8 cells).

The QuasArs represent the fastest and most sensitive GEVIs reported to-date. The 50 ms response time of QuasAr1 is more than 10-fold faster than the fastest previously reported GEVIs[57,112] and is comparable to fast voltage-sensitive dyes. QuasAr1 opens the possibility of accurate mapping of AP waveforms for even the fastest-spiking neurons[115]. The

QuasArs report voltage with greatly improved sensitivity and time resolution compared to the first generation of Arch-based GEVIs, despite requiring ~5-fold lower illumination intensity[71]. From a signal-to-noise perspective, QuasAr2 is superior to QuasAr1: the greater voltage sensitivity of QuasAr2 outweighs the greater brightness of QuasAr1. From a temporal resolution perspective, QuasAr1 is superior. We recommend QuasAr2 for spike counting and measurement of sub-threshold events, and QuasAr1 for measurement of microsecond-precision AP waveforms and timing. Furthermore, the far-red excitation of the QuasArs allows, in principle, combination with channelrhodopsin actuators or other GFP-based reporters.

2.2.2 CheRiff, a sensitive blue-shifted optogenetic actuator

We next sought to combine the QuasAr reporters with a blue light-activated channelrhodopsin. To achieve spatially precise optical excitation, the channelrhodopsin should trigger APs when only a subsection of a cell is excited. Existing optogenetic actuators have had only marginal success in achieving this goal[116]. To avoid optical crosstalk, the blue light intended for the channelrhodopsin should not perturb the GEVI fluorescence. Existing optogenetic actuators require blue light intensities that perturb QuasAr fluorescence (**Figure 3b-c**). We thus sought a more sensitive channelrhodopsin that could reliably trigger APs with sub-cellular illumination and at lower light intensity, while maintaining fast opening and closing kinetics.

During a screen of plant genomes[117] we identified a novel optogenetic actuator, *Scherffelia dubia* ChR (sdChR)[86], derived from a fresh-water green alga first isolated from a small pond in Essex, England (**Figure 6a**)[118]. SdChR had promising sensitivity and a blue action spectrum (λ_{max} = 474 nm). Addition of a trafficking sequence improved membrane targeting and expression in cultured hippocampal neurons (**Figure 6b-e**). Introduction of the mutation E154A sped up the kinetics and shifted the peak of the action spectrum to λ_{max} = 460 nm,

which decreased spurious channelrhodopsin activation by red light (**Figure 7a-b**). We dubbed the final construct CheRiff in reference to *Scherffelia*, its genus of origin.

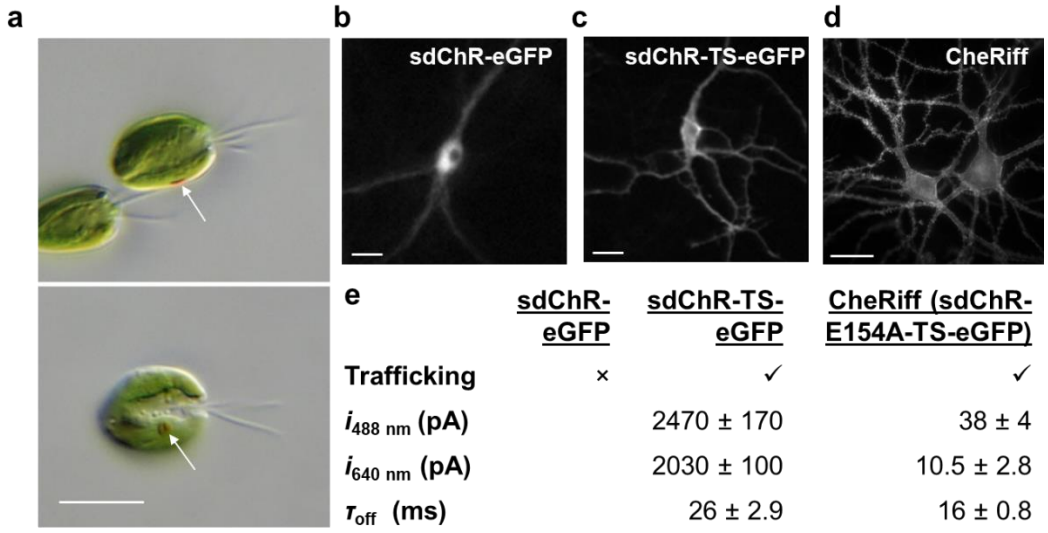

e	sdChR-eGFP	sdChR-TS-eGFP	CheRiff (sdChR-E154A-TS-eGFP)
Trafficking	×	✓	✓
$i_{488\ nm}$ (pA)		2470 ± 170	38 ± 4
$i_{640\ nm}$ (pA)		2030 ± 100	10.5 ± 2.8
τ_{off} (ms)		26 ± 2.9	16 ± 0.8

Figure 6. Improvements in trafficking leading to CheRiff.

a) Light micrographs (DIC) of *Scherffelia dubia* (strain CCAC 0053) in side view (top) and face view (bottom). Arrows mark eyespots (red). Scale bar 10 μm. Strain and micrographs courtesy of CCAC [http://www.ccac.uni-koeln.de/] and Sebastian Hess (Cologne Biocenter), respectively. **b**) Image of a cultured neuron expressing wild-type *Scherffelia dubia* Channelrhodopsin (sdChR). SdChR typically aggregated and formed puncta in the soma. Scale bar 25 μm. **c**) Image of a neuron expressing sdChR with an additional trafficking sequence from Kir2.1 between the C-terminus of sdChR and the N-terminus of eGFP (Methods 2.5.2). This trafficking sequence substantially reduced intracellular puncta. Scale bar 25 μm. **d**) Two neurons expressing CheRiff. Scale bar 25 μm. **e**) Spectroscopic and kinetic properties of *Scherffelia dubia* mutants. Inclusion of the E154A mutation reduced red light sensitivity and reduced τ_{off} while maintaining excellent membrane trafficking and blue light sensitivity. Photocurrents were measured in cultured rat hippocampal neurons under voltage-clamp at V_m = -65 mV. 488 nm intensity was 500 mW/cm^2, 640 nm intensity was 300 W/cm^2. All quantities are represented as mean ± s.e.m. for n = 5 to 7 cells.

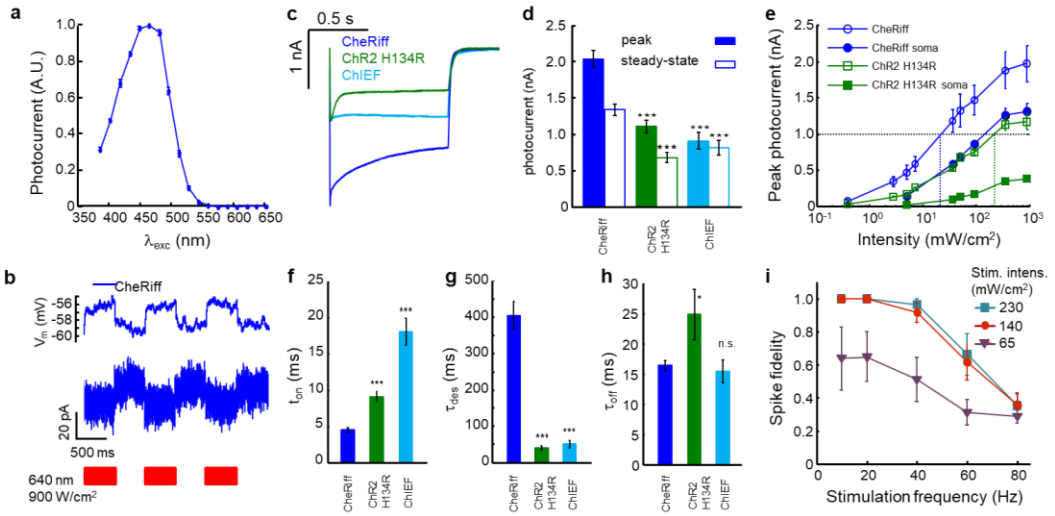

Figure 7. CheRiff is a fast and sensitive blue-shifted channelrhodopsin.

a) Action spectrum acquired in HEK293T cells (n = 6 cells). CheRiff had a blue-shifted action spectrum with a peak at λ_{max} ~ 460 nm. **b**) Activation of CheRiff by red light used for imaging QuasArs (640 nm, 900 W/cm^2, bottom) resulted in a small steady state depolarization of 3.1 ± 0.2 mV (n = 5 cells) when measured in current clamp, i = 0 (top) and a small inward photocurrent of 14.3 ± 3.1 pA (n = 5 cells) when measured in voltage clamp, V = -65 mV (middle). **c**) Photocurrents measured in response to a 1 second 488 nm (500 mW/cm^2), sufficient to open all the channels. **d**) Peak (I_{pk}) and steady state (I_{ss}) photocurrents in neurons expressing CheRiff (n = 10 cells), ChR2 H134R (n = 8 cells), and ChIEF[119] (n = 6 cells). CheRiff generated peak photocurrent of 2.0 ± 0.1 nA, approximately 2-fold larger than the peak photocurrents of ChR2 H134R (1.1 ± 0.1 nA, p < 0.001) or ChIEF (0.9 ± 0.1 nA, p < 0.001). CheRiff also generated significantly larger steady state photocurrents (1.3 ± 0.08 nA) than ChR2 H134R (0.68 ± 0.07 nA, p < 0.001) or ChIEF (0.81 ± 0.10 nA, p < 0.001). **e**) Comparison of photocurrents as a function of illumination intensity in matched neuronal cultures expressing CheRiff (n = 5 cells) or ChR2 H134R (n = 5 cells). Illumination was either over the whole cell or confined to the soma. **f**) In response to a step in illumination, CheRiff reached peak photocurrent in 4.5 ± 0.3 ms (n = 10 cells), significantly faster than ChR2 H134R (8.9 ± 0.5 ms, n = 8 cells, p < 0.001) or ChiEF (18 ± 1.5 ms, n = 6 cells, p < 0.001). **g**) Under continuous illumination CheRiff partially desensitized with a time constant of 400 ms. ChR2 H134R and ChIEF desensitized significantly faster (39 ± 4 ms, n = 8 cells, p < 0.001, and 49 ± 8 ms, n = 5 cells, p < 0.001, respectively). **h**) τ_{off} was measured in response to a 5 ms illumination pulse (500 mW/cm^2) as in ref. [114]. Channel closing time constant was comparable between CheRiff and ChIEF (16 ± 0.8 ms, n = 9 cells, and 15 ± 2 ms, n = 6 cells, respectively, p = 0.94), and faster than ChR2 H134R (25 ± 4 ms, n = 6 cells, p < 0.05). **i**) Spiking fidelity as a function of stimulation frequency and illumination intensity in neurons expressing CheRiff (n = 5 cells). Cells were stimulated with trains of 40 pulses (2 ms pulse width, 10 to 80 Hz) at three different blue light intensities. All comparisons were made on matched rat hippocampal cultures, DIV 14-15, with expression driven by a *CaMKIIa* promoter. All kinetics measurements were performed with 500 mW/cm^2 488 nm illumination at 23 °C. Error bars represent s.e.m. Statistical significance determined by one way ANOVA with Dunnett's post hoc test using CheRiff as the reference. * p < 0.05; ** p < 0.01; *** p < 0.001. **Table 3** contains a summary of the comparisons between CheRiff, ChR2 H134R, and ChIEF.

Table 3. Comparison of CheRiff, ChIEF, and ChR2 H134R.

	CheRiff	ChIEF	ChR2 H134R
$I_{488\ nm,\ peak}$ (nA)	2.0±0.1	0.9±0.1	1.1±0.1
$I_{488\ nm,\ steady\ state}$ (nA)	1.33±0.08	0.81±0.10	0.65±0.09
t_{on} (ms)	4.5±0.3	18±1.8	9.1±0.7
τ_{des} (ms)	400±40	51±10	40±5
τ_{off} (ms)	16±0.8	15±2	25±4
EPD50 (mW/cm^2)	22±4		43±4
$i_{640\ nm}$ (pA)	10.5 ± 2.8	15.0 ± 2.5	2.2 ± 0.9
$\Delta V_{640\ nm}$ (mV)	2.3 ± 0.3	2.1 ± 0.15	1.0

All parameters were measured in cultured rat hippocampal neurons. Photocurrents were measured under voltage-clamp at V_m = -65 mV. All quantities are represented as mean ± s.e.m. for n = 5 to 7 cells. EPD50 = intensity for 50% maximal photocurrent. 488 nm intensity was 500 mW/cm^2, 640 nm intensity was 300 W/cm^2.

Under typical neural culture conditions, rapid and robust AP initiation requires currents of approximately 1 nA (ref. 114). In a paired comparison, CheRiff passed a photocurrent of 1 nA at a whole-cell illumination intensity of 22 ± 10 mW/cm^2 (n = 5 neurons), 9-fold lower than was required for ChR2 H134R (200 ± 80 mW/cm^2, n = 5 neurons) (**Figure 7c-e**). For stimulation localized to the soma, CheRiff passed a photocurrent of 1 nA under illumination at 100 mW/cm^2, while ChR2 H134R did not achieve this photocurrent under any illumination intensity. Upon pulsed whole-cell illumination, CheRiff induced high-frequency and high-reliability spike trains (**Figure 7i**) at 5- to 10-fold lower illumination intensities than have been reported for ChR2 H134R, ChIEF, or ChETA[114] using the same protocol.

We measured the photophysical properties of CheRiff, ChR2 H134R and ChIEF in matched neuronal cultures (**Figure 7f-h**, **Table 3**). CheRiff showed 2-fold larger maximal photocurrents than ChR2 H134R or ChIEF. CheRiff had an opening rate 2-fold faster than ChR H134R and 4-fold faster than ChIEF. CheRiff had a similar closing rate to ChIEF, and was 1.5-fold faster than ChR H134R.

Finally, we tested for optical crosstalk between QuasArs and CheRiff in cultured neurons (**Table 4**). Illumination sufficient to induce high-frequency trains of APs (488 nm,

140 mW/cm^2) perturbed fluorescence of QuasArs by < 1% (**Figure 3b-c**). Illumination with high intensity red light (640 nm, 900 W/cm^2) induced an inward photocurrent through CheRiff of 14.3 ± 3.1 pA, which depolarized neurons by 3.1 ± 0.2 mV (n = 5 cells) (**Figure 7b**). For most applications this level of optical crosstalk is acceptable.

Of the many attributes that determine channelrhodopsin function, the most important in CheRiff are its greatly increased sensitivity at low illumination intensity and its fast opening kinetics. These properties allow sub-cellular and low-intensity triggering of precisely timed APs.

Table 4. Optical crosstalk between in Optopatch constructs.

	Peak CheRiff photocurrent (pA)	Fluorescence	
		QuasAr1	QuasAr2
Blue (500 mW/cm^2)	2030±100	0.02	0.017
Red (300 W/cm^2)	10.5±2.8	3.0	1

Photocurrents were measured in cultured rat hippocampal neurons under voltage-clamp at V_m = -65 mV. Photocurrents are represented as mean ± s.e.m. for n = 5 to 7 cells. Fluorescence values were measured in HEK293 cells. Fluorescence of QuasAr constructs is normalized to the value for QuasAr2 illuminated at 640 nm, 300 W/cm^2.

2.2.3 Optopatch constructs

Optopatch1 and Optopatch2 consisted of bicistronic vectors for co-expression of CheRiff-eGFP and QuasAr1- or QuasAr2-mOrange2, respectively (**Figure 8a**). We also made Optopatch variants which contained non-fluorescent eGFP and mOrange2 mutants, freeing the spectrum for other uses. The QuasAr and CheRiff constructs could also be delivered separately, but the bicistronic vector maintained a more uniform ratio of actuator to reporter expression levels.

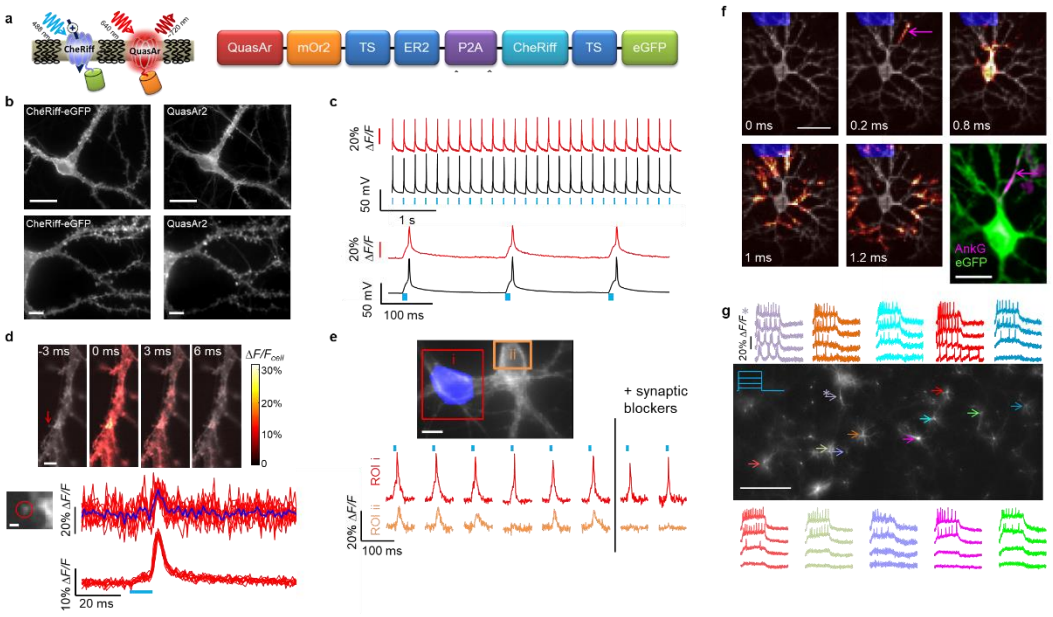

Figure 8. Optopatch enables high fidelity optical stimulation and recording in cultured neurons.

a) The co-expression of CheRiff and QuasAr in the cell plasma membrane (left) and design of Optopatch construct (right). **b**) Trafficking of Optopatch components in cultured rat hippocampal neurons. Left: CheRiff-eGFP, measured via eGFP fluorescence. Right: QuasAr2, measured via retinal fluorescence. Scale bars: top 20 μm, bottom 5 μm. **c**) Temporally precise optical initiation and monitoring of single APs. Blue: illumination. Red: whole-cell single-trial unfiltered fluorescence. Black: patch clamp recording. **d**) Optical mapping of an AP induced via illumination of the soma. Top: Filmstrip showing average of $n = 20$ temporally registered APs. Fluorescence is normalized to mean fluorescence of the dendrite. Images are composite of mean fluorescence (gray) and changes in fluorescence (heat map). Arrow indicates dendritic spine. Scale bar 5 μm. Bottom: Single-trial detection of back-propagating APs in a single dendritic spine. Scale bar 1 μm. Top traces: ten single-trial recordings from the spine (red) and their average (blue). Bottom traces: ten single-trial recordings from the parent dendrite. **e**) Synaptic transmission. Optical stimulation of one soma (highlighted in blue) induced single APs in the stimulated cell (i) and EPSPs in the neighboring cell (ii). Synaptic blockers suppressed the response in the postsynaptic cell but not in the presynaptic cell. **f**) Sub-frame interpolation of AP propagation in a neuron expressing Optopatch1. Scale bar 50 μm. Bottom right: Immunostaining of the same cell with anti-eGFP and anti-AnkyrinG. Scale bar 25 μm. Magenta arrows: site of action potential initiation, distal end of the AIS. **g**) Parallel optical recording under increasingly strong 0.5 s optical step-stimuli. Asterisk indicates a cell that showed periodic bursts of 3-4 APs under weak stimulation. Scale bar 500 μm. Image is of eGFP fluorescence. Data in (b, d, g) acquired on an sCMOS detector; data in (c, e, f) acquired on an EMCCD.

We characterized Optopatch2 in detail. When expressed under a *CaMKIIa* promoter in cultured rat hippocampal neurons, Optopatch2 showed high expression and good membrane trafficking of both CheRiff and QuasAr2 (**Figure 8b**). Patch clamp comparisons

of *CaMKIIa*-Optopatch2 and *CaMKIIa*-GFP expressing neurons found no statistically significant differences in membrane resistance (330 ± 66 MΩ vs. 290 ± 66 MΩ, $p = 0.72$), membrane capacitance (80 ± 11 pF vs. 77 ± 13 pF, $p = 0.87$), resting potential (-57 ± 4.5 mV vs. -55 ± 5.0 mV, $p = 0.31$), threshold current (670 ± 59 pA vs. 710 ± 61 pA, $p = 0.67$), or threshold potential (-27 ± 1.2 mV vs. -28 ± 0.74 mV, $p = 0.38$. For all comparisons, $n = 8$ cells for Optopatch2, $n = 7$ cells for GFP, with all p-values obtained by two-sided Student's t-test).

A neuron expressing Optopatch2 was exposed to whole-field illumination with pulses of blue light (10 ms, 25 mW/cm^2) to stimulate CheRiff, and simultaneous constant illumination with red light (800 W/cm^2) to excite fluorescence of QuasAr2. We imaged fluorescence of QuasAr2 at a 1 kHz frame rate and calculated fluorescence from whole-cell average intensity (Methods 2.5.8.2), while simultaneously recording membrane voltage via a patch pipette. The optical and electrical traces corresponded closely (**Figure 8c**).

Raw movies acquired at 1 kHz clearly showed fluorescence changes due to optically triggered APs. Averaging temporally registered AP movies over multiple trials improved the SNR for sub-cellular AP mapping. Under focused red illumination (2200 W/cm^2), back-propagating APs were detected in single dendritic spines on a single-trial basis, with an SNR of 2.5 (**Figure 8d**).

2.2.4 Probing synaptic transmission

With Optopatch, one can stimulate and record from independently selected and rapidly reconfigured regions of a neural circuit. We implemented this capability in culture using a digital micromirror device (DMD) to pattern the blue CheRiff excitation[120], and wide-field red illumination to monitor voltage throughout the field of view (Methods 2.5.7).

We probed synaptic transmission by optically stimulating the soma of single cells, and optically monitoring electrical responses in neighboring cells. Optically induced single APs in the presynaptic cell led to fluorescence transients indicative of excitatory post-synaptic

potentials (EPSPs), as well as occasional failures of synaptic transmission, in the postsynaptic cell (**Figure 8e**). The mean interval between the peak of the AP in the upstream cell and the onset of the optically detected EPSP in the downstream cell was <2 ms, indicating a monosynaptic connection[121]. Addition of synaptic blockers (10 μM NBQX, 20 μM Gabazine, 25 μM AP-V) quieted the fluorescence response in the postsynaptic cell, without perturbing presynaptic activity. Validation measurements with patch clamp recordings showed millivolt-level correspondence of optically and electrically recorded postsynaptic potentials, as well as inhibition of these signal by synaptic blockers (**Figure 9**).

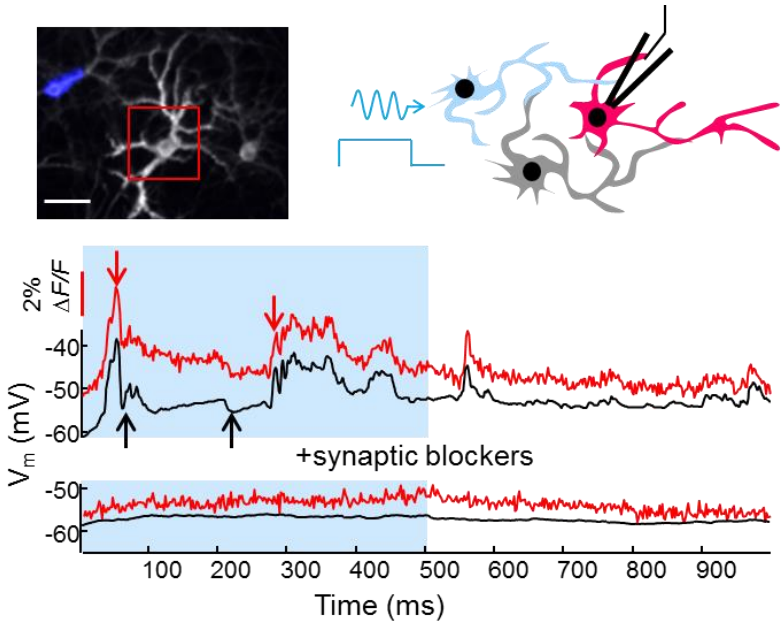

Figure 9. Optopatch measurements of post-synaptic responses.

Top: Three cells expressing Optopatch2 were imaged via eGFP fluorescence (after conclusion of the experiment). The blue shading shows the region optically stimulated in the leftmost cell (488 nm, 35 mW/cm^2, 500 ms pulses) to stimulate network activity. The red square shows the camera field of view used for imaging QuasAr2 fluorescence. The membrane voltage of the cell within this region was simultaneously monitored via QuasAr2 fluorescence and via whole-cell patch clamp. Middle: Simultaneous patch clamp (black line) and fluorescence (red line) recording of subthreshold activity in the postsynaptic cell (640 nm exc., 1200 W/cm^2). The presence of optically induced EPSPs (red arrows) and IPSPs (black arrows) in the same cell indicates recruitment of other cells in the network. Bottom: Synaptic blockers (10 μM NBQX, 20 μM gabazine, 25 μM AP-V) eliminated the response in the postsynaptic cell.

2.2.5 Probing AP propagation

We next sought to apply the extremely fast response of Optopatch1 (containing QuasAr1) to probe the microsecond-timescale dynamics of AP initiation and propagation within a single cell. We used the DMD to target optical stimulation to either a dendrite or the soma and recorded the fluorescence dynamics at a 1 kHz frame rate. To improve the SNR we averaged 100 to 400 temporally registered optically induced APs. These mean-AP movies showed spread of the subthreshold voltage outward from the stimulated region, followed by a sudden spike in cell-wide fluorescence that peaked within two frames. Thus, the native 1 kHz frame rate was insufficient to resolve the details of AP propagation.

To probe microsecond-level dynamics, we adapted the sub-frame interpolation approach of Foust *et al.*[122] and Popovic *et al.*[123] (**Figure 10**, Methods 2.5.8.5). By interpolating a smoothly varying spline to the fluorescence intensity time-trace at each pixel, we inferred the timing with which the fluorescence crossed a user-selected threshold (e.g. 50% maximum deviation) with a precision better than the exposure time of the camera. Mean deviation between optically inferred and electrically recorded AP timing at the soma was 40 – 70 ms (**Figure 10**). We then constructed a higher time-resolution movie highlighting each pixel at the sub-frame time of its wavefront crossing. This interpolation technique does not rely on an assumed AP waveform, nor does it assume wavelike propagation; it is compatible with APs that change shape within or between cells.

The visually striking propagation movies clearly showed AP initiation 30 – 50 μm from the soma in a single thin neurite, presumed to be the axon, in n = 8 of 8 measured cells (**Figure 10**), regardless of stimulus location. The AP then propagated down the putative axon and back into the soma and dendrites. Latencies between AP initiation and arrival in the soma were 320 ± 220 ms (n = 8 cells, mean ± s.d).

After acquiring Optopatch data, we fixed the cells and stained for ankyrin-G, a marker of the axon initial segment (AIS, **Figure 8f**). The optically detected zones of AP initiation

coincided with the distal end of the AIS, consistent with previous experiments using voltage-sensitive dyes[124]. Thus, Optopatch can resolve functionally significant sub-cellular and microsecond timescale details of AP dynamics.

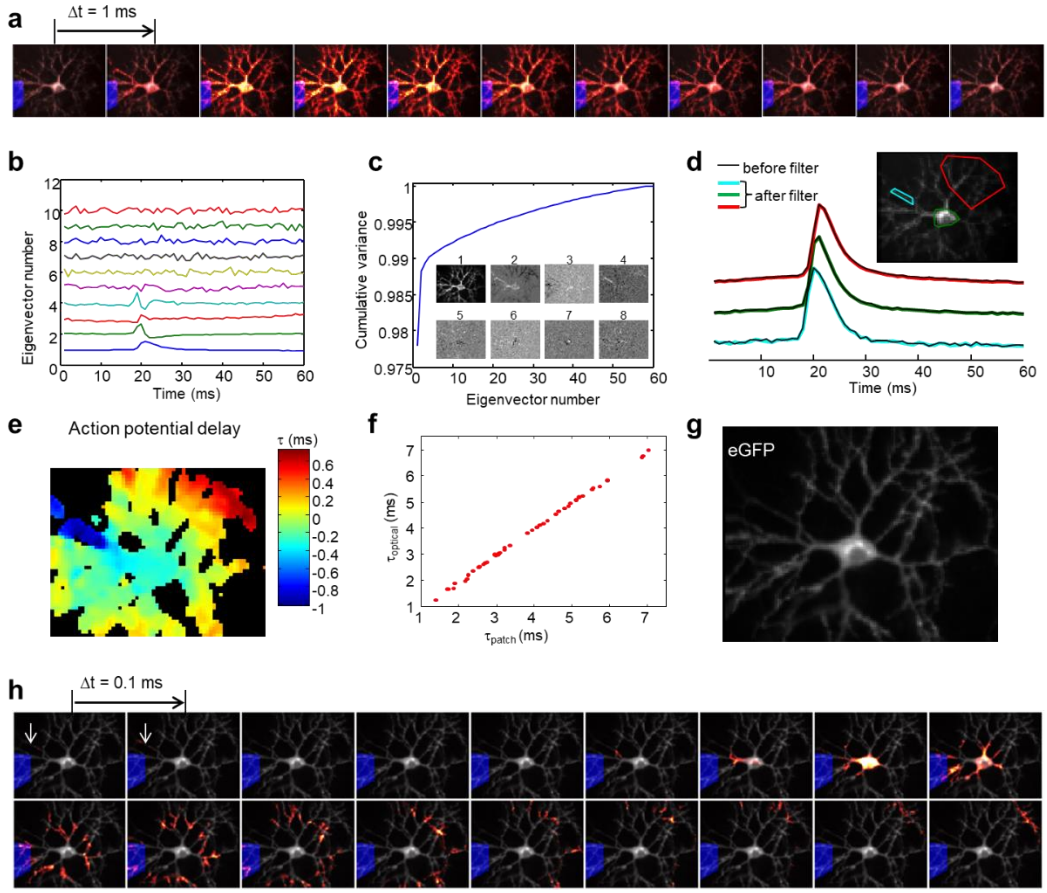

Figure 10. Sub-frame interpolation highlights subcellular timing differences in AP initiation.

a) Patterned optical excitation (blue region) was used to induce between 100 and 400 APs. Fluorescence movies of individual APs were acquired at 1,000 frames/s, temporally registered and averaged. The sub-threshold depolarization is greatest at the location of the optical stimulus, and propagates passively through the cell until it crosses the AP initiation threshold. **b**) The movie of a mean AP was passed through a mild spatial filter, and then Principal Components Analysis (PCA) was applied to AP waveforms at individual pixels. The first 5 PCA eigenvectors accounted for > 99% of the pixel-to-pixel variation in AP waveforms; the remaining eigenvectors were noise. **c**) Cumulative variance of the fluorescence signal accounted for by the first *n* eigenvectors. In this example the cumulative variances explained by the first five eigenvectors were: 97.8%, 98.8%, 98.9%, 99.0%, and 99.1%. Inset shows projection of the spike movie onto each of the first eight eigenvectors. **d**) Comparison of AP waveforms before and after the spatial and PCA smoothing operations. Black lines represent original movie, colored lines represent filtered data recorded in the axon (cyan), soma (green), and dendrites (red). **e**) Map of AP timing, calculated for the cell shown in (a) and (d). Here the timing was defined as the time to reach 50% of maximum intensity on the rising edge of

(Continued) the AP. Note the early timing in the axon initial segment on the left. **f**) Absolute accuracy of timing extracted by the sub-frame interpolation algorithm for voltage at the soma, compared to a simultaneously acquired patch clamp recording. The r.m.s. error between optically inferred and electrically recorded timing was 54 μs in this example. Note the absence of systematic offsets at the frame boundaries. **g**) High-resolution image of eGFP fluorescence, indicating CheRiff distribution. **h**) Frames from a sub-frame interpolated movie formed by mapping the timing information in (e) onto the high spatial resolution image in (g). White arrows mark zone of AP initiation in the presumed axon initial segment. Data is from the same cell as in **Figure 8f**, with images rotated 90°.

2.2.6 Parallel measurements in neuronal cultures

To achieve high-throughput functional characterization in neurons, one would like to apply the technique to many cells in parallel. We constructed a low-magnification, high-speed microscope (**Figure 11a**, Methods) which robustly reported APs and subthreshold dynamics in up to ~50 cells simultaneously. We used a DMD to pattern the blue illumination for targeted CheRiff excitation in user-selected regions. Optical stimulation of a segment of a synaptically connected culture induced network activity which manifested as action potentials and sub-threshold dynamics in the cells not directly stimulated (**Figure 11b-c**).

We developed an all-optical protocol to measure neuronal excitability. Synaptic blockers were added to suppress network activity. Cells were stimulated with pulses of blue light (500 ms at 6 s intervals) of increasing intensity (0 to 14 mW/cm^2), while firing patterns were recorded under continuous red illumination (100 W/cm^2). In wide-field measurements on n = 169 neurons expressing Optopatch2, we observed several distinct firing patterns, including fast-adapting and slow-adapting spike trains (**Figure 8g**). Two neurons showed intermittent bursting (one of these is indicated by a star in **Figure 8g**). The comparatively high throughput of Optopatch measurements enables detection of rare electrophysiological phenotypes that might be missed in a manual patch clamp measurement on a smaller number of cells.

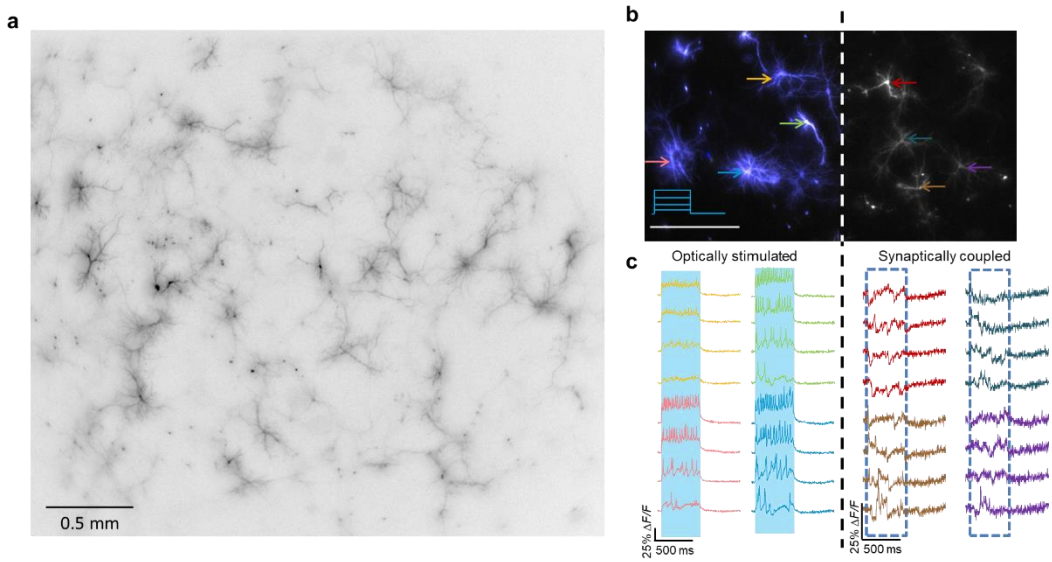

Figure 11. Low magnification imaging of many neurons.

a) Neurons expressing Optopatch2, imaged via eGFP fluorescence. More than 50 cells are visible in this field of view. Limitations on data-rate from the camera required that the field of view be compressed in the vertical direction to 0.6 mm for optical recordings at 1 kHz, or to 1.2 mm for optical recordings at 500 Hz. Colors are inverted for easier visualization. **b**) Image of eGFP fluorescence in a culture of neurons expressing Optopatch2. The left half of the field (colored blue) was stimulated with blue light of increasing intensity (0.5 s, 1 to 10 mW/cm^2) and the whole field was illuminated with red light (100 W/cm^2). **c**) Left: fluorescence traces showing APs in the neurons indicated in (A) with correspondingly colored arrows. Right: synaptically induced activity in the indicated neurons which did not receive direct optical stimulation. Scale bar 500 μm.

To test whether high-throughput Optopatch could quantify subtle electrophysiological shifts, we applied the all-optical excitability protocol to a model of homeostatic plasticity of intrinsic excitability (HPIE)[125], in which neurons adapt their excitability to maintain an approximately constant level of activity. Observation of HPIE in culture[126,127] and *in vivo*[128] has traditionally required laborious patch clamp measurements on many cells.

Neurons expressing Optopatch2 were incubated in tetrodotoxin (TTX, 1 μM) for 48 h and then measured in TTX-free medium in the presence of synaptic blockers[126]. Paired control cultures were incubated without TTX. Cells that had been treated with TTX (n = 94) subsequently showed significantly lower illumination threshold for spiking (p = 5×10^{-6}), shorter interval between first and second spike (p < 0.001), and more total spikes (p < 0.01)

than control cells (n = 75), but only a small change in time from light onset to first spike (**Figure 12**), consistent with previous reports[126]. Total data acquisition time was less than 1 h, a fraction of the time that would be required for manual measurements.

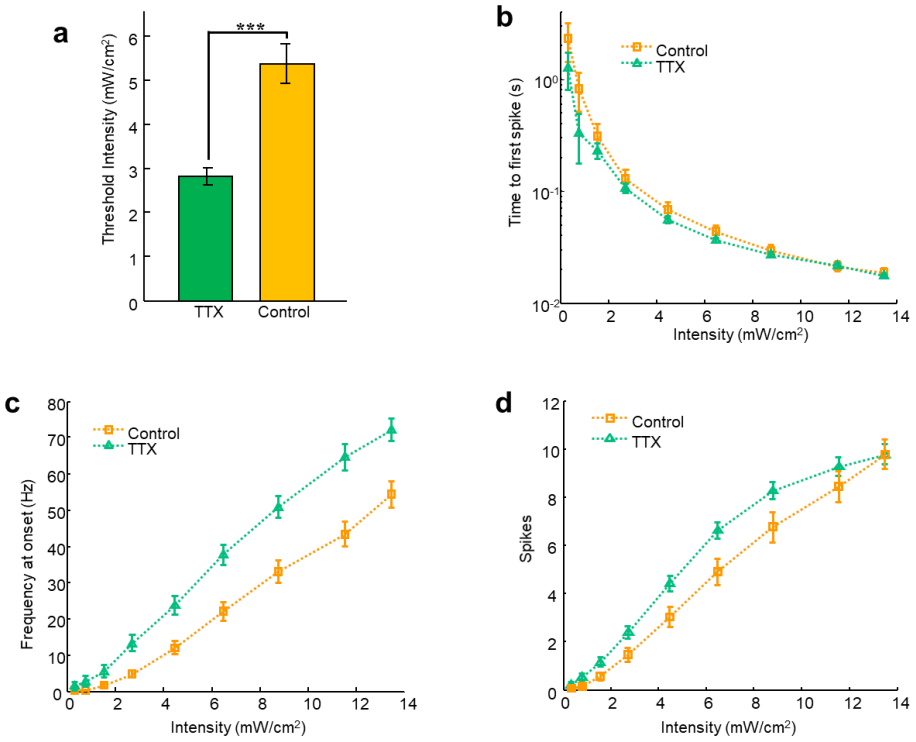

Figure 12. Homeostasis of intrinsic excitability in primary neurons induced by chronic exposure to TTX.

Neurons expressing Optopatch2 were incubated in 1 μM TTX for 48 hours starting at 16 days post plating, and then tested in TTX-free imaging medium. Paired control dishes from the same culture were incubated with vehicle alone. Data from n = 75 control cells and n = 94 TTX-treated cells. QuasAr2 fluorescence was monitored (640 nm, 100 W/cm^2) while cells were illuminated with pulses of blue light (500 ms) of increasing intensity (0 to 14 mW/cm^2, repeated twice). **a**) Threshold blue light stimulation intensity to induce at least one AP in 500 ms. TTX treated cells had a significantly lower threshold than controls ($p = 5\times10^{-6}$). **b**) Time from onset of illumination to first spike. TTX-treated and control cells did not differ substantially by this measure. **c**) Spike frequency at onset (inverse time between first and second spike). TTX-treated cells fired faster than control cells ($p < 0.001$ for each stimulation intensity ≥ 2.7 mW/cm^2). **d**) Number of spikes during 500 ms stimulus window. TTX-treated cells had more spikes than control cells ($p < 0.01$ for stimulus intensities between 0.8 and 8.8 mW/cm^2). Error bars represent s.e.m. *** $p < 0.001$. Statistical significance determined by two-tailed student's t-test or Mann–Whitney U test.

While the HPIE measurements showed population-level changes in excitability, a unique promise of Optopatch is the ability to measure the same cell over several days. In 8 of

10 trials, neurons measured with a 1-minute Optopatch protocol were identified and re-recorded 48 hrs later (**Figure 13**

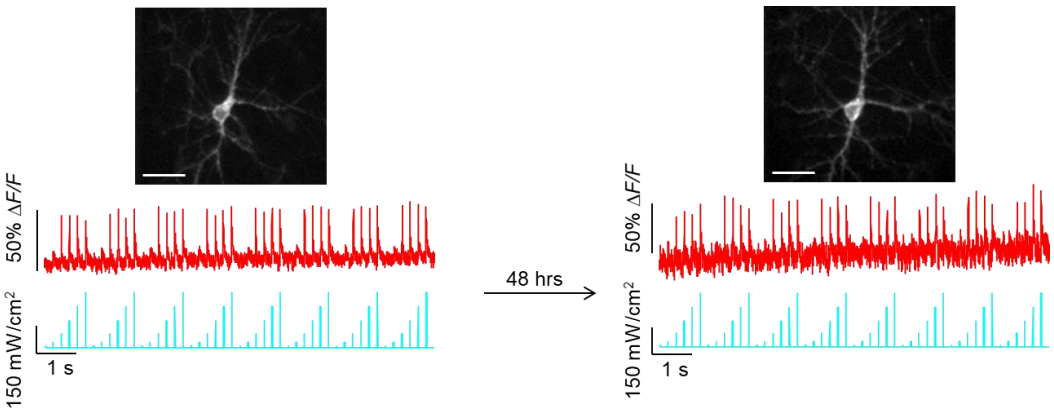

). This capability could be important in studying neuronal maturation or long-term effects of pharmacological, genetic, or environmental perturbations.

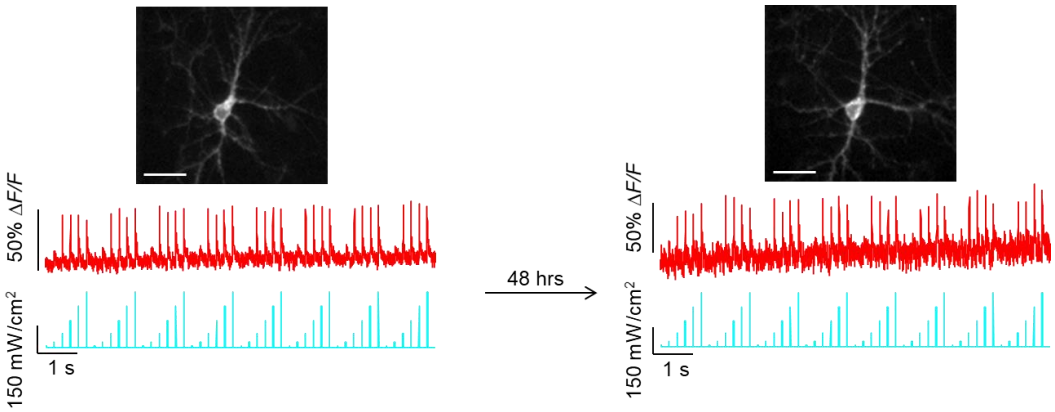

Figure 13. Repeated Optopatch recordings from neurons expressing Optopatch2.

Images show mOrange2 fluorescence. Scale bar 40 μm. Primary rat hippocampal neurons (left) were stimulated with pulses of blue light of increasing intensity, targeted to the soma (blue). Cells produced optically detected APs under the stronger stimuli. The stimulus and imaging protocol lasted 1 min. After the recording, the imaging medium was replaced with culture medium and the cells were returned to the incubator. 48 hrs later (right), the same cells were located in the microscope and the stimulus protocol was repeated. The cells responded similarly in the first and second trial. Paired recordings separated by 48 hrs were successful in $n = 8$ of 10 cells.

2.2.7 Probing excitability in hiPSC-derived neurons

Human-derived neurons show promise as a platform for studying human neurophysiology in health and disease[129]. However, variability arises at multiple levels in this

approach[111]. Each patient's genetic background modifies neuronal function, even for nominally monogenic diseases. Additional variability arises between iPSC clones from a single patient, between differentiations, and between cells cultured within a single well. Differing degrees of maturation are a particularly large source of cell-to-cell variability within a dish[130]. Furthermore, for disease-modeling efforts, one may wish to test many differentiation protocols or pharmacological perturbations. Together, these factors motivate a need for accurate functional characterization with robust statistics. The low throughput and selection bias of manual electrophysiology present a serious bottleneck.

We first assessed whether Optopatch expression perturbed electrophysiology in hiPSC-derived neurons. Cells were transfected with Optopatch2 and cultured on a rat glial monolayer. The *CamKIIa* promoter genetically targeted the measurement to mature neurons within this highly heterogeneous culture[130]. Patch clamp measurements on cells transfected with Optopatch2 ($n = 11$) or with GFP ($n = 11$) showed no significant difference in membrane resistance (2.7 ± 0.3 GΩ vs. 2.7 ± 0.4 GΩ, $p = 0.82$), membrane capacitance (21 ± 3.2 pF vs. 21 ± 1.6 pF, $p = 0.88$), resting potential (-53 ± 3.5 mV vs. 48 ± 3.3 mV, $p = 0.34$), or action potential activation threshold (-27 ± 1.1 mV vs. -28 ± 1.3 mV, $p = 0.78$). Optically evoked and optically monitored trains of APs showed the expected excitability changes upon addition of ion-channel blockers lidocaine and tetraethylamine (**Figure 14**).

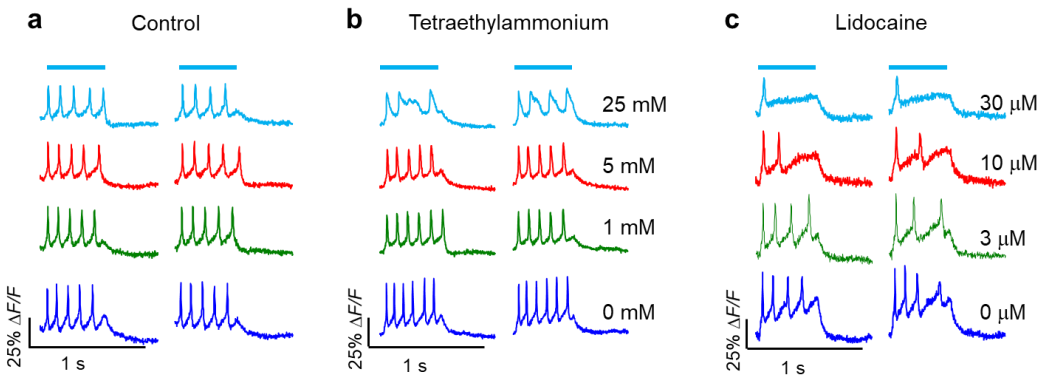

Figure 14. Influence of channel blockers on excitability of hiPSC-derived neurons.

a) Human iPSC-derived neurons were excited with 500 ms pulses of blue light to initiate a train of APs. Repeated stimulation with blue light led to repeatable trains of APs. **b**) Representative AP trains with increasing concentrations of tetraethylammonium (TEA), a voltage-gated potassium channel blocker. TEA blocked repolarization after AP initiation. **c**) Representative AP trains with increasing concentrations of lidocaine, an activity-dependent sodium channel blocker. Lidocaine prevented repetitive firing.

We then applied Optopatch to test for HPIE in hiPSC-derived neurons. This subtle electrophysiological effect is one of several forms of neural plasticity which have not previously been reported in human-derived neurons. HiPSC-derived neurons were incubated in 1 µM TTX for 48 h. Upon return to TTX-free medium, treated cells showed a substantial increase in subsequent optically measured excitability (n = 31 cells) relative to controls (n = 32 cells) (**Figure 15a-e**), demonstrating positive HPIE.

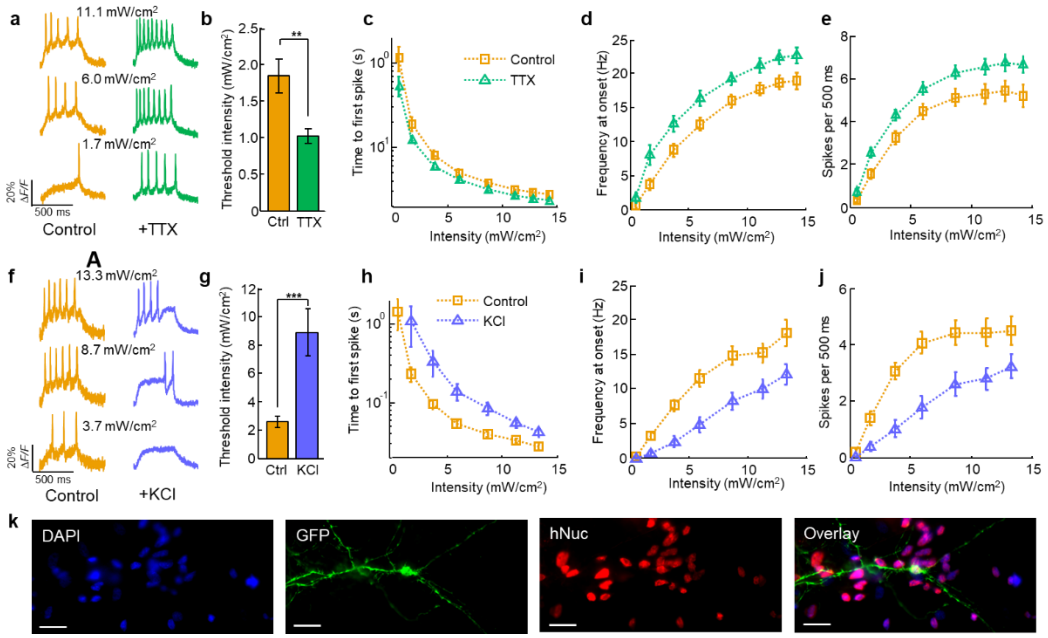

Figure 15. Homeostatic plasticity of intrinsic excitability in human iPSC-derived neurons probed via Optopatch2.

a-e) Positive HPIE. Data from n = 32 control cells and n = 31 TTX-treated cells **a**) Representative optical recordings from single neurons after incubation in TTX and matched control cells. **b**) Threshold stimulation intensity (488 nm) to induce at least one spike in 500 ms. TTX treated cells had a significantly lower threshold than controls (p = 0.004). **c**) Time from onset of illumination to first spike. **d**) Spike frequency at onset (inverse time between first and second spike). **e**) Total spikes per 500 ms stimulus. Measures in D and E showed significantly increased excitability in TTX-treated cells relative to control cells ($p < 0.05$ for each stimulation intensity ≥ 1.7 mW/cm^2). **f-j**) Negative HPIE. Data from n = 25 control cells and n = 28 KCl-treated cells. Panels are the same as (a-e). KCl treated cells had a significantly higher stimulation intensity threshold than controls ($p = 7\times10^{-6}$). Measures in (h-j) showed significantly decreased excitability in KCl-treated cells relative to control cells (h: $p < 0.01$ for all stimulus intensities; i: $p < 0.05$ for stimulus intensities ≥ 1.7 mW/cm^2; j: $p < 0.05$ for stimulus intensities ≤ 11.2 mW/cm^2). For all experiments fluorescence was excited at 300 W/cm^2, and collected at a 1 kHz frame rate on an EMCCD. All error bars represent s.e.m. Statistical significance determined by two-tailed student's t-test or Mann–Whitney U test. ** $P < 0.01$; *** $P < 0.001$. **k**) hiPSC-derived neurons used in experiments on homeostatic plasticity were fixed immediately after data acquisition and immunostained against eGFP to label transfected neurons and *hNuc* to label human nuclei. All eGFP expressing cells (277 of 277) showed colocalization of the *hNuc* with GFP. Scale bars 20 μm.

We next tested for negative HPIE: conditions that depolarize cells (e.g. high KCl) induce a gradual decrease in intrinsic excitability[127]. HiPSC-derived neurons were incubated in 15 mM KCl for 60 h. Upon return to baseline conditions (2.5 mM KCl), treated cells showed a substantial decrease in subsequent optically measured excitability (n = 28 cells) relative to

controls (n = 25 cells) (**Figure 15f-j**). Post-measurement immunostaining with anti-human nuclear antigen 1 and anti-GFP antibodies confirmed that all neurons tested were of human origin (**Figure 15k**). Validation measurements with manual patch clamp confirmed that the HPIE protocols did not change CheRiff photocurrents, judged by the level of GFP-expression (**Figure 16**).

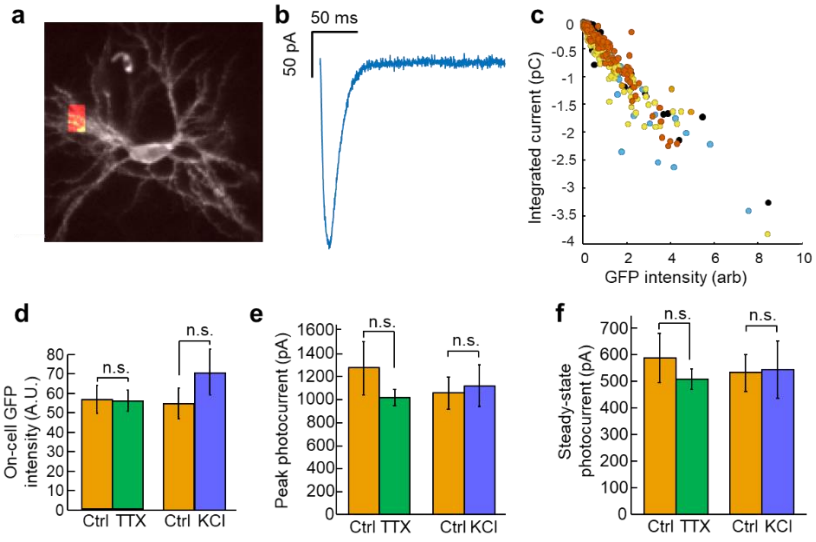

Figure 16. Tests of TTX or KCl chronic treatment on CheRiff expression and function in hiPSC-derived neurons.

a-c) Establishing eGFP signal as a proxy for CheRiff photocurrent. **a**) In cultured rat hippocampal neurons expressing CheRiff were visualized in the GFP channel. **b**) The image was divided in in 96 equal regions (one region highlighted in red) and each of these was stimulated for 10 ms with 488 nm light (1.7 W/cm^2) while recording the induced photocurrent (right). **c**) Plot of integrated photocurrent vs. GFP fluorescence for each region from n=5 cells (colors). GFP was highly correlated with integrate photocurrent (R^2 = 0.895). **d**) Images of eGFP fluorescence were acquired for all hIPSC-derived cells used in HPIE measurements. The mean eGFP fluorescence intensity was quantified for each cell. There was no significant difference in intensity levels between TTX treated cells (n = 31 cells) and their untreated controls (n = 32 cells, p = 0.59). There was also no significant difference in intensity levels between KCl treated cells (n = 28 cells) and their untreated controls (n = 25 cells, p = 0.29). **e-f**) Characterization of photocurrents in treated and untreated cells. Cells were transfected and treated identically to the optical HPIE experiments. Membrane voltage was held at V = -65 mV via manual patch clamp. Photocurrents were elicited by a blue light pulse (1 s, 488 nm, 500 mW/cm^2). There was no significant difference in peak or steady state photocurrents between TTX treated cells and untreated controls (n = 8 TTX treated cells, n = 10 untreated control cells, P = 0.31 for peak photocurrents, P = 0.44 for steady state photocurrents). There was also no significant difference in peak or steady state photocurrents between KCl treated cells and untreated controls (n = 7 KCl treated cells, n = 7 untreated control cells, p = 0.69 for

peak photocurrents, $P = 0.78$ for steady state photocurrents**).** Error bars represent s.e.m. Statistical significance determined by two-tailed student's *t*-test or Mann–Whitney U test.

These experiments demonstrate that human iPSC-derived neurons undergo bidirectional HPIE, and that Optopatch measurements can non-perturbatively report subtle differences in electrophysiology in these cells. High-throughput Optopatch measurements promise to be a powerful tool for functional characterization of neuronal populations in hiPSC-based disease modeling efforts.

2.3 Imaging in organotypic slice culture

Voltage imaging with GEVIs in intact tissue would enable functional mapping of sub-cellular and circuit-level signal processing. Application of GEVIs to recording of APs in mammalian brain tissue has been limited by the low voltage sensitivity and slow response of existing indicators[67,131]. No GEVI has been shown to report single-trial APs in tissue with high fidelity.

We expressed Optopatch2 in organotypic brain slice using biolistic gene delivery. Neurons that had taken up the gene were clearly visible via fluorescence of eGFP (indicating CheRiff) and QuasAr2 under wide-field epifluorescence imaging (20× N.A. 1.0 water immersion objective) (**Figure 17a**). Upon illumination with pulses of blue light (10 ms, repeated at 5 Hz, 7.5 mW/cm^2), the fluorescence under red excitation (1,200 W/cm^2 nominal incident intensity, not corrected for light scatter) showed clearly resolved single-trial APs in the soma and in dendrites (**Figure 17**). These traces represent raw fluorescence, without background subtraction or correction for photobleaching.

We performed Optopatch measurements on $n = 7$ separately prepared organotypic brain slices (**Figure 18**). AP amplitudes ranged from $\Delta F/F = 7.2$ to 26.1% (mean 15.9%, $n = 7$ cells), calculated without subtraction of background autofluorescence. Whole cell-body fluorescence reported APs with SNRs ranging from 7.8 to 65.6 (mean 31.9) in a 1 kHz bandwidth. At lower red excitation intensity (400 W/cm^2 nominal incident intensity, not

corrected for light scatter), whole cell-body fluorescence reported APs with SNRs ranging from 7.2 to 35.7 (mean 16.5) in a 1 kHz bandwidth.

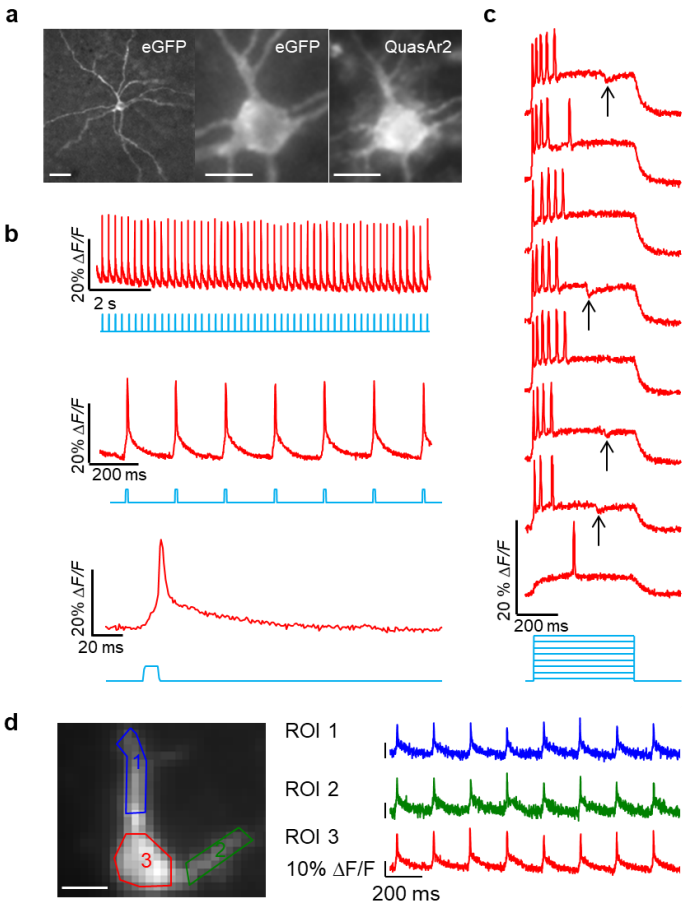

Figure 17. Optopatch2 in organotypic brain slice.

a) Left and middle: eGFP fluorescence, indicating CheRiff distribution. Right: QuasAr2 fluorescence. Scale bars from left to right: 50 μm, 20 μm, 20 μm. **b**) Single-trial optical recordings of APs initiated by pulses of blue illumination (10 ms, 7.5 mW/cm^2). Signal represents whole-soma fluorescence without photobleaching correction or background subtraction. **c**) Bursts of APs triggered by steps of blue illumination (500 ms, 1-10 mW/cm^2). Inhibitory potentials (arrows) were sometimes observed during the stimulation intervals, but not during rest intervals, suggesting inhibitory feedback arising from optically induced network activity. **d**) Optically evoked action potentials (10 ms, 7.5 mW/cm^2, repeated at 5 Hz) in a neuron expressing Optopatch2 in a brain slice. Subcellular fluorescence was extracted by selecting ROIs around two proximal dendrites and the cell body. Scale bar 15 μm. For **b-d**), red illumination was 1,200 W/cm^2 nominal incident intensity, not corrected for light scatter. Fluorescence collected at a frame rate of 1 kHz on an EMCCD camera.

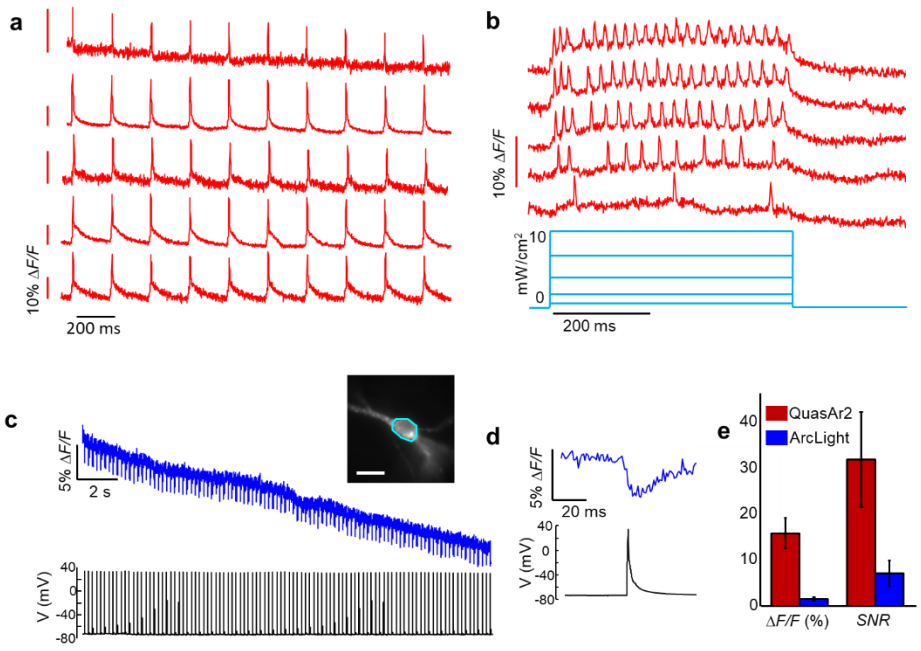

Figure 18. **Optopatch and ArcLight measurements in organotypic brain slice.**

a) Optical recordings of optically evoked action potentials in five cells from separately prepared brain slices expressing QuasAr2. Differences in signal-to-noise ratio reflect differences in cell depth and in expression level. Action potentials were induced with blue light (10 ms, 7.5-15 mW/cm^2, repeated at 5 Hz) and whole-soma fluorescence was recorded at a frame rate of 1 kHz on an EMCCD camera (640 nm illumination 1,200 W/cm^2 nominal incident intensity, not corrected for light scatter). **b**) Sustained spiking in response to steps in blue light intensity (488 nm, 500 ms, increasing intensity from 1 to 10 mW/cm^2). QuasAr2 fluorescence was excited with illumination at 640 nm, 400 W/cm^2 incident on the sample, not corrected for scattering. **c**) Trace of fluorescence transients in a neuron expressing ArcLight A242 (488 nm, 50 W/cm^2) in response to a train of APs. Inset: Image of the neuron. Scale bar 20 μm. Cyan box shows ROI used to extract fluorescence from a high-speed (1 kHz frame rate) movie. **d**) Single-trial fluorescence response of ArcLight (blue) to a single AP (black). **e**) Comparison of QuasAr2 and ArcLight in brain slice. For detection of a single AP, QuasAr2 $\Delta F/F$ was 15.9 ± 3.0% (n = 7 cells), 10-fold larger than ArcLight $\Delta F/F$ (1.5 ± 0.4%, n = 6 cells). QuasAr2 SNR was 31.9 ± 9.5, over 4-fold larger than ArcLight SNR of 7.1 ± 2.8. Illumination conditions for e) were: ArcLight, 488 nm, 50 W/cm^2; QuasAr2, 640 nm, 1200 W/cm^2. Fluorescence was extracted by manual ROI selection of the soma for both ArcLight and QuasAr2. All fluorescent traces and $\Delta F/F$ calculations are presented without background subtraction or correction for photobleaching.

We further tested the response of neurons in tissue to extended pulses of blue illumination (0.5 s, 1 to 10 mW/cm^2). This stimulus elicited a variety of firing patterns, including single spikes, bursts (**Figure 17c**) and sustained activation (**Figure 18**). Optically induced spike trains were often interrupted by hyperpolarizing fluorescence transients, which

we provisionally ascribe to inhibitory feedback in the local micro-circuit. We did not observe these inhibitory potentials in the absence of optical stimulation. These results demonstrate the feasibility of optically measuring single-cell, single-trial AP waveforms, excitability, and subthreshold dynamics in tissue with high SNR.

Finally, we compared Optopatch to ArcLight in organotypic slice (**Figure 18**). Under manual patch clamp stimulation, ArcLight fluorescence resolved single action potentials with a mean value of DF/F = -1.5 ± 0.4% and an SNR of 7.1 ± 2.8 (n = 6 cells) (excitation at 488 nm, 50 W/cm^2). The ArcLight fluorescence transients had a mean width (at 70% maximum deviation) of 21.5 ± 3.0 ms. Thus, QuasAr2 reports action potentials in tissue with greater sensitivity, higher SNR, and better temporal resolution than ArcLight.

2.4 Discussion

The combination of improved reporter and improved actuator in the Optopatch constructs facilitates rapid, non-invasive characterization of genetically defined cells across spatial scales from microns to millimeters, and temporal scales from microseconds to days. Optopatch has not yet been implemented with real-time feedback on the illumination, so it is not suited for voltage-clamp experiments. Nonetheless, with the assistance of computational modeling, open-loop voltage measurements can probe ionic conductances and membrane electrical properties[132,133]. Absolute voltage measurements with GEVIs are challenging due to variations in expression level and membrane trafficking. A recent report demonstrated measurements of absolute voltage through its effect on photocycle dynamics in an Archaerhodopsin mutant[134]. A similar strategy may apply to the QuasArs.

Optopatch is particularly effective for applications in cultured neurons, where large amounts of power can be delivered to the sample without thermal- or photo-damage. As a result, we could use Optopatch to measure pharmacologically-induced excitability phenotypes in primary rodent neurons. When extending to pharamacologically-induced excitability phenotypes in hiPSC-derived neurons, we discovered homeostatic plasticity in intrinsic

excitability similar to that observed in rodent neurons. In the future it will be natural to ask whether hiPSC-derived neurons with genetic perturbations also reveal distinct electrophysiological phenotypes as measured by Optopatch. Excitability assays may probe cell-autonomous functional phenotypes in hiPSC-based models of diseases such as ALS[135], epilepsy[136], and Parkinson's disease[137]. Other neurodevelopmental and neuropsychiatric diseases arise primarily through synaptic dysfunction. These include Rett syndrome[138], Fragile X[139], and Phelan-McDermid syndrome[130]. Development of robust assays of synaptic function will likely benefit from incorporation of cell patterning techniques to control the type and location of synaptic connections. A merit of optical electrophysiology for disease modeling and drug screening is that it does not require mechanical access; thus it is compatible with microfluidic compound delivery and high throughput experimental formats. Optopatch measurements preserve the sterility of the sample and the integrity of the cell membrane, and thus are compatible with studies of long-term responses to chronic pharmacological perturbations.

In addition to work in cultured neurons, we demonstrated Optopatch function in intact mammalian tissue. With extension to multiple genetically specified cells, Optopatch measurements in tissue may provide a useful tool for functional circuit mapping[108]. With improved optical sectioning capability, sub-cellular Optopatch measurements could enable inference of electrophysiological parameters in multi-compartment neural models of single-cell information processing.

Despite this promising illustration, for applications in acute slices and *in vivo,* the new QuasAr reporters are appropriate for measurements on only a few cells or small networks. This limitation occurs because the required laser power scales with the field of view, quickly running into phototoxicity limits in brain tissue. Background autofluorescence and scattering in mammalian brain tissue further complicate imaging and interpretation of QuasAr imaging. Thus *in vivo* applications to larger numbers of cells will likely require further improvements to

the indicator, primarily increased brightness, and exploration of two-photon excitability or other contrast modalities. Small transparent organisms, e.g. zebrafish and *C. elegans*, are early targets as most illumination passes through the body without depositing heat.

Following this work, significant progress has been made by our lab and others toward *in vivo* imaging in rodents, zebrafish, *C. elegans*, and *D. melanogaster* (see Chapter 5 for a summary of recent developments, and Appendix 1 for voltage imaging in fruit fly brain and mouse adrenal cortex).

2.5 Methods

2.5.1 Engineering of Arch.

We adopted a hierarchical approach to screening that prioritized brightness over multiple secondary selection criteria. The brightness screen was conducted by examining the fluorescence of large libraries of variants expressed in bacterial colonies. Subsequent screens for trafficking, speed, and voltage sensitivity were performed in HeLa cells subjected to field stimulation and induced transmembrane voltages, and then in HEK cells with patch clamp.

2.5.1.1 Molecular biology procedure.

Synthetic DNA oligonucleotides used for cloning and library construction were purchased from Integrated DNA Technologies. *Pfu* polymerase (Fermentas) or AccuPrime *Pfx* SuperMix (Invitrogen) were used for high fidelity non-mutagenic PCR amplifications in the buffer supplied by the respective manufacturer. *Taq* polymerase (New England Biolabs) in the presence of $MnCl_2$ (0.1 mM) was used for error-prone PCR. PCR products and products of restriction digests were routinely purified using preparative agarose gel electrophoresis followed by DNA isolation using the GeneJET gel extraction kit (Fermentas). Restriction endonucleases were purchased from Fermentas and used according to the manufacturer's recommended protocol. Ligations were performed using T4 ligase (Invitrogen) or Gibson Assembly (New England Biolabs). Small-scale isolation of plasmid DNA was performed by GeneJET miniprep kit (Fermentas). The cDNA sequences for all Arch variants and fusion

constructs were confirmed by dye terminator cycle sequencing using the BigDye Terminator Cycle Sequencing kit (Applied Biosystems). Site-directed mutagenesis and randomization of targeted codons was performed with either the QuikChange Lightning Single or Multi kit (Agilent Technologies).

2.5.1.2 Construction of Arch mutant libraries.

A library of $>10^4$ mutants was generated by error-prone PCR of the gene encoding Arch D95N. These variants were then joined with the gene encoding mOrange2 by a two-part overlap extension PCR. The 5' piece used in the overlap extension was prepared by error-prone PCR of Arch D95N as template with a mixture of the forward primer (Fw_XbaI_Arch) and reverse primer (RV_Arch). Primer Fw_XbaI_Arch contains an *XbaI* site and primer RV_Arch contains an overlap region with primer FW_Arch_FP. The 3' piece for use in the overlap extension was prepared by high fidelity PCR amplification of mOrange2 using a forward primer (FW_Arch_FP) and a reverse primer (RV_HindIII_FP). Primer RV_HindIII_FP contains a stop codon and a *HindIII* site. The full-length Arch-mOrange2 gene library was assembled by overlap extension PCR using an equimolar mixture of primers Fw_XbaI_Arch and RV_HindIII_FP together with a mixture of the 5' and 3' PCR fragments described above (50 ng each) as the template. In later rounds of directed evolution, error-prone PCR and StEP PCR DNA shuffling[140] were both used for construction of Arch-mOrange2 gene libraries.

The full-length PCR product (approximately 1,500 b.p.) was purified by agarose gel electrophoresis, doubly digested, and ligated between the *XbaI* and *HindIII* sites of a modified pBAD vector which was generated by deleting the ETorA tag between the *NcoI* and *XbaI* sites of the pTorPE vector[141] using Quikchange Lightning kit.

Following ligation, electrocompetent *E. coli* strain DH10B was transformed with the library of gene variants and cultured overnight at 37 °C on 10-cm Petri dishes of LB-agar supplemented with 100 mL of 4 mM retinal (Sigma), 100 mg/mL ampicillin (Sigma), and up

to 0.0020% (wt/vol) L-arabinose (Alfa Aesar). The retinal solution was added on the surface of LB-agar plates evenly and air-dried prior to plating the cell suspension. At concentrations of L-arabinose higher than 0.0020% (wt/vol) we observed abnormal colony morphologies and reduced fluorescent brightness, presumably due to cytotoxicity caused by overexpression.

2.5.1.3 Screening of Arch mutants in E. coli.

The imaging system used for library screening has previously been described in detail[141]. We screened 10,000–20,000 colonies (10–20 plates of bacterial colonies) per round of random mutagenesis. For libraries generated by randomization of one or more codons, we screened approximately 3-fold more colonies than the expected library diversity (e.g. 3,000 colonies for a 1,000-member library).

We acquired two images of colonies using filter sets for mOrange2 (exc. 540-580 nm, em. 600-660 nm) and Arch (exc. 604-640 nm and em. 660-700 nm). An image of the ratio of Arch: mOrange2 fluorescence was calculated, and the colonies with the top 0.01% to 0.1% highest ratios were manually picked. Picked clones were individually cultured in 2 mL liquid LB medium (200 mg/mL ampicillin) shaken (250 rpm) overnight at 37 °C.

Protein expression was induced by adding 2 mL of liquid LB medium containing 120 μM retinal, 200 mg/mL ampicillin and 0.2% L-arabinose to the overnight culture, followed by incubation at 37 °C for 3 hours. The cell pellets were collected by centrifugation, washed and resuspended in buffered M9 salt solution containing 7 g/L Na_2HPO_4, 3 g/L KH_2PO_4, 0.5 g/L NaCl and 1 g/L NH_4Cl. The suspension was then diluted 5-fold prior to acquisition of its fluorescence spectrum in a Safire 2 fluorescence microplate reader (Tecan).

The emission profiles of each variant under excitation at 525 nm and 600 nm were acquired and normalized by the absorbance at 600 nm. The cell pellets of the three variants with the highest ratios of Arch to mOrange2 and the two variants with the brightest absolute Arch fluorescence were treated for plasmid DNA extraction, and the pooled genes were used as templates for construction of gene libraries in the next round of directed evolution.

After five iterations we arrived at a non-pumping variant of Arch with five mutations relative to wild-type (P60S, T80S, D95N, D106Y, and F161V) and substantially improved brightness under excitation with low illumination intensity. This variant, designated Arch 3.5, was used as the template for subsequent efforts to address the secondary selection criteria.

2.5.1.4 Random mutagenesis at positions Asp95 and Asp106.

We next focused on tuning other properties of Arch including voltage sensitivity, response kinetics, membrane trafficking and the undesirable dependence of brightness on illumination intensity. Positions Asp95 and Asp106 of Arch are structurally aligned with positions Asp85 and Asp96 of bacteriorhodopsin, and have been reported to play key roles in proton translocation during the photocycle[142,143]. The voltage sensing mechanism of Arch is likely due to electric-field-dependent protonation of the retinal Schiff base[71,144], so we reasoned that perturbations of the proton translocation network around the Schiff base could potentially affect the voltage sensitivity, response kinetics, or complex photophysics[112].

We constructed libraries in which Asp95 and Asp106 were randomized to a subset of all possible amino acid substitutions. First, we randomized position 95 using codon HVS (where H = A, C or T; V= A, C, or G; S = C or G), which encodes for all amino acids except Ala, Gly, Asp, Glu and Val. This library was screened by fluorescence imaging of *E. coli* colonies. Variants that retained a high ratio of Arch to mOrange2 fluorescence were picked and expressed in HeLa cells for screening via induced transmembrane voltage (see below).

The mutation N95H emerged as the best from the first round of screening in HeLa cells. We then constructed a second library by randomizing position 106 to a subset of amino acids with polar or charged side chains (codon NRC, where N = A, C, G, or T; R = A or G), and screened these in HeLa cells. The variant with histidine at position 106 proved most promising and was designated QuasAr1.

2.5.1.5 Solubilization and spectroscopic characterization of QuasArs

E. coli expressing QuasAr1 and QuasAr2 were grown in 12 mL liquid LB medium with 200 mg/ml ampicillin overnight. The next day, 12 mL of liquid LB medium containing 50 μM retinal, 200 mg/ml ampicillin and 0.1% arabinose was added into the overnight culture, followed by additional incubation at 37 °C for 4 hours. The cell pellets were collected by centrifugation and lysed by suspension in B-PER solution (Pierce). The cytoplasmic fraction was discarded after centrifugation and the colored insoluble fraction was resuspended in phosphate buffered saline (PBS) containing 1.5% n-dodecyl-β-D-maltopyranoside (Affymetrix, Inc.). The suspension was homogenized by an ultrasonic homogenizer and centrifuged (17,000 g for 15 mins, 4 °C). The solubilized protein in the supernatant was used for *in vitro* spectroscopic characterization.

Absorption spectra were recorded on a DU-800 UV-visible spectrophotometer (Beckman) and fluorescence spectra were recorded on a Safire2 plate reader (Tecan). Cy5 carboxylic acid (Cyandye) was used as the reference for quantum yield measurement. Quantum yield measurements were performed on a series of dilutions of each protein solution and standard, with absorbance values ranging from 0.01 to 0.05 at 600 nm. The fluorescence emission spectra of each dilution were recorded with excitation at 600 nm and the total fluorescence intensities obtained by integration. Integrated fluorescence intensity vs. absorbance was plotted for each protein and each standard. Quantum yields, F, were determined from the slopes (*S*) of each line using the equation: $F_{protein} = F_{standard} \times (S_{protein}/S_{standard})$.

2.5.1.6 Expression vectors for HeLa cells.

To express Arch-mOrange2 variants in HeLa cells, the gene in the pBAD vector was first amplified by PCR using primers Fw_BamHI_Kozak_Arch and RV_FP_ERex_stp_XbaI. This reverse primer encodes the endoplasmic reticulum (ER) export sequence from the

inward-rectifier potassium channel Kir2.1 (FCYENE)[145], which has been reported to be effective for improving the membrane trafficking of Arch in mammalian cells[146].

The purified DNA was digested with BamHI and XbaI restriction enzymes and ligated into a purified pcDNA3.1 plasmid that had been digested with the same two enzymes. The ligation reaction was used for transformation of electrocompetent *E. coli* strain DH10B cells. Cells were plated on LB/agar supplemented with ampicillin and individual colonies were picked into 4 mL of LB/ampicillin following overnight incubation at 37 °C. Liquid cultures were shaken at 250 rpm and 37 °C for 12-15 h and then a small-scale isolation of plasmid DNA was performed. Each gene in pcDNA3.1 was fully sequenced using T7_FW, and BGH_RV primers. Plasmids were then used for cell transfection as described below.

2.5.1.7 Induced transmembrane voltage (ITV) in HeLa cells.

We co-expressed prospective Arch variants in HeLa cells with the inward rectifier potassium channel, Kir2.1. Expression of Kir2.1 lowered the resting potential to approximately -60 mV, close to the resting potential of neurons[147,148]. We reasoned that this effect would center the ITV close to the physiologically relevant range.

HeLa cells were grown to 40-60% confluence on home-made 35 mm glass bottom dishes or 24-well glass bottom plates. Cells were transfected with 1 μg of plasmid DNA comprising a 1:1 mixture of Arch variant and Kir2.1, using either 2 μL Turbofect (Thermo Scientific) or 2 μL Lipofectamine 2000 (Invitrogen) according to the manufacturer's instructions. After 3 h incubation, the medium was exchanged to DMEM with 10% fetal bovine serum. Cells were incubated for an additional 24 h at 37 °C in a CO_2 incubator. Immediately prior to imaging, cells were washed twice with Hanks balanced salt solution (HBSS) and then 1 mL of 20 mM HEPES buffered HBSS was added.

Cell imaging was performed with an inverted Eclipse Ti-E (Nikon) equipped with a Photometrics QuantEM 512SC camera, a 150 W mercury-xenon lamp (Hamamatsu), and a 10 mW 638 nm semiconductor diode laser (56ICS/S2669, Melles Griot CleanBeam) aligned

just above the angle for total internal reflection. The filters were: 590-650 nm (excitation), 668-738 nm (emission), and 666 nm (dichroic). Movies were acquired at 10 ms/frame. The NIS-Elements Advanced Research software (Nikon) was used for microscope and camera control and data acquisition. A schematic of the setup is shown in **Figure 1a**.

To probe the response kinetics and voltage sensitivity, we used a pair of parallel platinum electrodes to apply a reproducible electric field across the cell culture and induce transient asymmetries in the membrane voltage[149]. Platinum electrodes with a gap of 0.5 cm were mounted in a custom plastic support. The electrode pair was placed in the imaging dish or well, and voltage pulses from a 6824A 40V/25A DC Power Supply (HP / Agilent) were applied using waveforms generated by a pulse generator PG 58A (Gould Advance Ltd). The typical waveform had square-wave pulses lasting 20 ms, and pulse amplitudes from 25 – 35 V. Fluorescence was imaged at 100 Hz frame rate in 4×4 binning mode for 10 seconds. During each voltage pulse, opposite sides of the cell showed opposite fluorescence transients. Typical fluorescence traces are shown in **Figure 1**.

Raw fluorescence traces were corrected for background autofluorescence and photobleaching. The average voltage sensitivity ($\Delta F/F_{min}$) and signal-to-noise ratio of each Arch variant were compared to the best variant of the previous generation, and only the variants with equal or improved performance were chosen as templates for the next round of screening.

2.5.1.8 Expression vectors for HEK cells and neurons.

To enable more accurate electrophysiological characterization via patch clamp in HEK cells and primary neuron cultures, we cloned QuasAr1 into the BamHI/EcoRI sites of lentivirus vector FCK-Arch-GFP (Addgene: 22217). This vector contains a *CaMKIIa* promoter and a Woodchuck Hepatitis Virus Posttranscriptional Regulatory Element (WPRE) after the 3' end of the open reading frame. The Arch cDNA was generated by PCR using forward primer FW_BamHI_Kozak_Arch_ValSer and overlapping reverse primers

RV_FP_TS and RV_TS_ERex_ stp_EcoRI. These reverse primers introduce a trafficking signal (TS) motif and ER export signal peptide sequence at the C-terminus of the protein.

2.5.1.9 Simultaneous electrophysiology and fluorescence in HEK cells.

HEK293T cells (ATCC CRL-11268) were cultured and transfected following standard protocols[71]. Cells tested negative for mycoplasma. Briefly, HEK-293 cells were grown at 37 ˚C, 5% CO_2, in DMEM supplemented with 10% FBS and penicillin-streptomycin. 400 ng of plasmid DNA was transfected using Transit 293T (Mirus) following the manufacturer's instructions and assayed 48 hours later. The day before recording, cells were re-plated onto glass-bottom dishes (In Vitro Scientific) at a density of ~10,000 cells/cm^2.

Cells were supplemented with retinal by diluting stock retinal solutions (40 μM, DMSO) in growth medium to a final concentration of 5 μM, and then returning the cells to the incubator for 0.5 - 1 hour. All imaging and electrophysiology were performed in Tyrode buffer (containing, in mM: 125 NaCl, 2.5 KCl, 3 $CaCl_2$, 1 $MgCl_2$, 10 HEPES, 30 glucose pH 7.3, and adjusted to 305-310 mOsm with sucrose). A gap junction blocker, 2-aminoethoxydiphenyl borate (50 mM, Sigma), was added to eliminate electrical coupling between cells.

Filamented glass micropipettes (WPI) were pulled to a tip resistance of 5–10 MΩ, and filled with internal solution containing, in mM: 125 potassium gluconate, 8 NaCl, 0.6 $MgCl_2$, 0.1 $CaCl_2$, 1 EGTA, 10 HEPES, 4 Mg-ATP, 0.4 Na-GTP (pH 7.3); adjusted to 295 mOsm with sucrose. Pipettes were positioned with a Sutter MP285 manipulator. Whole-cell, voltage and current clamp recordings were acquired using an Axopatch 700B amplifier (Molecular Devices), filtered at 2 kHz with the internal Bessel filter and digitized with a National Instruments PCIE-6323 acquisition board at 5-10 kHz. Data was only acquired from HEK cells having reversal potentials between -10 and -40 mV, access resistance < 25 MW and membrane resistance > 0.5 GW.

Simultaneous whole-cell patch clamp recordings and fluorescence recordings were acquired on a home-built, inverted epifluorescence microscope, described previously[71] and described below in "Optopatch Apparatus". For step response measurements, voltage clamp electronics were compensated 90-95%. We examined variants of QuasAr1 with mutations at position 95 (Asn, Cys, Gln, His and Tyr) and position 106 (Arg, Asp, Asn, Cys, Glu, His, Lys and Tyr). These experiments confirmed that histidine at position 106 provided undetectable photocurrent, and the best combination of improved voltage sensitivity, and fast kinetics. Mutants with Gln, Cys, or Asn at position 95 exhibited better voltage sensitivity compared to QuasAr1, while retaining fast kinetics. We designated the H95Q mutant QuasAr2.

2.5.1.10 Analysis of mutations in QuasAr1 and QuasAr2.

We developed a structural model of Quasar1 (**Figure 19**) based on homologous protein Arch-2 (PDB: 2EI4, ref. 150). Arch-2 has 90% amino acid identity with Arch-3. Mutations T80S and F161V are in the periphery of the protein, while P60S is close to the Schiff base of the retinal chromophore. Given their location, we suspect that the T80S and F161V substitutions are unlikely to have a direct impact on the photophysical properties of the protein, and are more likely to have a role in improving the folding efficiency. In contrast, the close proximity of the P60S substitution to the Schiff base suggests that this mutation has a more direct influence on the photophysical properties.

We compared the Arch double mutants Arch(D95H, D106H) (termed "HH") and Arch(D95Q, D106H) (termed "QH") to the corresponding QuasAr1 and QuasAr2 mutants do determine whether the mutations in the proton-transport chain were sufficient to induce the improved sensor performance. QuasAr1 and QuasAr2 were both substantially brighter than the corresponding double mutants (**Figure 19**). Furthermore, the voltage sensitivity of the HH, QH, QuasAr1 and wild-type protein were comparable, and three-fold less than the sensitivity of QuasAr2. The QuasArs were faster than their corresponding double mutants.

Thus one or more of the three mutations outside the proton transport chain (P60S, T80S, F161V) plays an important role in the brightness, sensitivity, and speed of the QuasAr mutants.

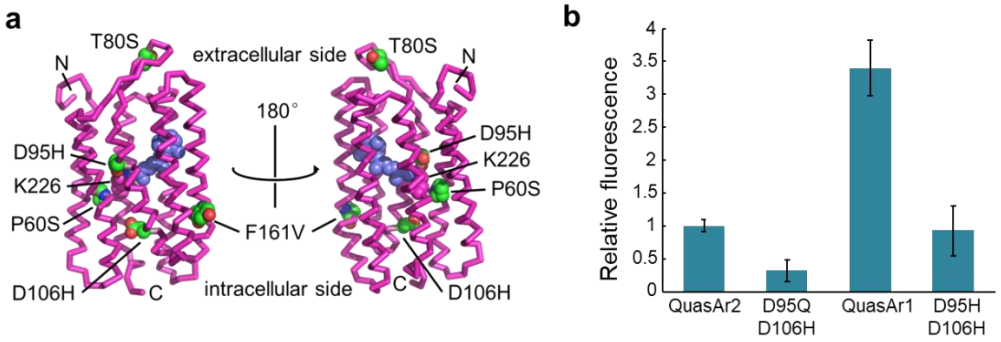

Figure 19. Locations of mutations in QuasAr1.

a) Mutations are modeled on the crystal structure of Arch-2. The retinal chromophore is colored blue and mutations are colored green. **b**) Comparison of fluorescence of QuasAr mutants and Arch double mutants, expressed as eGFP fusions in HEK cells. The double mutants had mutations at the locations of the proton acceptor (Asp95) and proton donor (Asp106) to the Schiff base. QuasAr1 includes mutations D95H, D106H, and QuasAr2 includes mutations D95Q, D106H. The three additional backbone mutations in the QuasArs (P60S, T80S, F161V) increased brightness relative to the double mutants. Fluorescence of each Arch mutant was measured with excitation at 640 nm and emission from 660 – 760 nm. To control for variation in expression level, fluorescence was normalized by eGFP fluorescence (λ_{exc} = 488 nm, λ_{em} = 510 – 550 nm). Error bars represent s.e.m. for measurements on n = 5 - 10 cells.

2.5.2 Engineering of CheRiff.

The gene for *Scherffelia dubia* Channelrhodopsin (sdChR) was synthesized with mouse codon optimization. This gene was selected from a screen of channelrhodopsins for its blue excitation peak (474 nm) and its large photocurrent relative to ChR2. However, the trafficking in neurons was poor (**Figure 6**). Addition of a trafficking sequence from Kir2.1 improved trafficking greatly[145]. Addition of the ER2 export motif did not appear to further improve trafficking, so this motif was not included in the final construct.

The improved membrane trafficking led to large photocurrents in neurons under blue excitation (2470 ± 170 pA peak, 488 nm, 500 mW/cm^2, n = 3 cells) but also led to unacceptably large photocurrents from the red laser used to illuminate the QuasArs (38 ± 4 pA, steady state, 640 nm, 300 W/cm^2). Furthermore, the off-time was undesirably slow (t_{off} =

26.0 ± 2.9 ms). Based on experience with mutations in other rhodopsins, we introduced the mutation E154A, which only slightly decreased the peak photocurrent under blue illumination (to 2030 ± 100 pA, n = 10), but decreased the crosstalk from red illumination (to 10.5 ± 2.8 pA) and shortened t_{off} to 16.0 ± 0.8 ms. This variant, termed CheRiff, showed excellent trafficking and neural activation at low illumination intensities.

The action spectrum of CheRiff was measured in HEK293 (n = 6 cells) with a monochromator (Till-Photonics Polychrome IV). 10 ms pulses of nearly equal photon fluxes (~2.5×10^{21} photons/s/m^2) were used across wavelengths. Small deviations in photon flux between wavelengths were corrected by dividing the recorded opsin response by the measured photon dose. For each cell, wavelengths were swept from blue-to-red and red-to-blue, and the responses were averaged.

2.5.3 Design of Optopatch.

We used a 2A peptide ribosomal skip sequence as a means to achieve approximately stoichiometric coexpression of the QuasArs and CheRiff. The porcine teschovirus-1 (P2A) sequence performed better than the *Thosea asigna* virus (T2A) sequence. Owing to the greater need for high expression of the voltage indicator than the actuator, we placed the QuasAr gene before the P2A sequence and the CheRiff gene after.

In some applications one might wish to use the visible spectrum for other imaging modalities, e.g. for a reporter of Ca^{2+} or a GFP expression marker. In such cases, it is inconvenient to have GFP and mOrange2 fused to CheRiff and Arch, respectively. Removal of the eGFP tag from Arch resulted in poor membrane localization in neurons. To maintain the beneficial trafficking properties of the eGFP tag while eliminating the eGFP fluorescence, we mutated the eGFP chromophore from TYG to GGG using site-directed mutagenesis (Agilent). This mutation has been reported to preserve folding of eGFP[151]. We also made versions of Optopatch in which the mOrange2 was mutated to a non-fluorescent form by the mutation TYG to TAG.

Optopatch constructs were incorporated into lentiviral vectors under the *CaMKIIa* promoter, adapted from Addgene plasmid 22217.

2.5.4 Neuronal culture and gene delivery.

All procedures involving animals were in accordance with the National Institutes of Health Guide for the care and use of laboratory animals and were approved by the Institutional Animal Care and Use Committee at the institution at which they were carried out.

2.5.4.1 Primary neurons.

Rat glial monolayers were prepared similarly to ref. 152. Briefly, 10^6 dissociated hippocampal cells from P0 rat pups (Sprague Dawley, Tocris)[153] were plated on a 10 cm culture dish in glial medium GM, comprised of 15% FBS (Life), 0.4% (w/v) D-glucose, 1% glutamax (Life), 1% penicillin/streptomycin (Life) in MEM (Life). When the dish reached confluence (1-2 weeks), cells were split using trypsin onto glass-bottomed dishes (In Vitro Scientific, D35-20-1.5-N) coated with poly-D-lysine and matrigel (BD biosciences) at a density of (3500 cells/cm^2). After ~ 3-6 days, glial monolayers were at or near confluence and the medium was replaced by GM with 2 μM cytarabine (cytosine-b-arabinofuranoside, Sigma). Dishes were maintained in GM with 2 μM cytarabine until use. Dishes were discarded if microglia or neurons were identified on the monolayers.

Hippocampal neurons from P0 rat pups were dissected and cultured in neurobasal-based medium (NBActiv4, Brainbits llc.) at a density of 30,000-40,000 cm^{-2} on the pre-established glial monolayers[153]. At one day *in vitro* (DIV), cytarabine was added to the neuronal culture medium at a final concentration of 2 μM to inhibit further glial growth[154]. Neurons were transfected on DIV 7 with the QuasArs or Optopatch plasmids via the calcium phosphate transfection method[155]. Measurements on neurons were taken between DIV 13-18.

For comparisons between CheRiff, ChR2 H134R and ChIEF, neurons were plated on glass-bottom dishes coated with poly-d-lysine (Sigma P7205) and matrigel (BD biosciences 356234) without pre-established glial monolayers. On DIV 3 cytarabine (2 mM) was added.

Cells were transfected on DIV 7 with channelrhodopsin-eGFP fusions, in identical lentiviral plasmids with a *CaMKIIa* promoter. All comparison measurements were taken between DIV14-15 at room temperature (23 °C).

For TTX-induced homeostatic plasticity, primary neurons were transfected via the calcium phosphate method on DIV7. TTX (1 μM) was added on DIV 16. Excitability was measured on DIV 18 in Tyrodes medium with synaptic blockers (10 μM NBQX, 25 μM AP-V, 20 μM Gabazine).

2.5.4.2 hiPSC-derived neurons.

Human iPSC-derived iCell neurons were purchased from Cellular Dynamics Inc. Neurons were tested negative for mycoplasma by the manufacturer. Neurons were thawed and resuspended in complete iCell Neuron Maintenance Medium (CM) following manufacturer protocols. Cells were then plated at a density 125,000/cm^2 on pre-established rat glial monolayers grown on glass-bottomed dishes. Medium was replaced 24 hours post plating with CM supplemented with 10 ng/mL BDNF (Peprotech). Thereafter, 50% media exchanges with CM were done every 5 days.

For TTX-induced homeostatic plasticity, hiPSC-derived neurons were transfected via the calcium phosphate method on DIV17. TTX (1 μM) was added on DIV 26. Excitability was measured on DIV 28 in Tyrodes medium with synaptic blockers (10 μM NBQX, 25 μM AP-V, 20 μM Gabazine).

For KCl-induced homeostatic plasticity, hiPSC-derived neurons were transfected on DIV 10. KCl (15 mM) was added from DIV 18 to DIV 21 (60 h). Excitability was measured on DIV 21 in Tyrodes medium with synaptic blockers (10 μM NBQX, 25 μM AP-V, 20 μM Gabazine).

2.5.4.3 Organotypic brain slice culture.

Organotypic hippocampal slices cultures were prepared from postnatal day 6-8 Sprague-Dawley rats as described previously[156]. The brain was taken out and immediately

placed in chilled dissection media. Transverse hippocampal slices were cut with 400 μm thickness and 4 to 6 slices were placed in a sterile culture plate insert (Millicell-CM, Millipore) in 6-well plates containing prewarmed media. Slices were biolistically transfected with a Helios Gene Gun (BioRad) at 2 days in vitro (DIV 2). Bullets were prepared using 12.5 mg of 1.6 μm gold particles and 80 - 100 mg of plasmid DNA. Slices were maintained until imaging at DIV 12-16.

Immediately prior to inverted imaging, slices were affixed to a nylon mesh weight and mounted upside down in a delta T brainslice adapter for inverted microscope imaging (Bioptechs). Artificial cerebrospinal fluid (ACSF) was bubbled with carbogen (95% O_2, 5% CO_2) and flowed over the slice at 1 mL/min at 23 °C.

2.5.5 Electrophysiology in neurons.

Measurements were performed on primary cultures at 13 - 15 DIV. Experiments were conducted in Tyrode's solution containing 125 mM NaCl, 2.5 mM KCl, 3 mM $CaCl_2$, 1 mM $MgCl_2$, 10 mM HEPES, 30 mM glucose (pH 7.3) and adjusted to 305–310 mOsm with sucrose. Prior to imaging, neurons were incubated with 5 μM all-*trans* retinal for 30 minutes and then washed with Tyrode's solution.

Synaptic blockers were added to the imaging medium for measurements of single-cell electrophysiology. The blockers comprised NBQX (10 μM, Tocris), D(−)-2-amino-5-phosphonovaleric acid (AP5; 25 μM, Tocris), and gabazine (SR-95531, 20 μM, Tocris). For measurements of channelrhodopsin photocurrents in neurons, TTX (1 μM, Tocris) was included along with the synaptic blockers to prevent recruitment of voltage gated sodium channels. Patch clamp data was used if and only if access resistance was < 25 MΩ, and did not vary over the experiment. Recordings were terminated if membrane resistance changed by > 10%. Experiments were performed at 23 ºC under ambient atmosphere unless otherwise noted.

For Comparison of QuasArs to ArcLight A242, ArcLight A242 was prepared in an identical lentiviral plasmid driven by a *CaMKIIa* promoter and was transfected (DIV 7) in parallel with the QuasAr plasmids in paired cultures. We used a standard ArcLight imaging intensity of 10 W/cm^2 at 488 nm. QuasAr expressing neurons were imaged at two intensities (300 and 800 W/cm^2). All recordings were made on the setup described below ("Optopatch apparatus") at a 1 kHz frame rate and 60x magnification. Due to its slow kinetics at room temperature, ArcLight recordings were made at 34 °C to enhance SNR and to match previously published conditions[72]. QuasAr2 reported APs with comparable SNR at 23 °C and 34 °C (41 ± 3, n = 8 cells, 300 W/cm^2). For comparisons in organotypic brain slice, ArcLight was imaged at 50 W/cm^2 on an upright microscope to enable simultaneous patch clamp stimulation and recordings. Recordings were made at a 1 kHz frame rate as described below ("Optopatch apparatus") and were acquired at 34 °C.

2.5.6 Immunostaining.

Cultures were fixed immediately following data acquisition in a solution of 4% paraformaldehyde and 4% sucrose (w/v) in PBS, pH 7.4 at room temperature for 8 minutes. Fixed cultures were then washed three times in Dulbecco's PBS supplemented with Ca^{2+} and Mg^{2+} (DPBS), pH 7.4, prior to permeabilization and blocking in a solution of 0.1% (w/v) gelatin and 0.3% Triton-X-100 (v/v) in PBS, pH 7.4 (GTB) for 12-48 hours at 4C.

For experiments using the sub-frame interpolation algorithm, primary cultures were fixed and stained using primary mouse monoclonal anti-ankyrin G (NeuroMab clone N106/36; 1:500), primary rabbit monoclonal anti-GFP (Abcam ab32146, lot YK011702CS, 1:1000), secondary goat anti-rabbit AlexaFluor 488 conjugated (Abcam ab150077, 1:500), and secondary goat anti-mouse AlexaFluor 647 conjugated (Abcam ab150115, 1:500) antibodies.

For experiments on human iPSC derived neurons, cultures were incubated with primary mouse anti-human nuclear antigen antibody (Millipore MAB1281 clone 235-1,1:500) in GTB overnight at 4 °C, then washed three times in DPBS, and incubated with rabbit anti-

GFP AlexaFluor 488 conjugated (polyclonal, Life A21311, 1:300) and secondary antibody donkey anti-mouse AlexaFluor 647 (Life A31571, 1:300) in GTB overnight at 4C. Cultures were washed three times in DPBS prior to mounting in DAPI Fluoromount-G (Southern Biotech).

2.5.7 Optopatch measurements.

Experiments were conducted on a home-built inverted fluorescence microscope[71]. Briefly, illumination from a red laser 640 nm, 140 mW (Coherent Obis 637-140 LX), was expanded and focused onto the back-focal plane of a 60× oil immersion objective, numerical aperture 1.45 (Olympus 1-U2B616). Imaging of brain slices was performed with a 20× water-immersion objective, numerical aperture 1.0 (Zeiss W Plan-Apo).

Illumination from a blue laser 488 nm 50 mW (Omicron PhoxX) was sent through an acousto-optic modulator (AOM; Gooch and Housego 48058-2.5-.55-5W) for rapid control over the blue intensity. The beam was then expanded and modulated by a digital micromirror device (DMD) with 608×684 pixels (Texas Instruments LightCrafter). The DMD was controlled via custom software (Matlab) through a TCP/IP protocol. The DMD chip was re-imaged through the objective onto the sample, with the blue and red beams merging via a dichroic mirror. Each pixel of the DMD corresponded to 0.65 μm in the sample plane. A 532 nm laser was combined with the red and blue beams for imaging of mOrange2. We wrote software to map DMD coordinates to camera coordinates, enabling precise optical targeting of any point in the sample.

To achieve precise optical stimulation of user-defined regions of a neuron, it was necessary to determine the mapping from pixels on the DMD to pixels on the camera. A uniform fluorescent film (exc. 488 nm, em. 515 nm) was loaded into the microscope. The DMD projected an array of dots of known dimensions onto the sample. The camera acquired an image of the fluorescence. Custom software located the centers of the dots in the image and created an affine transformation to map DMD coordinates onto camera pixel coordinates.

A dual-band dichroic (Chroma zt532/635rpc) separated fluorescence of mOrange2 and Arch from excitation light. A 531/40 nm bandpass filter (Semrock FF01-531/40-25) and 495 nm longpass dichroic (Semrock FF495-Di03) was used for eGFP imaging, a 710/100 nm bandpass filter (Chroma, HHQ710/100) was used for Arch imaging, and a quad-band emission filter (Chroma ZET405/488/532/642m) was used for mOrange2 imaging and pre-measurement calibrations. A variable-zoom camera lens (Sigma 18-200 mm f/3.5-6.3 II DC) was used to image the sample onto an EMCCD camera (Andor iXon$^+$ DU-860), with 128 × 128 pixels. The variable zoom enabled imaging at a range of magnifications while maintaining the high light collection efficiency of the oil or water immersion objectives.

In a typical experimental run, images of mOrange2 and QuasAr fluorescence were first acquired at full resolution (128 × 128 pixels). Data was then acquired with 2 × 2 pixel binning to achieve a frame rate of 1,000 frames/s. For experiments with infrequent stimulation (once every 5 s), the red illumination was only on from 1 s before stimulation to 50 ms after stimulation to minimize photobleaching. Cumulative red light exposure was typically limited to < 5 min. per neuron, although continuous red light exposure for 30 minutes was well tolerated (**Figure 4**). Full resolution eGFP images were taken after functional recordings to prevent CheRiff excitation prior to the experiment.

Low magnification wide-field imaging was performed with a custom microscope system based around a 2×, NA 0.5 objective (Olympus MVX-2). Illumination was provided by six lasers 640 nm, 500 mW (Dragon Lasers 635M500), combined in three groups of two. Illumination was coupled into the sample using a custom fused silica prism, without passing through the objective. Fluorescence was collected by the objective, passed through an emission filter, and imaged onto a scientific CMOS camera (Hamamatsu Orca Flash 4.0). This microscope imaged a 1.2 × 3.3 mm field of view with 3.25 μm spatial resolution and 2 ms temporal resolution, or a 4 × 4 mm field of view with 10 ms temporal resolution.

Blue illumination for channelrhodopsin stimulation was provided by a 473 nm, 1 W laser (Dragon Lasers), modulated in intensity by an AOM and spatially by a DMD (Digital Light Innovations DLi4130 – ALP HS). The DMD was re-imaged onto the sample via the 2× objective. The DMD provided targeted stimulation with excitation with 3.5 μm spatial resolution and 0.1 ms temporal resolution.

During an experimental run, we first acquired an image of a neuron using wide-field illumination at 640 nm to probe Arch fluorescence, and/or 532 nm to probe mOrange2 fluorescence. A user then selected one or more regions of interest on the image of the neuron, and specified a timecourse for the illumination in each region. The software mapped the user-selected pixels onto DMD coordinates and delivered the illumination instructions to the DMD.

Illumination parameters for the data in **Figure 8** were: c) Blue illumination: 488 nm, 25 mW/cm^2, 10 ms pulses, repeated at 5 Hz. d) Stimulation targeted to soma: 488 nm, 95 mW/cm^2, 10 ms pulses, repeated at 5 Hz. e) Stimulation targeted to soma in ROI 1: 488 nm, 140 mW/cm^2, 10 ms pulses, repeated every 15 s. f) Excitation targeted to dendrites: 488 nm, 100 mW/cm^2, 50 ms pulses, repeated at 5 Hz. Movie constructed from an average of 203 temporally registered APs. g) Whole-field stimulation: 488 nm, 0 to 10 mW/cm^2, 500 ms pulses, repeated at 6 s intervals.

Synaptic blockers were added to suppress network activity.

2.5.8 Data analysis.

2.5.8.1 Statistics.

All error ranges represent standard error of the mean, unless otherwise specified. For two-sample comparisons of a single variable, data was tested for normality using the Shapiro-Wilks test. If the data was detectably non-Gaussian, we performed a nonparametric Mann-Whitney U test. Otherwise we performed a two-tailed Student's *t*-test. Channelrhodopsin multi-way comparisons of a single variable were made using a one-way ANOVA with

Dunnett's post-hoc test, using CheRiff as a reference. No channelrhodopsin dataset was detectably non-Gaussian (Shapiro-Wilks). Probabilities of the null hypothesis $p < 0.05$ were judged to be statistically significant.

2.5.8.2 Extracting fluorescence from movies.

Fluorescence values were extracted from raw movies in one of two ways. One approach used the maximum likelihood pixel weighting algorithm described in ref. 17. Briefly, the fluorescence at each pixel was correlated with the whole-field average fluorescence. Pixels that showed stronger correlation to the mean were preferentially weighted. This algorithm automatically found the pixels carrying the most information, and de-emphasized background pixels. This approach was used for all experiments in cultured neurons. In images containing multiple neurons, the segmentation was performed semi-automatically using an independent components-based approach[157].

Alternatively, a user defined a region comprising the cell body and adjacent processes, and calculated fluorescence from the unweighted mean of pixel values within this region. With the improved trafficking of the QuasAr mutants compared to Arch, the maximum likelihood pixel-weighting algorithm was only marginally superior to manual definition of an ROI (**Figure 20**). For calculations of $\Delta F/F$ in culture, background fluorescence from a cell-free region was subtracted from the baseline fluorescence of the cell. In measurements in brain slice, fluorescence was calculated from manually defined ROIs with equal pixel weighting and no background subtraction or correction for photobleaching.

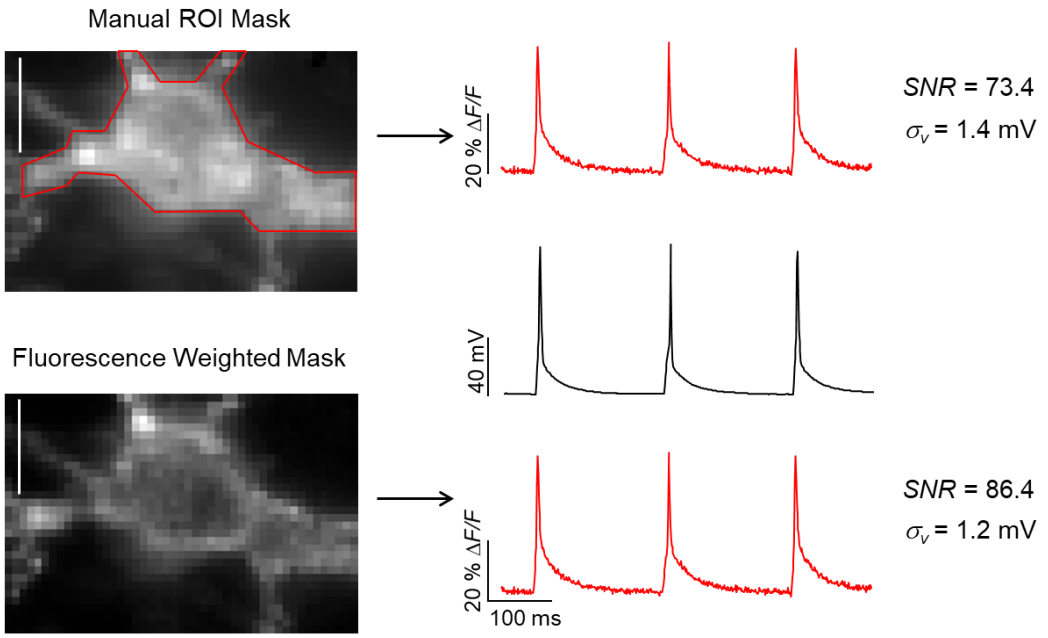

Figure 20. Extraction of fluorescence traces from QuasAr movies.

Fluorescence can either be calculated by manually defining a region of interest (ROI; top row), or by preferentially weighting the pixels whose intensity co-varies with the whole-field average (bottom row)[2]. The noise in the fluorescence trace when scaled to match the electrical recording is denoted σ_v. With the improved trafficking of the QuasAr mutants compared to Arch, the automated technique gave only slightly higher SNR than manual definition of the ROI. The technique makes no use of the electrode readout. Cell shown is the source of the data in **Figure 2h**. All comparisons of SNR in culture were made on measurements taken with the same 60x objective, collected on the same EMCCD, and extracted using this automated technique. For recordings on cultured neurons, values of $\Delta F/F$ were calculated after subtracting background autofluorescence from a cell-free region of the field of view. This background subtraction was not performed on recordings in tissue.

2.5.8.3 Precision of optically recorded AP timing.

To determine the temporal precision of the QuasAr indicators, we used the sub-frame interpolation algorithm[122,123] to infer the timing with which the fluorescence reached 70% of maximum at each AP, and compared to simultaneously acquired high time-resolution patch clamp recordings. Root-mean-square (r.m.s.) temporal jitter was 44 µs for QuasAr1 (n = 97 APs) and 61 µs for QuasAr2 (n = 99 APs). This jitter reflects the combined errors in timing intrinsic to the optical measurement (shot-noise and distortion of the waveform by the reporter) and errors introduced by temporal discretization of the camera frames and the sub-

frame interpolation. Thus optical recordings with QuasArs can determine spike timing with precision much greater than the camera exposure time.

2.5.8.4 Fitting channelrhodopsin photocurrents.

Photocurrents of the channelrhodopsins were characterized following previously described protocols[114]. Briefly, peak photocurrents in response to a light pulse (488 nm, 0.5W/cm^2, 1 s duration) were identified by first smoothing the traces using robust Loess method with a filter width of 2 ms, and then finding the extremum of the filtered trace after laser onset and subtracting the baseline current. Time to peak (t_{on}) was defined as the time between light onset and peak photocurrent of the filtered trace. The steady-state photocurrent was found by fitting a monoexponential curve to the filtered trace from 2 ms after the peak until laser offset. The offset of this fit was defined as the steady-state photocurrent. The time constant of this fit was defined as the desensitization rate (τ_{des}).The channel closure rate (τ_{off}) in response to a light pulse (488 nm, 0.5W/cm^2, 5 ms duration) was measured by fitting a monoexponential to the decay of the photocurrent after light offset.

Illumination intensities for 50% effective light power density[114] (EPD50, **Table 3**) values were determined from measurements of peak photocurrents versus a series of whole field illumination intensities. For each cell, peak photocurrents at each intensity were first normalized by the maximum peak photocurrent. The resulting curves were then fit with a simple binding model ($Y = B_{max} \times X / (EPD50 + X)$). The reported EPD50s are the average of the fit parameters from $n = 5$ cells.

2.5.8.5 Sub-frame interpolation of AP timing.

The sub-frame interpolation algorithm consists of a series of computational image-processing steps (**Figure 10**). Each step may be modified to account for experiment-specific attributes of the data.

A neuron was induced to fire through repeated optical stimulation of a user-selected subcellular compartment (typically soma or dendrite). We typically observed 5%

photobleaching over a 40 s acquisition. Photobleaching was typically dominated by non-specific background fluorescence, rather than by photobleaching of QuasAr, and often photobleaching did not follow a simple single-exponential decay. The photobleaching baseline was constructed from the whole-field intensity by a sliding minimum filter, followed by a sliding mean filter. Each frame of the movie was then corrected by dividing by this baseline.

QuasAr fluorescence intensity $F(t)$ was determined either by the regression algorithm described in ref. 17 or by whole-field average intensity. Both procedures gave similar results, with slightly better signal-to-noise ratio returned by the regression algorithm (**Figure 20**).

Determination of spike times was performed iteratively. A simple threshold-and-maximum procedure was applied to $F(t)$ to determine approximate spike times, $\{T_0\}$. Waveforms in a brief window bracketing each spike were averaged together to produce a preliminary spike kernel $K_0(t)$. We then calculated the cross-correlation of $K_0(t)$ with the original intensity trace $F(t)$. Whereas the timing of maxima in $F(t)$ was subject to errors from single-frame noise, the peaks in the cross-correlation, located at times $\{T\}$, were a robust measure of spike timing. A movie showing the mean AP propagation was constructed by averaging movies in brief windows bracketing spike times $\{T\}$. Typically 100 – 400 APs were included in this average. The AP movie had high signal-to-noise ratio, but did not clearly show signal propagation.

We applied spatial and temporal linear filters to further decrease the noise in AP movie. The spatial filter consisted of convolution with a Gaussian kernel, typically with a standard deviation of 1 pixel. The temporal filter was based upon Principal Components Analysis (PCA) of the set of single-pixel time traces. The time trace at each pixel was expressed in the basis of PCA eigenvectors. Typically the first 5 eigenvectors were sufficient to account for >99% of the pixel-to-pixel variability in AP waveforms, and thus the PCA eigendecomposition was truncated after 5 terms. The remaining eigenvectors represented uncorrelated shot noise (**Figure 10**). Projections of the movie onto the PCA eigenvectors only

showed spatial features above noise for the first 5 eigenvectors (**Figure 10c** inset). To verify that the spatial and PCA filtering did not distort the underlying AP waveforms, we compared mean AP waveforms in subcellular compartments before and after the smoothing steps (**Figure 10d**). We observed no systematic deviations in the AP waveforms in the axon, soma, or dendrites.

The user then set a threshold depolarization to track (represented as a fraction of the maximum fluorescence transient), and a sign for dV/dt (indicating rising or falling edge). We chose 50% maximal depolarization on the rising edge. The filtered data was fit with a quadratic spline interpolation and the time of threshold crossing was calculated for each pixel to create a map of the AP delay (**Figure 10e**).

The sub-frame timing precision of the algorithm was calibrated by patch clamp measurements. Optically induced APs were recorded simultaneously via QuasAr1 fluorescence in the soma and by conventional patch clamp, also in the soma (**Figure 10f**). The r.m.s. error in timing was 54 ms in this instance, and did not show systematic bias at the frame boundaries.

The fits were converted into movies showing AP propagation as follows. Each pixel was kept dark except for a brief flash timed to coincide with the timing of the user-selected AP feature at that pixel. The flash followed a Gaussian timecourse, with amplitude equal to the local AP amplitude, and duration equal to the cell-average time resolution, *s*. Frame times in the sub-frame interpolation movies were selected to be ~2-fold shorter than *s*.

Occasionally it was possible to enhance the spatial resolution of the high temporal resolution movies by mapping the timing data onto a higher spatial resolution static image of fluorescence of eGFP (from the CheRiff-eGFP fusion, **Figure 10g**) or of QuasAr1. The pixel matrix of the sub-frame interpolated movie was expanded to match the dimensions of the high resolution image and the amplitude at each pixel was then set equal to the mean brightness at that pixel. Selected frames from the resulting movie showed AP initiation at the axon initial

segment in the first two frames (**Figure 10h**). To assemble the color movies (**Figure 8f**, **Figure 10**), the timing signal was assigned to a colormap which was overlayed on a gray-scale image of mean QuasAr fluorescence. Optionally, the optically stimulated region of the cell was highlighted in blue.

2.6 Author contributions

Yongxin Zhao performed the directed evolution on Archaerhodopsin in the laboratory of Robert E. Campbell. Nathan Klapoetke and Yong Ku Cho performed the initial screen of algal channelrhodopsins in the laboratory of Edward S. Boyden's based on transcriptomic profiling from Michael Melkonian and Gane Ka-Shu Wong. Daniel R. Hochbaum and Samouil L. Farhi performed final optimization of QuasAr and CheRiff and developed the Optopatch construct. Daniel R. Hochbaum designed the high magnification Optopatch system and Christopher A. Werley designed the ultra-widefield Optopatch microscope. Daniel R. Hochbaum and Samouil L. Farhi acquired all-optical electrophysiology data. Peng Zou contributed biophysical characterization data on QuasAr. Dougal Maclaurin conceived the SNAPT algorithm. Joel Kralj performed acute drug measurements in hIPSC-derived neurons. Niklas Smedemark-Margulies and Jessica Saulnier assisted with sample preparation. Gabriella L. Boulting aided with immunostaining. Christoph Straub and Vikrant Kapoor assisted with slice electrophysiology. Daniel R. Hochbaum, Dougal Maclaurin, Samouil L. Farhi, and Adam E. Cohen analyzed data. D. Jed Harrison, Venkatesh N. Murthy, and Bernardo L. Sabatini supervised parts of the project. Adam E. Cohen conceived and supervised the project.

Namrata Anand, Lucy Rosenbaum, Tony Shen, and Vedha Nathan provided technical assistance. Adam Douglass, Alice Ting, Feng Zhang, Loren Looger, and Doug Kim provided helpful discussion; Cellular Dynamics Inc. offered technical assistance with hiPSC neurons.

This chapter was adapted from previously published work:

Hochbaum DR*, Zhao Y*, **Farhi SL**, Klapoetke N, Werley CA, Kapoor V, Zou P, Kralj JM, Maclaurin D, Smedemark-Margulies N, Saulnier J, Boulting GL, Straub C,

Cho YK, Melkonian M, Wong GK, Harrison DJ, Murthy VN, Sabatini BL, Boyden ES, Campbell RE, Cohen AE. All-optical electrophysiology in mammalian neurons using engineered microbial rhodopsins. *Nature Methods* **11**, 825-833 (2014).

3 FlicR1, a fast, bright, red-shifted voltage indicator

3.1 Background

In Chapter 2 we introduced the first genetically-encoded all-optical neurophysiology system, Optopatch. Despite its utility in cultured neurons, Optopatch proved difficult to apply to more than a handful of neurons in intact neural tissue, primarily because even the enhanced brightness QuasArs were much dimmer than conventional GFP-based fluorophores. To overcome this limitation, we sought to develop a fast and sensitive voltage indicator which would be red-shifted to enable combination with optogenetic stimulation and bright enough to image larger fields of view of intact tissue.

We decided to focus on proteins with a high degree of homology to GFP, which we refer to as fluorescent proteins (FPs). The design that has proven most successful for developing Ca^{2+} indicators with large dynamic range is based on fusing a circularly permuted (cp) FP[52] to a Ca^{2+}-sensing domain[53,141,158,159]. Similarly designed voltage indicators, constructed by fusing FPs to voltage-sensing domains, typically suffer from small response amplitude, slow kinetics, and/or poor membrane localization[54,55]. However, two recently reported green FP-based voltage indicators, ArcLight[72] and ASAP1[160], were able to resolve single action potentials in neurons in single trials.

Red-shifted fluorophores that require longer wavelength excitation light provide the added advantages of lower phototoxicity, deeper tissue penetration, and lower autofluorescent background[161]. Moreover, they are spectrally distinct from green fluorescent indicators and blue-light-excitable channelrhodopsin variants[162]. Unfortunately, the only reported attempt to engineer an indicator based on a cp red FP (cpRFP) resulted in indicators that are not practically useful due to small fluorescence responses (~1% $\Delta F/F$ to 200 mV step potentials)

and slow kinetics (τ_{on} ~60 ms and τ_{off} ~150 ms)[63]. We set out to develop a new FP-based voltage indicator that combined the advantages of red-shifted fluorescent emission with the higher brightness of FPs while also affording the fast kinetics required to report neuronal activity. Note that we follow the convention of referring to FPs that emit in the 590–620 nm range as "red," although such wavelengths are more accurately described as orange.

Here, we describe the development of a bright and fast red voltage indicator based on a fusion of a cpRFP (cpmApple) and the voltage-sensing domain from a *Ciona intestinalis* voltage-sensitive phosphatase[163]. This fusion was used as a template for directed protein evolution to improve brightness and voltage sensitivity. The end product is FlicR1 (fluorescent indicator for voltage imaging, red), with kinetics and relative response amplitude comparable to the best available green voltage indicators. We show that FlicR1 reports single action potentials in single-trial recordings from neurons and can track high-frequency voltage fluctuations (up to 100 Hz). We also demonstrate that FlicR1 can be combined with a blue-shifted channelrhodopsin, PsChR[164], and spatially patterned blue illumination to simultaneously perturb and image membrane potential in the same neuron. However, blue light photoactivation of the FlicR1 chromophore, as observed in R-GECO1, which has the same FP barrel and chromophore[165], presents a challenge for applications that require spatially overlapping yellow and blue excitation.

3.2 Results

3.2.1 Development of FlicR

The first step for creating the voltage indicator was to make a chimera from the genes for a red-shifted FP and a voltage-sensitive domain (**Figure 21a,b**). Our choice of the red-shifted FP to use as the template was inspired by the x-ray crystal structure[166] of the Ca^{2+} indicator R-GECO1[141]. The structure reveals that the Lys80 (R-GECO1 numbering) side chain from the surface of the cpmApple-derived β-barrel engages in an electrostatic interaction with the phenolate oxygen of the chromophore. This structural evidence, combined with

additional mutagenesis results[167], points to this interaction as the mechanistic basis for the response of R-GECO1. Because the lysine is part of the β-barrel (in contrast to GCaMP, in which the key interaction is with an arginine from CaM[168]), we reasoned that the cpmApple domain is likely a self-contained unit that would retain its fluorescence modulation mechanism even if the Ca^{2+} sensitive domain were replaced with an alternative sensing domain.

We chose to use *Ci*-VSP as the voltage-sensitive domain to fuse to cpmApple because it localizes properly to the cell membrane of mammalian cells, as demonstrated by its successful use in recent FP-based voltage indicators[60,62–64,67,72]. We elected to use a cpFP to increase the chance of coupling voltage-induced conformational changes in the voltage-sensitive domain to a change in the FP chromophore environment, likely through its influence on the conformation of the Lys80 side chain. Specifically, fusion of cpmApple to the C terminus of *Ci*-VSP should bring Lys80 and the chromophore near the mobile S4 helix of the voltage-sensitive domain. We hypothesized that this design should maximize the likelihood of developing an indicator with fast kinetics because movement of S4 could influence the chromophore environment directly.

Although directed protein evolution has been one of the main strategies to improve FP properties and FP-based Ca^{2+} indicators[53,141], it has not been widely implemented for voltage indicators. To facilitate our directed evolution strategy, we designed a high-throughput workflow for screening of voltage indicators (**Figure 21c**). This procedure was divided into two steps: an *E. coli* bacterial colony screen for brightness and a mammalian cell screen for voltage sensitivity. The second step of the screen also enabled us to assess the membrane localization of the engineered variants so that variants that do not localize properly can be excluded from further rounds of screening. In brief, libraries of genes encoding voltage indicator variants were inserted in a dual bacterial and mammalian expression vector and used to transform *E. coli*. After overnight growth on agar plates, the red fluorescence of the colonies was imaged using a custom fluorescence imaging setup[169] that can image ~1000 colonies

simultaneously, enabling the screening of tens of thousands of variants per round. The brightest variants were cultured and their plasmid DNA was used to transfect HeLa cells coexpressing ArcLight Q239 and an inward-rectifying potassium channel (Kir2.1). ArcLight Q239 provides an internal reference to assess voltage sensitivity. Kir2.1 hyperpolarizes the resting membrane potential of HeLa cells to ~−60 mV[147,170,171] to mimic that of neurons. The transfected cells were subjected to 10 ms electrical field pulses using a custom-built field stimulation system and fluorescence response to stimulation was recorded (**Figure 21d-g**). FlicR variants with the highest voltage sensitivity were selected to go on to the next round of directed evolution.

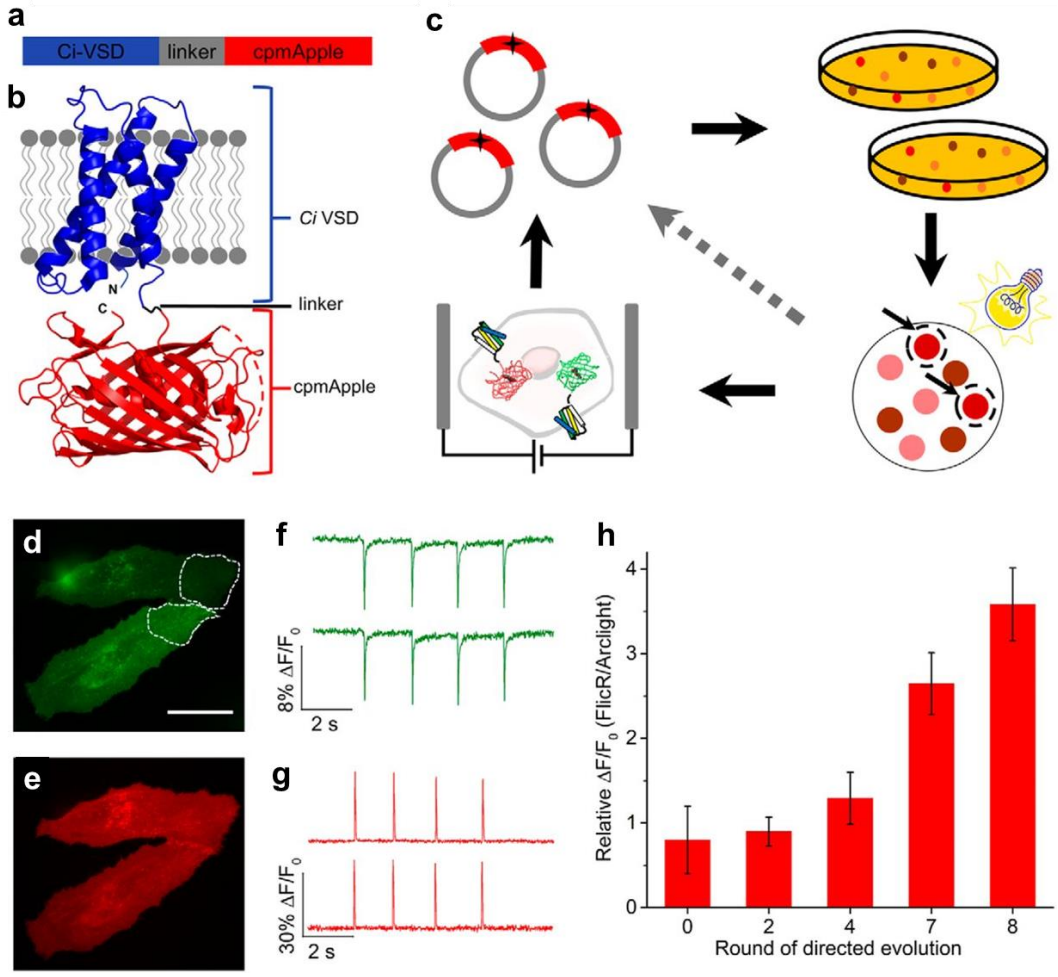

Figure 21. Schematic representation of FlicR indicator and directed evolution process.

a,b) Representation of FlicR indicator. **b**) Model of FlicR1 represented by the crystal structures of *Ci*-VSP (PDB ID 4G80)[172] and cpmApple (PDB ID 4I2Y)[166]. **c**), Schematic representation of directed evolution strategy used to develop FlicR1. First, libraries of DNA-encoding indicator genes were transformed into *E. coli* and cultured on agar plates. Second, *E. coli* colonies expressing FlicR1 were illuminated with yellow light. Colonies with bright red fluorescence were picked and screened for voltage sensitivity in mammalian cells. Voltage sensitivity of FlicR1 variants was then tested via field stimulation in HeLa cells coexpressing ArcLight. **d,e**) Image of HeLa cells coexpressing ArcLight Q239 (d) and FlicR1 (e), Scale bar,10 μm. **f**) ArcLight fluorescence response of two regions shown in (d) to electrical field stimulation pulses (10 ms, 25 V). **g**) FlicR1 fluorescence response of the same two regions shown in (d) to electrical field stimulation pulses (10 ms, 25 V). **h**) Improvement in voltage sensitivity of FlicR variants during directed evolution represented as a ratio of response amplitude in HeLa cells compared with ArcLight Q239. Error bars indicate SD (n = 10-15 cells). Fluorescence imaging for field stimulation measurements was performed at 100 Hz. Illumination intensities were 0.2 W/cm^2 for FlicR1 and 0.1 W/cm^2 for ArcLight Q239.

For our first-generation construct, we fused cpmApple (residues 60–304, R-GECO1 numbering (**Figure 22**)[166] to the C terminus of *Ci*-VSP truncated at residues 236–242 to construct seven variants. We chose these positions to bring cpmApple as close as possible to the S4 helix. The shortest linker that exhibited fluorescence was the variant with *Ci*-VSP truncated at 239. Our experience with evolving FP-based indicators[72,141,165,173] has shown that even small adjustments in the linker between the sensing domain and the FP are critical to the indicator function. In an effort to identify the optimal composition of the linker between *Ci*-VSP and the cpmApple domain, we created a library of 1024 gene variants (400 protein variants) by fully randomizing the codons for two residues immediately after residue 239 of *Ci*-VSP (Pro240 and Val241, respectively). Screening of this library for red fluorescence, followed by voltage sensitivity tests in HeLa cells subjected to field stimulation, led to the identification of a variant with mutation Pro240Arg. We designated this variant as our first-generation FlicR. This FlicR variant (FlicR0.1) exhibited dim fluorescence that was responsive to membrane potential changes in mammalian cells, albeit with a small response amplitude (**Figure 21h**). Notably, FlicR0.1 (and all subsequent variants) exhibits an increase in fluorescence in response to membrane depolarization, whereas ArcLight and ASAP1 exhibit decreases in fluorescence (**Figure 23**). To evolve FlicR0.1 brightness and voltage sensitivity,

we used both rational design and directed protein evolution by multiple rounds of construction and screening of libraries containing thousands of variants.

Figure 22. Sequence alignment of FlicR1.

Alignment of FlicR1 gene with the *Ci*-VSP domain (top) and cpmApple (residues 60–304, R-GECO1 numbering) from R-GECO1 (bottom). The red highlighted residues are the amino acid mutations of FlicR1 compared with the starting template. Residues MYG in the box correspond to the mApple chromophore. Calmodulin (CaM) and the M13 peptide are not shown in the R-GECO1 sequence.

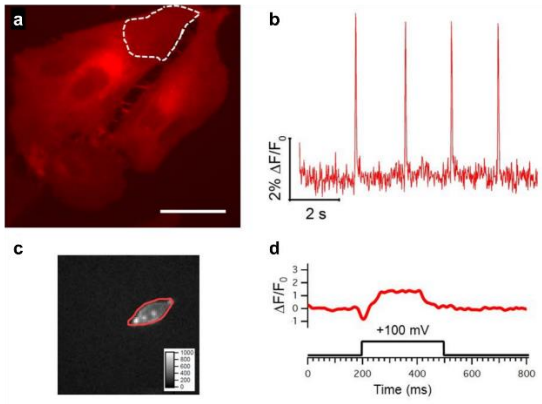

Figure 23. FlicR0.1 response to electric field stimulation in HeLa cells and membrane potential step in HEK293 cells.

a) Image of HeLa cells expressing FlicR0.1. Scale bar 10 μm. **b**) FlicR0.1 fluorescence response of regions shown in (a) to electrical field stimulation pulses (~50 V/cm, 20 ms). **c**) Image of HEK293 cells expressing FlicR0.1 under the CMV promoter. **d**) FlicR0.1 fluorescence response (top) to a 300 ms square wave in membrane potential (lower panel) from −70 mV to +30 mV acquired at 1 ms intervals. Fluorescence imaging for field stimulation measurements was performed at 100 Hz. Illumination intensity was 0.2 W/cm^2.

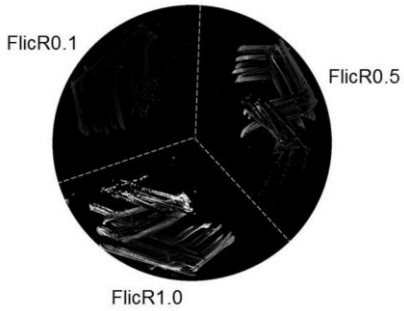

Figure 24. Evolution of FlicR brightness in *E. coli*.

Fluorescence image of *E. coli* expressing various FlicR variants using pcDuEx0.5.

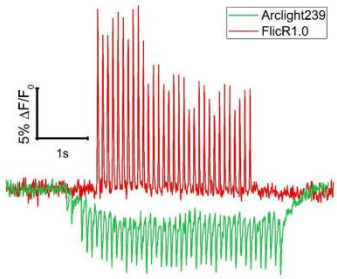

Figure 25. FlicR1 and ArcLight Q239 response to electric field stimulation in HeLa cells.

Fluorescence trace of FlicR1 (red) and ArcLight Q239 (green) to a train of electrical pulses (50V/cm, 10 ms) at 10 Hz. Traces were recorded consecutively in the same cell co-expressing FlicR1 and ArcLight Q239. Fluorescence traces were collected at 100 Hz using an EMCCD camera. Illumination intensities were 0.2 W/cm^2 for FlicR1 and 0.1 W/cm^2 for ArcLight Q239. Although ArcLight Q239 has a larger full response amplitude (35% ΔF/F per 100 mV)[72] than FlicR1 (6.6% ΔF/F per 100 mV), the slower kinetics of ArcLight Q239 prevent it from reaching its full response amplitude during a 10 ms pulse.

In a typical round of directed evolution, we used error-prone PCR to create a large library based on our most promising template(s) and then screened the library using the workflow described above. A mixture of the three to six variants with the brightest fluorescence, proper membrane localization, and largest responses to voltage change would then be used as the template for the next round of library creation by random mutagenesis.

Four rounds of this procedure led to FlicR0.5, which was 16 ± 3-fold brighter than FlicR0.1 (n = 100 colonies, **Figure 24**) and could easily be imaged with wide-field fluorescence microscopy when expressed in mammalian cells. Three more rounds of evolution were then performed, with greater emphasis placed on identifying variants with improved voltage sensitivity rather than improved brightness. This effort led to the identification of the Val207Ala mutation, located in the S3 to S4 linker of the *Ci*-VSP, which provided a pronounced improvement in voltage sensitivity. For the eighth round of evolution, we mutated position 207 to all 20 possible amino acids and screened the library as before. The best variant identified from this library harbored the Val207Phe mutation that further improved the voltage sensitivity (**Figure 21e,g**). This variant, which has 12 mutations relative to FlicR0.1 (**Figure 22**), was designated as FlicR1. Relative to ArcLight Q239, FlicR1 has a 3.6 ± 0.4-fold (n = 12 HeLa cells) greater fluorescence response to a 10 ms electrical pulse (**Figure 21d-h**). When stimulated with a train of electrical pulses at 10 Hz, FlicR1 fluorescence response showed faster response and decay kinetics compared with ArcLight Q239, which did not return to baseline between stimulations (**Figure 25**).

3.2.2 Characterization of FlicR1 in HEK cells

To quantify the voltage sensitivity and speed of FlicR1, we expressed it under a CMV promoter in HEK cells and used whole-cell voltage clamp to change membrane potential while recording FlicR1 fluorescence under 561 nm illumination (10 W/cm^2). FlicR1 trafficked well to the membrane of HEK cells (**Figure 26a**). When we applied a triangle wave of membrane voltage from −100 mV to +50 mV, fluorescence increased almost linearly with membrane voltage, with a fluorescence change ($\Delta F/F_0$) of 6.6 ± 0.6% (n = 5) per 100 mV (**Figure 26b,d**). This sensitivity is almost an order of magnitude larger than previously reported cpRFP-based voltage sensors[63]. To measure the kinetics of FlicR1, we stepped membrane voltage between −70 and +30 mV at 22°C (**Figure 26c**). These steps induced a rapid biexponential response in the fluorescence of FlicR1, with a dominant fast component that had a 3.0 ± 0.2 ms time

constant accounting for 90% of the activation response. For deactivation, the fast component made up 70% of the response and had a time constant of 2.8 ± 0.3 ms (**Figure 26f**, **Table 5**). These values compare favorably to ArcLight Q239 kinetics at 22°C, which follow a biexponential response to the same protocol with time constants of 28 ± 8 ms (39%) and 271 ± 6 ms (61%) for the rising edge and of 100 ± 20 ms (61%) and 280 ± 40 ms (39%) (n = 6) for deactivation (**Figure 26e,g,h**, **Table 5**). We repeated the FlicR1 measurements at 34°C and found that the time constant of the fast component decreased to 0.74 ± 0.06 ms (90%) for activation and 0.93 ± 0.07 ms (79%) for deactivation (n = 6) (**Figure 26f**, **Table 5**). The sensitivity at this temperature was 6 ± 1% per 100 mV and was not significantly different from the value at 22°C (n = 6, p = 0.49, two-tailed Student's t-test).

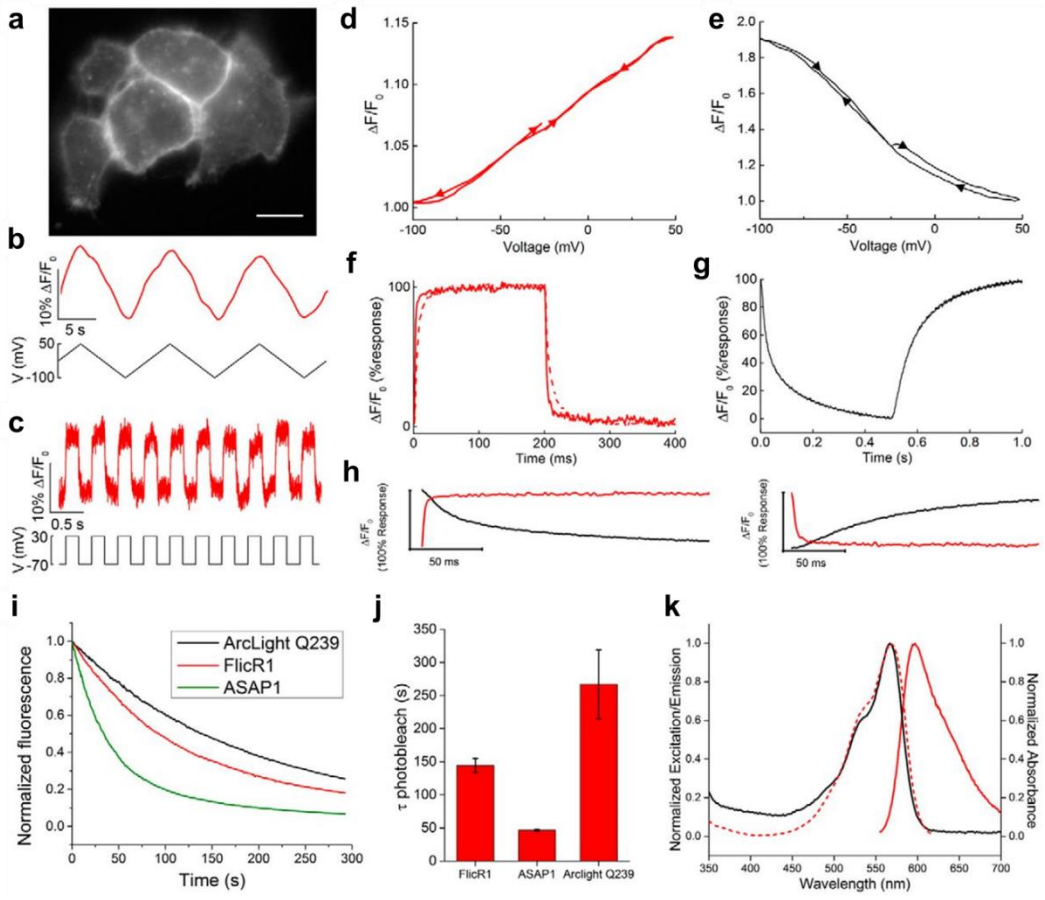

Figure 26. Characterization of FlicR1.

a), Image of HEK293 cells expressing FlicR1 under the CMV promoter. Scale bar, 10 μm. **b**), Fluorescence response (top) to a triangle wave in membrane potential (bottom) from −100 mV to +50 mV. Fluorescence trace (acquired at 10 Hz) is filtered using a 15 point moving-average low-pass filter. **c**) FlicR1 fluorescence response (top) from a representative cell to a square wave in membrane potential (bottom) from −70 mV to +30 mV. **d-e**) FlicR1 (d) and ArcLight Q239 (e) fluorescence as a function of membrane voltage in a representative HEK293 cell. Fluorescence is the mean of three ramp cycles from −100 mV to +50 mV and back. Fluorescence is plotted starting at −25 mV, depolarizing to +50 mV, hyperpolarizing to −100 mV, and then returning back up to −25 mV as marked by the arrows. Fluorescence showed little hysteresis between increasing and decreasing voltage ramps. **f**) FlicR1 fluorescence response to a 100 mV step potential in HEK293 cells. Solid line shows fluorescence response at 34°C. Dotted line shows fluorescence response at 22°C. **g**) ArcLight Q239 fluorescence response to a 100 mV step potential in HEK293 cells 22°C. Note the different time axis compared with (f). **h**) Magnification of the "on" and "off" portions of 22°C fluorescence traces from FlicR (red) and ArcLight (black). **i**) Normalized bleaching curves for FlicR1, ArcLight, and ASAP1 in HEK239 cells. **j**) Time constants for photobleaching of FlicR1, ASAP1, and ArcLight Q239 in HEK293 cells using continuous 10 W/cm^2 561 nm light illumination for FlicR1 and continuous 10 W/cm^2 488 nm light illumination for ASAP1 and ArcLight Q239. Fluorescence was captured every 500 ms. Time constants are based on single exponential fits. Error bars indicate SEM for FlicR1 (n = 5 cells), ASAP1 (n = 5 cells), and ArcLight Q239 (n = 4 cells). **k**) Spectral characterization of FlicR1 *in vitro*. Shown are absorbance (solid black line), excitation (dotted red line), and emission (solid red line) of FlicR1. Fluorescence imaging for voltage-sensitivity measurements was performed at 10 Hz. Step responses were recorded at 2 kHz for FlicR1 and 1 kHz for ArcLight Q239. Illumination intensities were 10 W/cm^2.

	22°C		34°C	
	Activation -70 to +30 mV	Deactivation +30 to -70 mV	Activation -70 to +30 mV	Deactivation +30 to -70 mV
FlicR1				
τ_1 fast (ms)	3.0 ± 0.2	2.8 ± 0.3	0.74 ± 0.06	0.93 ± 0.07
τ_2 fast (ms)	41 ± 7	18 ± 3	27 ± 6	14 ± 6
% fast component	90 ± 2	70 ± 4	90 ± 2	79 ± 4
n	5	5	6	6
ArcLight Q239				
τ_1 fast (ms)	28 ± 8	100 ± 20	9 ± 1	17 ± 1
τ_2 fast (ms)	271 ± 6	280 ± 40	48 ± 4	60 ± 7
% fast component	39 ± 8	61 ± 15	50 ± 3	79 ± 3
n	6	6	6	6

Table 5. FlicR1 and Arclight Q239 kinetics in HEK293 cells.

Values for ArcLight Q239 at 34 °C are reproduced from ref. 72.

We compared the rate of photobleaching of FlicR1 with other FP-based voltage indicators using 10 W/cm^2 of either 561 nm (FlicR1) or 488 nm light (ASAP1 and ArcLight Q239) (**Figure 26i**). Single exponential fits gave photobleaching time constants of 150 ± 10 s (n = 5 cells) for FlicR1, 47 ± 1 s (n = 5 cells) for ASAP1, and 300 ± 30 s (n = 4 cells) for

ArcLight Q239 (**Figure 26j**). Measurement of the absorbance, excitation, and emission spectra of FlicR1 *in vitro* (**Figure 26k**) revealed excitation and emission maxima of 570 and 597 nm, respectively.

The fact that the absorption spectrum of FlicR1 is red shifted relative to other FP-based voltage sensors made it a promising candidate for two-photon excitation in the 1100–1300 nm range. To test the utility of FlicR1 for two-photon imaging, a two-photon scanning-beam microscope set to deliver 1120 nm excitation pulses was used to image HEK cells expressing FlicR1. Under whole-cell voltage clamp, the membrane voltage was varied in a square wave between −100 and +100 mV at 2 Hz. FlicR1 responded with a fluorescence change $\Delta F/F$ of 9 ± 1% per 100 mV (n = 8 cells) (**Figure 27a**).

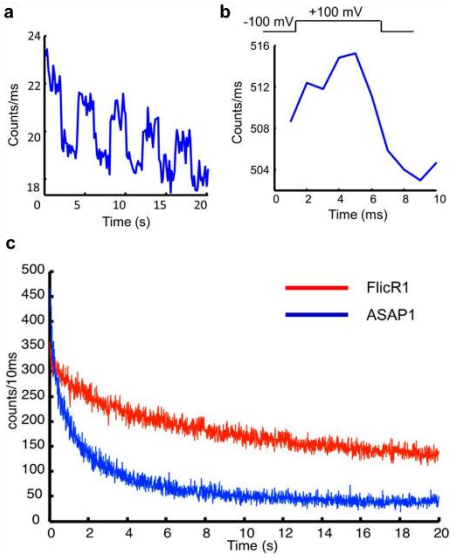

Figure 27. Two-photon imaging of FlicR1 in HEK cells.

a), Uncorrected fluorescence response of FlicR1 during −100 to +100 mV voltage steps (0.25 Hz square wave, 2 s +100 mV, 2 s −100 mV) when excited at 1120 nm in image-scanning mode (6.5 frames/s). **b**) Fluorescence intensity as a function of time for a 1000 Hz point scan of FlicR1 fluorescence during a 100 Hz voltage square wave (5 ms +100 mV, 5 ms −100 mV; n = 50 cycles averaged). **c**) Fluorescence intensity as a function of time for a point scan of ASAP1 excited at 950 nm and FlicR1 excited at 1120 nm. Fluorescence is sampled at 100 Hz, with excitation power (~1 mW at both wavelengths) tuned to achieve ~400 counts per bin initially.

The speed of the FlicR1 response to a voltage step under two-photon excitation was tested in point-recording mode. Cells were subjected to a square wave in voltage from −100

to +100 mV at 100 Hz and fluorescence was recorded at 1 kHz from a single point on the cell membrane (**Figure 27b**). FlicR1 is an order of magnitude more stable to two-photon photobleaching compared with ASAP1 (**Figure 27c**), which enabled us to do point measurements. FlicR1 was fast and sensitive enough to resolve these voltage changes, although the signal amplitude was limited to ~2% per 200 mV at 100 Hz (**Figure 27b**). Due to rapid photobleaching under static two-photon illumination, we did not pursue two-photon voltage imaging further. However, imaging with a beam that rapidly traces the contour of a cell membrane could ameliorate photobleaching and provide a viable option for further exploration[174].

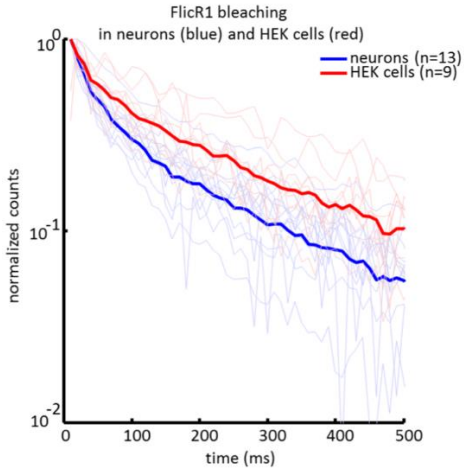

Figure 28. Comparison of photobleaching rates of FlicR1 in neurons and HEK cells.

Under 2- photon excitation, FlicR1 bleaches faster in neurons than in HEK cells (n = 13 neurons, n = 9 HEK cells) all recorded with excitation at 1120 nm with ~10 mW power. Thick lines are averages of their kind. Traces taken as point recordings without scanning the 2-photon excitation beam

3.2.3 Imaging and characterization of FlicR1 in cultured neurons

An important benchmark for a voltage indicator is to resolve single action potentials in single neurons with single-trial recording. Based on the characterization in HEK cells, we reasoned that the combination of the high fluorescence response and fast kinetics of the FlicR1 fluorescence signal would allow it to record neuronal activity in single-trial recordings.

To test this hypothesis, we transfected cultured hippocampal neurons with FlicR1 driven under the control of human synapsin I promoter.

FlicR1 labeled the plasma membrane both at the cell body and in individual dendrites (**Figure 29a**). It also showed intracellular puncta in the cell bodies similar to other cpmApple-derived indicators. When imaged at 100 Hz using a wide-field fluorescence microscope with a 200 W lamp (0.2 W/cm^2 power fluence at sample), membrane-localized FlicR1 clearly reported spontaneous activity of the transfected neurons (**Figure 29b,c**) with a signal amplitude of $\Delta F/F = 4.3 \pm 0.6\%$ ($n = 7$) corresponding to an SNR of 9 ± 2 ($n = 7$).

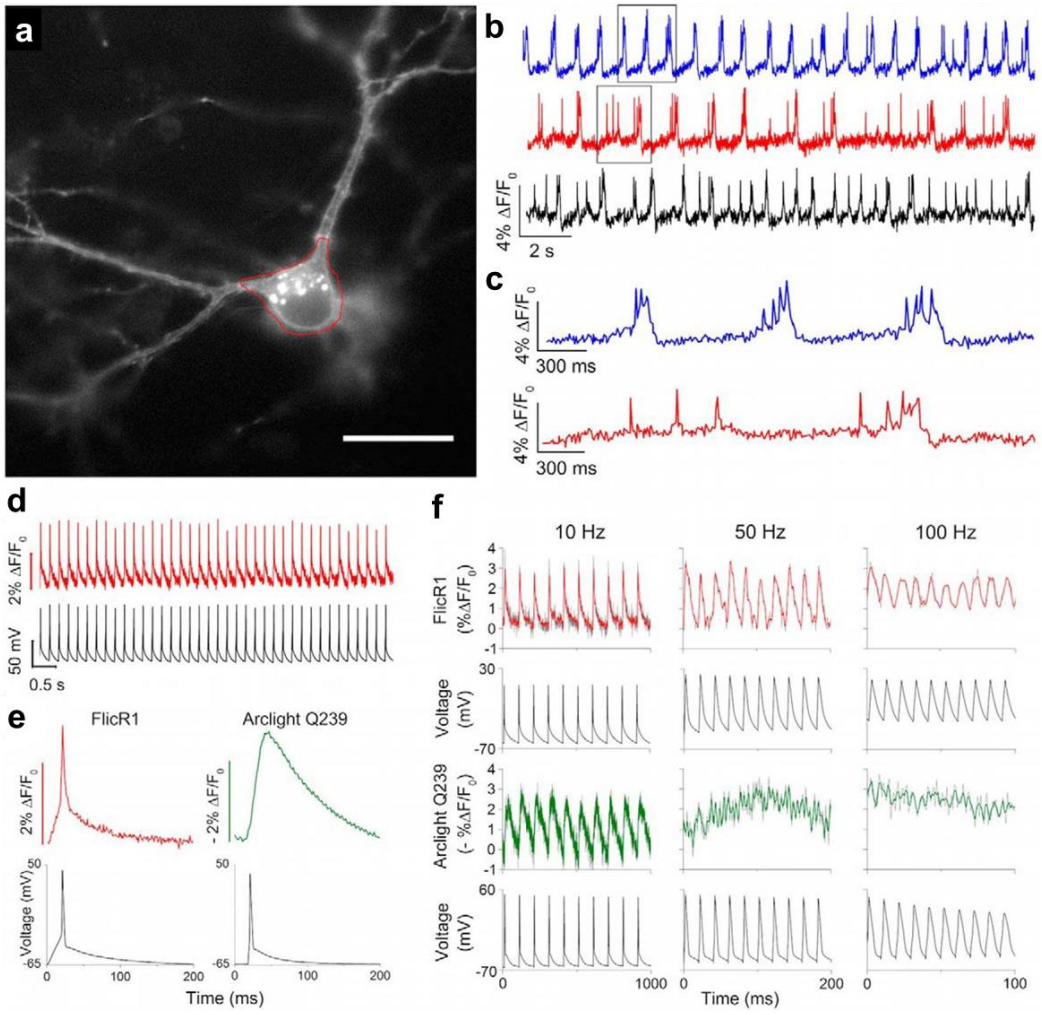

Figure 29. FlicR1 characterization in neurons.

a) Image of cultured hippocampal neuron expressing FlicR1. Scale bar, 30 μm. **b**) Detection of spontaneous activity waveforms in rat hippocampal neuron culture with FlicR1 indicator. Sample single-trial recordings of spontaneous action potential bursts from three neurons. Red trace is from cell in (a). **c**) Magnification of regions marked in (b). **d**) FlicR1 fluorescence response to 5 Hz stimulated action potential train. **e**) Mean fluorescence response of FlicR1 (left) and ArcLight Q239 (right). **f**) FlicR1 (top) and ArcLight (bottom) response to 10, 50, and 100 Hz stimulated action potential trains in neurons. Colored traces are filtered with Savitzky–Golay smoothing (5 points) and are overlaid over the grayscale unfiltered traces. All traces have single exponential correction of bleach. For (a-c), fluorescence was recorded at 100 Hz frame rate and illumination intensity was 0.2 W/cm^2. For (d-f), fluorescence was acquired at a 1 kHz frame rate and 10 W/cm^2 illumination intensity. Colored traces in (d-f) are filtered with Savitzky–Golay smoothing (5 points) for both FlicR1 and ArcLight Q239.

We next characterized the response of FlicR1 to action potentials in neurons. All measurements were performed at 22°C at a frame rate of 1 kHz while illuminating with 10 W/cm^2 561 nm light. In whole-cell current-clamp mode, we stimulated action potentials in neurons transfected with either FlicR1 or ArcLight Q293. FlicR1 faithfully reported single action potentials with a change in fluorescence of $\Delta F/F = 2.6 \pm 0.8\%$ ($n = 7$), averaging over the entire cell body (**Figure 29d**), corresponding to an SNR of 6 ± 1 ($n = 7$). ArcLight Q239 showed a similar fluorescence response amplitude to single action potentials ($\Delta F/F = -3.4 \pm 0.9\%$, $n = 5$). However, because FlicR1 had faster kinetics than ArcLight, the fluorescence signal of FlicR1 more closely matched the electrical trace and was not broadened to the extent that it was with ArcLight Q239 (**Figure 29e**). To investigate FlicR1's ability to track high-frequency firing in neurons, we stimulated action potentials at frequencies from 5 Hz to 100 Hz ($n = 7$). FlicR1 reported voltage fluctuations of up to 100 Hz, clearly discriminating individual peaks in single trial recordings (**Figure 29f**). In contrast, ArcLight Q239 was not able to discriminate peaks at speeds >10 Hz and only showed increased baseline fluorescence (**Figure 29f**). We detected no significant differences in action potential amplitude ($p = 0.16$, two-tailed Student's t test), membrane resistance ($p = 0.67$), or membrane capacitance ($p = 0.21$) between ArcLight Q239 ($n = 6$) and FlicR1 ($n = 7$) transfected cells.

3.2.4 Imaging brain slice activity with FlicR1

To test whether FlicR1 provides sufficient spatial and temporal resolution to report spontaneous activity in neuronal tissue, we expressed and imaged FlicR1 in organotypic rat

brain slices. Organotypic rat hippocampal slices have been shown to maintain native hippocampal morphology and function and show spontaneous network activity[175]. FlicR1 was delivered under human synapsin I promoter using *ex vivo* electroporation. To test the long-term effect of expression of FlicR1, hippocampal slices were cultured for 22–25 d (18–21 d after transfection). Transfected neurons were clearly visible under wide-field epifluorescence imaging (**Figure 30a,d**). Wide-field epifluorescence imaging of FlicR1 successfully reported spontaneous activity of transfected neurons in single-trial optical recordings when excited with constant yellow light illumination using a 100 W mercury lamp (0.4 W/cm^2 power fluence at sample). A signal amplitude of $\Delta F/F = 4 \pm 1\%$ and an SNR of 8 ± 2 ($n = 12$ cells) was obtained when averaging over the whole cell body. This was compared with a signal amplitude of $\Delta F/F = 9 \pm 2\%$ ($n = 12$ cells) and an SNR of 8 ± 2 obtained by averaging multiple ROIs in dendritic regions (**Figure 30b,c**). We attribute the difference in signal amplitude to the presence of unresponsive puncta in the cell bodies. We also used theophylline to pharmacologically excite FlicR1-transfected neurons in organotypic brain slices. Theophylline has been shown to evoke sustained rhythmic, seizure-like activities in different neuronal networks including hippocampal neurons[176]. Indeed, upon treatment with theophylline, FlicR1 successfully reported seizure-like voltage oscillations when imaged at 50 Hz using the same 100 W mercury lamp with a signal amplitude of $\Delta F/F = 9 \pm 2\%$ ($n = 12$ cells), which corresponds to an SNR of 14 ± 2 ($n = 12$) (**Figure 30e**).

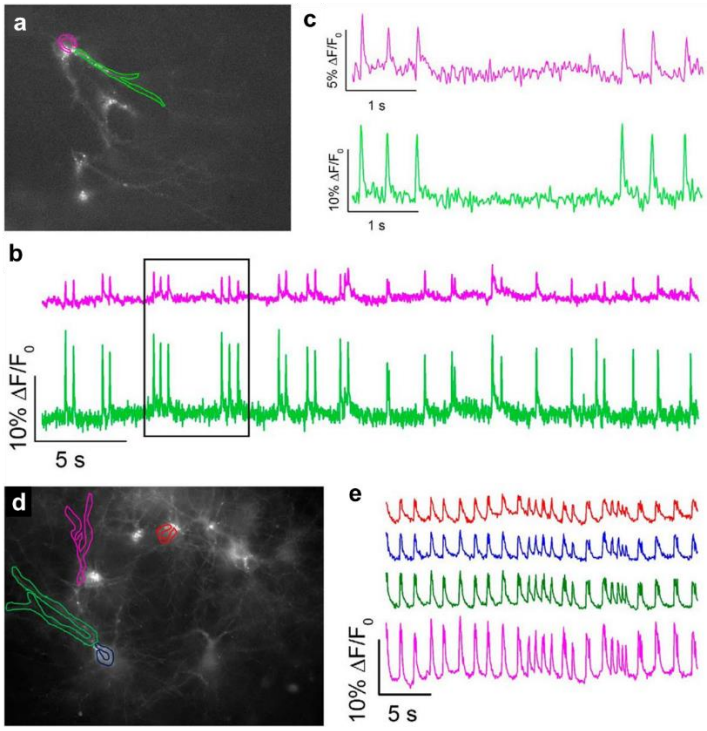

Figure 30. Detection of spontaneous activity and theophylline-induced activity in rat hippocampal brain slice with FlicR1 indicator.

a) Fluorescence image of hippocampal brain slice transfected with FlicR1 and imaged 21 d after transfection. Neuron processes are clearly labeled with FlicR1. Both cell bodies and processes show some fluorescence puncta. **b**) Single-trial fluorescence traces of activity in neuron cell bodies and neuron processes imaged with FlicR1. The traces correspond to the regions in the image marked with the same color. These traces are from wide-field fluorescence data acquired using a 100 W mercury lamp at 100 Hz imaging frequency. **c**) Magnification of traces in (b)marked with black borderline. **d**) Fluorescence image of hippocampal brain slice transfected with FlicR1 and imaged 18 d after transfection. Neuron processes are clearly labeled with FlicR1. Both cell bodies and processes show some fluorescent puncta. **e**) Fluorescence traces acquired at 50 Hz of theophylline-induced membrane depolarization in neuron cell bodies and neuron processes imaged with FlicR1. The traces correspond to the regions in the image marked with the same color. All fluorescence traces are bleach corrected and traces in (b) and (c) are filtered with Savitzky–Golay smoothing (5 pts). Fluorescence traces were recorded at 100 Hz (a-c) and 50 Hz (d,e) frame rate. Illumination intensity was 0.4 W/cm^2.

3.2.5 All-optical electrophysiology

Next, we explored the utility of FlicR1 as a voltage indicator in an all-optical electrophysiology setup. One advantage of a red voltage indicator is its orthogonal spectrum to blue-light-excitable channelrhodopsin actuators, suggesting a pairing of FlicR1 with a blue-light excitable channelrhodopsin for all-optical electrophysiology. As a proof-of-concept

experiment, we cotransfected HeLa cells with FlicR1 and the channel rhodopsin variant ChIEF[82]. Both FlicR1 and ChIEF showed high expression and good membrane trafficking when expressed in HeLa cells (**Figure 31a,b**). FlicR1 successfully reported blue light (405 nm, 20 mW/cm^2)-stimulated depolarization of HeLa cells with a fluorescence change of $\Delta F/F$ = 6.1 ± 0.7% (n = 8) (**Figure 31d,e**). As expected, at the image acquisition rate of 100 Hz, FlicR1 did not show any delay in response to the blue light stimulation of ChIEF. Although FlicR1 is based on mApple, the same FP backbone as the R-GECO1 Ca^{2+} indicator, which shows blue light photoactivation[165] (**Figure 31g,k**), control cells transfected with FlicR1 alone showed no photoactivation with the 20 mW/cm^2 405 nm blue light used to stimulate HeLa cells (**Figure 31c,f**).

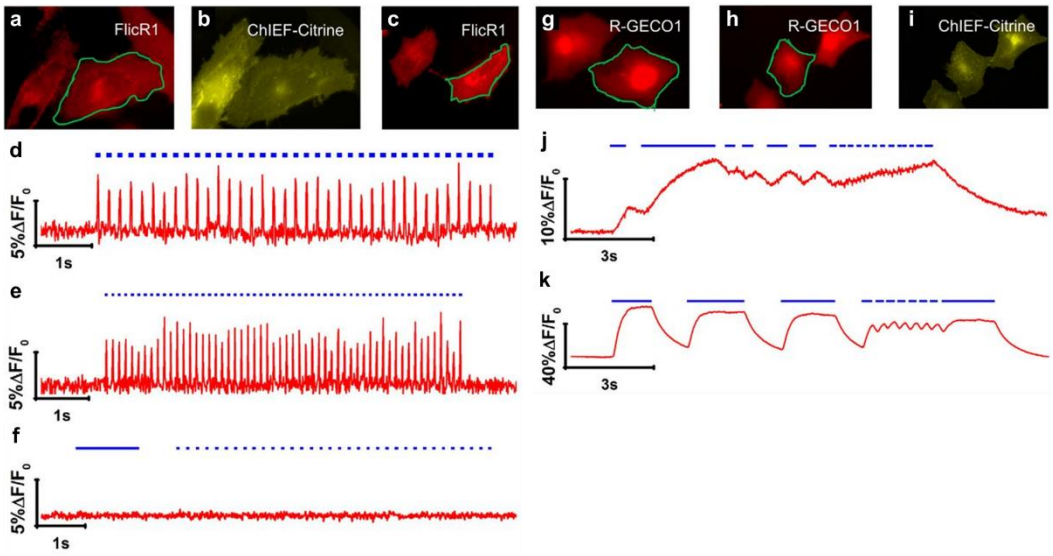

Figure 31. All optical electrophysiology with FlicR1 indicator in mammalian cells and comparison with R-GECO1 photoactivation.

a,b) Image of HeLa cells coexpressing FlicR1 (a) and ChIEF-Citrine (b). **c**) Image of HeLa cells expressing FlicR1 only. **d**) Fluorescence trace of FlicR1 in HeLa cells activated by 5 Hz stimulation of ChIEF using 405 nm laser pulses. Shown is a trace from the cell in (a). **e**) Fluorescence trace of FlicR1 in HeLa cells activated by 10 Hz stimulation of ChIEF using 405 nm laser pulses. Shown is a trace from the cell in (a). **f**) Control fluorescence trace for FlicR1 in HeLa cells using 405 nm laser pulses without coexpression of ChIEF. Shown is a trace from the cell in (c). **g**) Image of HeLa cells expressing R-GECO1 only. **h,i**) Image of HeLa cells coexpressing R-GECO1 (h) and ChIEF-Citrine (i). **j**) Control fluorescence trace for R-GECO1 in HeLa cells using 405 nm laser pulses. Shown is a trace from the cell in (g). **k**) Fluorescence trace of R-GECO1 in HeLa cells activated by stimulation of ChIEF using 405 nm laser pulses. Shown is a trace from the cell in (h)**.** Fluorescence traces were recorded at

100 Hz. The intensity of yellow light used to image FlicR1 and R-GECO1 was 60 mW/cm^2. 405 nm laser intensity to activate ChIEF was 20 mW/cm^2 in all experiments.

Although we were encouraged by these results, the 405 nm light intensity in our proof-of-concept experiment was 10-fold smaller than the light intensities necessary to induce action potentials reliably in cultured hippocampal neurons with most commonly used channelrhodopsin actuators[114]. We therefore characterized the response of FlicR1 under blue light illumination conditions comparable to those necessary for neuronal experiments. We transfected HEK cells with FlicR1 and monitored their fluorescence with a 100 Hz imaging rate under 10 W/cm^2 561 nm illumination while using whole-cell patch clamp to vary the membrane voltage for three cycles between −100 to +50 mV. For the third cycle, we also illuminated the cell with 208 mW/cm^2 458 nm light. The fluorescence traces showed significant photoactivation of FlicR1 by the blue light and a simultaneous decrease in voltage sensitivity (**Figure 32**). We also repeated the measurement with 25 mW/cm^2 405 nm light and observed a similar photoactivation effect in one of four runs. These results indicated that, under the blue light illumination conditions necessary to drive action potentials with channelrhodopsin actuators, photoactivation of FlicR1 could still present a challenge. Nevertheless, we attempted to use FlicR1 for all-optical electrophysiology in neurons. We cotransfected cultured rat hippocampal neurons with FlicR1 and TsChR, a blue-shifted channelrhodopsin[86], and attempted to elicit action potentials with blue light illumination while monitoring FlicR1 fluorescence. We found that illumination pulses of 10–1000 ms at 5–210 mW/cm^2 for both 458 and 488 nm light (data not shown) caused sufficient photoactivation of FlicR1 to obscure its voltage response. This is in contrast to HeLa cells, in which 20 mW/cm^2 of 405 nm light did not cause photoactivation. We suspect that the difference between neurons and HeLa cells is attributable to intracellular puncta that are present in neurons but absent in HeLa cells. These puncta represent a large pool of protein that does not contribute to the voltage-sensitive response yet can undergo photoactivation.

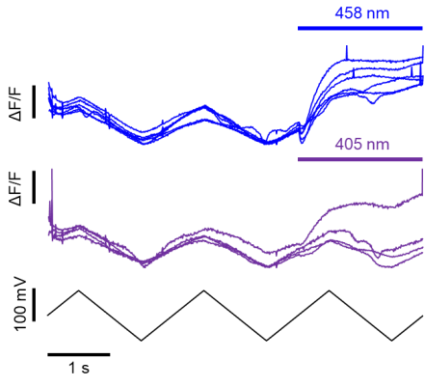

Figure 32. Photoactivation and voltage sensitivity of FlicR1 during blue light illumination.

Fluorescence intensity of FlicR1 expressed in HEK cells to a triangle wave in membrane potential from −100 mV to +50 mV. Illumination at 458 nm (208 mW/cm^2) or 405 nm (25 mW/cm^2) is indicated by blue bars. The traces show three runs each from two cells for 458 nm and two runs each from two cells at 405 nm. Traces were acquired at a frame rate of 100 Hz using 561 nm excitation at an intensity of 10 W/cm^2.

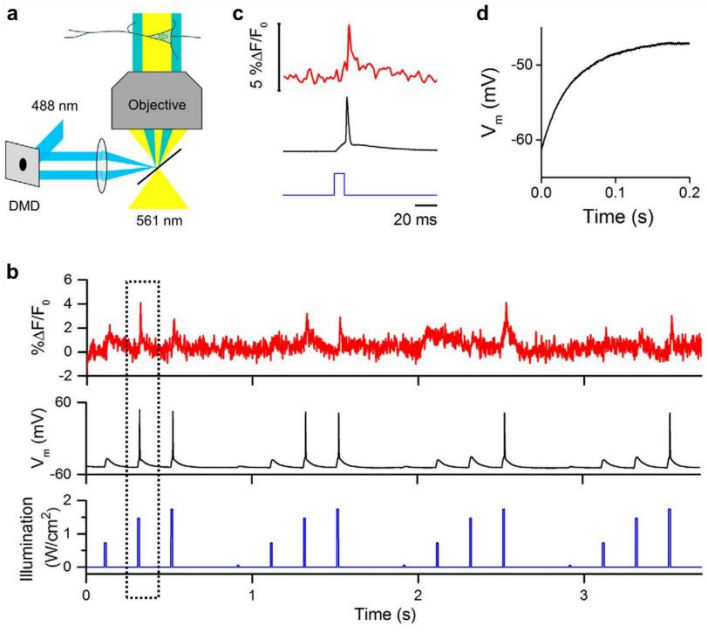

Figure 33. All-optical electrophysiology using FlicR1 in cultured hippocampal neurons.

a) Diagram showing experimental setup using a digital micromirror device (DMD) to target the blue light to the neuronal processes. **b**) Red, FlicR1 fluorescence readout from single-trial optical recording of single action potentials initiated by pulses of blue light illumination using the experimental setup shown in (a). Yellow illumination to image FlicR1 was 10 W/cm^2. Black, patch-clamp recording. Blue, 488 nm illumination (10 ms, 0.5–2 W/cm^2). **c**) Magnification of traces in (b) marked with black borderline. **d**) Patch-clamp recording of

neuron expressing PsChR when exposed to 561 nm laser (10 W/cm^2). This illumination depolarized the cell by 14 mV, but did not induce action potentials on its own. All fluorescence traces are bleach corrected. Fluorescence trace was collected at a frame rate of 500 Hz using an EMCCD camera. Fluorescence trace in (c) is filtered with Savitzky–Golay smoothing (5 points).

To circumvent photoactivation of FlicR1 in neurons, we used a digital micromirror device (**Figure 33a**) to target spatially 488 nm illumination pulses (5 mW/cm^2 to 1.7 W/cm^2, 10 or 50 ms duration) to the neuronal processes of cells coexpressing FlicR1 and either ChR2-H134R, TsChR, or PsChR[164], another blue-shifted channelrhodopsin, while avoiding blue illumination of the soma. We illuminated the whole cell with 561 nm light at 10 W/cm^2 and collected FlicR1 fluorescence from the soma. We used simultaneous manual patch clamp in current-clamp mode to provide independent detection of action potentials. When blue illumination was excluded from the soma, cells coexpressing FlicR1 and ChR2-H134R did not produce sufficient photocurrents to induce action potentials under any illumination parameters, consistent with previous reports[170]. In a neuron expressing both FlicR1 and PsChR, FlicR1 could report optically-induced action potentials with a similar SNR as electrically induced action potentials (**Figure 33b,c**). The 561 nm illumination used for eliciting FlicR1 fluorescence depolarized the cell by 14 mV (**Figure 33d**), but did not induce action potentials on its own. This result suggests that FlicR1 could be used for all-optical electrophysiology under the appropriate expression conditions.

3.3 Discussion

FlicR1 is a red indicator with performance comparable to state-of-the-art green voltage indicators such as ASAP1 and ArcLight. FlicR1 was designed with the rationale that fusion of a cpRFP to a voltage-sensitive domain would maximize the chance of coupling voltage-induced conformational changes to the FP chromophore, leading to a large response amplitude and fast kinetics. Indeed, the large and fast response of FlicR1 indicates that the S4 movement rapidly changes the environment around the mApple chromophore. In contrast to ASAP1, FlicR1 has the cpFP linked to the end of the S4 helix. Fusion to the end of the S4

helix bestows FlicR1 with a fluorescence voltage response that is dominated by a fast component (~3 ms) for both on and off kinetics (90% on and 78% off) at room temperature. Although ASAP1 has slightly faster kinetics (~2 ms)[160], the fast component of the FlicR1 response has ~1.5-fold and ~2-fold increased weight for on and off, respectively, compared with ASAP1 (60% on and 43% off). The comparable responses to single action potentials for both ASAP1 and FlicR1 is consistent with this increased weight of the fast component, because a greater fraction of the full FlicR1 response amplitude is used to report neuronal activity.

Our screening strategy was crucial to engineer FlicR1 to be a fast, bright voltage indicator with large response amplitude. Simply fusing the cpRFP resulted in a dim indicator that had a small response amplitude to voltage changes. Other reports of manually inserting cpFPs to the C terminus of *Ci*-VSP resulted in indicators with low response amplitude[63,64] and/or slow kinetics[63]. Only using our screening strategy did we discover variants that are both bright and highly responsive to membrane potential changes.

One of the most intriguing mutations that resulted from random mutagenesis is Val207Ala, located in the S3 to S4 linker of the *Ci*-VSP. Subsequent randomization of this position led to the discovery of the further beneficial Val207Phe substitution. We initially reasoned that this mutation must be important for modulating the voltage sensitivity of FlicR1. The recently reported x-ray crystal structures of *Ci*-VSP in both the activated and resting state[172] show that this residue is part of an α helix that unwinds when the voltage-sensitive domain is in the activated (depolarized) state. Based on this insight, we suggest that this mutation might be increasing the rate and/or extent with which the S4 helix moves, thus improving FlicR1's response to membrane depolarization.

We showed that FlicR1 traffics well to the cell membrane in neurons and is suitable for long-term expression in organotypic slices. However, some fraction of the protein resides in intracellular puncta when expressed in neurons. We believe that these puncta are due to the

anthozoa-derived mApple FP body of FlicR1 because related FPs often form intracellular puncta in neurons[177]. These puncta, however, did not interfere with long-term expression of FlicR1 in organotypic slices. After 3 weeks of FlicR1 expression, neurons in organotypic slices showed spontaneous activity and responded to stimulation as expected.

FlicR1 is ~30-fold brighter than archaerhodopsin-based voltage indicators, requiring only 10 W/cm^2 to image, rather than the >300 W/cm^2 required for QuasAr imaging[170]. FlicR1's fast responses to single action potentials and ability to track high-frequency trains makes it an appealing sensor for action potential detection in rapid firing events in situations where QuasAr's dimness prevents its use. In situations where QuasArs can be visualized, however, their higher sensitivity and photostability result in higher signal-to-noise recordings. Unfortunately, the higher brightness of FlicR1 could not be leveraged for performing all-optical measurements in large numbers of cells in intact tissue due to the loss of voltage sensitivity under blue light illumination.

3.4 Methods

3.4.1 Molecular biology to construct FlicR variants.

PCR amplification was used to construct the DNA template for FlicR. Synthetic oligonucleotides (Integrated DNA Technologies) were used as primers for amplification and Pfu polymerase (Thermo Fisher Scientific) was used to maintain high-fidelity DNA replication. Overlap PCR was used to link *Ci*-VSP to cpmApple FP. Random mutagenesis was performed with error-prone PCR amplification using Taq polymerase (New England Biolabs) in the presence of $MnCl_2$ (0.1 mM) and 800 μM excess dTTP and dCTP. Randomization of targeted codons was performed with QuikChange Lightning kits (Agilent Technologies). Restriction endonucleases (Thermo Fisher Scientific) were used to digest PCR products and expression vectors. Agarose gel electrophoresis was used to purify DNA products from PCR and restriction digestion reactions. The DNA was extracted from the gels using the GeneJET

gel extraction kit (Thermo Fisher Scientific). Ligations were performed using T4 DNA ligase (Thermo Fisher Scientific).

DNA encoding the first 242 aa from *Ci*-VSP (VSD242) was generated by PCR amplification of *Ci*-VSP domain from the voltage sensor VSFP3.1[60] using forward primer (FW-BamHI-VSD) and reverse primer (RV-cpmApple-VSD242). DNA encoding the cpmApple variant was generated by PCR amplification of gene encoding R-GECO1 using forward primer (FW-VSD242-cpmApple) and reverse primer (RV-XbaI-cpmApple). Primers RV-cpmApple-VSD242 and FW-VSD242-cpmApple contain an overlap region that was used to join these two genes together by overlap PCR. Primers RV-cpmApple-VSD242 and FW-VSD242-cpmApple also contained two fully randomized codons (NNK codons) that link the two genes together, generating 1024 variants. The length of the voltage-sensitive domain amplified by PCR was varied (VSD 236, VSD237, VSD238, VSD239, VSD240, and VSD241). Other sets of overlap primers, along with FW-BamHI-VSD primer and RV-XbaI-cpmApple primer, were used to link DNA encoding cpmApple to the shorter voltage-sensitive domains as outlined above for VSD242. This led to a library of 1024 FlicR variants for each length of voltage-sensitive domain.

Error-prone PCR together with DNA shuffling were used to construct libraries in the following rounds of directed evolution on FlicR variants from VSD239 library. PCR products were purified by agarose gel electrophoresis, digested, and ligated into a modified pcDNA3.1(+) vector as described below.

3.4.2 Plasmid for dual E. coli *and mammalian cell expression*

A vector for expression in prokaryotic and eukaryotic systems was constructed based on mammalian expression vector pcDNA3.1(+). To facilitate prokaryotic expression, an *E. coli* ribosome-binding site (aggaggaa) for prokaryotic translation was introduced using a QuikChange reaction (Agilent Technologies). We named the resulting vector pcDuEx0.5. The transcription of the encoded genes relies on the weak activity of the cytomegalovirus (CMV)

promoter in *E. coli* cells[178]. pcDuEx0.5 exhibited moderate expression of FlicR variants in *E. coli* cells and showed comparable expression levels in HeLa cells compared with the original pcDNA3.1(+). We used pcDuEx0.5 as the vector for screening of FlicR libraries. Other dual expression vectors have been developed previously[179].

3.4.3 Plasmid for neuronal expression

To express FlicR1 in neurons, FlicR1 was cloned from plasmid pcDuEx0.5 into the BamHI/HindIII sites of an AAV2 vector using FW-BamHI-VSD and RV-HindIII-cpmApple primers. FlicR1 expression was controlled using human synapsin I promoter to preferentially express in neurons. A 3' Woodchuck Hepatitis Virus Posttranscriptional Regulatory Element (WPRE) sequence was used to enhance expression. For channelrhodopsin expression, a TsChR-TS-eGFP fusion was cloned into the same plasmid, where TS represents a KiR2.1-trafficking sequence used to improve membrane trafficking of channelrhodopsins. The amino acid sequence of the TS sequence is KSRITSEGEYIPLDQIDINV. ChR2(H134R)-eGFP was expressed from a lentiviral construct under a *CaMKIIa* promoter described previously[170].

3.4.4 Screening of FlicR library variants in E. coli

Gene libraries of FlicR variants were transformed into electrocompetent *E. coli* strain DH10B (Invitrogen). *E. coli* cells were then plated and cultured at 37°C on LB agar plates supplemented with ampicillin (400 μg/ml) to obtain 500–1000 colonies per plate. Colonies were then imaged using a custom imaging setup described previously[169]. To screen for FlicR mutant brightness, plate images were acquired using a 560/40 nm excitation filter and 630/60 nm emission filter. For each round of random mutagenesis, ~10,000 colonies (10–20 plates) were screened. For each library generated by codon randomization, approximately three times more colonies than the expected randomization library size were screened. Colonies with the top 0.01% fluorescence brightness were manually picked and cultured in 4 ml of LB medium supplemented with ampicillin (100 μg/ml). Plasmids were then extracted using the GeneJET plasmid miniprep kit (Thermo Fisher Scientific).

3.4.5 Expression and in vitro *spectroscopic characterization of FlicR1*

To purify FlicR1, the pcDuEx0.5 plasmid harboring FlicR1 was used to transform electrocompetent *E. coli* DH10B cells (Invitrogen). The *E. coli* were grown on LB agar plates supplemented with ampicillin (400 μg/ml). A colony was used to inoculate 8 ml of LB liquid medium (100 μg/ml ampicillin) and grown overnight at 37°C. The next day, the 8 ml of bacterial culture was added to 500 ml of LB medium (100 μg/ml ampicillin) and grown for 4 h at 37°C, and then grown for 48 h at 25°C. The cell pellets were then collected by centrifugation and lysed by suspension in B-PER solution (Pierce). The insoluble fraction (containing the membrane proteins) was collected after centrifugation and resuspended in a solution of 2% *n*-dodecyl-β-D-maltopyranoside (Anatrace) in Tris-buffered saline. The suspension was then homogenized by an ultrasonic homogenizer and centrifuged at 4°C. Solubilized FlicR1 protein in the supernatant was used to measure the fluorescence spectrum on a Safire2 plate reader (Tecan) and the absorbance spectrum on a DU-800 UV-visible spectrophotometer (Beckman).

3.4.6 Cell culture

HeLa cells (CCL-2; ATCC) were cultured in DMEM supplemented with 10% FBS (Sigma-Aldrich), 2 mM GlutaMax (Invitrogen), and penicillin–streptomycin and the cells were incubated for 48 h at 37°C and 5% CO_2. Cells were split and cultured on collagen-coated 35 mm glass bottom dishes (Matsunami) to ~50% confluency. Transfection was performed by incubating HeLa cells with the mixture of 1 μg of plasmid DNA and 2 μl of Turbofect (Thermo Fisher Scientific) for 2 h following the manufacturer's instructions. Imaging was performed 24–48 h after transfection.

Human embryonic kidney 293T (HEK293T) cells (CRL-11268; ATCC) were cultured and transfected following standard protocols[71]. Briefly, HEK293T cells were grown at 37°C and 5% CO_2 in DMEM supplemented with 10% FBS and penicillin–streptomycin. Cells were transfected with 400 ng of DNA using Transit 293T (Mirus) following the manufacturer's

instructions. After 24 h, cells were replated onto glass-bottom dishes (D35-20-1.5-N; In Vitro Scientific) coated with Matrigel (BD Biosciences) at ~10,000 cells/cm^2. Measurements were performed 48 h after transfection.

3.4.7 Rat hippocampal neurons

Rat glial monolayers were prepared similarly to reference [152]. Briefly, dissociated hippocampal cells from postnatal day 0 (P0) rat pups of either sex (Sprague Dawley; Tocris Bioscience)[153] were plated on a 10 cm culture dish in glial medium (GM) composed of 15% FBS (Life Technologies), 0.4% (w/v) D-glucose, 1% Glutamax (Life Technologies), and 1% penicillin–streptomycin (Life Technologies) in MEM (Life Technologies). After reaching confluence, cells were replated onto glass-bottomed dishes (D35-20-1.5-N; In Vitro Scientific) coated with Matrigel (BD Biosciences) at a density of 3500 cells/cm^2. When the glial monolayers reached confluence again, the medium was replaced by GM with 2 μM cytarabine (cytosine-β-arabinofuranoside; Sigma-Aldrich). Dishes were maintained in GM with 2 μM cytarabine until use.

Hippocampi dissected from P0 rat pups were dissociated using papain and plated in plating medium (PM) at 8000 cells/cm^2 on the preestablished glial monolayers[153]. At 1 d *in vitro* (DIV), PM was exchanged for 2 μM cytarabine in neurobasal-based medium (NBActiv4; Brainbits). Neurons were subsequently fed every 5 d by replacing 1 ml of culture medium with NBActiv4 without cytarabine. Neurons were transfected on DIV 9 via calcium phosphate as described previously[155]. Measurements on neurons were performed on DIV 14. For all-optical electrophysiology experiments in neurons, cells were cotransfected by calcium phosphate with channelrhodopsin and FlicR1 DNA on DIV 9 and measured on DIV 12–13.

For measurements of spontaneous activity, dissociated E18 Sprague Dawley hippocampal cells in hibernate EB complete media were purchased from BrainBits. The cells were grown on 35 mm glass bottom dish (In Vitro Scientific) coated with poly-D-lysine (A-003-E; Millipore) containing 2 ml of NbActiv4 (BrainBits) supplemented with 2% FBS,

penicillin-G potassium salt (25 units/ml), and streptomycin sulfate (25 μg/ml). Half of the culture medium was replaced every 3 d. Neuronal cells were transfected on day 8 using Lipofectamine 2000 (Life Technologies) following the manufacturer's instructions. Briefly, 1–2 μg of plasmid DNA and 4 μl of Lipofectamine 2000 (Life Technologies) were added to 100 μl of NbActive4 medium to make the transfection medium. This medium was then incubated at room temperature for 10–15 min. Half of the culture medium (1 ml) from each neuron dish was taken out and combined with an equal volume of fresh NbActiv4 medium (supplemented with 2% FBS, penicillin-G potassium salt, and streptomycin sulfate) to make a 1:1 mixture and incubated at 37°C and 5% CO_2. Next, 1 ml of fresh conditioned (at 37°C and 5% CO_2) NbActiv4 medium was then added to each neuron dish. The transfection medium was then added and the neuron dishes were incubated for 2–3 h at 37°C in a CO_2 incubator. The medium was then replaced using the conditioned 1:1 medium prepared previously. The cells were incubated for 48–72 h at 37°C in a CO_2 incubator before imaging.

3.4.8 Induced transmembrane voltage screening

For induced transmembrane voltage (ITV) screening, FlicR variants were coexpressed in HeLa cells, together with the inward rectifier potassium channel, Kir2.1 (Addgene #32641) and ArcLight Q239 (Addgene #36856) as an internal reference. Expression of Kir2.1 in HeLa cells helped maintain the resting potential of ∼−60 mV, which is appropriate for screening neuronal voltage indicators. A uniform electric field of ∼50 V/cm was applied across the cell culture to create an ITV. A pulse generator (PG 58A; Gould Advanced) was used to apply a 10 ms square-wave pulse at ∼0.5 Hz. An amplifier (6824A 40V/25A; Agilent Technologies) was used to obtain a pulse amplitude of 25 V. A pair of parallel platinum electrodes (0.5 cm apart) were used to deliver the pulses to the cell culture. Fluorescence was imaged simultaneously with multiple electric field pulses for ITV at a frame rate of a 100 Hz for 10 s.

3.4.9 Imaging ITV in HeLa cells

Imaging was performed in HEPES (25 mM)-buffered Hanks' balanced salt solution (HBSS). An inverted fluorescence microscope (Eclipse Ti-E; Nikon) equipped with a 200 W metal halide lamp (PRIOR Lumen) and a 60× oil objective was used to image HeLa cells. Images were acquired at 100 Hz with 4 × 4 binning using a 16-bit QuantEM 512SC electron-multiplying CCD camera (Photometrics). A FITC/Cy2 filter set (470/40 nm (excitation), 525/50 nm (emission), and a 495LP dichroic mirror (set number 49002; Chroma) was used to image ArcLight Q239. A TRITC/Cy3 filter set (545/30 nm (excitation), 620/60 nm (emission), and a 570LP dichroic mirror (set number 49005; Chroma) was used to image FlicR1. NIS Elements Advanced Research software (Nikon) was used to control the microscope and camera. The raw fluorescence traces of both FlicR and ArcLight were extracted from identical regions of interest in cells expressing both constructs and exported into a customized Microsoft Excel spreadsheet. Background subtraction, photobleaching corrections, calculations of average $\Delta F/F_{min}$, and calculation of signal-to-noise ratios (SNRs) were performed automatically in Excel. The average $\Delta F/F_{min}$ and SNR of FlicR signals were compared with those of ArcLight signals from the same cells and the ratios of $\Delta F/F_{min}$ of FlicR versus ArcLight were reported. At least 10 cells coexpressing FlicR and ArcLight were analyzed for each variant. The best variant with maximum mean ratio in each library was determined and sequenced.

3.4.10 Imaging spontaneous activity in primary neuron culture.

Imaging was performed in HEPES (25 mM)-buffered HBSS. Wide-field imaging was performed on an inverted Nikon Eclipse Ti-E microscope equipped with a 200 W metal halide lamp (PRIOR Lumen), 60× oil objectives (numerical aperture, NA = 1.4; Nikon), and a 16-bit QuantEM 512SC electron-multiplying CCD camera (Photometrics). A TRITC/Cy3 filter set (545/30 nm (excitation), 620/60 nm (emission), and a 570LP dichroic mirror (#49005; Chroma) was used to image FlicR1. For time-lapse imaging, neurons were imaged at 100 Hz

imaging frequency with 4 × 4 binning. Raw fluorescence traces were corrected for background autofluorescence and photobleaching. As seen in **Figure 29a**, FlicR1 shows some intracellular puncta. Mounting evidence points to these structures being lysosomes in which the protein is accumulating faster than it is being degraded[180].

3.4.11 Simultaneous electrophysiology and fluorescence in cultured cells.

All imaging and electrophysiology measurements were performed in Tyrode's buffer containing the following (in mM): 125 NaCl, 2.5 KCl, 3 $CaCl_2$, 1 $MgCl_2$, 15 HEPES, and 30 glucose, pH 7.3. For HEK cell measurements, 2-aminoethoxydiphenyl borate (100 μM; Sigma-Aldrich) was added to block endogenous gap junctions. Measurements at 34°C were performed by perfusing in Tyrode's buffer at 1 ml/min while maintaining elevated temperature with an inline heater (Warner Instruments) and an objective heater (Bioptechs).

Filamented glass micropipettes (WPI) were pulled to a tip resistance of 4–8 MΩ and filled with internal solution containing the following (in mM): 125 potassium gluconate, 8 NaCl, 0.6 $MgCl_2$, 0.1 $CaCl_2$, 1 EGTA, 10 HEPES, 4 Mg-ATP, and 0.4 Na-GTP, pH 7.3, adjusted to 295 mOsm with sucrose. Pipettes were positioned with a Sutter Instruments MP285 manipulator. Whole-cell, voltage and current-clamp recordings were acquired using an Axopatch 700B amplifier (Molecular Devices), filtered at 2 kHz with the internal Bessel filter, and digitized with a National Instruments PCIE-6323 acquisition board at 10 kHz. Data were only acquired from cells with access resistance <25 MΩ. To determine the minimal current injection necessary for action potential generation before imaging, square waves of increasing amplitudes were injected in step sizes of 50–100 pA while recording the voltage. The minimal current value that resulted in robust AP generation was used to generate action potentials for imaging experiments.

Illumination light was provided by a 561 nm 100 mW diode-pumped solid-state laser (Cobolt Jive 100 561 nm) for FlicR1 imaging and by a 488 nm 50 mW laser (Omicron PhoxX) for ArcLight imaging. The beam was expanded and focused onto the back-focal plane of a

60× oil-immersion objective (Olympus APON 60XOTIRF 1.49 NA). The imaging intensity at the sample was 10 W/cm^2. For all-optical electrophysiology measurements in neurons, the 488 nm beam was expanded and modulated by a digital micromirror device (Texas Instruments DLP LightCrafter Evaluation Module) controlled using built-in software. FlicR1 fluorescence was separated from excitation light and filtered using the dichroic and emission filters from a Cy3-4040C-OMF-ZERO filter set (Semrock). ArcLight fluorescence was separated with a long pass dichroic (Semrock catalog #FF495-Di03) and filtered with a 531/40 nm band-pass filter (Semrock catalog #FF01-531/40-25). The sample was imaged onto an EMCCD camera (Andor iXon$^+$ DU-860) with 128 × 128 pixels. For measurements of FlicR1's speed, movies were acquired at a 2 kHz frame rate with 2 × 2 binning. Sensitivity measurements were acquired at 10 Hz with no binning. Photobleaching traces were acquired at 2 Hz with no binning. Neuronal data were acquired at 1 kHz with 2 × 2 binning or at 500 Hz with 1 × 1 binning.

Some of the screening of all-optical electrophysiology conditions was performed on another custom-built microscope equipped with a higher-resolution camera. Illumination light was provided by a 561 nm 100 mW Cobolt Jive (catalog #0561-04-01-0100-500), a 488 nm 100 mW Coherent Obis (catalog #1226419), or a 405 nm 30 mW Dragon Laser (catalog #11042443). Laser lines were combined with dichroic mirrors and intensities were modulated using acousto-optical tunable filters (Gooch & Housego, catalog #TF525-250-6-3-GH18A or #48058-2.5-.55-5W). The 488 nm laser line was expanded to illuminate the chip of a digital micromirror device (Texas Instruments DLP LightCrafter with DLP 0.3 WVGA chipset) that was subsequently reimaged onto the sample plane. The 561 and 488 nm lines were focused at the back focal plane of an APON 60XOTIRF 1.49 NA objective (Olympus). Collimated 405 nm laser light at the back focal plane of the objective was defocused to obtain a 5 μm spot at the sample and was guided at the sample plane using galvonometric mirrors (Thorlabs catalog #GVS202) located in a conjugate plane. Fluorescence light was separated from illumination

light using a quadband dichroic mirror (Semrock catalog #Di01-R405/488/561/635). The fluorescence light was passed through a knife-edge split into two channels using a dichroic mirror, which were recombined and reimaged onto two halves of the chip of a scientific CMOS camera (Hamamatsu ORCA-Flash 4.0). The splitting and recombining were accomplished using dichroic mirrors (Semrock FF662-FDi01). Green and orange fluorescence was filtered using a HQ550/50m band-pass filter (Chroma) for 488 nm excitation, or an ET595/50m bandpass filter (Chroma) for 561 nm illumination. 458 nm illumination light was provided by an LED (LED Supply 07040-PR000-B) positioned above the sample filtered by a D480/60x excitation filter (Chroma) and controlled by a four-channel LED driver (Thorlabs DC4104). Electrophysiological recordings on this microscope were performed as above, but using an Axopatch 200B amplifier and CV203BU headstage (Molecular Devices). Signals were filtered at 5 kHz with the internal Bessel filter and digitized at 10 kHz using a National Instruments PCIe-6259 acquisition board.

Measurements on ArcLightQ239 kinetics were performed using 488 nm illumination light from a Coherent Obis 488-50 laser focused onto the back focal plane of a 60× water-immersion objective (Olympus UIS2 UPlanSApo × 60/1.20 W, NA 1.20) to a power fluence of 2–4 W/cm^2 at the sample. Fluorescence light was split from the excitation light using a Semrock Di01-R405/488/594 dichroic, passed through a 525/30 band-pass emission filter, and imaged onto a scientific CMOS camera (Hamamatsu ORCA-Flash 4.0). Whole-cell voltage recordings were performed with a patch-clamp amplifier (A-M Systems Model 2400), filtered at 5 kHz with the internal filter, and digitized with a National Instruments PCIE-6323 acquisition board at 10 kHz.

FlicR's two-photon voltage sensitivity was tested on a homebuilt beam-scanning two-photon microscope with an 80 MHz, 100 fs tunable pulsed laser (SpectraPhysics Insight DeepSee). Measurements were performed at 1120 nm excitation wavelength with a time-averaged excitation power of 60 mW, or 0.8 nJ per pulse, in imaging mode, and ~6 mW or 80

pJ per pulse in point-recording mode. Pulses were focused down to an ~500 nm spot with a 1.2 NA water-immersion objective (Olympus UplanSapo). Imaging measurements were performed with linear scan speeds of ~8 cm s^{-1}. Excitation light and fluorescence were separated using an FF775-Di01 dichroic mirror and FF01-790/SP-25 short-pass filter (both Semrock). Fluorescence was detected using a Hamamatsu R943-02 photomultiplier tube in photon counting mode cooled to −20°C. The PMT signal was amplified through an SRS PR325 amplifier and discretized with a Hamamatsu Photon counting unit C9744. Data were acquired using an NI pci-6259 DAQ card. The setup was controlled by Labview software written in house.

3.4.12 HeLa cell all optical electrophysiology.

Imaging was performed in HEPES (25 mM)-buffered HBSS. An inverted fluorescence microscope (Eclipse Ti-E; Nikon) equipped with a 200 W metal halide lamp (PRIOR Lumen) and a 60× oil objective was used. Images were acquired at 100 Hz with 4 × 4 binning using a 16-bit QuantEM 512SC electron-multiplying CCD camera (Photometrics). Cells expressing R-GECO1 only, R-GECO1 and ChIEF-Citrine, FlicR1 only, or FlicR1 and ChIEF-Citrine were exposed to whole-field illumination with pulses of blue light (405 nm laser, 20 ms, 5 Hz and 10 Hz, 5 mW/mm^2) to stimulate ChIEF. Cells were simultaneously illuminated with yellow light to excite fluorescence of R-GECO1 or FlicR1. A TRITC/Cy3 filter set (545/30 nm (excitation), 620/60 nm (emission), and a 570LP dichroic mirror (#49005; Chroma) was used to image R-GECO1 or FlicR1 fluorescence. The NIS Elements Advanced Research software (Nikon) was used to control the microscope and camera. Fluorescence changes were calculated by averaging over the whole cell. Raw fluorescence traces were corrected for background autofluorescence and photobleaching.

Different opsins were explored in an effort to minimize optical crosstalk with FlicR1. The yellow light intensity used to image FlicR1 in HeLa cells at 100 Hz acquisition rate (60 mW/cm^2) is much lower than that required to image AP transients in neurons (10 W/cm^2).

As mentioned above, we used ChIEF in our proof-of-concept experiments because 60 mW/cm^2 of yellow light is not enough to cause activation of ChIEF. However, we had to switch to more blue-shifted opsins (TsChR and PsChR) to try to avoid optical crosstalk with the relatively higher illumination intensity required to image FlicR1 in neurons at 1 kHz (see **Figure 33**).

3.4.13 Preparation of rat hippocampal organotypic brain slices.

Horizontal brain slices (250 μm thickness) from a P0 Sprague-Dawley rat of either sex were generated in ice-cold HBSS containing 1.3 mM $CaCl_2$ and 1 mM $MgSO_4$ with a vibrating microtome (Leica VT1000S) as described previously[176]. All procedures were performed in compliance with the guidelines of the Canadian Council for Animal Care and with the approval of the University of Alberta Animal Care and Use Committee for Health Science. Hippocampal regions were cut from horizontal brain slices and placed on a sterile 0.4 μm pore membrane cell culture insert (Millipore PICMORG50). The insert and slice were then placed in a Petri dish containing 1.5 ml of NbActiv4 (BrainBits) supplemented with 5% FBS, penicillin-G potassium salt (50 units/ml), and streptomycin sulfate (50 μg/ml). Slices were cultured at 37°C and 5% CO_2 for 3–5 d before transfection.

3.4.14 Ex vivo *electroporation of organotypic brain slices*

The Millipore insert and the slice cultured on it were placed between a platinum plate Petri dish electrode (CUY700-P2E; Nepa Gene) and a square platinum electrode (CUY700-P2L; Nepa Gene). The gap between the dish electrode and the membrane was filled with electroporation buffer (HBSS with 1.5 mM $MgCl_2$ and 10 mM glucose). Plasmid pAAV2-hSyn-FlicR1 was dissolved in electroporation buffer at a concentration of 1 μg/μl and sufficient volume was added to fill the gap between the slice and the top electrode. Five 20 V pulses (5 ms each, 1 Hz) were applied using a function generator (PG 58A; Gould) and an amplifier (6824A; Agilent Technologies). The direction of electrical field was then reversed and a second set of five pulses with the same settings were applied. After transfection, the slices were

returned to the incubator at 37°C with 5% CO_2. It normally takes 2–3 d for full expression of FlicR1 in cultured brain slices using this transfection method.

3.4.15 Imaging of rat organotypic hippocampal slices

For organotypic brain slice imaging, an upright FV1000 confocal microscope (Olympus) equipped with FluoView1000 software (Olympus) and a 20× XLUMPlanF1 water-immersion objective (NA 1.00; Olympus) was used. Illumination light was provided by a 100 W mercury arc lamp (Olympus).

The brain slice on the Millipore insert was placed in a custom-made chamber to hold it in place during imaging. Immediately before imaging, the slices were perfused with artificial CSF (ACSF) superfusate containing the following (in mM): 120 NaCl, 3 KCl, 1 $CaCl_2$, 2 $MgSO_4$, 26 $NaHCO_3$, 1.25 NaH_2PO_4, and 10 D-glucose, pH adjusted to 7.4 by gassing with 95% O_2, 5% CO_2, at 5 ml/min using a peristaltic pump (Watson-Marlow Alitea) and buffer temperature was controlled at 34°C. Imaging was started within 10 min after activation of the perfusion system.

To image FlicR1, the hippocampal slice was excited with the 100 W mercury arc lamp using a filter cube with 565/30 nm excitation filter, a 620/50 nm emission filter and 585 nm dichroic (Semrock). Images were acquired at 100 Hz at 2 × 2 binning (see **Figure 30b**, spontaneous activity) and 50 Hz (see **Figure 30e**, stimulated activity) using a digital sCMOS camera (Hamamatsu Orca-Flash2.8; Hamamatsu Photonics). For stimulation with theophylline, ~30 s after the start of the experiment, the superfusate was changed from control ACSF to ACSF containing 10 mM theophylline (Sigma-Aldrich, directly dissolved in ACSF). Approximately 10 min later, the superfusate was changed back to control ACSF. Four organotypic brain slices transfected with FlicR1 were imaged and showed similar responses. **Figure 30** shows representative fluorescence traces from neurons in organotypic slices.

3.4.16 Data analysis

For measurements of speed and sensitivity in HEK cells, fluorescence traces were extracted using the maximum likelihood pixel weighting algorithm described previously[71]. Briefly, each pixel's fluorescence was correlated with the average whole-field fluorescence. Pixels with stronger correlation to the mean were weighted preferentially in the measurement of fluorescence, emphasizing the pixels containing the most information. The 5% of pixels with the highest correlation to the mean were used for characterization of protein speed and sensitivity. Fluorescent responses to step functions were averaged over 100 trials and fit with a double exponential function to acquire the time constants of FlicR1's fluorescent response. Sensitivities were defined as the maximum percentage change in fluorescence over a 150 mV change in voltage.

Photobleaching traces were obtained by subtracting the average fluorescence of a region of user-defined background region from the average fluorescence of the user-defined region of the cell. The resulting traces were then fit to a single exponential with a baseline offset to obtain the photobleaching time constant. FlicR1 showed transient photoactivation in the first 100 s, which was ignored for photobleach calculations.

For neuronal measurements, the cell body and dendrites were selected manually and the average intensity of all included pixels was averaged. The background intensity of a user-defined background region was subtracted from the raw signal. A photobleaching baseline was constructed from the whole-field intensity by a sliding minimum filter, followed by a sliding mean filter. Each frame of the movie was then corrected by dividing by this baseline. SNRs were calculated as the maximum fluorescence response to action potential (as identified by the patch-clamp recording) divided by the SD of the baseline fluorescence.

Data were analyzed using custom MATLAB codes and Microsoft Excel. A Q–Q plot was used to test the normality of datasets being compared. Both datasets were determined to have equal variance using the *F* test ($\alpha = 0.05$). Unless noted otherwise, values reported are mean

± SEM. A statistical method was not used to justify sample sizes, but sample sizes are similar to those used by others in the field. Data selection criteria for experiments are stated in the Materials and Methods section for each experiment and are similar to those used by others in the field.

3.5 Author contributions

Vincent A. Pieribone, Klaus Ballanyi, Adam E. Cohen, and Robert E. Cohen designed experiments. Ahmed S. Abdelfattah and Yonxin Zhao performed the directed evolution work on FlicR1. Samouil L. Farhi performed electrophysiological and optical-electrophysiology measurements. Daan Brinks performed 2-photon measurements. Peng Zou contributed Arclight characterization data. Araya Ruangkittisakul and Jelena Platisa performed research. Ahmed S. Abdelfattah, Samouil L. Farhi, Yongxin Zhao, Daan Brinks, and Peng Zou analyzed data. Ahmed S. Abdelfattah, Samouil L. Farhi, Adam E. Cohen, and Robert E. Campbell wrote the paper, which was previously published as:

> Abdelfattah AS, **Farhi SL***, Zhao Y*, Brinks D, Zou P, Ruangkittisakul A, Platisa J, Pieribone V, Ballanyi K, Cohen AE, Campbell RE. A bright and fast red fluorescent protein voltage indicator that reports neuronal activity in organotypic brain slices. *Journal of Neuroscience* **36**, 2458-2472 (2016).

4 Ultra-widefield all-optical neurophysiology

4.1 Introduction

The AON tools shown in the previous chapters have been well suited for cultured cells. AON also provides a promising approach to mapping neural excitability and synaptic strength across wide regions of brain tissue[181,182]. Realizing this promise requires improvements both in optics and in molecular actuators and reporters. When applied in acute brain slices, such tools offer the promise to create brain-wide maps of excitability or synaptic strength; and to probe the effects of chemical, physical or genetic perturbations thereon.

Much effort has been devoted to wide-area *in vivo* fluorescence imaging using, for example, light sheet[183], swept confocally aligned planar excitation (SCAPE)[184], light-field[185], and two photon (2P)[186,187] approaches. However, technical challenges arise when seeking to apply these methods in an ultrawide-field format, e.g. for brain-wide activity mapping. The wide-field format necessitates use of a very large objective lens, typically with a large diameter back aperture and a high optical etendue. Only a few designs have been adapted to these challenging conditions. Scanning 2P microscopy was recently demonstrated with an ultra-large objective, but due to the requirements of point scanning, 2P mesoscopes face a limited data rate of $< 2\times10^7$ pixels/s[188–190] and require a large number of custom and expensive components.

In the context of imaging activity in brain slices, neither the depth penetration nor the high spatial resolution of 2P imaging is essential. 1P wide-field excitation offers the promise of a higher overall data-rate, but faces the challenge to distinguish in-focus signal from out-of-focus or scattered background. A family of structured illumination microscopy (SIM) techniques seek to address this challenge[188]. A sample is illuminated with time-varying patterns of light, so signals emanating from the focal plane are modulated to allow separation of in-focus signal from out-of-focus background. As a camera-based approach, SIM offers

intrinsically high bandwidths (up to 4×10^8 pixels/s with modern scientific CMOS cameras). Linear SIM achieves optical sectioning by modulating the illumination in a stripe pattern[189]. However, this method is susceptible to refractive aberrations which lead to image artifacts, especially in thick tissues[190]. Alternative approaches such as HiLo[191] and blind-SIM[192] rely on models of the signal source, which can introduce imaging artifacts when the sample does not conform to the model. As a result, 1P-SIM is typically performed on thin, semi-transparent samples.

Scattering is also a problem in mobile phone networks, where spread-spectrum encoding techniques are widely used to avoid interference. One such technique, Hadamard-Walsh coding, uses pseudo-random binary sequences to encode signals. We sought to apply the same concept to optical microscopy. We developed a digital micromirror device (DMD)-based structured illumination system in which adjacent sample locations were illuminated with temporally orthogonal pseudo-random Hadamard codes. Optical sections were then demodulated by matched filtering of the image stack with the Hadamard codes.

The Hadamard microscope was constructed mostly from off-the-shelf components at a small fraction of the cost of a 2-photon microscope. This approach produced crisp multi-color optically sectioned and low aberration images in brain tissue over a 4.6 × 4.6 mm FOV. Due to the high speed of sCMOS cameras, the system achieved a frame rate of 5.6 Hz in a 4.6 x 2.3 mm sub-field, sufficient for Ca^{2+} imaging.

AON in acute brain slices requires an optogenetic actuator and reporter which can be used together with minimal 1P optical crosstalk. All channelrhodopsins have an asymmetric action spectrum, with a long blue tail and a comparatively sharp red cutoff. A red-shifted channelrhodopsin has been combined with a GCaMP Ca^{2+} indicator for 2P AON *in vivo*[193–195], but optical crosstalk prevents use of this pair with 1-photon optics. Lower optical crosstalk is achieved by pairing a blue-shifted channelrhodopsin with a red-shifted reporter. This approach has been successful with a red voltage indicator[170], but voltage signals are too fast to

resolve by Hadamard microscopy. Red genetically encoded Ca^{2+} indicators (RGECIs) have improved dramatically in recent years, but their combination with optogenetic stimulation has been hampered by blue-light induced photoswitching of the mApple-based chromophores used in the most sensitive RGECIs[166,196,197].

TsChR (derived from *Tetraselmis striata*)[86] is the most blue-shifted channelrhodopsin reported to-date, but its initial characterization yielded a poor photocurrent so it has not previously been used in optogenetic experiments. Here we show that an optimized version of TsChR drives robust spiking in cultured neurons and in tissue. Combination of TsChR with a nuclear-localized red-shifted Ca^{2+} reporter, H2B-jRGECO1a, achieves spectral orthogonality for 1-photon AON. Hadamard microscopy of these reporters enabled simultaneous functional characterization of > 6,000 neurons, spread over a region 2.3 x 2.3 mm in acute brain slice. Maps of excitability highlighted distinct cortical layers, which otherwise appeared homogeneous in their fluorescence.

Most neuro-active drugs act throughout the brain and affect multiple cell types. At present there is no robust way to profile broadly a drug's effect with cellular resolution, short of laborious manual patch clamp measurements. We combined Hadamard microscopy and AON to profile the effects of anti-epileptic drugs (AEDs). Different drugs showed region-specific effects on excitability which in the case of a K_v7 agonist correlated with expression of the target ion channel. Finally, we show that by expressing the optogenetic actuator CheRiff and the Ca^{2+} reporter H2B-jRGECO1a in distinct sets of neurons, this technique can probe synaptic connectivity. The combination of Hadamard microscopy with AON provides a powerful tool for wide-area investigations of neural function in brain tissue.

4.2 Results

4.2.1 Optical sectioning in ultra-widefield images of acute brain slices

We designed an epifluorescence microscope with 2.25 μm lateral resolution and a 4.6 mm FOV, large enough to image one hemisphere of a coronal brain slice (**Figure 34a**). The

system was built around a low magnification high numerical aperture objective (Olympus MVPLAPO 2 XC, NA 0.5) and used large-area dichroic mirrors (60 x 85 x 3 mm) and emission filters (Ø 60 mm). Apart from the optical filters and the mechanical mounts, all elements of the microscope were off-the-shelf components (Methods).

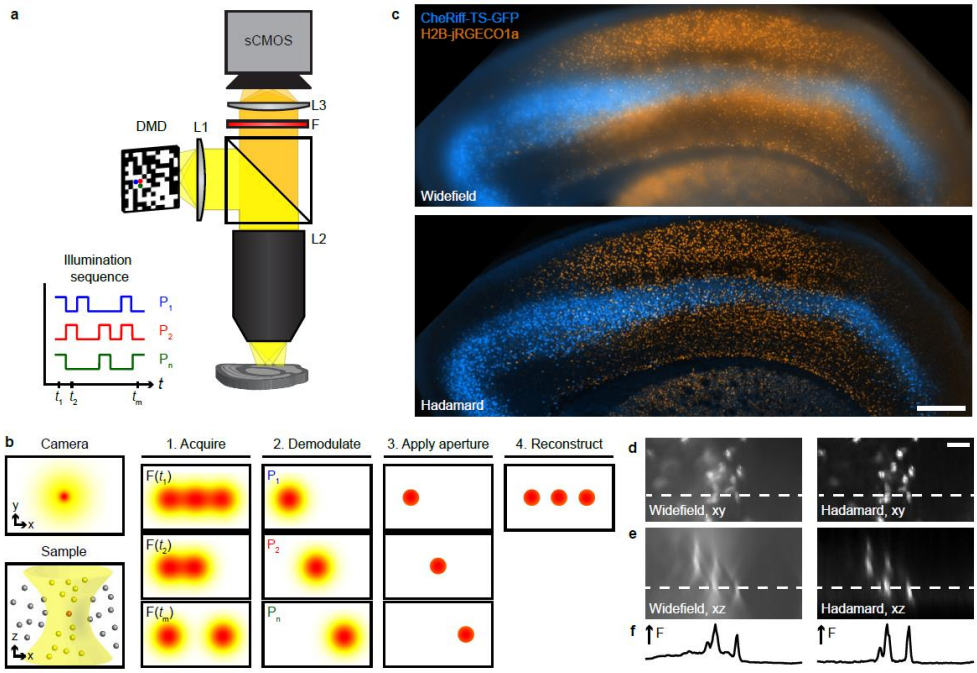

Figure 34. Optical sectioning by Hadamard microscopy.

(**a**) Schematic of ultra-widefield microscope, showing orthogonal illumination sequences in neighboring DMD pixels (P_1, P_2, …, P_n). (**b**) Left: In a thick, scattering sample, the in-focus light (red) is dispersed by scattering and mixed with out-of-focus light (yellow). Right: Hadamard microscopy protocol. (1) The sample is illuminated with orthogonal functions at adjacent points. (2) The images are demodulated by matched filtering with the illumination sequence. (3) Scattered light is rejected by a software aperture. (4) The optically sectioned image is reconstructed from a sum of the demodulated images. (**c**) Two-color fluorescence maximum-intensity projection acquired from acute brain slice expressing H2B-jRGECO1a and membrane targeted CheRiff-TS-GFP. Left: wide-field epifluorescence. Right: Hadamard image. Scale bar 500 µm. (**d-e**) Comparison of widefield and Hadamard image planes in a fixed brain slice expressing membrane-targeted mCitrine illustrating Hadamard background rejection and an improved point-spread function. Scale bars 50 µm. (**f**) Intensity profile from dotted line in (d-e).

In wide-field epifluorescence images of 300 µm thick acute brain slices, out-of-focus fluorescence led to high background, and light scattering led to loss of in-focus spatial resolution. Together these effects degraded wide-field image quality so that single cells were not resolvable. To address these challenges, we developed a novel structured illumination

approach based on Hadamard encoding. A digital micromirror device (DMD) modulated the excitation light with a series of binary illumination patterns such that neighboring sample locations were illuminated with temporally orthogonal intensity sequences (P_1, P_2, …, P_n in **Figure 34a**). Raw data consisted of a series of images ($F(t_1)$, $F(t_2)$, …, $F(t_m)$ in **Figure 34b-1**) acquired with each illumination pattern, which were then demodulated to yield images of the scattered light for each illumination location (**Figure 34b-2**). Software binary masks then rejected scattered light (**Figure 34b-3**), akin to physical pinholes used in confocal microscopy. The sum of images over all illumination locations yielded an optical section (**Figure 34b-4**).

To make all projected DMD pixels mutually orthogonal would require prohibitively long digital codes (~10^6 samples), but because light scatter is mostly local, repeating the codes periodically at separations larger than the scattering point-spread function resulted in minimal crosstalk. Residual crosstalk between repeated codes was scrambled by flipping the sign of a randomly selected 50% subset of the pixels (**Figure 35a**, Methods). This procedure resulted in series of patterns with 50% duty cycle, uniform mean illumination across the sample, and uniform spatial and temporal spectral density.

To determine the precise mapping of DMD pixels onto camera pixels, reference sets of Hadamard images were acquired in an optically thin, spatially homogeneous fluorescent film. After acquisition of experimental data (e.g. in brain slice), the demodulation and spatial masking steps were combined by element-wise multiplication of the experimental data with the reference images (**Figure 35b**, Methods). A sum of the demodulated and masked images yielded the optical section. Code for acquiring and analyzing Hadamard images is available upon request.

The Hadamard code length, equal to the number of patterns used, dictated the maximum acquisition speed. Structural images were acquired with 64 patterns over 1.5 s and functional recordings were acquired with 12 patterns over 180 ms (5.6 Hz frame rate).

Repeated Hadamard images were combined from the same focal plane to make activity movies or from different planes to make z-stacks (**Figure 35c-d**).

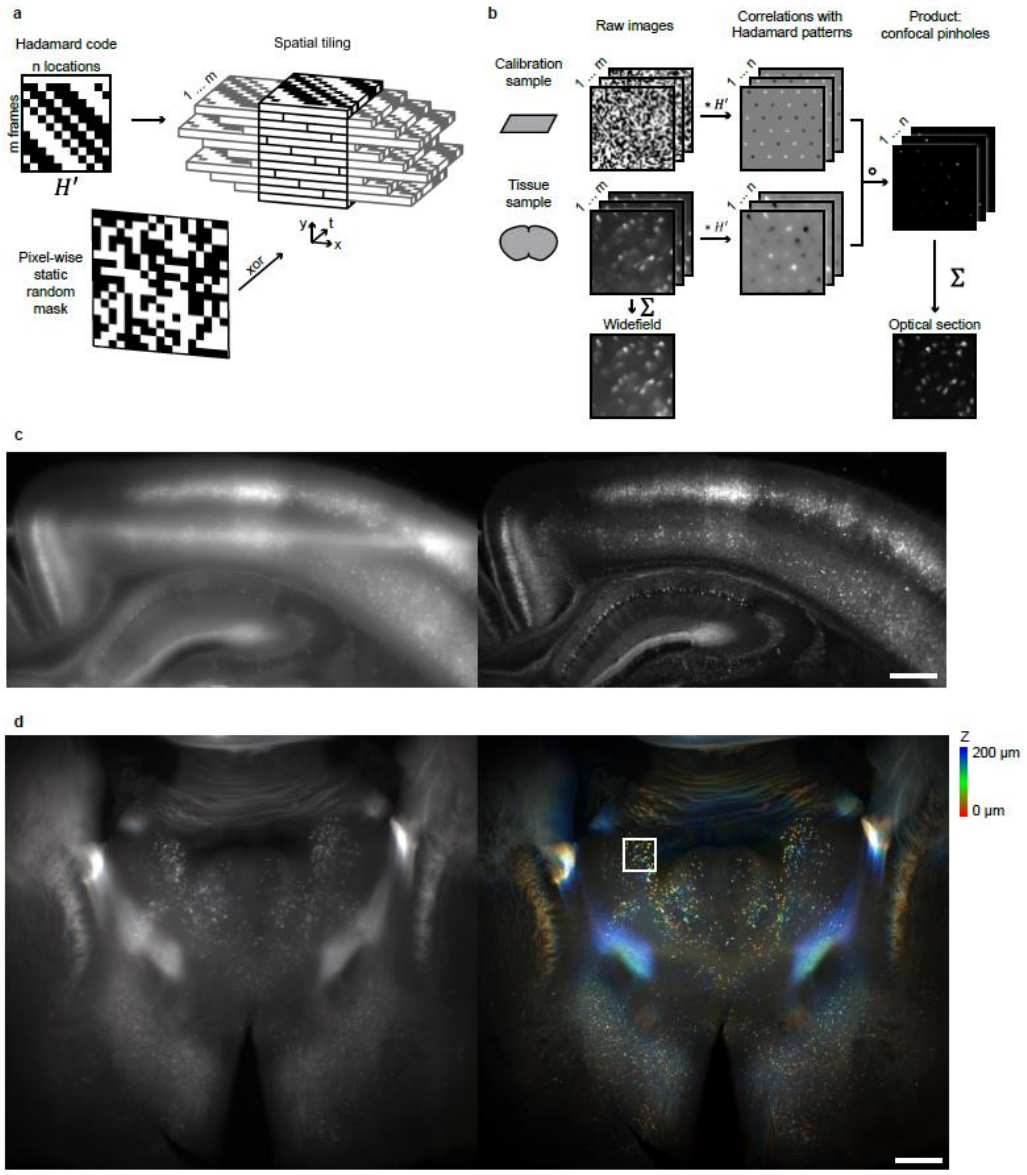

Figure 35. **Hadamard microscopy enables wide-field optical sectioning in brain tissue.**

(**a**) Codes from a Hadamard matrix were tiled to fill image space. The number of elements in the Hadamard code determined the number of frames in the pattern sequence. A random mask was applied to invert the code in 50% of illumination pixels, yielding pseudorandom patterns with flat spatial and temporal power spectra. (**b**) Raw images were acquired in a calibration sample and a tissue sample, one frame per Hadamard pattern. Cross-correlation maps between microscope data and Hadamard codes produced arrays of peaks corresponding to signals from distinct sample regions. Negative peaks corresponded to pixels whose Hadamard sequence was inverted. Pixel-wise multiplication of the demodulated images from

the calibration sample and from the tissue sample led to multi-point confocal images. These images were summed to produce an image reconstruction. Detailed description in **Methods**. (**c**) Maximum-intensity projection of an acute brain slice expressing membrane-targeted Citrine in *CaMKIIa*-Cre$^{+/-}$ positive cells. Left: wide-field epifluorescence. Right: Hadamard microscopy. Scale bar 500 μm. (**d**) Depth-colored Hadamard z-stack obtained using the full field of view of the Hadamard microscope showing membrane-targeted Citrine in Rbp4-Cre positive cells. Left: wide-field epifluorescence. Right: Hadamard microscopy. Scale bar 500 μm. White box indicates FOV in **Figure 34e-g**.

Figure 34c shows a 2-color Hadamard optical section of the cortex and striatum in an acute 300 μm-thick coronal brain slice. This sample expressed nuclear-targeted jRGECO1a (orange) throughout cortex and striatum, and membrane-targeted CheRiff-GFP restricted by an Rbp4-Cre driver to a subset of Layer 5 (L5) pyramidal cells (blue). Axons of the L5 cells are visible in the striatum. In fixed slices expressing membrane targeted mCitrine, Hadamard imaging rejected out-of-focus and scattered light, resolved fluorescence signals by focal plane, and enabled clear separation of distinct somata (**Figure 34d-f**).

We compared Hadamard, linear SIM and HiLo z-stacks from 300 μm thick acute brain slices expressing H2B-jRGECO1a (**Figure 36**, Methods). Hadamard microscopy avoided the out-of-focus wings in the point-spread function which arose in the other SIM techniques and which introduced spurious out-of-focus signals. With Hadamard imaging, nuclei had a full-width half-maximum (FWHM) of 5.5 μm laterally and 50 μm axially. The signal-to-noise ratio (SNR) of Hadamard images decayed as a function of image depth with a length constant of 27 μm in acute brain slices and 113 μm in fixed slices. Hadamard microscopy thus enabled optically sectioned imaging with single-cell resolution over wide fields of view in brain slices.

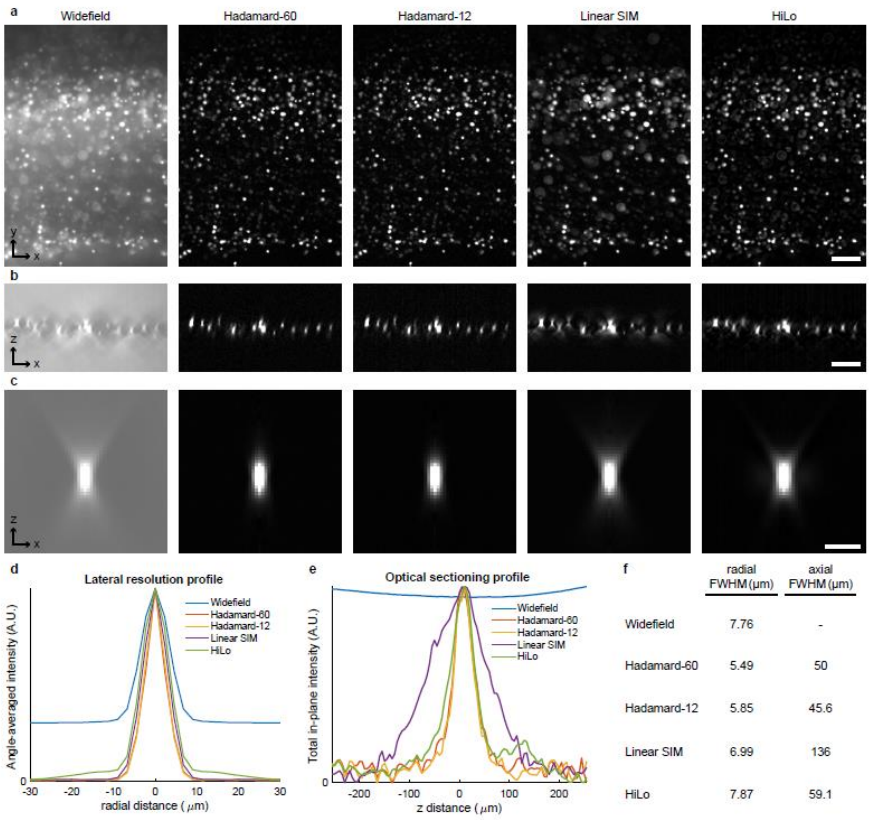

Figure 36. Comparison of optical sectioning techniques in acute brain slices.

(**a**) Comparisons of image quality in 1P optical sectioning methods. Images were acquired in the same sample with matched conditions (illumination intensity, acquisition time). The sample comprised an acute cortical brain slice expressing H2B-jRGECO1a. Images show (left to right): Wide-field epifluorescence, Hadamard microscopy using two different code lengths, linear SIM with period 4 pixels and four phases, and HiLo microscopy using DMD-projected speckle patterns. Scale bar 100 μm. (**b**) XZ cross sections of same data as in (a). Scale bar 100 μm. (**c**) An isolated nucleus from the dataset in (a-b) provided an approximation to the point spread function for the different imaging modalities. Scale bar 25 μm. (**d**) Radially averaged lateral profile of data in (b). (**e**) XY-integrated axial intensity profile of the data in (b). (**f**) Full-width half maxima of data in (d-e).

4.2.2 A spectrally orthogonal Ca^{2+} sensor and ChR for 1-photon AON

AON requires a spectrally orthogonal optogenetic actuator and activity reporter (**Figure 37a**). Examination of channelrhodopsin action spectra and Ca^{2+} reporter excitation spectra suggested that the best approach for 1-photon AON was to use a blue-shifted channelrhodopsin and a red-shifted genetically encoded Ca^{2+} indicator (RGECI). We thus set out to identify protein pairs suitable for this purpose.

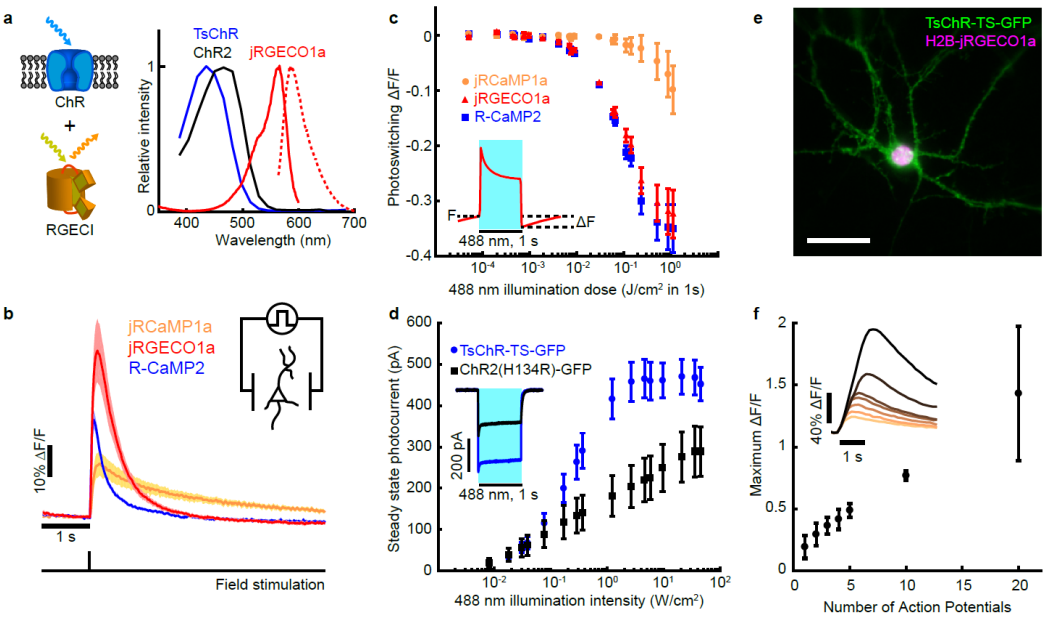

Figure 37. All-optical neurophysiology with a blue-shifted channelrhodopsin and a red-shifted Ca^{2+} indicator.

(**a**) Left: Schematic of a spectrally orthogonal channelrhodopsin and RGECI. Right: action spectra of proteins used in this work. Spectra are reproduced with permission from Refs. 86 and [197]. (**b**) Single action potential responses of RGECIs in cultured rat hippocampal neurons. Dark lines indicate the average of 3 FOVs, ~30 cells/FOV, for R-CaMP2 and 4 FOVs for jRGECO1a and jRCaMP1a. Colored bands indicate +/- SEM. Dishes were stimulated with 1 ms field stimulation pulses. RGECI fluorescence was recorded at 50 Hz. (**c**) Blue-light induced photoswitching of RGECIs in HEK293T cells under basal Ca^{2+} levels. RGECI fluorescence was recorded at 50 Hz with illumination at 561 nm, 80 mw/cm^2. Blue illumination (1 s pulses, 488 nm varying intensity) was added to the yellow illumination. Photoswitching was quantified as the decrease in fluorescence following blue light illumination compared to the initial fluorescence (inset), n = 3 FOV, ~50 cells/FOV, for each construct. (**d**) Steady state photocurrents of TsChR and ChR2(H134R) in cultured neurons held at -65 mV (1 s pulses, 488 nm, n = 6 cells for each construct). Inset: photocurrent response to 2 W/cm^2 488 nm illumination. (**e**) Cultured hippocampal neuron coexpressing H2B-jRGECO1a (magenta) and TsChR-TS-GFP (green). Scale bar 10 μm. (**f**) Example traces of H2B-jRGECO1a fluorescence response to increasing numbers of action potentials driven via current injection (inset) and maximum ΔF/F vs. number of evoked action potentials, n = 3 cells. Calcium imaging was performed at 7 Hz. Error bars in (c) and (d) indicate mean +/- SEM.

We began by comparing the single action potential responses of RGECIs in cultured neurons. jRGECO1a was the most sensitive ($\Delta F/F$ = 54 ± 10%, n = ~120 neurons), followed by R-CaMP2 and jRCaMP1a, consistent with previous reports (**Figure 37b**, **Table 6**)[197]. R-CaMP2 had the fastest kinetics (τ_{on} = 26 ± 10 ms, τ_{off} = 270 ± 20 ms, n = ~120 neurons), followed by jRGECO1a and jRCAMP1a (**Figure 38a**, **Table 6**). In HEK293T cells, under

basal Ca^{2+} conditions, jRGECO1a had the longest photobleaching time constant (τ_{bleach} = 81 ± 5 s, I_{561} = 44 W/cm^2, n = 9 cells), followed by R-CaMP2 and jRCaMP1a (**Table 6**). Under typical imaging conditions (I_{561} = 0.1 W/cm^2, 1 hr. cumulative exposure), photobleaching of jRGECO1a was thus negligible. Blue light (488 nm) excited direct fluorescence of all three proteins, an effect readily mitigated by interleaved excitation and imaging (**Figure 38b**). Blue light also photoswitched the mApple-based jRGECO1a and R-CaMP2 into a dark state in a blue light dose-dependent manner. The dark state recovered with a time constant of 0.4 s for RCaMP2 and 0.3 s for jRGECO1a, under 1 W/cm^2 561 illumination (**Figure 37c**, **Figure 38b**, Appendix 2).

	Single AP max ΔF/F (%)	τ_{on} (ms)	τ_{off} (ms)	τ_{bleach} (s)
jRGECO1a	54 ± 10, n = 4 FOV, ~30 cells/FOV	47.2 ± 1.0	443 ± 38	80.5 ± 5.1, n = 9 cells
R-CaMP2	31 ± 3, n = 3 FOV, ~30 cells/FOV	26.3 ±1.0	271 ± 20	61.9 ± 2.8, n =8 cells
jRCaMP1a	17 ± 4, n = 4 FOV, ~30 cells/FOV	61.2 ±2.1	1600 ± 160	37.8 ± 2.1, n =8 cells

Table 6. ***In vitro*** **characterization of RGECIs.**

Quantification of action potential responses in cultured neurons in **Figure 37b** and **Figure 38a**, and photobleaching kinetics in HEK293T cells. Action potential magnitudes and sensor kinetics are from 3 FOVs for R-CaMP2 and 4 FOVs for jRGECO1a and jRCaMP1a in separate dishes. Dishes were stimulated with 1 ms field stimulation pulses while imaging RGECI fluorescence at 50 Hz with 2.45 W/cm^2 561 nm illumination. Photobleaching measuremeents were performed in HEK293T cells under 44 W/cm^2 561 nm illumination (compared to 0.1 W/cm^2 used in slice imaging). All values are reported as mean ± SEM.

Photoswitching of the RGECI was a potential problem for AON because it produced slowly varying fluorescence signals that could masquerade as Ca^{2+} dynamics. To assess this problem, we compared the blue light doses needed for channelrhodopsin activation and for photoswitching. In cultured neurons expressing ChR2(H134R), optical induction of 10 action potentials at 20 Hz with 80% fidelity requires ~40 mJ/cm^2 of blue light[114]. This dose would induce > 10% photoswitching for jRGECO1a and R-CaMP2. While this artifact is small compared to the single-spike response in cultured neurons, in the more demanding tissue environment it could prove unacceptably high.

We reasoned that a more sensitive channelrhodopsin would be activated at lower blue light levels, leading to less photoswitching of the RGECIs. However, an increase in ChR sensitivity without a spectral shift would increase the spurious activation of the ChR by yellow light used for Ca^{2+} imaging. We thus sought a far blue-shifted channelrhodopsin. TsChR is the most blue-shifted published ChR (**Figure 37a**), but was initially reported to produce only ~40% as much photocurrent as ChR2(H134R)[86] and so has not previously been used in optogenetic applications.

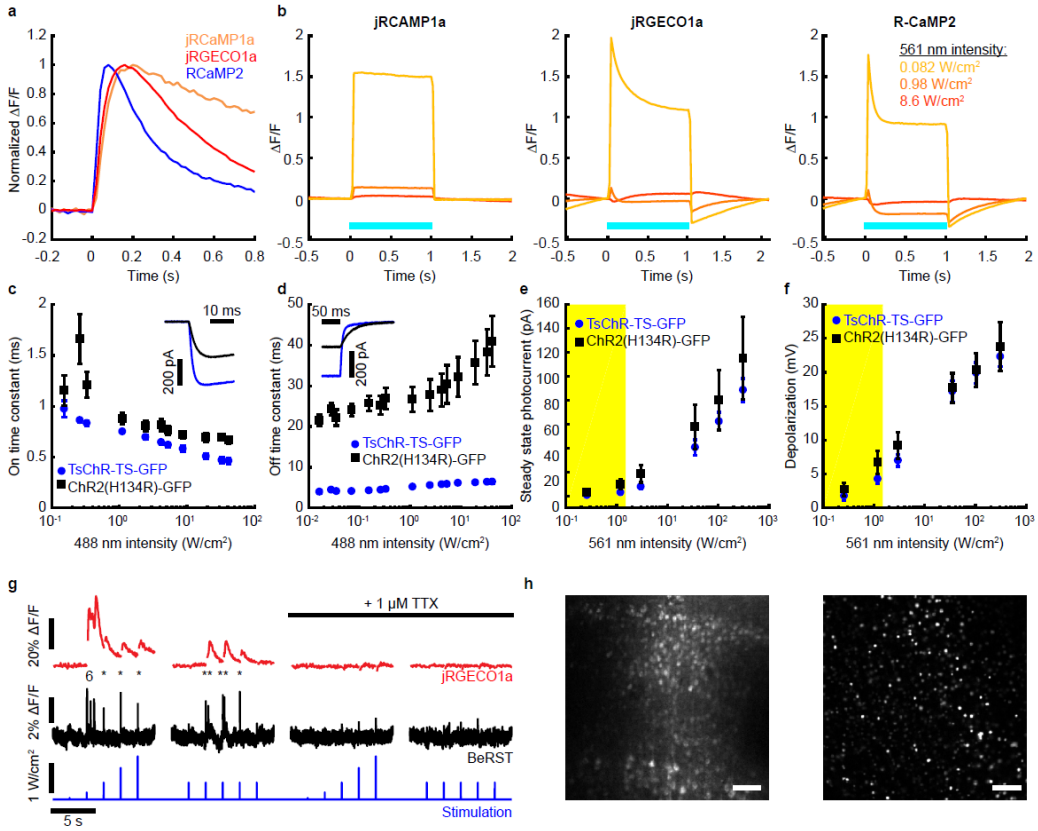

Figure 38. Photophysical characterization of RGECIs and TsChR.

(**a**) Kinetics of the RGECIs, shown by plotting data in **Figure 37b** normalized to peak ΔF/F. (**b**) Blue light-induced photoswitching of RGECIs in HEK293T cells. Fluorescence of the RGECI was excited at 561 nm with the indicated illumination intensity. A 1 s pulse of blue illumination (1.1 W/cm² 488 nm light) was added to the yellow illumination (blue bars). In jRGECO1a and R-Camp2 the blue illumination switched the protein into a state with reduced fluorescence. (**c**) Channelrhodopsin activation time constant as a function of 488 nm illumination intensity. Inset: Photocurrents at illumination start. (**d**) Closing time constants. (**e**) Activation of channelrhodopsins by yellow (561 nm) light. Steady state photocurrents in cultured neurons voltage clamped at -65 mV as a function of 561 nm illumination intensity. Yellow bar indicates typical jRGECO1a imaging intensities. (**f**) Same as (e) but showing voltage

(Continued) depolarization under current-clamp conditions with an initial potential of -65 mV. Data in (c-f) acquired from cultured rat hippocampal neurons, n = 6 for each construct. All error bars indicate mean +/- SEM. (**g**) Optogenetic stimulation induced action potentials and corresponding fluorescence transients in cultured neurons expressing jRGECO1a and TsChR-TS-GFP. Pulses of blue light (488 nm, 10 ms) of the indicated intensities drove action potentials (*), which were identified via fluorescence of a far-red voltage-sensitive dye, BeRST1 (1 μM, black trace)[28]. Spontaneous events were also detected. Fluorescence transients of jRGECO1a accompanied each action potential (red trace). Right: TTX (1 μM) silenced activity in both the voltage and Ca^{2+} channels, confirming that signals arose from neural activity. Voltage imaging was performed at 500 Hz with 0.7 W/cm^2 640 nm light and calcium imaging was performed at 20 Hz with 1.1 W/cm^2 561 nm light. (**h**) Maximum intensity projections of Hadamard z-stacks from acute cortical slices prepared from mice injected with cytosolic AAV1-syn-NES-jRGECO1a (left) or nuclear-targeted AAV9-syn-DO-H2B-jRGECO1a (right) at P1. Scale bars 100 μm.

Addition of a K_{ir}2.1 trafficking sequence (TS) and a GFP expression tag to TsChR led to excellent trafficking in cultured neurons (**Figure 37d-e**). Compared to ChR2(H134R), TsChR-TS-GFP had higher steady state photocurrents (470 ± 42 vs. 288 ± 60 pA, p = 0.034, Student's t-test, n = 6 neurons each), higher maximum steady state photocurrent densities (13.2 ± 1.2 pA/pF vs. 7.8 ± 2.0 pA/pF, p = 0.044, Student's t-test, n = 6) and faster on- and off- kinetics (**Figure 37d**, **Figure 38c-d**). At the highest blue light intensity tested (33 W/cm^2), ChR2(H134R) passed a steady state photocurrent of 288 ± 60 pA; TsChR passed the same steady state photocurrent at a 100-fold lower intensity (0.33 W/cm^2; **Figure 37d**). As a result, TsChR could drive action potentials with a 100-fold lower light dose, resulting in a correspondingly smaller level of jRGECO1a photoswitching.

	TsChR-TS-GFP	ChR2(H134R)-GFP	*p*-value, Student's *t*-test
Access resistance (MΩ)	12.3 ± 1.5	12.4 ± 1.3	0.96
Membrane resistance (MΩ)	633 ± 84	467 ± 88	0.20
Membrane capacitance (pF)	36.5 ± 4.8	44.9 ± 9.7	0.45
Resting potential (mV)	-36.5 ± 4.8	-44.3 ± 2.9	0.13

Table 7. Patch characterization of TsChR.

Patch parameters of cells in **Figure 37d** and **Figure 38c-f**. All values are reported as mean ± SEM, n = 6 cells throughout.

Despite the greater blue sensitivity of TsChR than ChR2(H134R), the yellow (561 nm) light used for RGECI imaging induced a smaller photocurrent in TsChR than in ChR2(H134R) (**Figure 38e-f**). Finally, TsChR-TS-GFP did not significantly affect neurons'

electrophysiological properties compared to ChR2(H134R)-GFP (**Table 7**). Together, these properties made TsChR a promising actuator to combine with RGECIs for crosstalk-free AON.

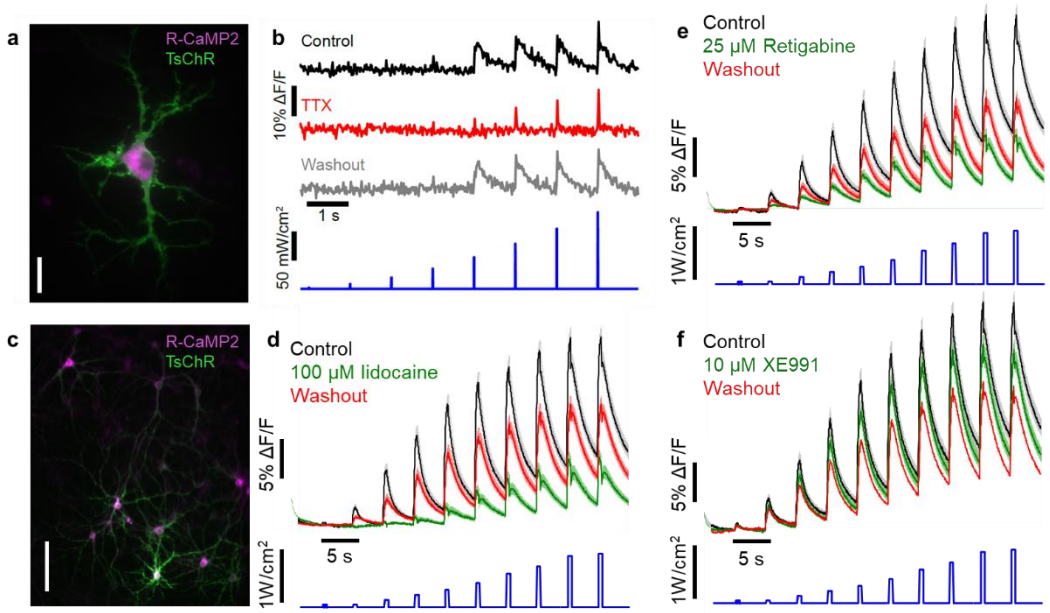

Figure 39. Calcium-based AON in cultured neurons.

(**a**) CaMKIIa-R-CaMP2 and CaMKIIa-TsChR-TS-GFP were cotransfected via calcium phosphate into cultured rat hippocampal neurons. Scale bar = 20 μm. (**b**) Blue light (bottom) evoked all-or-nothing fluorescence transients which were reversibly blocked by the addition of 1 μM TTX. (**c**) Same as (a) but neurons were transduced with lentivirally packaged constructs and imaged under a lower magnification. Scale bar = 100 μm. (**d-f**) Average response of manually selected cells to 500 ms blue light stimulations of the indicated intensity before, in the presence of, and after washing out 100 μM lidocaine (n =124 neurons), 25 μM retigabine (n =118 neurons), or 10 μM XE991 (n =118 neurons). Light fields indicate ±1 SEM. Sampling rate was 50 Hz throughout.

The ability to activate TsChR at blue light levels that did not appreciably photoswitch mApple-based RGECIs permitted us to combine it with R-CaMP2 and jRGECO1a. In cultured neurons, coexpression of R-CaMP2 and TsChR could optically induce and record fluorescence transients (**Figure 39a-b**). Fluorescence transients were caused by action potentials as they were reversibly blocked by TTX. Similar assays could distinguish excitability phenotypes induced by the addition of the used-dependent sodium channel blocker lidocaine,

the Kv7 channel positive allosteric modulator retigabine, and the the Kv7 channel blocker XE991 (**Figure 39c-f**).

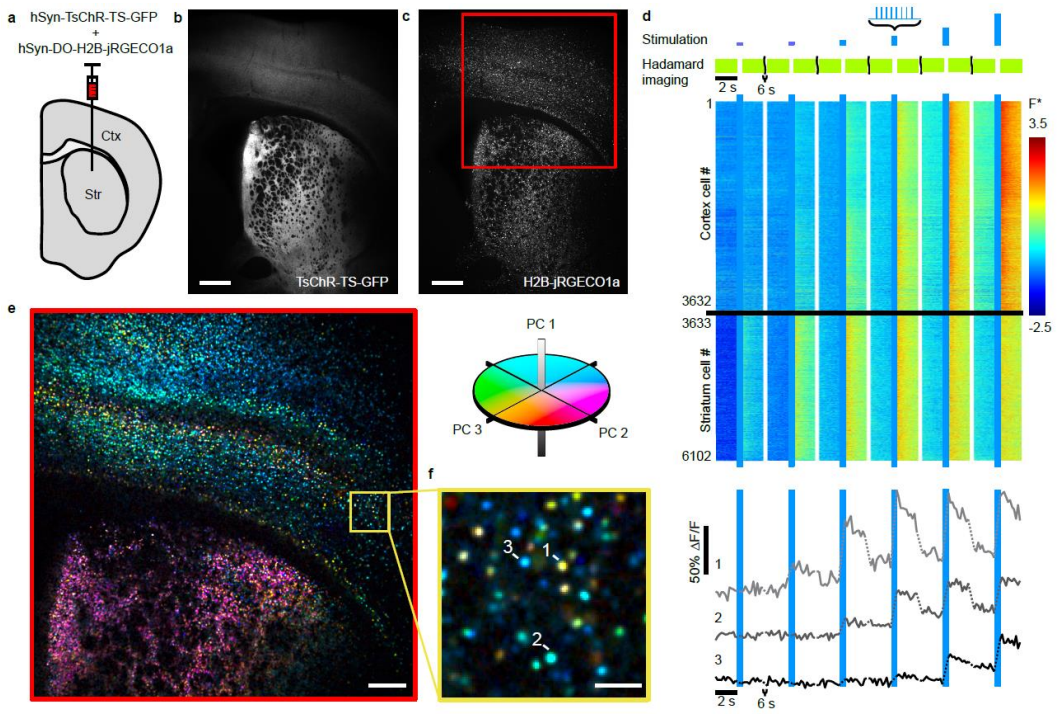

Figure 40. Ultra-widefield AON in acute brain slices.

(**a**) AAV9 viruses coding for hSyn-TsChR-TS-GFP and hSyn-DO-H2B-jRGECO1a were co-injected in neonatal mouse cortex and striatum. (**b**) Maximum intensity projection of a Hadamard z-stack of TsChR-TS-GFP expression in a coronal corticostriatal slice from a P21 mouse. (**c**) Same as (b) in the H2B-jRGECO1a channel. Functional data were acquired within the red square. (**d**) Top: Stimulation and imaging protocol. The highlighted FOV in (c) was stimulated with eight 5 ms pulses of 488 nm light at 20 Hz with intensities of 15, 30, 60, 120, 240, and 480 mW/cm^2. Bottom: heat map of 6,102 single-cell fluorescence traces extracted from slice in (b-c). Individual fluorescence intensities traces are normalized as F* = (F - mean(F))/std(F). White breaks separate measurements at different optogenetic stimulus intensities. (**e**) Left: red region in (c) with cells colored by the principle component amplitudes of the functional responses. See Methods for additional details. (**f**) Left: close-up of the yellow boxed region of (e). Right: three example single-cell fluorescence traces. Dotted lines indicate pauses in Hadamard imaging (400 ms during optogenetic stimulation, 6 s between stimuli). $\Delta F/F$ is defined relative to the intensity in the first imaging epoch. Scale bars 250 μm in (b, c, e) and 50 μm in (f).

We also evaluated the more sensitive RGECI, jRGECO1a, for imaging. In cultured neurons cotransfected with TsChR and jRGECO1a, blue light pulses induced action potentials whose accompanying Ca^{2+} transients were readily observed via jRGECO1a fluorescence (**Figure 38g**). However, when we expressed jRGECO1a densely in an acute brain slice and

imaged by Hadamard microscopy, we found residual fluorescence between cell somata due to reporter molecules in the neuropil (**Figure 38h**). To address this source of background, we localized jRGECO1a to the nucleus by replacing the nuclear export sequence on jRGECO1a with a Histone-2B tag (H2B), as previously done for whole-brain zebrafish imaging[198–200]. In cultured neurons, H2B-jRGECO1a responded to single action potentials with good sensitivity (max $\Delta F/F = 19.4 \pm 5.3\%$, $n = 3$ cells), but with slower kinetics than the cytosolic reporter, ($\tau_{on} = 167 \pm 27$ ms, $\tau_{off} = 1{,}400 \pm 270$ ms) consistent with previous measurements of nuclear Ca^{2+} dynamics (**Figure 37e-f**)[201,202]. In Hadamard images of acute slices expressing H2B-jRGECO1a, cells were visible as well resolved bright puncta (**Figure 38h**).

4.2.3 Mapping excitability in acute slices with single-cell resolution

To map neural excitability, we applied Hadamard microscopy with simultaneous optogenetic stimulation in acute mouse brain slices expressing the actuator-reporter pair. We co-injected AAV9-hSyn-DO-H2B-jRGECO1a and AAV9-hSyn-TsChR-TS-GFP in cortex and striatum of wild-type P0-2 mouse neonates (**Figure 40a**). Both proteins expressed well and were readily visualized via Hadamard imaging in 300 μm acute brain slices from 3-week-old animals (**Figure 40b-c**). We performed Hadamard AON measurements in a region 2.3 × 2.3 mm, set by the size of the expressing region.

To probe excitability, we exposed the slice to a series of wide-field blue stimuli of increasing strength, interleaved with Hadamard imaging (**Figure 40d**). Hadamard images were first acquired for 2 s to establish baseline fluorescence. Then a brief burst of blue light pulses (470 nm, 8 pulses, 15 mW/cm^2, 5 ms duration, 20 Hz) evoked neural activity, followed by another 2 s of Hadamard imaging to record the response. This image-stimulate-image procedure was repeated at 10 s intervals, six times, with the intensity of the blue light doubling upon each repetition to a maximum of 480 mW/cm^2. This measurement protocol reported the changes in intracellular Ca^{2+} concentration as a function of optogenetic stimulus strength.

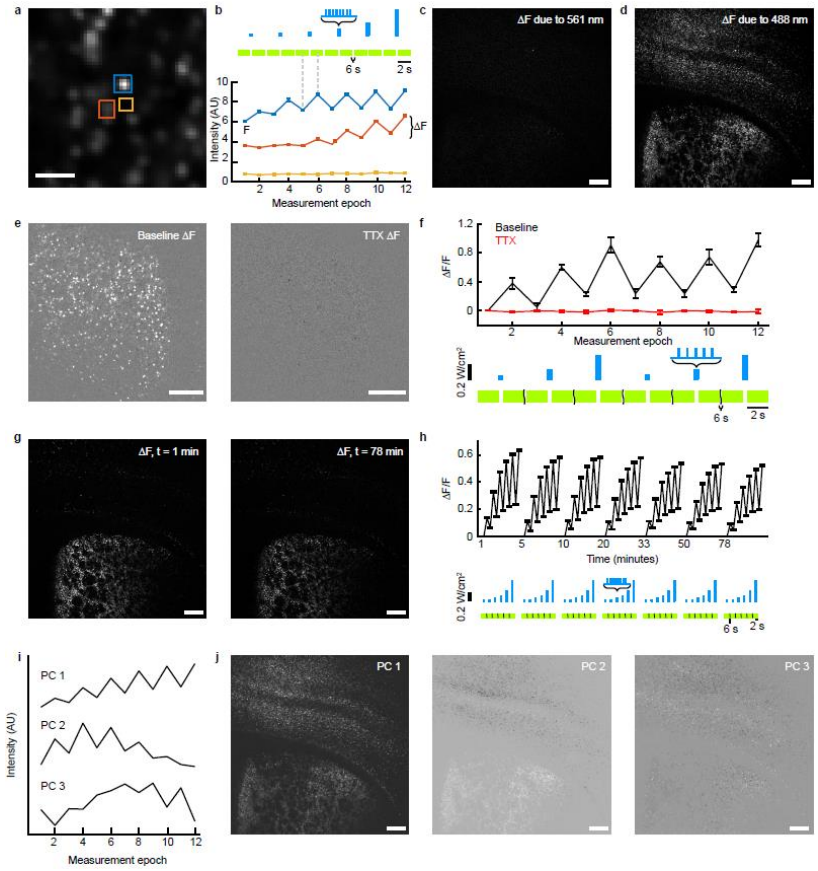

Figure 41. Crosstalk and stability of ultra-widefield AON in acute brain slices.

(**a**) Magnified view of region of **Figure 40e** showing single-cell resolution. (**b**) Fluorescence traces from regions indicated in (a). Two cells showed optogenetically induced fluorescence transients, while a region between the cells showed no signal. Here the sets of 11 images acquired before and after each optogenetic stimulus were averaged to form single pre- and post-stimulus fluorescence values. Error bars represent SEM over n = 11 Hadamard images. Scale bar 25 μm. F is defined as the average intensity of the first imaging epoch and ΔF is the signal increase following blue light stimulation. (**c**) Measurement of spurious TsChR activation by yellow (561 nm) light. The image shows the difference between mean fluorescence of H2B-jRGECO1a in the second and first second after onset of yellow light for Ca^{2+} imaging. Image represents a mean of n = 3 repetitions of the measurement. Spurious TsChR activation would cause neural firing, which would lead to an increase in H2B-jRGECO1a fluorescence. (**d**) Mean ΔF induced by blue light stimulation, averaged over three runs. (c) and (d) are scaled identically. (**e**) Mean ΔF images from striatum before (left) and after (right) addition of TTX (1 μM). Images are scaled identically. (**f**) Mean ΔF/F per measurement epoch from n = 360 cells in (f) before TTX addition (black) and after TTX addition (red). Blue light stimulation consisted of 5 pulses at 12.5 Hz of 488 nm light at 60, 120, and 300 mW/cm², repeated twice. (**g**) One slice was repeatedly stimulated and imaged over 78 minutes with protocol in **Figure 40**. Mean ΔF images from first run (left) and last run (right), scaled identically. (**h**) Average ΔF/F per measurement epoch for n = 3,195 cells in each run in slice shown in (g). (**i**) Waveforms of main principal components from n = 31,754 cells. (**j**) Principal components from (i) projected into pixel space for slice in **Figure 40e**. Unless otherwise stated, all scale bars = 250 μm. Error bars indicate +/-SEM.

We used a 2D peak-finding algorithm to identify n = 6,102 responding cells in the Hadamard images (**Figure 40d**). Neighboring cells often showed distinct patterns of Ca^{2+} dynamics, while interstitial regions showed undetectable fluorescence (**Figure 41a,b**), confirming that Hadamard microscopy effectively rejected scatter and out-of-focus background. The yellow light (561 nm, 100 mW/cm^2) used for Ca^{2+} imaging induced activity in only 12 of the 6,102 cells, (**Figure 41c,d**), establishing that the imaging light only weakly activated TsChR. The sodium channel blocker tetrodotoxin (TTX, 1 μM) abolished blue light evoked responses slice wide, confirming that Ca^{2+} responses were due to action potential firing (**Figure 41e,f**) and, furthermore, that blue light-induced photoswitching was undetectable.

We tested the long-term stability of the preparation in another slice. The optogenetically induced Ca^{2+} signal was stable over a 78 minute session comprising 7 repeated imaging cycles (**Figure 41g,h**). During this period the population-average optically evoked $\Delta F/F$ at the strongest stimulus decreased modestly from 64 ± 0.7% to 52 ± 0.7%, n = 3,195 cells. These results demonstrate the capability for repeated measurements over > 1 h in a single sample.

Cells showed different patterns of response in the striatum vs. cortex, but we also observed cell-to-cell variability within the cortex. To characterize this variability, we applied principal components analysis (PCA) to a set of single-cell recordings. First, we repeated the excitability measurement on 9 slices from 2 animals, recording from a total of n = 32,103 cells across cortex and striatum. Measurement runs (comprising six measure-stimulate-measure sequences) were repeated at 5 minute intervals, 3 times per slice. PCA identified 3 main temporal components in the single-cell fluorescence responses (**Figure 41i**, Methods). Examination of the PC temporal waveforms showed that PC1 measured overall fluorescence response amplitude, PC2 captured a left-right shift in the sigmoidal excitability profile, and PC3 largely captured a stimulus-dependent increase in baseline fluorescence.

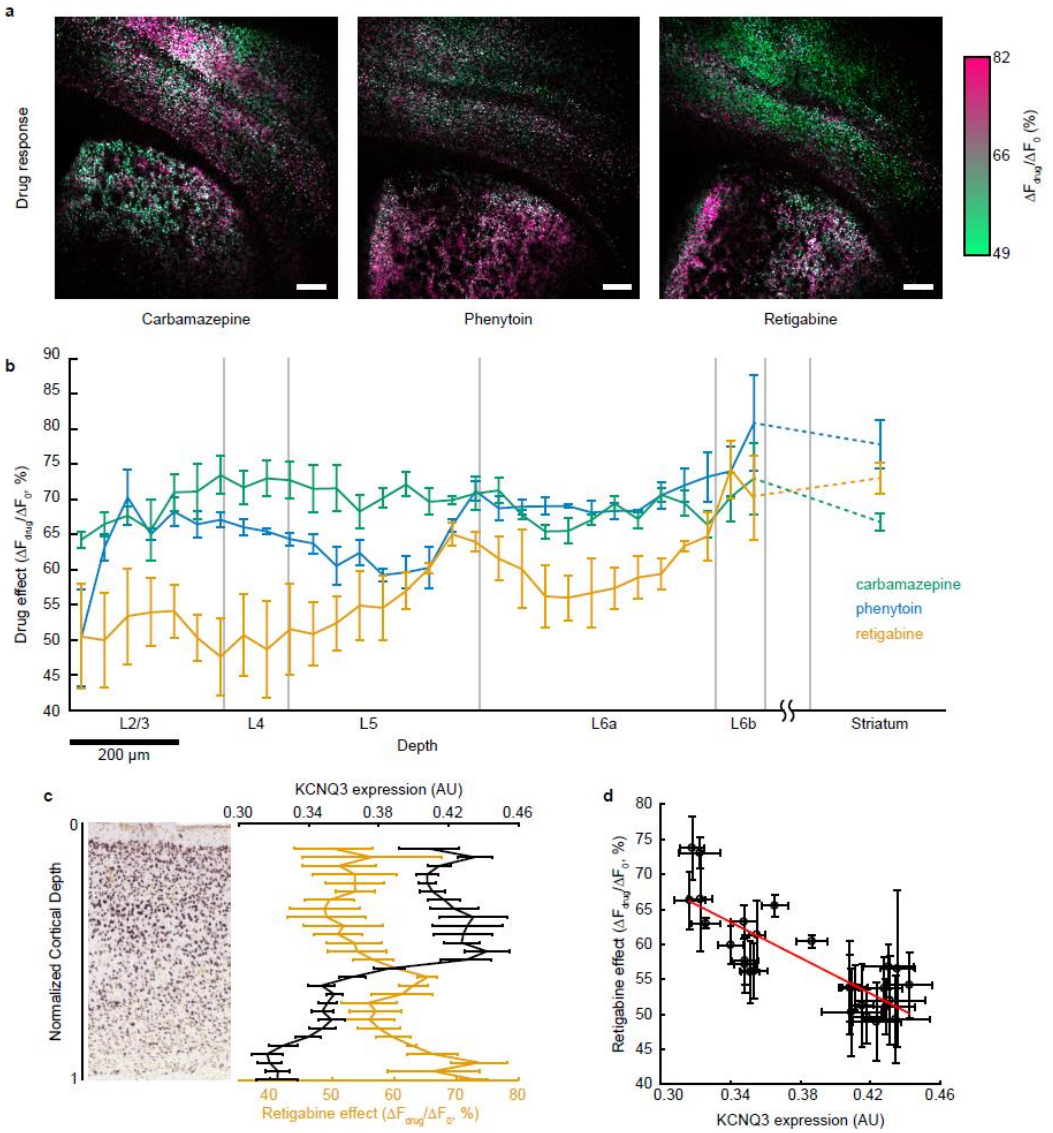

Figure 42. Mapping effects of anti-epileptic drugs (AEDs) on excitability.

(**a**) Maps of AED effects on excitability. Slices were measured using the excitability protocol as in **Figure 40**. The protocol was repeated five times before drug addition and four times after addition of carbamazepine (100 µM), phenytoin (100 µM), or retigabine (25 µM). The ratio of mean optogenetically induced change in fluorescence for each cell before (ΔF_0) and after drug addition (ΔF_{drug}) is encoded as color in a green to pink axis. Scale bars 250 µm. (**b**) Average drug response ($\Delta F_{drug}/\Delta F_0$) as a function of cortical depth for n = 3 slices for each drug. All striatal cells in a slice were pooled into a single bin. Data represents n = 9,793 cells for carbamazepine, 11,858 cells for phenytoin, and 10,103 cells for retigabine. Error bars represent SEM over n = 3 slices for each drug. (**c**) Left: *in situ* hybridization image from Allen Brain Atlas experiment #100041071 showing KCNQ3 expression in somatosensory cortex of a P28 mouse. Right: cortical depth dependence of retigabine drug effect (same as **Figure 42b**) and KCNQ3 expression level determined from *in situ* hybridization images of n = 11 slices from the Allen Brain Atlas. (**d**) Data from (c) showing effect of retigabine on excitability vs. KCNQ3 expression. Best fit line is indicated in red. Error bars are mean +/- SEM, treating each slice as an independent measurement.

We then decomposed the fluorescence waveform at each pixel into its principal components (PCs), and color-coded each pixel by its PC amplitudes (**Figure 40e**, **Figure 41j**, methods). Despite coloring each pixel independently, individual cells appeared homogeneously colored in the resulting image (**Figure 40f**). These maps revealed striking colored bands running along the cortical layers, demonstrating different functional responses in different brain regions. Intriguingly, some layers appeared relatively homogeneous (L2/3, L4, L6), while cells in L5 had larger cell-to-cell variations in response. These results demonstrate that Hadamard AON can map excitability over large areas of acute brain slice with single cell precision.

4.2.4 Mapping drug responses with Hadamard AON

Wide-area AON offers a means to map the cell type and region-specific effects of drugs or other perturbations on neural excitability. We performed excitability measurements on acute slices before and after applying the antiepileptic drugs (AEDs) retigabine (25 μM), carbamazepine (100 μM), and phenytoin (100 μM). To quantify the drug effect, we measured the pixel-by-pixel change in mean amplitude, ΔF, of the optogenetically induced response—a parameter close to the first principal component that emerged from the unsupervised analysis above. Each drug had different effects in striatum and cortex, and attenuated cortical excitability in a distinctive spatial pattern (**Figure 42a**).

We sorted cells into bins based on their cortical depth and visualized mean AED response as a function of cortical depth, averaged over $n = 3$ slices per drug (**Figure 42b**). Carbamazepine and phenytoin, both sodium channel blockers, showed relatively uniform suppression of excitability as a function of cortical depth, but retigabine showed a graded response, strongest in L2/3 and weakest in L6b.

Retigabine is a specific positive allosteric modulator of K_v7 channels, and its primary target is thought to be the $K_v7.2/7.3$ heteromer[203], coded for by the genes KCNQ2 and KCNQ3. We examined the Allen Brain Atlas map of the expression level of KCNQ3, as

determined by RNA *in situ* hybridization (ISH), and found statistically significant correlation between expression level and effect of retigabine (Pearson's r = -0.40, 95% confidence interval between -0.022 and -0.69 obtained by bootstrapping, **Figure 42c-d**). Higher expression of KCNQ3 correlated with greater inhibition of excitability by retigabine, as one would expect for a potassium channel activator. An independent ISH study in adult animals reported a similar distribution of KCNQ2 and KCNQ3 RNA[204]. These results establish a connection between the Hadamard AON measurements and the underlying pattern of channels.

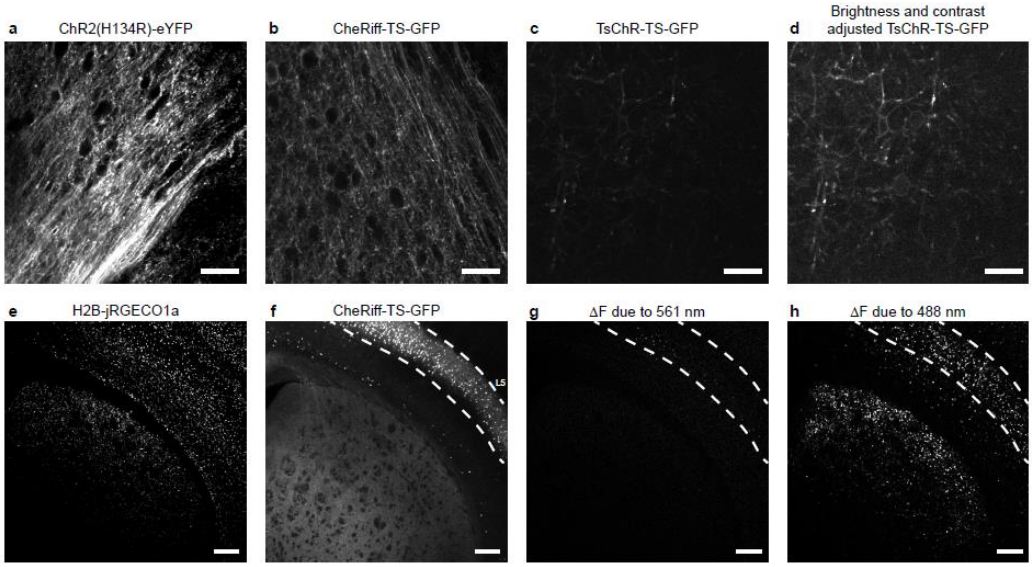

Figure 43. Trafficking of optogenetic actuators in axons in tissue.

(**a-c**) Representative images of axonal trafficking of ChR2(H134R)-YFP, CheRiff-TS-GFP, and TsChR-TS-GFP, scaled to the same counts. (**d**) Same image as in (c) with brightness and contrast adjusted to show low level axonal expression of TsChR. Equal volumes of AAV2/9-hSyn-ChR2(H134R)-eYFP, AAV2/9-hSyn-CheRiff-TS-GFP, and AAV2/9-hSyn-TsChR-TS-GFP were injected in one hemisphere and coronal slices of the contralateral hemisphere were prepared after > 4 weeks. Images near the corpus callosum were acquired with 2-photon microscopy. (**e-g**) Characterization of spurious CheRiff activation by yellow light used for Ca^{2+} imaging. A brain slice co-expressing H2B-jRGECO1a and CheRiff-TS-GFP was prepared as in **Figure 44a**. (**e**) Image of H2B-jRGECO1a. (**f**) Same slice as (e) showing CheRiff-TS-GFP. (**g**) Measurement of spurious CheRiff activation by yellow (561 nm) light. The image shows the difference between mean fluorescence of H2B-jRGECO1a in the second and first second after onset of yellow light for Ca^{2+} imaging. Image represents a mean of n = 3 repetitions of the measurement. Spurious CheRiff activation would cause neural firing, which would lead to an increase in H2B-jRGECO1a fluorescence. Yellow light used for Ca^{2+} imaging (100 mW/cm^2) induced Ca^{2+} transients in a small number of cortical L5 cells which co-expressed the actuator and reporter (27 of 436 cells), indicating a slightly higher level of optical crosstalk into the actuator than with TsChR (compare to **Figure 41c**). However, yellow

(Continued) light induced a Ca^{2+} transient in only 1 of 859 striatal cells establishing that the crosstalk was insufficient to drive post-synaptic spiking. (**h**) Mean ΔF induced by blue light stimulation, averaged over three runs. (g) and (h) are scaled identically. Scale bars 50 μm in (a-d), 250 μm in (e-h). Dashed lines in (f-h) indicate Layer 5 of the cortex.

4.2.5 Probing synaptic connections with ultra-widefield AON

We next sought to extend the Hadamard AON platform to measurements of synaptic connectivity. Although slicing interrupts many long-range projections, optogenetic stimulation of axon terminals can nonetheless evoke local neurotransmitter release and postsynaptic responses[205]. We reasoned that sufficiently strong presynaptic stimulation would drive postsynaptic spikes, which could be detected via H2B-jRGECO1a.

TsChR did not traffic down long-range projections, preventing its use for this application (**Figure 43a-d**). CheRiff-TS-GFP[170] trafficked well in axons, so we used this blue-shifted actuator instead. We coinjected a 1:3.6 ratio of AAV2/9-hSyn-DO-H2B-jRGECO1a (Cre-off) and AAV2/9-CAG-DIO-CheRiff-TS-GFP (Cre-on) in the cortex and striatum of neonatal Rbp4-$Cre^{+/-}$ mice. Rbp4-Cre labels a population of L5 cells, and has been used to investigate cortico-cortical and cortico-striatal connections, including via optogenetic axon-terminal stimulation[206,207]. In this configuration, CheRiff-TS-GFP expressed in a subset of cells in L5 of the cortex, while H2B-jRGECO1a expressed in cells across the cortex and striatum (**Figure 44a**). We verified that the yellow light used for imaging caused only minimal activation of CheRiff-positive axon terminals (**Figure 43e-h**).

We then repeated the blue-light stimulation and imaging protocol previously used for excitability measurements. Blue light induced nuclear Ca^{2+} transients across the cortex and striatum (**Figure 44b**). Blockers of excitatory transmission, NBQX and CPP, reversibly eliminated the responses in the striatum, Layer 6, and Layer 2/3, confirming that these responses were synaptically evoked (**Figure 44c**).

To our surprise, addition of NBQX and CPP reversibly increased optogenetically induced activity in a population of cells in L5a (**Figure 44d**). The location of these cells amidst the Rbp4 population suggested that these cells expressed both the actuator and reporter (likely

a consequence of imperfect silencing of DO-H2B-jRGECO1a in Rbp4-Cre^{+} neurons[208]). The increase in excitability upon excitatory blockade then implies a disinhibitory mechanism, i.e. that these L5a cells received disynaptic inhibition from Rbp4-Cre labeled L5 pyramidal cells, which was relieved under excitatory blockade. This finding is consistent with previous findings that excitation of corticostriatal neurons can suppress local activity in cortex[209]. These intermixed responses highlight the importance of performing single cell resolution measurements with Hadamard microscopy.

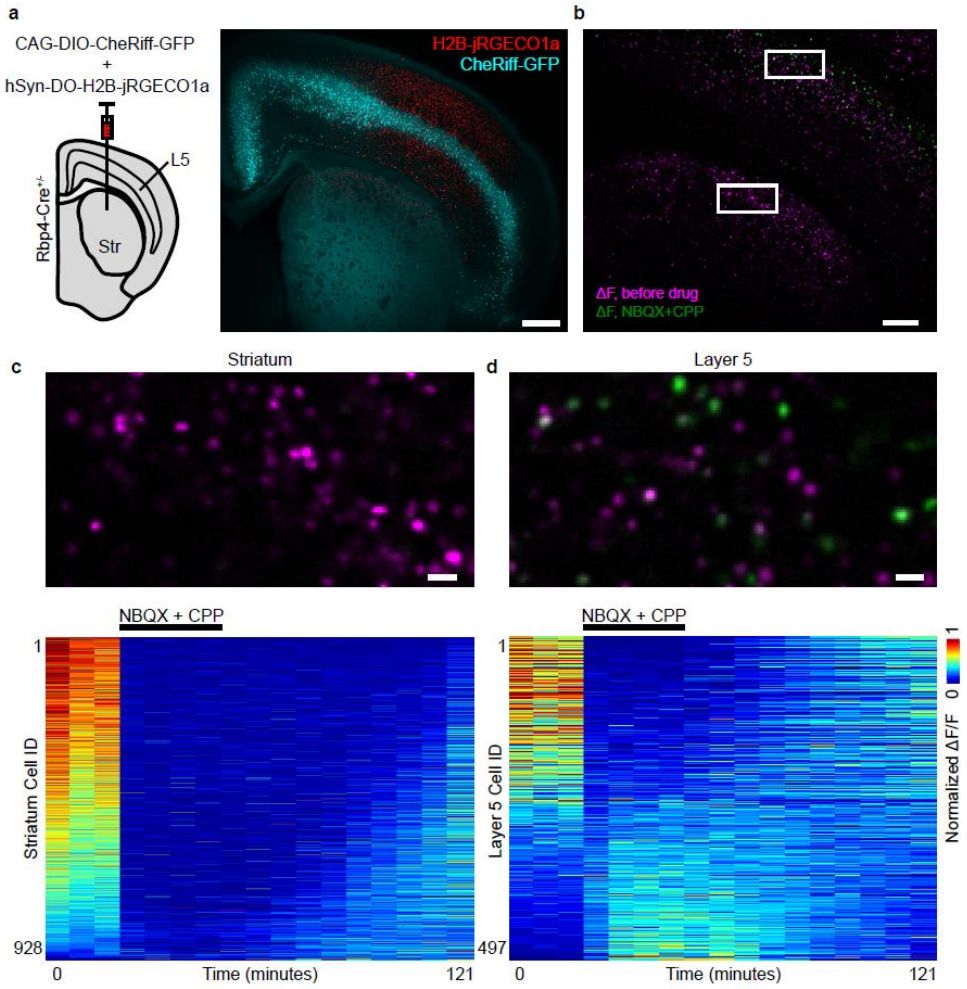

Figure 44. Mapping synaptic connections.

(**a**) Left: viral constructs for mapping synaptic connections. Cre-dependent AAV9-CAG-DIO-CheRiff-GFP and AAV9-hSyn-DO-H2B-jRGECO1a were co-injected in Rbp4-Cre$^{+/-}$ neonatal mice. Right: at P21, CheRiff-GFP expressed in Cre^{+} L5 pyramidal cells, including corticostriatal projection neurons. H2B-jRGECO1a expressed broadly in cortex and striatum. Images represent a maximum intensity projection of a Hadamard z-stack. Scale bar 500 μm.

(Continued, **b**) Mean optogenetically induced fluorescence transients, ΔF, before (magenta) and after (green) addition of excitatory blockers, NBQX (10 μM) and CPP (10 μM). Stimulation was performed as in **Figure 40**. Images are the median of 3 runs before and 4 runs after adding excitatory blockers. Scale bar 250 μm**.** (**c**) Magnified views of indicated regions in striatum and Layer 5 in (b). Scale bar 25 μm. (**d**) Mean optogenetically induced fluorescence response, ΔF, for each cell before, in the presence of, and during washout of excitatory blockers. Left: striatum. Right: Layer 5. Each column represents the mean optogenetically induced ΔF of an experimental protocol as in **Figure 40d**. The slice was measured over 121 minutes (5-10 minutes between measurements, 22 minutes before last measurement). For visualization, each cell trace was normalized by its mean.

4.3 Discussion

The combination of Hadamard microscopy and optogenetic constructs for 1P AON enables wide-area mapping of excitability and of synaptic transmission in brain tissue, and studies on the effects of perturbations thereon. We demonstrated these capabilities by mapping the effects of AEDs on cortical excitability, and by mapping the downstream synaptic partners of Layer 5 pyramidal neurons through the addition of synaptic blockers. Expanding these measurements to other drugs may provide insights into cellular and regional targets and mechanisms, where these are not *a priori* known. Hadamard AON could also be used to probe the effects of neuropeptides, neuromodulators, hormones, genetic mutations, or environmental perturbations (e.g. temperature, oxygen, metabolites) on brain-wide patterns of neural excitability or synaptic transmission. One could use the technique to map changes in function associated with learning and memory, as well as with genetic, age-related, or injury-induced neural disorders.

Both Hadamard microscopy and 1P AON can be used independently and neither technique is limited to neuroscience applications. Hadamard imaging could be used to visualize any of the vast array of fluorescent sensors that report on distinct aspects of cellular function, including reporters of neurotransmitter release, of intracellular signaling, and of physiological variables such as pH, ATP, and reactive oxygen species[46,210]. Development of red-shifted sensors for these other modalities will facilitate combination with optogenetic stimulation for measures of activity-dependent functional changes. Hadamard microscopy may also be useful

for high throughput structural mapping of samples expressing fluorescent proteins, or stained with fluorescent markers.

As with other SIM approaches, Hadamard microscopy rejects defocused signals, but not the shot noise associated with their detection. Since the Hadamard optical section is calculated with a pixel-wise ±1-weighted sum of patterned images, its shot noise is the same as that of the widefield image obtained by direct sum—without demodulation—of the patterned images. In comparison to point-scanning confocal, the additional shot noise in Hadamard microscopy is precisely compensated by the increased duty cycle of illumination which leads to a higher total number of photons collected per pixel. From a shot-noise perspective, the two techniques are equivalent, but for Hadamard microscopy the signal and noise are accumulated uniformly during image acquisition, while for confocal they are accumulated at each pixel in a single burst.

Hadamard microscopy bears some similarity to fluctuation-based imaging techniques such as PALM/STORM[211] and SOFI[212]. In those techniques, uncorrelated spontaneous fluctuations in the intensity of individual molecules are used to resolve signal sources whose point spread functions overlap. In Hadamard microscopy, the fluctuations in intensity of adjacent sample regions are defined by the illumination, and thus are precisely uncorrelated, not just statistically so. Foreknowledge of the fluctuation patterns in Hadamard microscopy further facilitates the image reconstruction steps. Whereas single-molecule superresolution microscopies seek to counteract the effect of diffraction on the PSF, Hadamard seeks to counteract the effect of light scattering.

2P mesoscopes currently hold the record for most single neurons (~3000) recorded simultaneously in tissue[213]. 2P-mesoscopes have greater depth penetration than SIM techniques, making them more suitable for *in vivo* studies at present, but Hadamard microscopy shows comparable performance for brain-slice measurements. Point-scanning based mesoscopes have achieved pixel rates of ~2×10^7/s over 0.6 × 0.6 mm FOVs but the

requirement to translate the beam long distances limits pixel rates over large FOVs (4.4 × 4.2 mm) to 5.6×10^6/s. With 12-pattern Hadamard, we achieved comparable data rates of 1.2 $\times10^7$/s over a 4.6 × 2.3 mm FOV. With additional optimization, pixel rates of 3.3×10^7 pixels/s over the entire 4.6 × 4.6 mm FOV are possible with current camera technology. Finally, in contrast to 2P-mesoscopes, Hadamard microscopy is readily applied across a broad range of excitation wavelengths and is comparatively inexpensive to implement.

In the present AON work, the maximum number of neurons recorded in parallel (6,102) was limited not by data rate but by the expression pattern of the virally delivered constructs. In transgenic animals or with recently developed systemic gene delivery techniques[214], Hadamard microscopy could tile a complete sagittal slice in 7 FOVs, fast enough for functional measurements over acute slices from an entire mouse brain. The resulting brain-wide functional mapping could provide an unbiased approach to studying excitability and synaptic function.

4.4 Methods

4.4.1 DNA constructs.

R-CaMP2 was a gift from Haruhiko Bito. TsChR was a gift from Ed Boyden. jRGECO1a and jRCAMP1a were obtained from Addgene (Plasmids #61563 and #61562). All RGECIs were cloned between the BamHI and EcoRI sites of the backbone from FCK-Arch-GFP (Addgene Plasmid #22217) for expression in cultured neurons and for lentiviral production. For photophysical characterization, RGECIs were also cloned into an analog of the FCK vector replacing the *CaMKIIa* promoter with a CAG promoter, a configuration we refer to as FCAG. The jRCaMP1a and jRGECO1a constructs included the nuclear export sequences found in the original publication[197]. For nuclear localization, the nuclear export sequence of jRGECO1a was replaced with an H2B tag, and cloned into an AAV-hSyn-DO Cre-off vector. TsChR, including an N-terminal Kir2.1 trafficking sequence followed by a GFP fluorescent tag, was cloned into FCK and into an AAV expression vector under control

of the human synapsin promoter (AAV-hSyn). CheRiff-TS-GFP (Addgene Plasmid # 51693) was cloned into an AAV-CAG-DIO expression vector. FCK-ChR2(H134R)-GFP was used as a reference for TsChR characterization. FCK-VSV-G (Addgene Plasmid #8454) and psPAX2 (Addgene Plasmid #12260) were used in lentiviral production. pUC19 (NEB #N3041) was used as a diluent in calcium phosphate transfections.

4.4.2 Cell culture and gene expression.

4.4.2.1 HEK cell culture and gene expression.

Photophysical measurements of RGECIs were performed in HEK293T cells (ATCC CRL-11268) cultured as previously described[170]. Cells were grown at 37 °C, 5% CO_2 in DMEM containing 10% FBS (Life Technologies 10082-147) and 50 U/mL penicillin-streptomycin (Life Technologies 15060-063). Cells were split with trypsin-EDTA (Life Technologies 25300054) every 2-3 days and used before passage 25. For gene delivery, cells were grown to 70% confluence in 24 well plates or 35 mm plastic dishes. 200 ng (for 24 well plates) or 400 ng (for 35 mm plastic dishes) of FCAG-RGECI DNA was transfected using TransIT-293 (Mirus 2705) following manufacturer instructions. After 24 hours, cells were split onto Matrigel (Fisher Scientific 356234) coated glass bottom plates (In Vitro Scientific D35-14-1.5-N) and imaged 24 hours later.

4.4.2.2 Low titer lentivirus production.

HEK293T cells were cultured as in the previous section, except that cells were split daily and the cell density was always maintained between 30 and 70%. Prior to P11, cells were split onto gelatin coated plates, prepared by incubating 15 cm plastic dishes (Nunc) for 20 minutes at room temperature with 10 mL EmbryoMax 0.1% Gelatin solution (Millipore FS-006-B) and aspirating to dryness. 10 cm dishes were also used, and all amounts were scaled to the smaller surface area. After cells reached 80% confluency, cells were switched to 16 mL pre-warmed DMEM without FBS for 1-2 hours. For each dish, the following were added, in order, to 1.2 mL DMEM: 14 μg of FCK-RGECI plasmid, 9 μg psPAX2, and 4 μg VsVg were

combined with 36 μL of 1 mg/mL PEI in water (Aldrich #408727). The tube was vortexed and incubated at room temperature for 10 minutes. The mixture was then pipetted dropwise over the surface area of the dish and the cells were returned to the incubator for 4 hours. After the incubation, the medium was replaced with 16 mL DMEM + 10% FBS without antibiotics. 36-48 hours later, the medium was collected and centrifuged for 5 min at 500 × g. The supernatant was filtered through a 0.45 μm filter blocked with DMEM + 10% FBS and aliquoted in 1-5 mL fractions. Aliquots were kept at -80°C until use.

4.4.2.3 Primary neuron culture and gene expression.

Cultured rat hippocampal neurons on astrocyte monolayers were prepared as previously described[170], with two modifications: (1) In Vitro Scientific dishes model D35-14-1.5-N were used instead of D35-20-1.5-N, while keeping the cell densities the same and (2) neurons were cultured in Neurobasal-A (Life Technologies 10888-022) supplemented with B27 (Life Technologies 17504044) instead of Brainbits' NbActiv4. For electrophysiological and AON measurements, neurons were transfected via calcium phosphate, as previously described[170] on DIV7 and used on DIV14-16. For comparison of RGECI performance by field stimulation (**Figure 37b**, **Figure 38a**), cultured neurons were lentivirally transduced. On DIV 7, half of the media from each dish (1 mL) was reserved and replaced with 250 μL of low titer FCK-RGECI lentivirus. After two days, all of the media was removed and replaced with the reserved media supplemented with an additional 1 mL of Neurobasal-A + B27 supplement.

4.4.3 Imaging and electrophysiology in culture

4.4.3.1 Microscope.

A custom-built epifluorescence microscope was used for measurements in HEK293T cells and in cultured neurons. Illumination was provided by a 561 nm 100 mW laser (Cobolt Jive 0561-04-01-0100-500) or a 488 nm 100 mW laser (Coherent Obis 1226419). The laser lines were combined and focused in the back focal plane of the objective (Olympus Fluor 4x

0.24 NA for single action potential measurements of RGECIs; Olympus LCPlanFL 20x 0.40 NA for RGECI photobleaching measurements; Olympus UPlanSApo 10x 0.40 NA for RGECI photoswitching characterization; Olympus ApoN 60x 1.49 NA Oil for TsChR characterization). Fast modulation of the 488 nm laser was achieved with an acousto-optic tunable filter (Gooch&Housego TF525-250-6-4-GH18A). Both laser lines were additionally modulated by neutral density filters as necessary. Fluorescence light was separated from illumination light using a quadband dichroic (Semrock Di01-R405/488/561/635). HQ550/50m or ET595/50 bandpass emission filters (Chroma) were used to isolate GFP or RGECI fluorescence, respectively, before capturing on a scientific CMOS camera (Hamamatsu Orca Flash 4.0). For photobleaching measurements, an additional 1 OD filter was inserted in the imaging path to avoid saturating the camera. Illumination profiles were acquired on bead samples before experiments each day and spot size was determined using a $1/e^2$ cutoff. Laser powers were measured at the sample plane. A digital acquisition (DAQ) card (National Instruments PCIe 6259) was used to synchronize command and recording waveforms. Imaging frame rates and illumination powers are indicated in figure captions for each experiment.

4.4.3.2 Imaging and electrical recordings.

In all imaging measurements, culture medium was replaced with imaging buffer containing, in mM, 125 NaCl, 2.5 KCl, 2.5 HEPES, 30 glucose, 1 $MgCl_2$, 3 $CaCl_2$. The buffer pH was adjusted to 7.3 and osmolarity was 310 mOsm. Measurements were carried out at room temperature. 10 μM CNQX, 20 μM gabazine, and 25 μM APV (all Tocris) were included in cultured neuron experiments to block synaptic transmission. Channelrhodopsin characterization measurements were performed in synaptic blockers with the addition of 1 μM tetrodotoxin (Tocris). No additional all-*trans* retinal was added.

Field stimulation (**Figure 37b**, **Figure 38a**) was performed by inserting two chlorided silver wire loops 2 cm apart into the glass-bottomed imaging dish, touching the plastic on

either side of the coverslip. A high voltage amplifier (Krohn-hite 7600M) was used to amplify 1 ms pulses generated by the DAQ card to 60-120 V. 3-4 FOVs were acquired for each construct, using a fresh dish each time.

For patch clamp electrophysiology measurements of neuronal activity (**Figure 37d**, **Figure 38c-f**), 3-5 MΩ borosilicate glass pipettes (WPI) were filled with internal solution containing, in mM, 125 potassium gluconate, 8 NaCl, 0.6 $MgCl_2$, 0.1 $CaCl_2$, 1 EGTA, 10 HEPES, 4 Mg-ATP, 0.4 Na-GTP, adjusted to pH 7.5 and 295 mOsm with sucrose. Voltage- and current-clamp recordings were obtained with a Multiclamp 700B amplifier (Molecular Devices) while illuminating with 1 s 488 nm pulses or 2s 561 nm pulses of intensities indicated in figure captions. In voltage clamp measurements, cells were held at -65 mV. In current-clamp measurements, an offset current was injected to maintain the resting membrane potential at -65 mV. Signals were filtered at 5 kHz with the amplifier's internal Bessel filter and digitized at 10 kHz.

4.4.3.3 Data analysis.

All values are expressed as mean ± standard error of the mean (SEM). *P* values were obtained from Student's *t*-tests unless otherwise indicated.

Whole FOV RGECI single action potential responses (**Figure 37b**, **Figure 38a**, **Table 6**) were extracted as previously described[53]. Activation time constants were extracted from monoexponential fits between stimulation onset and maximum ΔF/F. For inactivation time constants, the fluorescence trace after the maximum ΔF/F was fit to a sum of two exponential decays, and the τ_{off} was taken as the time for the fit to decay to half its maximum value. Photobleaching traces (**Table 6**) were extracted from separate cells and fit to a monoexponential to obtain time constant τ_{bleach}.

Movies of blue light photoswitching (**Figure 37c**, **Figure 38b**) were preprocessed to reject saturated pixels and a threshold equal to half the average of movie was used to separate foreground from background. Background intensity was subtracted from the original movies

and the averages of the resulting foreground traces (combining 10-20 cells each) were used in downstream analysis. Traces were converted to ΔF/F using the fluorescence value before blue light stimulation as F_0 (**Figure 38b**). "Photoswitching ΔF/F" was defined as the ΔF/F immediately after blue light illumination ends (**Figure 37c**, inset).

For comparison of channelrhodopsins (**Figure 37d**, **Figure 38c-e**), cells were rejected if they required >100 pA holding current to maintain -65 mV in current clamp or if their baselines drifted by more than the smallest steady state photocurrent amplitude in voltage clamp mode. Steady-state 488 nm photocurrents were extracted as the average photocurrent over the last 100 ms of blue light illumination. Steady state 561 nm photocurrents and depolarizations were extracted from 1 s of data. On time constants were obtained from single exponential fits to the first 1.5 ms of 488 nm illumination. Off time constants were obtained from single exponential fits to the 99.5 ms following blue light 488 illumination.

Recordings of jRGECO1a fluorescence in **Figure 38g** were corrected for photobleaching with a di-exponential fit to the initial period in each movie, before stimulation, while recordings of BeRST1 fluorescence were corrected for photobleaching by a sliding, 1000 point, median filter. Both traces were converted to ΔF/F based on the fluorescence before blue light stimulation. Frames acquired during blue light stimulation were dropped to avoid optical crosstalk.

4.4.4 Hadamard imaging

4.4.4.1 Microscope.

In the ultra-widefield microscope (**Figure 34a**), a 561 nm laser beam (MPB Communications F-04306-02) was transmitted through a rotating diffuser, and merged with a 470 nm LED beam (Thorlabs M470L3). Both were expanded, focused, and coupled through free space to fill with high NA illumination a digital micromirror device (DMD) module (Vialux V-7001; 1024x768 pixels, 13.7 μm pitch). Multiple diffraction orders emitted from the DMD pattern were transmitted by a 100 mm projection tube lens (Zeiss Makro-Planar 100

mm, L1 in **Figure 34a**), reflected off a dichroic mirror (Semrock Di01-R405/488/561/635-t3-60x85), and imaged onto the sample by a 50 mm objective lens (Olympus MVPLAPO 2XC, NA 0.5, L2 in **Figure 34a**). The 3 mm substrate thickness of the dichroic mirror minimized warping-induced projection aberrations. Fluorescence emission was collected through the same objective and dichroic, an emission filter (Semrock FF01-520/35-60-D or Chroma ET600/50m, F in **Figure 34a**), and a 135 mm imaging tube lens (Zeiss Apo-Sonnar 135 mm, L3 in **Figure 34a**) onto a scientific CMOS camera (Hamamatsu Orca Flash 4.0, 2048x2048 pixels). The FOV was 4.6x4.6 mm^2 in the sample plane, corresponding to a magnification of 2.89x onto the camera, and 2.17x onto the DMD. Camera and DMD pixels were 2.25 μm and 6.3 μm wide in the sample, respectively. Hardware and triggers were programmed in LabView, with pattern generation and data analysis performed in MATLAB.

4.4.4.2 Illumination patterns.

To reject light scattered within the sample, pattern sequences were designed such that in the projected series of 2D images, neighboring locations of the sample were illuminated with orthogonal functions of intensity vs. time. A Hadamard matrix, H, of size m is a binary square matrix with elements $\{-1,1\}$ that fulfills $H^T H = mI_m$, where I_m is the identity matrix of size m; its normalized form has value 1 in the first column and first row. Illumination intensities could not be negative, so the projected intensity patterns were defined as $P = (H' + 1)/2$ where $H' = H[1, \dots, m; m - n + 1, \dots, m]$ was an incomplete orthogonal basis given by the last n columns of a normalized Hadamard matrix, with $n < m$.

The illumination patterns P thus had binary values $\{0,1\}$ corresponding to DMD mirror positions OFF and ON respectively. Each location was illuminated with a positive temporal function orthogonal to all other designed Hadamard codes, as verified by $P^T H' = I_n * m/2$. For a given number of locations, a Hadamard matrix provided a set of shortest possible binary orthogonal functions. To arrange the n codes in P into illumination patterns,

$m = n + 1$ images were defined assigning code $k_{i,j} \in \{1..n\}$ to DMD pixel (i, j), as $k_{i,j} = \mathrm{mod}(i * q + j, n) + 1$, where q was an offset parameter that maximized spatial separation of repeated codes. (n, q) was set to (11,3) for functional imaging, and to (63,14) or (59,8) for structural imaging. To further reduce spurious scattering cross-talk, a random binary mask R was generated to flip the sign of 50% of DMD pixels, applied as an exclusive OR operation on all DMD patterns against the same mask R.

4.4.4.3 Calibration.

To prepare the system for each imaging session, a calibration data-set C was obtained by placing a thin fluorescent sample at the focal plane, and acquiring an image with each illumination pattern. The sample consisted of green or orange neon Sharpie (Newell Brands, NJ) ink painted on (or sandwiched between) glass coverslips, to match imaging conditions of subsequent acute (fixed) tissue experiments. For each camera pixel, the time series of its photon counts was cross-correlated against each Hadamard sequence as $C^T H'$. The resulting cross-correlation images displayed sharp peaks indicating the projected DMD locations for each code, with positive or negative correlation given by R. A synthetic approximation to the cross-correlation maps was calculated by finding the code with maximum absolute correlation for each pixel, yielding homogeneous, noise-free cross-correlation maps.

4.4.4.4 Reconstruction.

A Hadamard sequence data-set D was acquired after replacing the calibration sample with a tissue sample. Photon counts at each camera pixel were cross-correlated against each Hadamard sequence as $D^T H'$. Cross-correlation images displayed a set of peaks modulated by the local fluorophore density, and broadened by off-focus fluorescence and light scattering in the sample. Each peak characterized the scattering function of the corresponding tissue location, i.e. its absolute value represents the image one would record with an illumination spot focused solely at that location in the tissue. The next step was to apply a set of computational 'pinholes' to select the unscattered in-focus photons, and to reject all others.

The spatial filter was implemented through the element-wise product of calibration correlation maps and tissue correlation maps, resulting in the positive filtered maps $F = C^T H' \circ D^T H'$. This computational process was akin to sifting emitted light through an array of pinholes as happens physically in spinning disk confocal microscopy. The final computation step was to aggregate the unscattered light by direct sum of the filtered images over all code maps, defining an optical section image $\phi_i = \sum_{k=1}^{n} F_{i,k}$.

All image computations in this work were accelerated by computing $\phi_i = \sum_{k=1}^{m} G_{i,k}$, with $G = C^T \circ D^T$. This approach is numerically equivalent to the more involved process described above, as proved by:

$$\phi_i = \sum_{k=1}^{n} F_{i,k},$$

$$= \sum_{k=1}^{n} \sum_{p=1}^{m} C_{i,p} H_{k,p} \sum_{q=1}^{m} D_{i,q} H_{k,q},$$

$$= \sum_{p=1}^{m} \sum_{q=1}^{m} C_{i,p} D_{i,q} \sum_{k=1}^{n} H_{k,p} H_{k,q},$$

$$= \sum_{p=1}^{m} \sum_{q=1}^{m} C_{i,p} D_{i,q} \delta_{p,q},$$

$$= \sum_{q=1}^{m} C_{i,q} D_{i,q},$$

$$= \sum_{k=1}^{m} G_{i,k},$$

where $\delta_{p,q}$ is a Kronecker delta. The resulting optical section preserved unscattered light emitted from the focal plane, while rejecting scattered light and background emissions. Standard wide-field epifluorescence images were also computed from each Hadamard dataset by computing a direct sum of all frames in the raw images, $W_i = \sum_{k=1}^{m} D_{i,k}$.

4.4.4.5 Hadamard image formation.

To understand the optical sectioning process, Hadamard microscopy was modeled as an incoherent illumination, intensity-linear space-invariant optical system, in which the intensity after propagation is given by a convolution between intensity before propagation and an intensity impulse response function. In a discrete representation, the circulant convolution matrix S_1^T represented three-dimensional excitation intensity at the object, in response to an

impulse function reflectance at the DMD plane (turning on one DMD pixel). Similarly, S_2 was defined as the intensity collected by an impulse detector at the camera plane from emitted fluorescence in a three-dimensional object (analogous to detection from one camera pixel). The data collected from tissue with fluorophore distribution G upon illumination with a structured illumination pattern P was represented as $D = S_2 \operatorname{diag} G\, S_1^T P$, where diag denoted rearrangement between vector and diagonal matrix. Calibration with a thin uniform fluorescent object and no scattering was represented as $C = P$. After assuming that P contains an orthonormal Hadamard code with no spatial repetition, it followed that $C^T H' = I_n$, and $D^T H' = S_2 \operatorname{diag} G\, S_1^T I_n$. Then $\phi = \sum_k C^T H' \circ D^T H' = \operatorname{diag}(S_2 \operatorname{diag} G\, S_1^T)$, or $\phi = (S_1 \circ S_2)G$. The reconstructed optical section ϕ was proportional to the object G convolved with the confocal scattering function $S = S_1 \circ S_2$ that resulted from the element-wise product of the projection and collection scattering functions.

4.4.4.6 Image processing and filtering.

The lines between DMD pixels led to a periodic grid artifact in Hadamard optical sections. A Gaussian stopband filter was used to attenuate these artifacts. The filter parameters were not changed after initial set-up.

The size of the computational pinholes could be adjusted in software to trade optical signal level for z-resolution. Tuning of pinhole sizes was achieved by applying a spatial Gaussian filter to the calibration patterns, with σ = 5.6 μm for functional images, and σ = 3.4 μm for structural images. Further increases in σ to sizes larger than the spacing of pinholes resulted in a continuous transition to wide-field epifluorescence imaging.

An additional source of systematic error came from local inhomogeneity of illumination patterns. While the projected patterns have 50% duty cycle on average, variations in local illumination can change the relative contributions of in-plane signal and background, resulting in imperfect background cancellation manifested as regions with periodic background artifacts. This effect was minimized for Hadamard images in **Figure 36a** by

dividing raw tissue data by its low spatial frequency component, calculated with a Gaussian filter with σ=33.8 μm for m=60, and σ=22.5 μm for m=12. Images in all figures were linearly mapped to grayscale setting 0 to black and saturating to white the 0.01 percentile of highest intensity values unless otherwise indicated.

4.4.4.7 Characterization.

To evaluate the performance of Hadamard imaging in comparison with other structured illumination methods for optical sectioning, a z-stack of optical sections was acquired with multiple patterned illumination strategies in an acute mouse brain slice expressing H2B-jRGECO1a. Illumination patterns for Hadamard codes of length 60 and 12, together with striped illumination with period 4 pixels and 4 phases, were interleaved and repeat-averaged to match total photons and photobleaching conditions across datasets. Linear SIM optical sections were calculated as $\phi = \left|\sum_{k=0}^{m-1} I_k e^{-i2\pi k/m}\right|$, with m=4. HiLo optical sections were calculated using the same data as Hadamard of length 12, with uniform image given by the sum of raw images. Each pseudorandom pattern image was used to calculate one HiLo image, and then the 12 resulting HiLo images were averaged.

4.4.5 Animals and acute slice measurements

4.4.5.1 Animals.

All procedures involving animals were in accordance with the National Institutes of Health Guide for the care and use of laboratory animals and were approved by the Institutional Animal Care and Use Committee (IACUC) at Harvard University. Excitability measurements and characterization of functional Hadamard imaging were performed in wild type C57Bl6 (Charles River Labs #027) mice. Synaptic transmission assays were performed in Rbp4-Cre$^{+/-}$ mice donated by Bernardo Sabatini's lab and originally generated in the GenSat project (#KL100). For structural imaging of membrane bound mCitrine, FLOXed Optopatch-3 mice (Jackson Labs #029679) were crossed with Rbp4-Cre$^{+/-}$ mice or with *CaMKIIa*-Cre$^{+/-}$ mice (Jackson Labs, #005359).

4.4.5.2 AAV injection.

AAV2/9-hSyn-DO-H2B-jRGECO1a (1.60×10^{13} GC/mL) and AAV2/9-hSyn-TsChR-TS-GFP (2.22×10^{13} GC/mL) were produced at Massachusetts Eye and Ear Infirmary Vector Core. AAV2/9-CAG-DIO-CheRiff-TS-GFP (5.80×10^{13} GC/mL) was produced by the Stanford Vector Core. AAV1-hSyn-NES-jRGECO1a (2.44×10^{13} GC/mL) was purchased from the University of Pennsylvania Vector Core. When two viruses were coinjected, they were mixed in a one-to-one volume ratio. The final mixture was mixed in a 7:1 ratio with 0.4% Trypan Blue to aid in visualization during injection. For viral injections, neonatal (P0-2) animals were cold-anesthetized and taped to an aluminum heatsink submerged in an ice bath, with their heads resting on a modeling clay support. A stereotaxic injector (WPI #UMC4) mounted on a stereotaxic frame (Stoelting) was used to inject virus 1.6 mm anterior and 1.6 mm lateral to lambda every 0.4 mm starting from 3 mm beneath the surface of the skull. 40 nL of virus was delivered at each depth at a rate of 5 nL/s. If only one virus was used, only 20 nL were injected per depth. Expression levels were sufficiently high for Hadamard imaging from 12 days until at least 9 weeks after injection.

4.4.5.3 Acute slice preparation and imaging.

Acute slices were prepared from P21-28 animals. Animals were deeply anesthetized via isoflurane inhalation and transcardially perfused with ice-cold choline cutting solution, containing, in mM 110 choline chloride, 25 sodium bicarbonate, 2.5 potassium chloride, 7 magnesium chloride, 0.5 calcium chloride, 1.25 monobasic sodium phosphate, 25 glucose, 11.6 ascorbic acid, and 3.1 pyruvic acid (310 mOsm/kg). The brain was blocked with one coronal cut just anterior to the tectum and mounted with Krazy glue on the specimen disk of a Leica VT1200s vibratome. After mounting, hemispheres were separated with a sagittal cut down the midline of the brain. The brain was covered with more ice-cold choline solution and then sliced in 300 μm steps. Slices containing the striatum were recovered for 45 minutes in a 34 °C artificial-cerebrospinal fluid (ACSF) bath containing, in mM, 125 NaCl, 2.5 KCl, 25

$NaHCO_3$, 2 $CaCl_2$, 1 $MgCl_2$, 1.25 NaH_2PO_4, 25 glucose (295 mOsm/kg). Slices were kept in room temperature ACSF until ready to measure and were used within 8 hours. All solutions were bubbled with carbogen (95% O_2, 5% CO_2) for the duration of the preparation and subsequent experiment.

For imaging, slices were mounted on Poly-L-Lysine (PLL) coated coverslips. Coverslips (Fisher #12-545-80) were plasma cleaned for 3 minutes, covered with 50-100 μL 0.1% (w/v) PLL (150-300 kD) solution (Sigma #P8920) and allowed to dry under vacuum. Coverslips were thoroughly washed with nanopore water and dried before use. To mount the tissue, a slice was transferred to the PLL-coated face of the coverslip with a Pasteur pipette. Excess ACSF was pipetted or wicked away with filter paper, in the process flattening out the brain slice and adhering it to the glass. We found that this method worked reliably for coronal slices from one hemisphere but not for coronal slices from the entire brain. Coverslips were placed in a custom built flow chamber with a microscope slide bottom and #1.5 coverslip lid. ACSF was perfused at a rate of 1 mL/min with a VWR peristaltic pump.

The imaging protocol consisted of a 2 s imaging epoch followed by a 400 ms stimulation period and another 2 s imaging epoch. Each imaging epoch comprised 11 frames of functional Hadamard acquired with a 180 ms period under 100 mW/cm^2 561 nm illumination. Blue light stimulation protocols are described in figure captions. The slice was allowed 6 s to recover before starting another imaging epoch. One run consisted of 6 imaging and stimulation rounds over one minute. Runs were repeated several times, spaced out by at least five minutes. NBQX and CPP, or TTX (Tocris) or retigabine, phenytoin, or carbamazepine (Sigma) were added to the ACSF from 1000x stock solutions after several baseline runs.

4.4.6 Analysis of slice data.

4.4.6.1 Registration.

After reconstruction of Hadamard images (see Methods above), frames for each epoch were averaged together. Small movements and deformations in the slice over the course of multiple runs were corrected by automatic non-rigid registration[215]. Functional Hadamard recording and structural Hadamard images were manually registered using a 2D affine transformation.

4.4.6.2 Cell selection.

ΔF images were calculated for each registered run by subtracting images acquired before blue light stimulation from images acquired immediately after blue light stimulation. Peaks in ΔF images corresponded to individual cells, but noise in ΔF varied as a result of brightness inhomogeneities in the slice, making it difficult to extract peaks directly. To correct for this noise, a widefield image for each slice was blurred with a 2D Gaussian with an 8 pixel (19.2 μm) standard deviation, to remove nucleus sized objects. The square root of this image was used to normalize the ΔF image of the slice. High spatial frequency noise was removed with a 2d Gaussian filter with a 0.5 pixel (1.2 μm) standard deviation. Regions without expression were manually selected and standard deviations in these regions were chosen as a noise floor. Cells were identified as peaks in the normalized ΔF image which had an amplitude larger than the noise floor by a user-defined factor, typically 7 – 10. Cells were required to have a minimum distance in space of 4 pixels (9.6 μm) to avoid double counting cells. Once cell locations were identified, single-cell fluorescence traces were extracted from corresponding locations in movies of unnormalized data blurred with 2d Gaussian filter with 1 pixel standard deviation.

4.4.6.3 Exclusion of spontaneously active and dying cells.

While measuring a large number of cells in an acute slice, a portion of cells showed spontaneous activity, characterized by transient fluorescent increases uncorrelated with blue

light stimulation; and cell death, characterized by a large and irreversible increase in fluorescence. For PCA analysis in **Figure 40** and in **Figure 42**, slices were imaged nine times, five times before AED application and four times after. Imaging epochs were averaged to generate movies with 108 frames (12 epochs per run x 9 runs). After extracting cell traces from these movies for all slices in the experiment, each cell's mean and standard deviation per run were calculated. Least squares fits on the mean and standard deviation were performed on 3-pre drug runs and projected to the full nine runs. Cells were excluded from further analysis if any projected mean or standard deviation was less than 1/15 of the cell's mean value or if the root mean square error of the fit was larger than 1/15 of the cell's mean value. This procedure rejected < 17% of cells.

4.4.6.4 Generation of excitability maps.

To generate the maps in **Figure 40e** and **Figure 41j** the fluorescence trace for each included cell was normalized by subtracting its mean fluorescence values for each run and normalizing by the standard deviation for each run. For each cell, 3 pre-drug runs were averaged together to yield a 12 element vector corresponding to normalized F in each epoch. Principal component analysis yielded 3 main principal components which were then back-projected into pixel space for each slice, yielding the black and white images in **Figure 41j**. Color images were generated using L*a*b colorspace, by projecting PC1 into lightness, L, and PC2 and PC3 into the red-green and blue-yellow axes, *a* and *b*.

To generate maps of changes in drug response in **Figure 42b**, ΔF images from four runs before and after drug addition were averaged together, median filtered with a 3 pixel kernel, saturated at their 99.5^{th} percentile, and displayed in the green and red channels, respectively. The blue channel is the average of the red and green images. Color saturation was adjusted in L*a*b space to aid in visualization. In **Figure 44a** ΔF images are scaled to the same absolute counts and shown in separate color channels.

4.4.6.5 Cortical layer analysis.

All striatal cells were pooled and treated separately. For cortical cells, cortex boundaries were manually defined in structural images as the surface of the brain and the bottom of Layer 6. Boundaries were registered to functional images (above) and cells were assigned a normalized depth coordinate based on these boundaries. Drug response, defined as $\Delta F_{drug}/\Delta F_0$, could then be related to normalized cortical depth. For each slice, cells were binned by cortical depth and the drug response per cell averaged over cells. Extreme cell responses were excluded from each bin using the generalized extreme Studentized deviate test. Layer boundary locations were taken from the primary somatosensory cortex in the matched coronal slices of the Allen Brain Reference Atlas.

KCNQ3 expression levels were acquired from Allen Brain Institute experiment #100041071. The somatosensory cortex was manually defined in 11 sagittal slices from a P28 male mouse. The available expression image was used to mask the raw data, but expression values were obtained directly from the raw ISH data. The edges of the cortex and cortical depth bins were defined as above and expression values were averaged together across slices from the same experiment.

4.5 Author contributions

Samouil L. Farhi identified and characterized the protein pair for all-optical physiology. Vicente Parot developed Hadamard microscopy, with early help from J.J. Kim. Samouil L. Farhi and Vicente Parot acquired and analyzed all acute slice data together, with early help from Yoav Adam. Shan Lou provided fixed slice samples. Abhinav Grama performed *in vitro* electrophysiology on H2B-jRGECO1a in David D. Cox's lab. Masahito Yamagata cloned the H2B-jRGECO1a construct. Ahmed S. Abdelfattah and Robert E. Campbell provided the TsChR construct. Katherine Williams and Melinda Lee provided technical assistance.

This work is submitted for publication:

Farhi SL*, Parot, V*, Grama A, Yamagata M, Abdelfattah AS, Adam Y, Lou S, Kim JJ, Campbell RE, Cox DD, Cohen AE. Hadamard microscopy and all-optical neurophysiology enable wide-area profiling of neural function. *In review.*

5 All-optical neurophysiology approaches and opportunities

Chapter 1 introduced early work on optical and all-optical measurements in neurons until circa 2012. The subsequent chapters described three advances generated in our lab in the subsequent years. Of course, the field outside our lab has remained vibrant and growing. New molecules for optical detection and optical actuation of neuronal activity have been developed by numerous labs while other workers have focused on improving existing imaging modalities or generating new geometries. I'll thus contextualize our work in light of recent technological developments in optical physiology, the newly enabled biological applications, and the challenges and opportunities in the future.

5.1 AON approaches

With improvements in optogenetic actuators and indicators, a spate of AON methods has been developed. These methods can be loosely classified by the imaging modality used to record neural activity: 1P voltage imaging, 1P calcium imaging, or 2P calcium imaging.

5.1.1 1P voltage imaging

Of the large family of GEVIs that has been developed in recent years, rhodopsin-based GEVIs have been the best partners for optogenetic stimulation. Despite this current dominance, other red-shifted or 2P stimulated of voltage sensitive domain based GEVIs could provide an alternative solution. Hybrid approaches using small molecules dyes are still in their infancy but could be a powerful complement to fully genetically encoded AON.

5.1.1.1 Rhodopsin-based GEVIs

Microbial rhodopsins were the first protein-based fluorescent sensors to report voltage changes with high sensitivity and kinetics, relying on their native, dim fluorescence. The first variant, PROPS, was demonstrated in *E. coli*, but did not traffic well in mammalian

neurons[216]. Follow-up work showed that Archaerhodopsin-3 (Arch), previously used for optogenetic inhibition, could also be used to measure voltage with single spike resolution in mammalian neurons but perturbed the neuron's resting potential through its native photocurrent[71]. Several subsequent point mutants, ArchD59N[71], ArchEEQ[113], and ArchEEN[113] removed the photocurrent while maintaining voltage sensitivity. AON with ArchEEQ was demonstrated using 1P ChR2 stimulation, but ArchEEQ's slow response kinetics made the combination unappealing.

Directed evolution efforts from several labs generated improved sensors: the second-generation, Arch-based QuasArs (Chapter 2), and Archers[170,217,218]; and the third-generation, QuasAr2-based QuasAr3[219] and Archon1[220]. Of these, only the Archer family was incompatible with simultaneous optogenetic stimulation since Arch's photocurrent function was left intact. The rest of the proteins have all been combined with simultaneous 1P CheRiff stimulation, though careful crosstalk characterization has not yet been performed on the third-generation proteins. Archon1 has also been paired with CoChR, though the photocurrent of this high-photocurrent channelrhodopsin under 640 nm light was not measured[220]. AON with QuasAr2[221] and QuasAr3[219] transgenic mice has also been illustrated, though applications were limited to *ex vivo* experiments due to the lower GEVI expression compared with AAV-based expression.

A V59A mutant QuasAr3, also called paQuasAr3, showed blue or 2P-induced increases photoactivation to QuasAr3, increasing the effective SNR[219]. AON with CheRiff paQuasAr3 was possible, but required post hoc correction of the blue light induced photoartifact in the voltage imaging recording. Directed evolution for proteins with enhanced photoactivation yielded NovArch, which could be useful for extracting signal from deeper cells in scattering brain tissue[222]. NovArch was combined with CheRiff by using 2P light to photoactivate the voltage indicator (at low enough intensity not to excite CheRiff), while using blue light to drive CheRiff activity (at low enough intensity not to photoactivate NovArch).

Therefore, though AON with both paQuasAr3 and NovArch is possible, the comparative technical simplicity and comparable signal to noise of Archon1 make it the current preferred voltage indicator for combination with optogenetic stimulation.

In addition to their direct voltage-sensitive fluorescence, Arch-based indicators undergo voltage-dependent shifts in their absorption spectrum. Several labs have harnessed this effect by using microbial rhodospins as acceptors for brighter, conventional fluorescent proteins. This electrochromic FRET (eFRET) was first demonstrated with fusions of mCitrine to the rhodopsin MacQ[223] and of various fluorescent proteins to QuasAr2[171]. Ace-mNeon substantially improved on these early versions, yielding a bright and fast voltage indicator, capable of voltage recording from single neurons in live mice[224]. The eFRET approach shows significant promise for voltage imaging, but it also necessarily blue-shifts the imaging excitation wavelength. Thus, until eFRET indicators can be imaged with comparable intensities to those used in calcium imaging, they will likely remain difficult to pair with optogenetic actuators.

5.1.1.2 Voltage sensitive domain based GEVIs

ArcLight was the first *Ci*-VSP-based GEVI to report single action potential with a high signal-to-noise ratio[72], with slow kinetics presenting the biggest problem. Screening mutants of the ArcLight scaffold yielded the faster Bongwoori[225] and Bongwoori-R3[226]. In parallel, investigating voltage sensitive domain alternatives to *Ci*-VSP in the VSFP2.x scaffold yielded several other fast indicators[160,173,227]. The most useful variant was ASAP1[160], offering single-digit millisecond response time constants. Importantly, ASAP1 could be imaged with 2P illumination, though it was prone to photobleaching[174]. A modified protein, ASAP2f, with slightly higher sensitivity, showed better photostability under 2-photon illumination[228] in *D. melanogaster*. An additional modification, ASAP2s, with slower kinetics, was capable of 2P imaging of voltage dynamics both in mouse organotypic slice and *D. melanogaster*[229]. FlicR1, described in Chapter 3, presents yet another way to increase ArcLight kinetics. FlicR1 shares

ArcLight's architecture and voltage sensitive domain, but uses a cpFP similarly to ASAP1 and ElectricPK[64]. Like both of those proteins, it shows fast response kinetics. Unfortunately, also like ASAP1, FlicR1 bleaches relatively quickly compared to ArcLight. FlicR1 has also been rendered photoconvertible (FlicGR1), which could result in interesting sectioning applications in the future[230].

AON measurements with voltage sensitive domain-based indicators remain the least advanced, but offer significant promise. FlicR1 remains the only red-shifted protein in the class which has been demonstrated in neurons, and its utility for AON is limited (though a split-FusionRed VSFP scaffold was recently reported in HEK cells)[231]. Until a GEVI using a brighter, non-photoswitchable red-fluorescent scaffold is developed, 1P based AON with this family of proteins will remain out of reach, similar to the eFRET proteins in the previous section. The promise of the scaffold, however, comes from the 2-photon cross sections shown by the ASAP and FlicR proteins. For reasons still unclear, no rhodopsin-based GEVI has shown reliable voltage sensitive signals under 2P illumination. If voltage imaging could be performed in 2P with voltage sensitive domain-based indicators, the spontaneous activation of channelrhodopsins could be avoided and one of the biggest AON hurdles would be removed.

5.1.1.3 Small-molecule and hybrid voltage sensors

As discussed in Chapter 1, all-optical VSD-based approaches have been successful in heart and in culture but have been less useful for AON. The highest SNR all-optical measurements in neurons have been performed with BeRST1[28]. In intact tissue, VSD based AON on single neurons still requires electrode loading of individual cells[232–234]. The best use case for VSD based AON remains mesoscale, population-wide imaging to identify brain regions downstream of a particular population of neurons[105,106,235,236]. To grow the utility of small molecule indicators in voltage imaging, several labs have undertaken hybrid approaches, combining small molecules with genetically encoded targeting.

Early hybrid sensors relied on FRET between a genetically encoded membrane-anchored fluorophore and a voltage-dependent redistribution of small molecule[237–239]. As for the analogous small-molecule based approach, these sensors added a significant capacitative load to the cell. eFRET-based small molecules have also been attempted, with promising results in HEK293 cells[240]. In both FRET approaches, as for genetically eFRET, the blue-shifting of the fluorophore likely precludes AON. An alternative hybrid strategy uses a genetically encoded enzyme to uncage a VSDs only in the genetically specified cells[241,242]. This approach is currently incompatible with channelrhodopsin stimulation due to the blue excitation of the voltage dyes, but, in principle, a red-shifted dye such as BeRST[28], or a 2-photon activated dye such as RVF5 could be used instead. Finally, a bioluminescent voltage sensor, LOTUS-V, has been reported. LOTUS-V uses NanoLuc as a FRET donor to an FP in a VSFP-Butterfly1.2 configuration[243]. The resulting protein is slow (~200 ms response) and requires delivery of NanoLuc's substrate furimazine, but shows no background, making it compatible with optogenetic stimulation with any wavelength.

5.1.2 1P calcium imaging

Unlike GEVIs, there are currently no highly performing GECIs excited beyond 600 nm. As such, combinations of 1P GECI imaging with optogenetic stimulation has been more difficult to accomplish. The first published attempt combined the original ChR2[244] (not H134R) and G-CaMP[159] in *C. elegans*[245]. The high degree of spectral overlap was overcome by using low power blue light for imaging G-CaMP and increasing the intensity for ChR2 stimulation. This approach relied on the comparatively poor performance of ChR2 and accepting low-quality calcium recording. A more refined optical implementation combined computer generated holographic stimulation of ChR2 and structured illumination imaging of GCaMP5-G in a fiber scope configuration for *in vivo* mouse studies[246]. Despite this optical sophistication, GCaMP5-G imaging intensities had to be maintained at <5 mW/cm^2, giving up imaging quality. Yet another approach using green GECIs has been to combine a red-

shifted actuator with GCaMP (either C1V1 with GCaMP3[247] or bReaChES with GCaMP6f[248]) in a fiber photometry configuration, where, by averaging signal from multiple cells, it was acceptable to reduce the GCaMP imaging intensity to avoid stimulation of the actuator. A similar approach found that in cultured neurons, the allowable GCaMP3 imaging power when pairing with C1V1 was only 0.7 mW/cm^2 for crosstalk-free measurements[166].

Because of the difficulty of using green GECIs for AON, attention turned to red GECIs instead. With the publication of RGECO-1[141], two studies were quickly published combining RGECO-1 or a derivative R-CaMP1.07 with ChR2[249,250], but their validity was almost immediately questioned for ignoring the blue-light induced photoswitching behavior of the RGECO-1 scaffold[166]. In the latter study a non-photoswitching RGECI, RCaMP1e was successfully combined with ChR2, but the sensor was too poorly performing for practical use.

Of the latest generation RGECIs, RCaMP-2, jRGECO1a, and jRCaMP1a, all have been tested for combination with ChR2[196,197]. RCaMP-2 and jRGECO1a showed undesirable levels of photoswitching to blue light, while jRCaMP1a's performance as a sensor was comparatively poor. The work we present here in Chapter 4 and Appendix 2 is the first to show how the high sensitivity and photostability of jRGECO1a can be harnessed for AON using a blue-shifted channelrhodopsin, TsChR. In the future, enhancements on existing scaffolds, or on the newly developed K-GECO scaffold[251] may further relax the constraints on 1P calcium based AON. The ultimate development would be a NIR-excitable GECI with sensitivity and brightness comparable to GCaMP6.

Two other non-standard approaches for 1P-calcium based AON should also be mentioned. In one approach, GCaMP6 imaging is combined with a step-function opsin, CheRiff C128S[252]. Intense orange or red light is used to close the channel during periods when stimulation is not wanted, while imaging GCaMP6 with high intensity blue light throughout. Currently the intensities of light required limit the practicality of this approach, but further engineering of an appropriate step-function opsin may change this.

The other non-standard approach uses calcium integrators rather than traditional intensity-based calcium sensors. CaMPARI, converts from green-fluorescent to a red-fluorescent state in the simultaneous presence of 405 nm light and calcium ions[253] and can be combined with CsChrimson[253] and with ChR2[254] for one shot all-optical measurements. The recently published light- and calcium-gated transcription factor, FLARE[255], could be used the same way, using protein expression rather than photoconversion as a readout. Careful control experiments and calibration of the degree of activation of the channelrhodopsin must be performed for every new system investigated, but this approach could be powerful for screening-type experiments in intact tissue or in pooled libraries of cultured cells.

5.1.3 2P calcium imaging

One way to solve the spectral overlap challenges involved in 1P calcium imaging-based AON is to switch to 2P imaging. It was realized early that 2P raster imaging of calcium indicators over moderate fields of view (>100×100 μm) would not significantly activate ChR2, as the imaging beam does not reside on the same cell for long enough to open enough channels to initiate an action potential[256]. This property was first leveraged in a system combining 2P Oregon Green BAPTA (OGB1) imaging and 1P ChR2 photostimulation with a small focused spot guided by galvo mirrors[257,258]. This first illustration suffered from several drawbacks. OGB1 imaging has poor cellular resolution in brain tissue. The spectral overlap of OGB1 and ChR2, blue light stimulation induces extra fluorescence from OGB1 which must be corrected. Finally, due to the scattering nature of mammalian brain tissue, 1P blue light stimulation could only be accomplished with cellular resolution in sparse populations of neurons, such as layer 1, parvalbumin, or somatostatin cells in the cortex.

The basic designs in this initial study have been refined several times with subsequent advances in 2P imaging, 2P stimulation, and new optogenetic actuators. Nearly all subsequent studies have used the top-of-the-line GECI, GCaMP6. The main goal of these efforts has been to achieve single-cell resolution optogenetic stimulation. It is worth noting that if an

approach works with 2P stimulation, 1P will likely also work, at the cost of requiring blanking of the detector during stimulation and losing cellular resolution[259].

To improve the cellular resolution of optogenetic stimulation in intact tissue, a systematic effort was undertaken to generate a ChR which had a high 2P absorption cross-section combined with slow kinetics, so that a larger number of channels could be activated simultaneously by a 2-photon beam[260]. The resulting $C1V1_T$ was slow enough to efficiently drive activity when raster scanning over a 15 × 15 μm ROI over the cell soma. The protein was also red-shifted, raising hopes of spectrally orthogonal 2P GCaMP imaging and 2P stimulation.

AON in awake mice with C1V1 was published soon after by the Tank and Häusser labs with GCaMP3[194] and GCaMP6s[193], respectively. Both studies used two independent 2P laser paths, one at 910 nm for GCaMP imaging and one at 1064 nm for C1V1 stimulation. For stimulation, these studies leveraged two recent methods for delivery 2P. The Tank lab took advantage of temporal focusing (TF), a method using a diffraction grating to split a 2P beam into its spectral components and only recombining them for high intensity stimulation in the desired focal plane[261]. The primary effect is to enable expansion of the 2P focal spot laterally to the size of a cell soma without the corresponding increase in axial size, allowing one shot stimulation of a single cell without fast rastering. In contrast, the Häusser lab used computer generated holography (CGH) implemented with a spatial light modulator (SLM) phase mask to apply an array of dots on cells of interest, and scanned all dots in a spiral simultaneously with galvo mirrors to enable stimulation of multiple cells in parallel (up to 20 in one plane in this study). The latter approach was used to write and recall patterns of co-firing cells—"ensembles"—into visual cortex in an awake mouse[195]. The same combination of C1V1 and GCaMP6s has recently been demonstrated in awake rhesus macaques[259].

The largest problem with these approaches was the flexibility in stimulating arbitrary collections of cells with arbitrary temporal patterns. TF can be combined with CGH or

generalized phase contrast (GPC) to stimulate multiple neurons in parallel[262,263]. These approaches work well for stimulating neurons in a single plane. 3D spot placement is also possible with CGH[264], but combinations with TF were hampered by an inability to simultaneously focus multiple focal planes on the same diffraction grating. A workaround was developed, using a second SLM after the diffraction grating to set the axial focus to one of several discrete depths while retaining spatial resolution[265]. A more practical approach eschews the SLM before the diffraction grating—and along with it the ability to shape arbitrary patterns in xy—but enables continuous control over the axial position of the stimulation spots[266,267]. In a different implementation, the spiral scanning approach of the Häusser lab could be combined with 3D CGH, enabling arbitrary stimulation of up to 80 neurons in parallel in 3D[268].

The choice between a stimulating a cell in 2P with a single large spot (with or without TF) or with spiral scanning of small spot comes down to light efficiency: spiral scanning using diffraction limited spots is more photon efficient than a defocused or temporally focused spot of the same area. In principle, this should allow for more cells to be stimulated in parallel before damaging the tissue. Large spots, however, allows tighter temporal control of spiking patterns by stimulating the whole cell soma simultaneously. With large spots, it has been possible to replace C1V1 with the faster ChR2[262,264], as well as the later generation ChRs, ReachR, CoChR, and ChrimsonR[263,269], allowing tighter temporal control of activity patterns with their faster kinetics and higher photocurrents. Stimulating with large spots may also result in crosstalk between target somas and nearby neuropil expressing membrane-targeted ChR. To decrease neuropil expression, somatic-localization sequences from Kv2.1 have been appended to ChR2[270]. More recently, the Boyden lab demonstrated that the kainate receptor KA2 trafficking sequence could impart somatic localization to CoChR with greater preference for soma over proximal dendrites[271]. The expansion of the available 2P optogenetic actuator palette has had an added benefit of decreasing the 2P spectral crosstalk between the actuator

and GCaMP6. Another way to avoid this crosstalk is to shift to using an RGECI instead of GCaMP. This was done by the Fellin lab, combining 2P jRCaMP1a imaging with 2P ChR2 photostimulation[272]. This paper is notable for being one of only two to show 2P calcium imaging combined with optogenetic inhibition, using GtACR2. The earlier paper, also by the Fellin lab combines 2P GCaMP6 imaging with 1P Arch photoinhibition for blocking entire populations of cells in the field of view[273].

5.2 Which AON method for which problem?

In the face of the menagerie of available methods, how should one choose a method for a particular application? The answer depends primarily on the optical characteristics of the model system. Preparations can be classified into cultured cells, where scattering and out of focus fluorescence are not a problem; thick, transparent preparations, such as *C. elegans* and larval zebrafish which have no scattering but require optical sectioning; and thick, scattering samples, such as mammalian brain, requiring methods to deal with scattering and out-of-focus fluorescence. In each of these systems, several approaches with different trade-offs are possible. The decision tree of for choosing an experimental method is shown in **Figure 45**.

All AON approaches have been proven in cultured primary rodent neurons. Only Optopatch has been shown to work in iPSC-derived neurons, but other methods should be equally compatible. Of all approaches, however, Optopatch (Chapter 2) has been most thoroughly investigated in cultured neurons, revealing both single-cell and synaptic phenotypes, and offers higher quality data than calcium-based or BeRST based AON. This data is further improved by replacing QuasAr2 in the original Optopatch with Archon1[220]. The times to consider other methods are when 1) calcium, or another moiety, is of greater interest than voltage; 2) when the technical requirements of voltage imaging including intense red laser illumination and a fast camera are prohibitive; and 3) when the cells of interest are homogenenous and heavily synchronized. In the first two cases, 1P calcium imaging-based

AON (Chapter 4) is preferable. In the last case, BeRST imaged with a bright red LED onto a PMT through low-magnification optics may suffice.

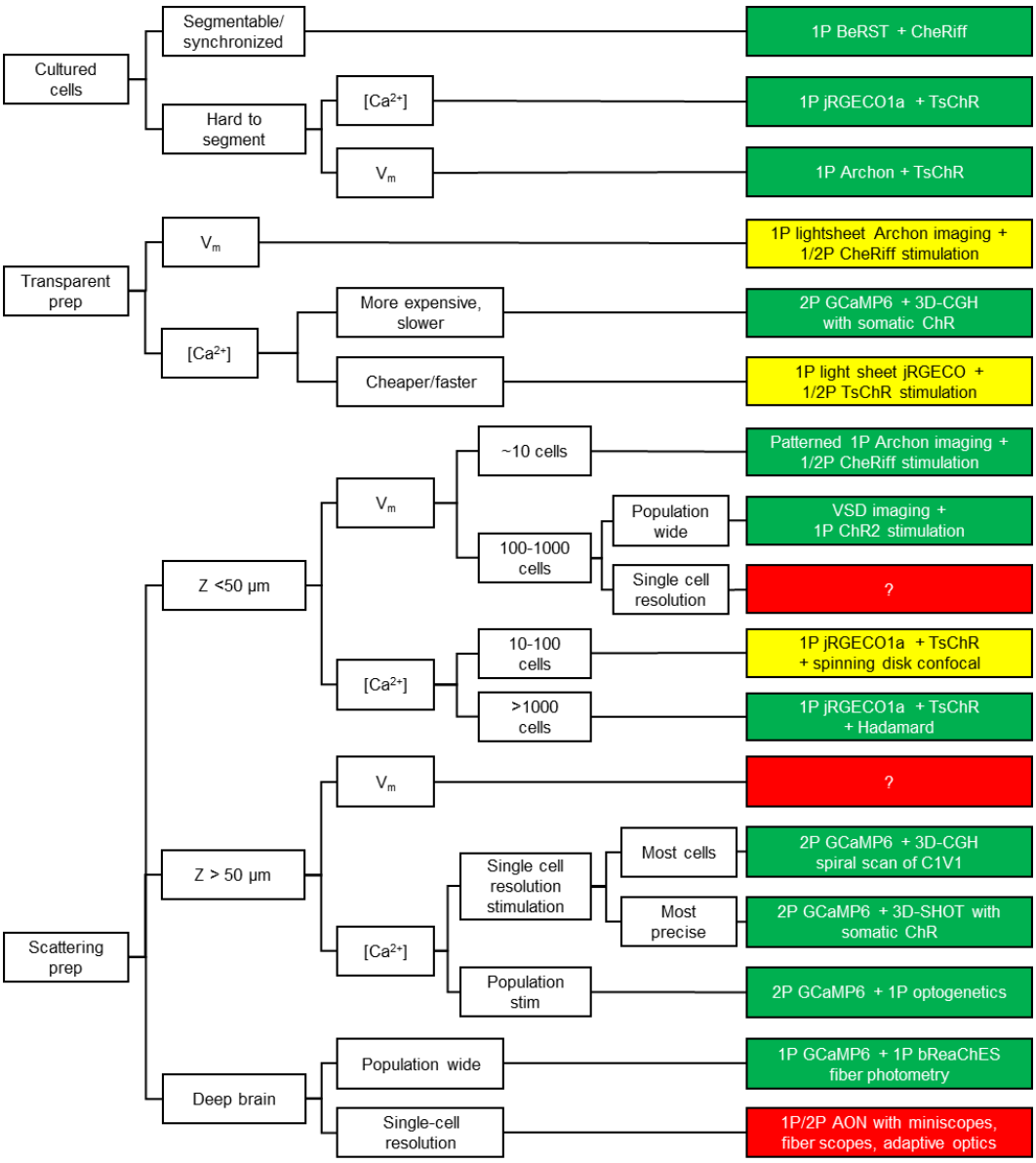

Figure 45. Available AON methods for various experimental applications.

Green boxes have been published and demonstrated. Yellow boxes have not yet been demonstrated but are natural extensions of existing technologies. Methods in red boxes do not yet exist.

Transparent preparations have received less attention from AON developers than scattering brain. The only well-performing published applications rely on 2P GCaMP6 imaging combined with 3D-CGH stimulation of ChR2[264,265]. However, the 1P approaches developed

for cultured neurons are in principle readily generalizable to zebrafish and *C. elegans* measurements. Archon1 and jRGECO1a have both already been shown to report activity in both model systems[197,220]. It should, then, be possible to use 1P light sheet imaging[183] combined with 2P optogenetic stimulation[198] to produce single cell resolved AON at lower cost than 2P/2P approaches.

AON in thick, scattering tissues such as live mice and brain slices presents a much greater challenge than transparent or cultured preparations. Distinct methods have been developed for applications roughly one scattering length away from the surface of the preparation (~50 μm), for applications deeper than 50 μm but still optically accessible by 2P methods (50-500 μm), and for optically inaccessible deep brain regions.

Close to the surface of the brain, 1P methods can still be applied. Voltage-based AON has been demonstrated in acute slices, L1 of the cortex, superficial hippocampus (with cortex aspirated), and olfactory bulb[219,221]. These approaches require patterning the imaging light to only the cells of interest and are currently limited to ~10 cells measured in parallel. Population wide AON measurements are possible with VSDs coupled with ChR2, but lose cellular resolution entirely[106]. Voltage based-AON on 100's to 1000's of cells with single cell resolution has still not been shown. 1P calcium-based AON on thousands of cells has been demonstrated (Chapter 4) with jRGECO1a, TsChR, Hadamard microscopy. If cells over a smaller FOV are sufficient, spinning disk confocal should be a viable alternative, though the particular combination of jRGECO1a, TsChR, and spinning disk has not been demonstrated.

Going deeper into the tissue requires 2P based approaches. Due to the lack of 2P-excitable voltage indicators, there are currently no options for AON deeper than 50 μm in brain tissue. 2P-calcium based AON is technologically sophisticated and requires careful consideration of the experimental demands. If single cell resolution stimulation is required, 3D-CGH with spiral scanning enables stimulating the most cells simultaneously with red-shifted opsins[268], while 3D-SHOT is the best method for stimulating cells with high temporal

precision[266,267]. In either case, a somatically targeted ChR such as soCoChR should be used[271]. If single-cell stimulation is not required (as for fiber tract stimulation), 1P optogenetic excitation or inhibition can be used instead.

Beyond 500 μm deep, AON has been largely untested. The only options are for population wide stimulation and recording methods using GCaMP6 and bReaCheS with fiber photometry[248]. Optical techniques for deep brain imaging such as 1P/2P miniscopes, fiber scopes, and adaptive optics have not been evaluated for compatibility with AON—and thus present an area for future focus of tool developers.

5.3 Technological outlook

The previous section highlighted several unmet experimental needs. This section will elaborate on the protein and optical tools which could improve AON in the future.

5.3.1 Molecular tools

Improvements in the reporters of neural activity will likely yield the biggest gains in AON performance. Development of GECIs which are brighter under 2P illumination could increase the number of cells recorded with 2P-calcium based AON[274]. RGECIs with comparable performance to GCaMP6 would enable 2P AON from deeper layers, and aid with spectral crosstalk with the better performing blue-shifted optogenetic actuators. Such RGECIs would also improve the performance of Hadamard microscopy in terms of recording SNR (Chapter 4). Removing the photoswitching behavior of jRGECO1a would be particularly helpful in this case, perhaps with sensors based on K-GECO[251]. Finally, NIR-FP[275,276] based calcium sensors could offer 3-color AON, allowing independent excitation of two cell populations or bidirectional control of the same population.

Better GEVIs are necessary for voltage-based AON. It is not clear that the scaffold for the ideal voltage sensor has been discovered, and new voltage sensitive domains should still be investigated[277]. Even with Archon1, brighter red sensors for voltage imaging are still needed[220]. FRET-based approaches for AON are unlikely to bear fruit unless a far-red shifted

voltage sensitive acceptor can be identified. A systematic screen of large numbers of voltage sensitive, fluorescent microbial rhodopsins could help with both goals but has not been performed. The ultimate goal should be a voltage sensor compatible with 2P excitation, which would bring voltage based AON to deeper cortical layers[174,222].

Although indicators offer more room for improvement of AON than actuators, improved optogenetic actuators should still be sought out. In the 1P regime, studies growing the palette of available actuators has been instrumental for the work presented in this thesis[86]. Highly performing red-shifted opsins are already available, and after extensive directed evolution and searches in nature, it seems unlikely to identify an opsin without blue-light induced photocurrent. The blue-shifted side of the spectrum offers more promise. It is interesting that all three blue-shifted ChRs (CheRiff, PsChR, and TsChR) used in this study come from the *Chlorodendraceae* algae family: CheRiff from *Scherffelia dubia*, PsChR from *Tetraselmis subcordiformis*, and TsChR from *Tetraselmis striata*. TcChR[86], from *Tetraselmis cordiformis*, should be investigated for blue shifted and sensitive photocurrents, as should other members of the *Chlorodendraceae* family. The key blue-shifting mutation in the *Tetraselmis* proteins are likely T198G/G202A, which have also been shown to blueshift the spectrum of C1C2[278]. These mutations should be investigated in the context of other sensitive rhodopsins.

In addition to color, optogenetic actuators could be improved in their 2P cross-sections and absolute photocurrents, to enable simultaneous stimulation of more cells with better temporal resolution. Inhibitory opsins with exceedingly high currents have been identified[96], but no such excitatory proteins exist. Directed evolution for optogenetic actuators with improved 2P cross section presents a technological challenge but could also yield large dividends.

5.3.2 Optical tools

AON methodologies rely on careful optical design to achieve maximal performance. At present, most challenges lie in more tightly controlled imaging and stimulation in scattering

brain tissues. Adaptive optics[279] combined with 1P Archon1 imaging could increase the depth penetration into the brain until 2P GEVIs become available. Once such sensors are available, 2P scanning modalities capable of kHz imaging will be necessary. Similarly, in 1P or 2P, faster sCMOS cameras could increase the acquisition rates or fields of view for 1P voltage or calcium-based AON.

A large number of 1P and 2P techniques for visualizing GCaMP6 have been developed in recent years, but AON has been applied with only a few[280]. AON on mesoscopes[213] and miniscopes[281] is particularly appealing, enabling large fields of view or deep-brain imaging *in vivo*, respectively. The challenge for mesoscopes is to activate meaningfully-large clusters of cells given available SLM chip sizes and permissible power limits. The challenge for miniscopes is to miniaturize optical sectioning and stimulation optics to allow reliable single-cell measurements and render them compatible with the lower NA lenses required. In deep-brain contexts where cellular resolution is not necessary, improved fiber photometry approaches, such as TEMPO[282], could be combined with AON.

A final problem to be considered is how to make AON tools broadly available to biologists. The more sophisticated 2P-imaging/2P-stimulation approaches require two separate femtosecond-pulsed lasers. Such a home-built microscope can cost as much $0.5M, with commercial microscopes (if available) frequently reaching >$1M. Even culture-based measurements with Arch-based indicators require more optical expertise than available in most biology labs. Concerted efforts must therefore be made to increase the availability of these tools to more than the best funded and best equipped labs in the world[283]. Open source microscopes will likely play a role in this effort[281,284], as will cheaper light sources[285] and microscope components[286]. All optical method developers should take the extra step after publication to disseminate their techniques, whether by coming up with low cost alternatives to their measurements, publishing clear assembly and alignment instructions, or setting up imaging facilities accessible by outside users.

5.4 Biological vistas

The development of new tools is justified by the discoveries those tools enable. AON is still very much in its infancy, yet it has begun to answer biological questions.

In cultured neurons, Optopatch has been used to investigate differences in excitability in cultured neurons. It has also been shown that Optopatch can be coexpressed with voltage-gated channels in heterologous cell lines to identify specific channel blockers[287]. The assays made possible by Optopatch, or by combinations of BeRST1 with ChRs, are now being leveraged for pharmaceutical screens in cultured neurons[288–290], cardiomyocytes[291–293], and immortalized cell lines[287,294]. This promises to be a fruitful direction in drug discovery based on electrophysiological phenotypes. From a basic biology standpoint, Optopatch has been used to show homeostatic plasticity in intrinsic excitability of hIPSC-derived neurons, hIPSC-derived neuron protocols are constantly evolving and require characterization of cells' electrical properties, which is currently done with multi-electrode arrays or patch-clamp based measurements. Both methods must contend with the variability native to differentiation protocols. By virtue of its higher throughput, Optopatch is better suited to find phenotypic differences between hIPSC-derived neurons from healthy and diseased patients in the face of this variability[295].

AON's opportunities beyond cultured cells are equally exciting. AON in brain slices is particularly valuable in terminal experiments on valuable animals such as disease models, multiple transgenics, and animals which have undergone extensive behavioral training. In each case, the ability to measure more cells from a single animal is invaluable. Toward that end, excitability profiling with voltage- or calcium-based AON have been used to find firing pattern differences between genetically-distinct populations[221] or invoked by pharmacological addition (Chapter 4). Further, with disjoint expression of the optogenetic actuator and indicator, synaptic connections and surprising phenotypes can be discovered (Chapter 4). Voltage-based AON for synaptic transmission has not yet been published, but Archon1 can detect field-

evoked EPSPs in slice[220], and recent work in our lab has demonstrated the same in an AON format. These proof-of-concept demonstrations can be expanded to seek distinct cell populations based on their electrophysiological profiles and to profile synaptic connectivity and excitability across brain regions. With improved methods to tag cells in brain tissue[296,297], genetic information can be integrated into these experiments as well. These approaches could be particularly useful in determining the connectivity rules for activity-labeled, or engram, cells[298]; for finding the functional differences between newly identified cell types[299,300]; and for generating connectivity matrices for local and long-range circuits[9].

In live fish, AON has already been used for discovering functionally connected cell types[269], and to identify the sufficient groups of cells in the optic tectum to evoke tail movement[264]. In mice, using 2P GCaMP6 imaging is used to identify cells active during a behavior, and to then elucidate their contribution to the system with 2P stimulation. This approach revealed that manipulation of single CA1 place cells can modulate activity of other nearby cells[194]. In visual cortex, populations of coactive cells were identified or written with 2P stimulation, which could subsequently be recalled by stimulation of a single cell of the group[195]. Future work with these techniques will be able to investigate modulation of synaptic strength during behavioral modulation; to study the impulse response of intact networks; and to track the connectivity matrices the network over time through various behavioral states. Finally, AON can reveal differences in excitability of cells during different behavioral states[219], which will help understand how cells are recruited to firing during particular behaviors. Considering the range of behaviors protocols established in mice, AON in live animals promises to be a fruitful approach for years to come.

Appendix 1: Voltage measurements outside of rodent neurons

The work in this thesis has been exclusively focused on AON in rodent neurons and rodent brain slices, but the tools developed have applications in a broader range of biological systems. In this appendix I will briefly describe attempts to measure voltage in the neurons of living *Drosophila melanogaster* (*Drosophila)* and measurements of voltage in the aldosterone-secreting cells of the zona granulosa in slices of mouse adrenal cortex.

Voltage imaging in *Drosophila*

Drosophila is an appealing model system for neuroscience because it offers readily tractable genetics and a small brain size while retaining a large behavioral repertoire[301]. Acquiring information from multiple neurons simultaneously to address systems level questions is necessary in the fly as in mice. Insect neurons are different in many respects from mammalian neurons, informing the chosen approach for parallel recordings. Insect neurons are frequently pseudo unipolar, allowing signal to propagate from the dendrites to axons without eliciting a calcium response in the soma. Calcium imaging is thus prone to under-reporting activity. At the same time, in *Drosophila*, a large portion of cell bodies reside on the surface of the brain, making them appealing for 1P voltage imaging. When we began our efforts, voltage imaging with wild-type Arch had been used to dissect the channel contributions to the pre-synaptic action potential in individual *Drosophila* larval neuromuscular junction[302]. Voltage imaging had also been achieved with ArcLight, but the slow kinetics of that indicator were insufficient to resolve individual action potentials in the typically fast-spiking *Drosophila* neurons[131]. Once we had identified QuasAr1 and QuasAr2 in Chapter 2, it was natural to ask if they could be applied to *in vivo Drosophila*, with the goal of achieving single-cell, single-spike voltage imaging.

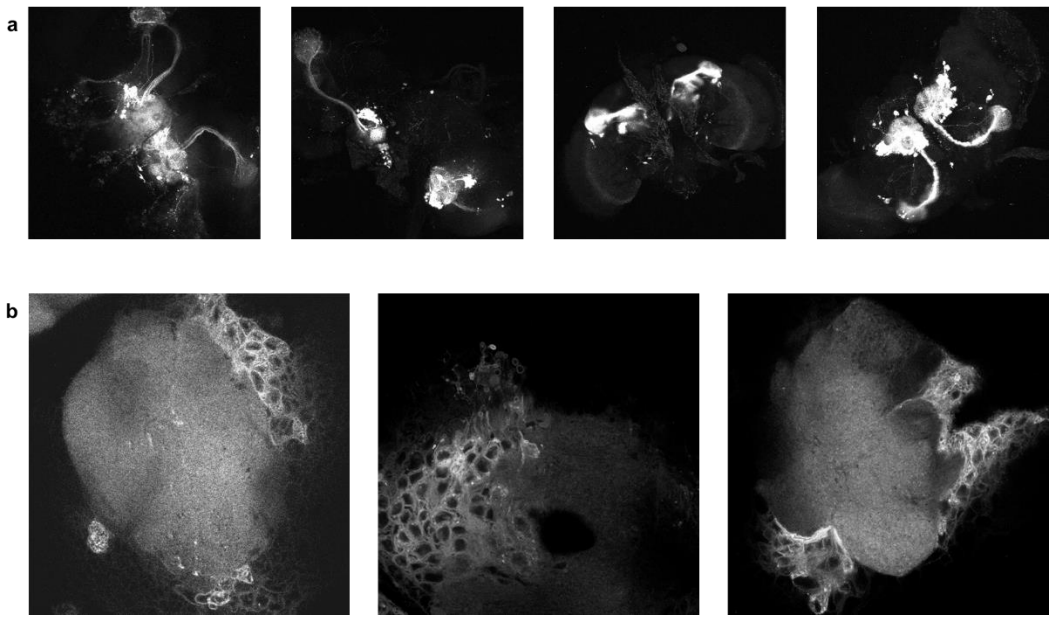

Figure 46. Confocal characterization of GH146-Gal4$^{+/-}$; UAS-QuasAr-GFP$^{+/-}$.

(**a**) Representative z-stack maximum-intensity projections of whole brain explants from GH146-Gal4$^{+/-}$; UAS-QuasAr1-GFP$^{+/-}$ flies of different ages and genders. From left to right, in order, are an old female, a 2-day old female, an old male, and a 2-day old male. Data was acquired by confocal microscope with a 20x objective. (**b**) Single section, higher magnification images of AL in brain explants from GH146-Gal4$^{+/-}$; UAS-CD8-GFP$^{+/-}$ (a membrane localized GFP, left), GH146-Gal4$^{+/-}$; UAS-QuasAr1-GFP$^{+/-}$ (middle), and GH146-Gal4$^{+/-}$; UAS-QuasAr2-GFP$^{+/-}$ (right).

We cloned QuasAr1 and QuasAr2 GFP and mOrange2 fusions into the pJFRC7[303] and UAS-QuasAr-FP lines were generated by Genetic Services, Inc. For initial experiments, we drove expression in olfactory projection neurons of the antennal lobe (AL) with the GH146-Gal4 line[304]. The electrophysiological responses of these neurons to olfactory stimulation is well studied and could serve as a basis for comparison[305]. For all experiments, fly feed was supplemented with all-*trans* retinal prior to imaging. After screening several flies for each line, QuasAr-mOrange2 showed lower overall FP expression than QuasAr-GFP and was abandoned. We examined the effect of gender and age vs. GFP expression on whole brain explants by confocal microscopy. In QuasAr1-GFP flies, 2-day old flies had stronger GFP expression than old flies, with 2-day old males showing the highest expression (**Figure 46a**).

Under high magnification confocal, both QuasAr1- and QuasAr2-GFP appeared to localize to the membrane, similar to the membrane localized CD8-GFP (**Figure 46b**).

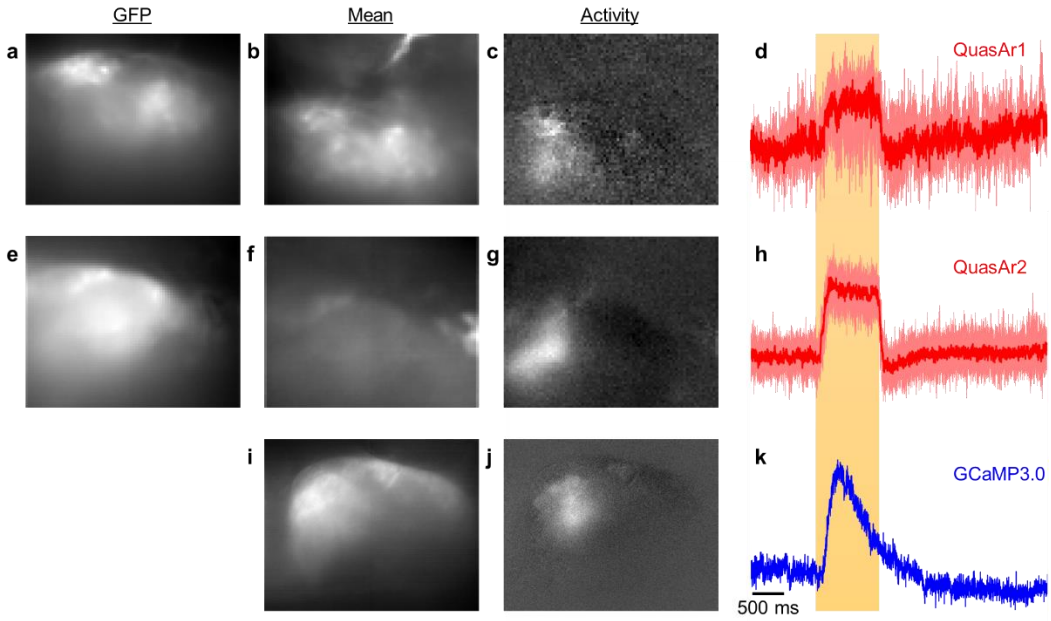

Figure 47. Population wide responses of AL to odorant stimulation.

(**a**) GFP expression in a GH146-Gal4$^{+/+}$; UAS-QuasAr1-GFP$^{+/+}$ fly. (**b**) QuasAr1 expression in same fly as (a). (**c**-**d**) PCA-ICA extraction of response to odor stimulation in same AL as (a) and (b). Components corresponding to motion and bleaching were discarded, leaving behind one component with spatial profile (c) and temporal profile (d). The temporal profile showed a transient elevation which was locked to the onset of odor stimulation (1s, yellow bar). Pink lines correspond to 10 individual trials and the thick red line is their average. Vertical scale is arbitrary. (**e**-**h**) Same as (a-d), but for GH146-Gal4$^{+/+}$; UAS-QuasAr2-GFP$^{+/+}$. (**i**-**k**). Same as (a-d) but for Pebbled-GCaMP3.0.

We next exposed the AL for imaging in live GH146-Gal4$^{+/-}$; UAS-QuasAr1-GFP$^{+/-}$ flies, while presenting pulses of positive valence odorant to their antennae. Even with extensive optimization of the imaging optics (including switching the illumination wavelength 594nm, where QuasArs are brighter but less sensitive), we were only able to measure clear odor-evoked responses in one fly. We reasoned that higher expression was needed and thus generated double homozygous flies, GH146-Gal4$^{+/+}$; UAS-QuasAr-GFP$^{+/+}$. In double homozygous flies we were able to acquire population-wide odor-evoked responses from both QuasAr1 and QuasAr2 (**Figure 47**). Including both QuasAr1 and QuasAr2 flies, we were only able to measure odor-evoked responses from 8 out of 17 animals, with no consistent

differences in signal to noise between the two constructs. Odor-evoked responses had a faster onset than for control Pebbled-GCaMP3.0 flies (**Figure 47**), as expected for the faster kinetics of the underlying signal and indicators. Signals had relatively low magnitude, were frequently obscured by motion artifacts in the preparation, and rarely lasted for more than 2 minutes of recording. Furthermore, we were not able to resolve single cell or single spike signals, even at higher magnification.

We saw several possible explanations for the poor resolution of the voltage signals. In AL neurons, spikes are relatively fast and short; it's possible that QuasAr was still too slow or not sensitive enough to report these events. Additionally, it was possible that we were averaging signal out over multiple cells due to our lack of spatial resolution. Finally, to avoid motion artifacts, a spontaneously active cell type would be ideal. To address all issues simultaneously, we used a GMR-24C12-Gal4 line to limit expression to 6 neurons in each lateral accessory lobe (LAL). Work in the Wilson lab (unpublished) had found that these neurons fire spontaneously with ~100 mV action potentials at <10 Hz. In double heterozygous QuasAr1-GFP flies, we were able see expression in QuasAr and GFP channels for QuasAr1-GFP and in the GFP channel only for QuasAr2-GFP. Despite seemingly adequate expression, we could see no clearly-resolved action potentials from QuasAr1. We crossed to obtain double homozygotes again but could still only see static expression and no fast signals corresponding to electrical activity.

We sought to obtain ground truth measurements of alongside voltage imaging. Cell-attached recordings from a QuasAr1 expressing neuron showed spontaneous spiking of the expected rate. Surprisingly, upon 594 nm illumination, spiking ceased, rendering it impossible to obtain optical spike recordings (**Figure 48**). The abrogation of spiking was both wavelength and intensity dependent, with 488 nm eliciting a light-triggered response at much weaker intensities (**Figure 48**). The perturbation of spiking behavior began at light powers much lower than those necessary to recover QuasAr signals on a single-cell, single-spike basis.

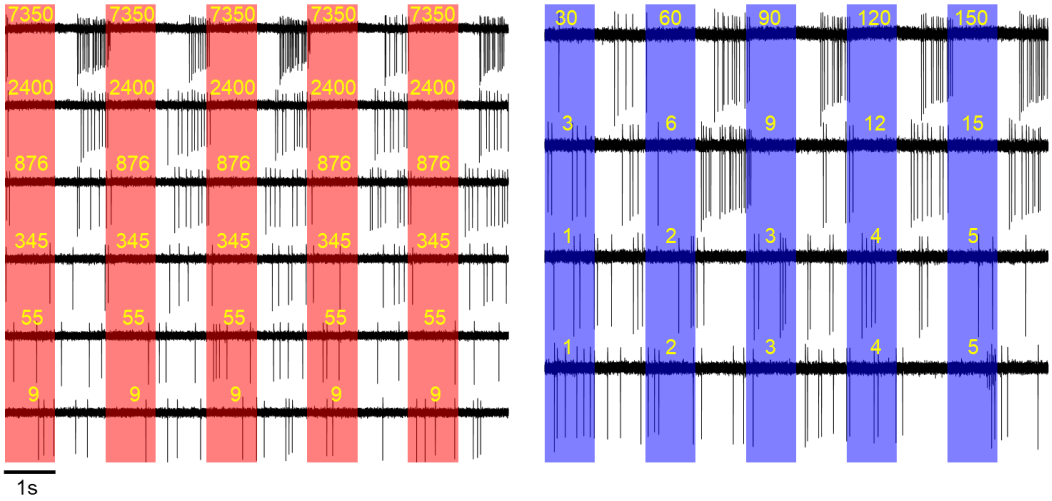

Figure 48. Cell attached recording in live *Drosophila*.

Spontaneous activity in GMR-24C12-Gal4 neuron recorded in a cell attached confirmation while turning light of different colors (red bars = 594 nm, blue bars = 488 nm) and intensities, (yellow numbers, in W/cm^2) on and off. Different lines are separate runs on the same cell. This neuron expressed QuasAr1-GFP.

Based on the results in **Figure 48**, we concluded that single-cell, single-action potential recordings with QuasArs in live *Drosophila* is not possible. Population wide measurements, such as those in AL could be done at lower red light intensities, which explains why we had better luck repeating measurements multiple times and averaging rather than increasing the light intensity during single trial recordings. Our results should also urge caution in interpreting voltage imaging work with other indicators. We were able to see clear, single-trial perturbation of spiking with 5 W/cm^2 488 nm light. Two other studies have performed GEVI imaging in live flies: one with Arclight, at 1-12 W/cm^2 488 nm light in GH-146-Gal4 labeled neurons[131]; and one with Ace2N-2A-mNeon, at 2W/cm^2 in GMR-55D11-Gal4 labeled neurons, an apparent subpopulation of the GMR-24C12-Gal4 used here[224]. These intensities could be high enough to perturb spiking when imaging for longer than 1s. We encourage future studies to identify non-perturbative light intensities for new cell-type studied with blue-excited GEVIs. 2P imaging in live flies with ASAP2f[228] and ASAP2s[229] has been demonstrated, and the IR light used for those measurements seems less likely to perturb neuronal activity.

Voltage imaging in adrenal cortex

Neurons and cardiac cells are the typical objects of electrophysiological study, but many other cell types in the body are also electrically active. In particular, endocrine cells such as pancreatic α-, *β*-, and δ-cells[306], all secretory cells in the pituitary gland[307], pinealocytes[308], and thyrocytes[309] are all polarized and express voltage-gated ion channels. These cells have not all been shown to fire action potentials, but these studies are susceptible to experimental artifacts due intrinsic to whole-cell patch clamp measurements or to removing and dissociating the cells of interest.

In the adrenal cortex, cells of the zona glomerulosa (ZG) release aldosterone to maintain water and electrolyte balance in the body. Hyperaldosteronism can contribute to hypertension, motivating the study of aldosterone release[310]. Dissociated ZG cells have been shown to be polarized but non-excitable when dissociated, but our collaborators at the University of Virginia recently discovered that in slices these cells fired oscillating action potentials[311]. Action potentials are coupled to aldosterone release, but questions remain about the modulation of spike patterns, the relationship between spike patterns and hormone release, and the role of possible electrical communication between cells[311]. Solving these problems electrophysiologically is challenging. ZG cells *in situ* are arranged in rosettes covered by a sheath which makes them difficult to access with electrodes. Further, ZG cells are suspected to be mechanically sensitive, and will be activated by electrode contact. As for all electrophysiological measurements, studying multiple cells at once is particularly technically challenging and has not been attempted.

We thus turned to voltage imaging to study the electrical dynamics in ZG. The ZG has many advantages for voltage imaging. The cells of interest reside on the surface of the adrenal cortex, meaning that scattering and optical sectioning is much less of a problem than in neuronal tissue. ZG rosettes are small enough to be visualized in a single FOV at high magnification. Finally, the action potentials in ZG cells are slow compared to neurons and can

be fully captured at a 50 Hz sampling rate rather than 1 kHz. One challenge is that the same sheath that makes patching difficult in ZG keeps out VSDs and AAVs from reaching the underlying cells. However, ZG cells can be labeled specifically with aldosterone synthase-Cre (AS-Cre) mice[312].

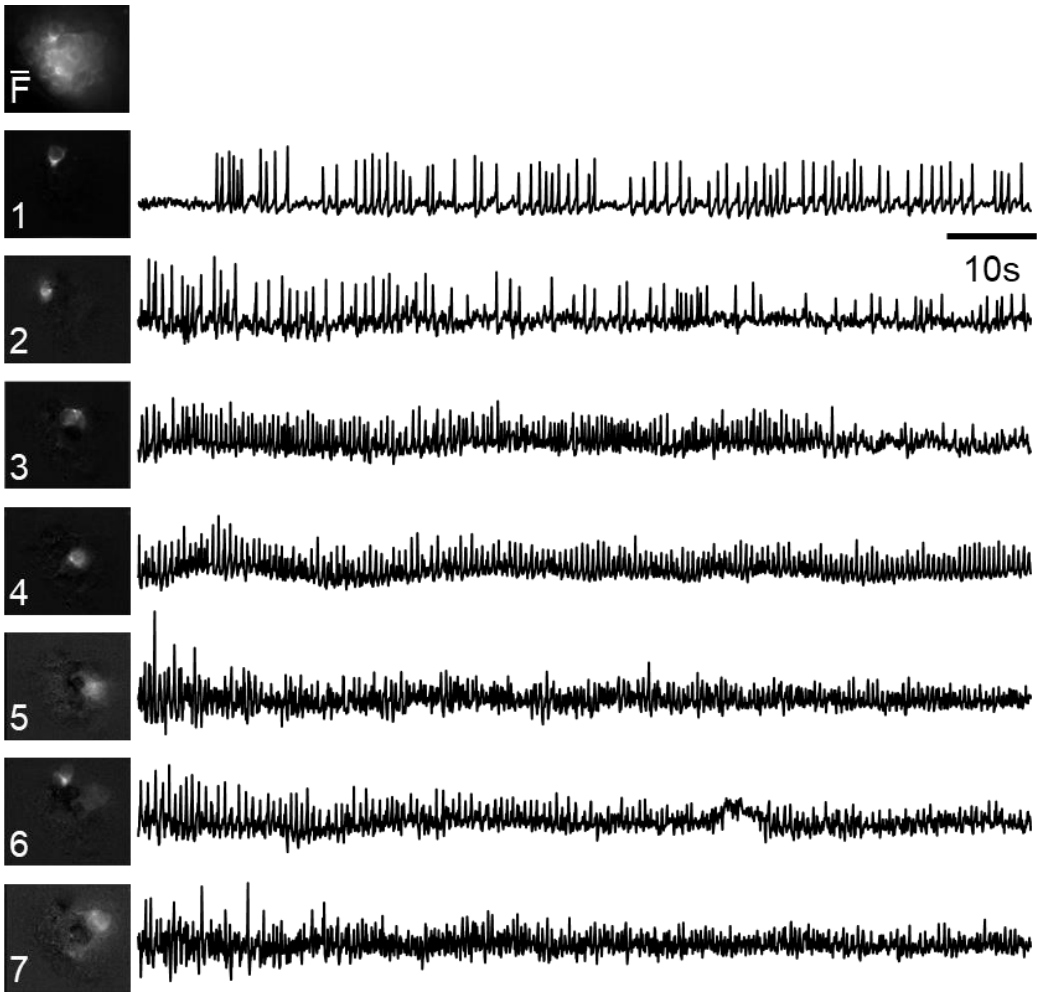

Figure 49. Optopatch2 measurements in ZG.

Top, image of average fluorescence of QuasAr2 in one ZG rosette in a slice of mouse adrenal cortex. Bottom, PCA-ICA components corresponding to 7 cells firing during angiotensin-3 stimulation. Vertical scale is arbitrary. Slice was prepared from an AS-Cre$^{+/-}$; Optopatch-2$^{+/-}$ animal. Imaging was performed at 20 Hz.

To study ZG electrophysiology, we crossed AS-Cre mice with Optopatch-2 and Optopatch-3 mice[219,221]. To our surprise, even with double homozygous mice, Optopatch-3 mice showed no expression in the ZG, while Optopatch-2 showed high expression. We

suspect this is due to better accessibility of the Rosa26 locus of Optopatch-2 mice compared to the TIGRE locus of Optopatch-3. Regardless, expression of Optopatch-2 was sufficiently high for voltage imaging. The baseline spiking rate in Optopatch-2 expressing ZG cells is low (unlike the reported electrode measurements[311]), but stimulation with angiotensin-3 led to an increase in spiking. Preliminary measurements and simple PCA-ICA segmentation enabled simultaneous measurement of 7 ZG cells (**Figure 49**). Future work will calculate cross-correlations between cells before and after stimulation with different concentrations of angiotensin-3. These cells also express CheRiff-GFP, which will allow us to drive arbitrary spiking patterns in single cells and monitor the resulting changes in firing in adjacent cells.

This work is still in its nascent stages, but our preliminary results show that Optopatch transgenic mice can be a powerful tool for studying voltage dynamics in non-neuronal cells. The advantages of the ZG for voltage imaging also hold for other secretory cells. It would interesting to perform similar measurements in the pancreas, thyroid, pineal, and pancreatic glands. These measurements can be performed in slices, though, given the likelihood of slicing and culture artifacts, effort should be expended to measure directly *in vivo*. Voltage imaging with implantable fiberscopes has not yet been attempted in the brain because of the lower light collection efficiencies of such optics. With the slower firing rates of endocrine cells, however, photon efficiency may not be as big problem. Being able to study the dynamics of cells directly *in vivo* would be of great help for generating quantitative models of endocrine function. Further, voltage-gated channels are common drug targets, so discoveries are likely to be readily translated to therapeutic interventions[313]. Thus, voltage imaging in the endocrine system could be a deep and fruitful area of research in the future.

Author contributions

For *Drosophila* work, Samouil L. Farhi designed constructs in Adam E. Cohen's lab and Sasha Rayshubskiy generated fly lines in Rachel Wilson's lab. Sasha Rayshubskiy and Samouil L. Farhi performed all imaging measurements together.

Transgenic mouse slices for adrenal cortex work were prepared in Paula Q. Barrett's lab by Nick A. Guagliardo and imaged in Mark P. Beenhakker's lab. Samouil L. Farhi designed imaging experiments and performed data analysis.

Appendix 2: Photophysics of of mApple-based RGECIs

Rationale and methods

Reasoning that 1P calcium imaging should enable large FOV AON measurements, we investigated RGECIs for compatibility with optogenetic stimulation. The best performing RGECIs are based on the photoswitching mApple fluorescent protein also used in FlicR1 (refs. 196,197). Our experience with FlicR1 indicated that the photoswitching properties of mApple based fluorophores could significantly complicate their implementation in all-optical neurophysiology. Further, literature data on mApple-photoswitching in RGECIs is inconsistent. Fluorimetric characterization of purified R-GECO1 shows that an initial decrease in fluorescence following blue light exposure, followed by gradual activation up to original levels[166]. However, the second generation jRGECO1a, only showed an increase in fluorescence in neurons illuminated with 488 nm light to drive ChR2 (ref. 197), like the behavior we observed in FlicR1 (Chapter 3). We reasoned that part of the discrepancy could be due to the different light intensities typically used in fluorimeters compared to microscopes.

To better understand the photophysical properties of mApple based-RGECIs we expressed jRGECO1a, R-CaMP2, and jRCaMP1a in HEK293T cells from identical constructs. As shown in **Table 6**, we found that the mRuby-based jRCaMP1a bleached faster than R-CaMP2 and jRGECO1a, consistent with previous reports. Its fast photobleaching combined with its comparatively poor response to single action potentials provided further incentive for developing all-optical neurophysiology with the better performing mApple-based jRGECO1a and R-CaMP2.

We then exposed each construct to 1s pulses of 488 nm nm light between 0 and 1.2 W/cm^2 while co-illuminating with 561 nm light of 0-10 W/cm^2 in both basal (low) calcium

conditions and in high-calcium conditions achieved by adding 2 μM of the calcium ionophore ionomycin (extracellular [Ca^{2+}] = 3 mM). Similar measurements were performed at 458 nm, with comparable results (not shown).

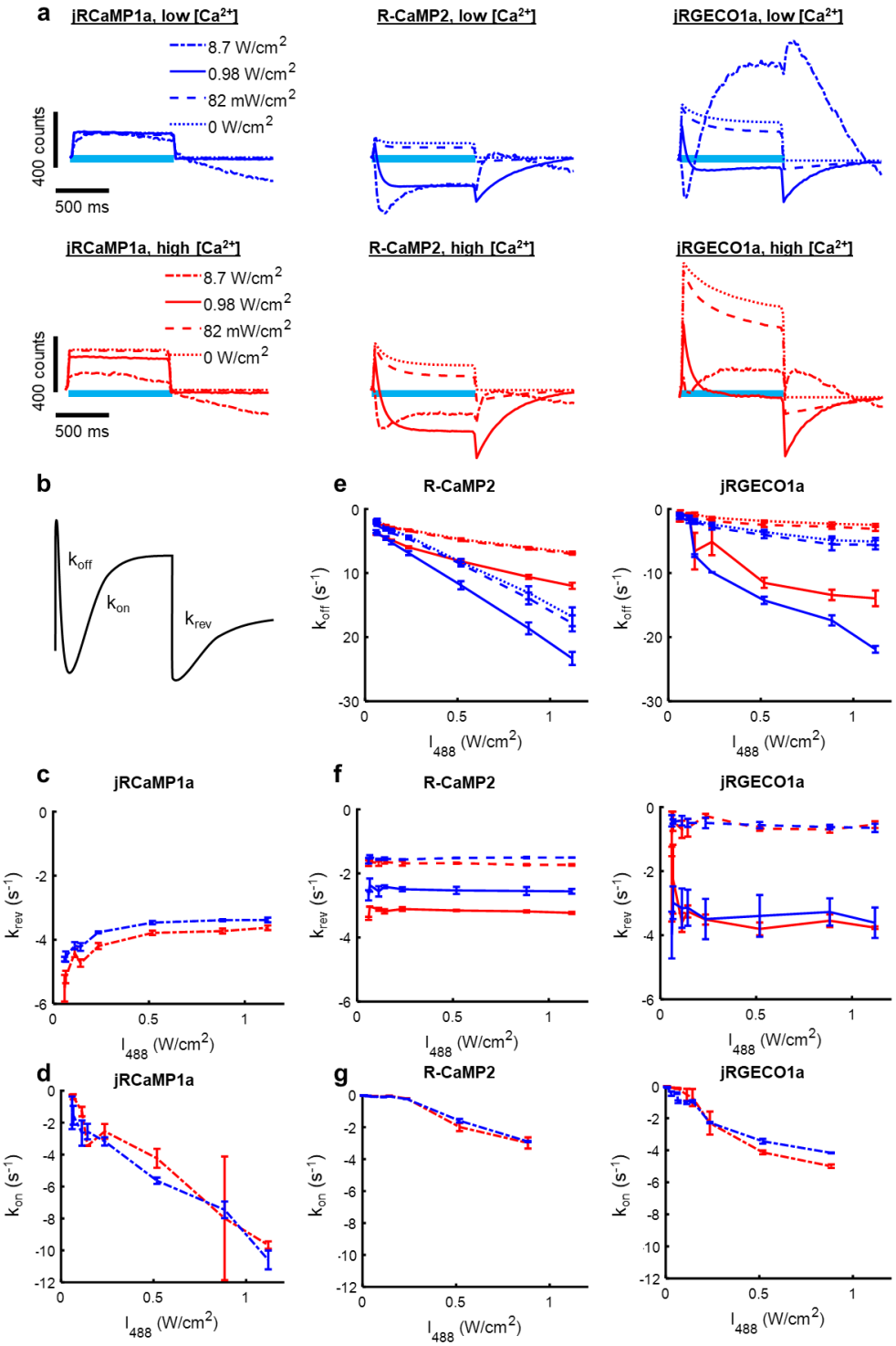

Figure 50. **Photoswitching kinetics of RGECIs.**

HEK293T cells expressing RGECIs under control of the CAG promoter were illuminated with 1s pulses of 488 nm light of various intensities under constant illumination of 561 nm light of various intensities, while imaging at 20 Hz. Data was acquired by averaging background-subtracted signal from ~20 cells per field of view. Traces were photobleach corrected with a mono-exponential, except for the highest 561 nm intensity which used a sliding median filter. (**a**) Representative traces of blue-light evoked changes in signal from one field of view for each RGECI. Traces are shown in minimum-subtracted camera counts. (**b**) Cartoon representation of the rate constants extracted from each trace and displayed in (c-g)**.** (**c**) Reversion rate constant of jRCaMP1a as a function of the preceding blue light intensity. (**d**) Photoactivation rate constant of jRCaMP1a as a function of the blue light intensity. (**e**) Rate constant for switching to the dark state of R-CaMP2 and jRGECO1a. (**f**) Same as (c) for R-CaMP2 and jRGECO1a. (**g**) Same as (d) for R-CaMP2 and jRGECO1a. Line-style throughout the figure indicate the 561 nm intensity in the measurement--see legend in (a), while color represents baseline calcium conditions (blue) or elevated calcium conditions (red), accomplished by adding 2 μM ionomycin to the cell culture. All rate constants were extracted from monoexponential fits to the appropriate region of the average trace of one field of view and are plotted as mean ± SEM over 3 fields of view.

Photoactivation of jRCaMP1a at high intensities

At 561 nm intensities < 1W/cm^2, jRCaMP1a showed simple, instantaneous excitation with blue light, consistent with its published absorbance spectrum[197]. At high 561 nm intensities (8.7 W/cm^2), slow photoactivation in response to blue light in both the low and high calcium conditions became noticeable (**Figure 50a**). Photoactivation during blue light illumination was first order in 488 nm intensity, with no differences in kinetics at high [Ca^{2+}] and low [Ca^{2+}] (**Figure 50d**). Recovery kinetics from the photoactivated state was weakly dependent of the previous 488 nm intensity (**Figure 50c**). Thus, if jRCaMP1a is to be used for high time resolution calcium measurements requiring high 561 nm excitation intensities, this photoactivation must be considered. Further, caution should be exercised when other indicators based on mRuby, such as the Ace-mRuby indicator currently in development, are combined with optogenetic activation.

Photoconversion of jRGECO1a and R-CaMP2

As expected, jRGECO1a and R-CaMP2 showed more complicated blue-light induced photophysics. In addition to the directly driven fluorescence, both constructs showed a slow decrease in the recorded fluorescence under sustained blue light (**Figure 50a**). The decay was

well-fit to a monoexponential, consistent with transition to a dark state. We measured the decay rate constant (k_{off}) at various blue light intensity intensities at 3 yellow light intensities, including a yellow-off condition using the blue-light driven fluorescence. R-CaMP2's k_{off} was linear with blue light intensity, while jRGECO1a's k_{off} appeared to saturate at higher blue light intensities (**Figure 50e**). Increasing 561 nm imaging intensity increased k_{off}, and, at the highest yellow intensities (8.6 W/cm^2), the fluorescence decrease was too fast to fit accurately with the 50 Hz sampling rate used (**Figure 50a**). We conclude that yellow as well as blue light induced transition to a dark state (**Figure 50e**). Recovery rate constants from the dark state (k_{rev}) when blue light was turned off was not dependent on blue light, but did depend on yellow light intensity, speeding up at higher 561 nm intensities (**Figure 50f**).

At high 561 nm intensity (8.6W/cm^2), R-CaMP2 and jRGECO1a displayed a photoactivation following the blue-light induced decay. The rate constants of this photoactivation (k_{on}) between the two constructs were comparable and roughly linear with blue light intensity, though exact values were difficult to obtain because these traces are very sensitive to the precise photobleaching correction method used (**Figure 50g**). Compared to jRCaMP1a, the k_{on} for both constructs was smaller but the amplitude of the change was much larger. In fact, for jRGECO1a, sustained blue light would lead to an *increase* in fluorescence at high 561 nm intensity, suggesting that the population was shifting to a second, brighter fluorescent state.

When comparing high vs. low [Ca^{2+}] states, R-CaMP2's k_{off} values were consistently ~2 fold smaller in the high [Ca^{2+}] than the low [Ca^{2+}] conditions, while k_{rev} values were larger in high [Ca^{2+}] than low [Ca^{2+}]. Photoactivation rates for R-CaMP2 did not depend on calcium levels. Unlike R-CaMP2, jRGECO1a showed no differences in photoswitching rates between the low and high [Ca^{2+}] states. Amplitudes are difficult to compare between low and high [Ca^{2+}] since both sensors become brighter in the presence of high calcium.

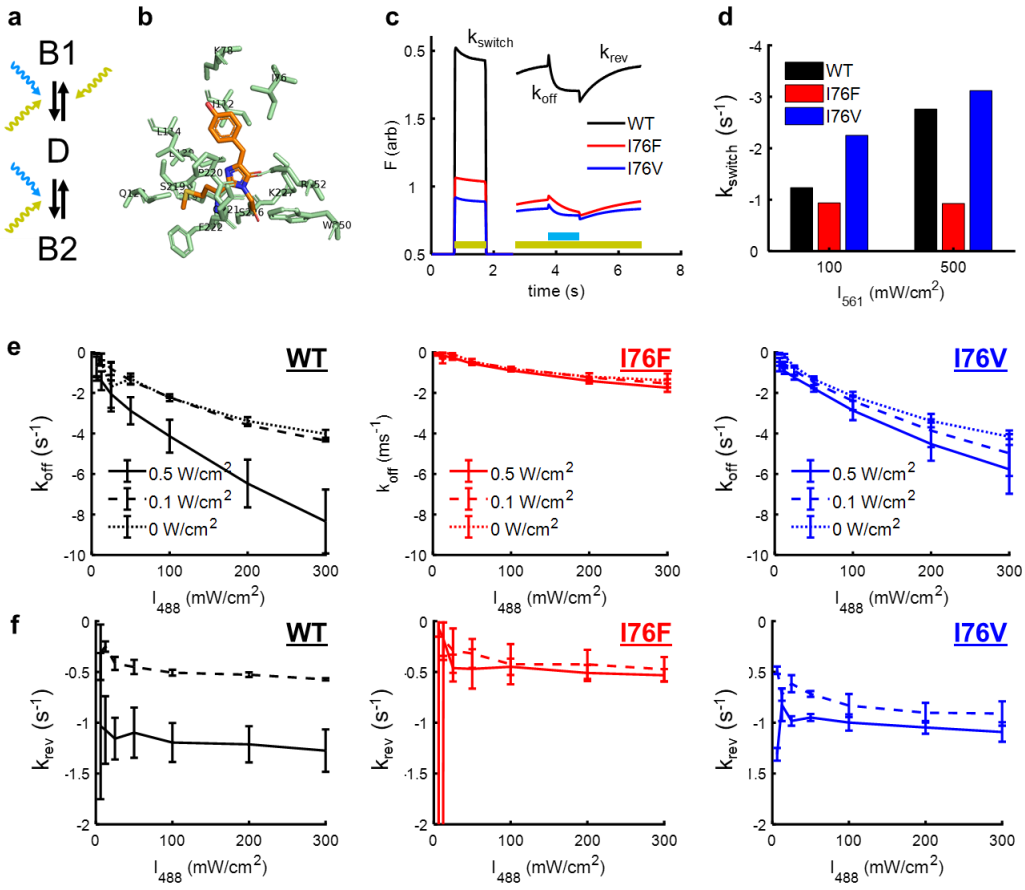

Figure 51. Chromophore isomerization is the cause of photoswitching in jRGECO1a.

(**a**) Proposed photophysical model for photoswitching of mApple-based RGECIs. Blue and yellow arrows indicate that the transition depends on 488 or 561 nm light intensity, respectively. (**b**) Crystal structure of chromophore and surrounding region of RGECO1, adapted from ref. [166]. (**c**) Representative traces of photoswitching experiment of jRGECO1a WT and mutants I76F and I76V. Experiments were repeated at various blue and yellow light intensities as indicated throughout the figure. Inset: cartoon representation of the rate constants extracted from each trace and displayed in (d-f). (**d**) Rate constants of reversible photobleaching for three mutants at two 561 nm intensities. (**e**) Same as **Figure 50e** for jRGECO1a WT and I76F and I76V. (**e**) Same as **Figure 50f** for jRGECO1a WT and I76F and I76V. Rate constants for all traces were extracted as described in **Figure 50**.

Photophysical model mApple-based GEVIs

A possible photophyscal model to explain these observations is that R-CaMP2 and jRGECO1a can transition from its fluorescent state, B1, to a dark state, D under blue or yellow illumination (**Figure 51a**). D can further be photoconverted by 488 nm or 561 nm light to a second fluorescent state, B2. The reversion from D to B1 depends on 561 nm absorption.

Our experimental design could not probe the light dependence of the reversion from B2 to D. Under this model, the commonly made statement that blue light photoactivates mApple is incomplete. Rather, upon blue light illumination, the total intensity and duration of blue and yellow light determines whether mApple into a darker state (D) or a brighter state (B2). The model explains the literature discrepancy between the photoinactivation[166] reported for RGECO1 and the photoactivation[197] reported for jRGECO1a. The RGECO1a measurements were performed in a fluorimeter at minimal 561 nm intensities, and thus never engaged the D → B2 transition, while the jRGECO1a measurements used excessively high 561 nm imaging intensities (4W/cm^2) for 1P imaging, resulting in photoactivation of the protein. It is likely that the reversions from D →B1 can also occur thermally, which would explain the reversible photobleaching previously reported for mApple[314]

We wondered what mechanism underlies the reversible photoswitching of R-CaMP2 and jRGECO1a. Cis-trans isomerization of the chromophore is a common mechanism for photoswitching of FPs, and likely underlies the photoswitching of mApple as well[315]. Most engineering efforts on RGECIs have focused on the calcium binding domains rather than the core of the FP itself[196,197], and therefore mutations in the chromophore region have not been published or characterized. We identified residue I76 in the crystal structure of RGECO1[166] a site which could modulate the kinetics of isomerization of the chromophore, as has previously been found in Dronpa[316].

We made two mutations in jRGECO1a, I76F and I76V and measured the rate constant of reversible photobleaching k_{switch} and of photoswitching into the dark state D, k_{off} and k_{rev}, all in a low [Ca^{2+}] state (**Figure 51**). We used intensities of 561 nm light too low to push jRGECO1a into the B2 state. For each indicator, the kinetic trends measured in **Figure 51** match those in **Figure 50**, suggesting that both mutants can be described by the same model (**Figure 51a**). In each condition, however, I76F showed lower rates of photoswitching while I76V showed increased rates. This is consistent with a cis-trans isomerization

mechanism of photoswitching, as steric hinderance of a larger residue at position 76 discourages flipping of the chromophore to the dark trans state.

This photophysical characterization informs the use of RGECIs in combination with optical stimulation, highlighting the importance of carefully controlling both blue and yellow light intensities to avoid photoswitching artifacts. In the future it would be interesting to carefully explore the dependence on blue wavelength, as many cis-trans isomerizations are differently dependent on 488 and 405 nm light[315]. Finally, this work suggests an avenue for engineering of future RGECIs: though the decreased photoswitching of jRGECO1a-I76F comes with a 3-fold decrease in brightness (**Figure 51c**), compensatory mutations may be able to restore brightness while keeping the slower photoswitching kinetics.

Bibliography

1. Buzsáki, G. Large-scale recording of neuronal ensembles. *Nat. Neurosci.* **7,** 446–451 (2004).

2. Petersen, C. C. H. Whole-Cell Recording of Neuronal Membrane Potential during Behavior. *Neuron* **95,** 1266–1281 (2017).

3. Davie, J. T. *et al.* Dendritic patch-clamp recording. *Nat. Protoc.* **1,** 1235–1247 (2006).

4. Williams, S. R. Spatial compartmentalization and functional impact of conductance in pyramidal neurons. *Nat. Neurosci.* **7,** 961–967 (2004).

5. Walz, W. Perforated Patch-Clamp Technique. in *Patch-Clamp Applications and Protocols* 155–172 (Humana Press, 1995). doi:10.1385/0-89603-311-2:155

6. Jun, J. J. *et al.* Fully integrated silicon probes for high-density recording of neural activity. *Nature* **551,** 232–236 (2017).

7. Jiang, X., Wang, G., Lee, A. J., Stornetta, R. L. & Zhu, J. J. The organization of two new cortical interneuronal circuits. *Nat. Neurosci.* **16,** 210–218 (2013).

8. Wang, G. *et al.* An optogenetics- and imaging-assisted simultaneous multiple patch-clamp recording system for decoding complex neural circuits. *Nat. Protoc.* **10,** 397–412 (2015).

9. Jiang, X. *et al.* Principles of connectivity among morphologically defined cell types in adult neocortex. *Science* **350,** aac9462 (2015).

10. Markram, H. *et al.* Reconstruction and Simulation of Neocortical Microcircuitry. *Cell* **163,** 456–92 (2015).

11. Williams, R. W. Mapping Genes that Modulate Mouse Brain Development: A Quantitative Genetic Approach. in 21–49 (Springer, Berlin, Heidelberg, 2000). doi:10.1007/978-3-540-48002-0_2

12. Herculano-Houzel, S. The human brain in numbers: a linearly scaled-up primate brain. *Front. Hum. Neurosci.* **3,** 31 (2009).

13. Cohen, L. B., Keynes, R. D. & Hille, B. Light scattering and birefringence changes during nerve activity. *Nature* **218,** 438–441 (1968).

14. Braubach, O., Cohen, L. B. & Choi, Y. Historical overview and general methods of membrane potential imaging. in *Membrane Potential Imaging in the Nervous System and Heart* 3–26 (Springer, Cham, 2015). doi:10.1007/978-3-319-17641-3_1

15. Miller, E. W. Small molecule fluorescent voltage indicators for studying membrane potential. *Curr. Opin. Chem. Biol.* **33,** 74–80 (2016).

16. Loew, L. M., Bonneville, G. W. & Surow, J. Charge shift optical probes of membrane potential. Theory. *Biochemistry* **17,** 4065–4071 (1978).

17. Fluhler, E., Burnham, V. G. & Loew, L. M. Spectra, membrane binding, and potentiometric responses of new charge shift probes. *Biochemistry* **24,** 5749–5755 (1985).

18. Yan, P. *et al.* Palette of fluorinated voltage-sensitive hemicyanine dyes. *Proc. Natl. Acad. Sci. U. S. A.* **109,** 20443–8 (2012).

19. Kuhn, B. & Fromherz, P. Anellated Hemicyanine Dyes in a Neuron Membrane: Molecular Stark Effect and Optical Voltage Recording. *J. Phys. Chem. B* **107,** 7903–7913 (2003).

20. Fromherz, P., Hübener, G., Kuhn, B. & Hinner, M. J. ANNINE-6plus, a voltage-sensitive dye with good solubility, strong membrane binding and high sensitivity. *Eur. Biophys. J.* **37,** 509–14 (2008).

21. Shoham, D. *et al.* Imaging Cortical Dynamics at High Spatial and Temporal Resolution with Novel Blue Voltage-Sensitive Dyes. *Neuron* **24,** 791–802 (1999).

22. Lebeuf, R., Férézou, I., Rossier, J., Arseniyadis, S. & Cossy, J. Straightforward Synthesis of the Near-Infrared Fluorescent Voltage-Sensitive Dye RH1691 and Analogues Thereof. *Org. Lett.* **11,** 4822–4825 (2009).

23. Bradley, J., Luo, R., Otis, T. S. & DiGregorio, D. A. Submillisecond Optical Reporting of Membrane Potential In Situ Using a Neuronal Tracer Dye. *J. Neurosci.* **29,** 9197–9209 (2009).

24. González, J. E. & Tsien, R. Y. Improved indicators of cell membrane potential that use fluorescence resonance energy transfer. *Chem. Biol.* **4,** 269–277 (1997).

25. Fernández, J. M., Taylor, R. E. & Bezanilla, F. Induced capacitance in the squid giant axon. Lipophilic ion displacement currents. *J. Gen. Physiol.* **82,** 331–46 (1983).

26. Miller, E. W. *et al.* Optically monitoring voltage in neurons by photo-induced electron transfer through molecular wires. *Proc. Natl. Acad. Sci. U. S. A.* **109,** 2114–9 (2012).

27. Woodford, C. R. *et al.* Improved PeT Molecules for Optically Sensing Voltage in Neurons. *J. Am. Chem. Soc.* **137,** 1817–1824 (2015).

28. Huang, Y.-L., Walker, A. S. & Miller, E. W. A Photostable Silicon Rhodamine Platform for Optical Voltage Sensing. *J. Am. Chem. Soc.* **137,** 10767–10776 (2015).

29. Kulkarni, R. U. *et al.* A Rationally Designed, General Strategy for Membrane Orientation of Photoinduced Electron Transfer-Based Voltage-Sensitive Dyes. *ACS Chem. Biol.* **12,** 407–413 (2017).

30. Kulkarni, R. U. *et al.* Voltage-sensitive rhodol with enhanced two-photon brightness. *Proc. Natl. Acad. Sci. U. S. A.* **114,** 2813–2818 (2017).

31. Gandolfi, D., Mapelli, J. & D'Angelo, E. Long-Term Spatiotemporal Reconfiguration of Neuronal Activity Revealed by Voltage-Sensitive Dye Imaging in the Cerebellar Granular Layer. *Neural Plast.* **2015,** 284986 (2015).

32. Popovic, M. A., Carnevale, N., Rozsa, B. & Zecevic, D. Electrical behaviour of dendritic spines as revealed by voltage imaging. *Nat. Commun.* **6,** 8436 (2015).

33. Brown, J. E. *et al.* Rapid changes in intracellular free calcium concentration. Detection by metallochromic indicator dyes in squid giant axon. *Biophys. J.* **15,** 1155–1160 (1975).

34. Thomas, M. V. Arsenazo III forms 2:1 complexes with Ca and 1:1 complexes with Mg under physiological conditions. Estimates of the apparent dissociation constants. *Biophys. J.* **25,** 541–8 (1979).

35. Tsien, R. Y. New calcium indicators and buffers with high selectivity against magnesium and protons: design, synthesis, and properties of prototype structures. *Biochemistry* **19,** 2396–2404 (1980).

36. Grynkiewicz, G., Poenie, M. & Tsien, R. Y. A new generation of Ca2+ indicators with greatly improved fluorescence properties. *J. Biol. Chem.* **260,** 3440–50 (1985).

37. Gee, K. R. *et al.* Chemical and physiological characterization of fluo-4 Ca2+-indicator dyes. *Cell Calcium* **27,** 97–106 (2000).

38. Connor, J. A. Digital imaging of free calcium changes and of spatial gradients in growing processes in single, mammalian central nervous system cells. *Proc. Natl. Acad. Sci. U. S. A.* **83,** 6179–83 (1986).

39. Williams, D. A. Quantitative intracellular calcium imaging with laser-scanning confocal microscopy. *Cell Calcium* **11,** 589–597 (1990).

40. Denk, W. *et al.* Anatomical and functional imaging of neurons using 2-photon laser scanning microscopy. *J. Neurosci. Methods* **54,** 151–162 (1994).

41. Garaschuk, O., Linn, J., Eilers, J. & Konnerth, A. Large-scale oscillatory calcium waves in the immature cortex. *Nat. Neurosci.* **3,** 452–459 (2000).

42. Stosiek, C., Garaschuk, O., Holthoff, K. & Konnerth, A. In vivo two-photon calcium imaging of neuronal networks. *Proc. Natl. Acad. Sci. U. S. A.* **100,** 7319–24 (2003).

43. Kaplitt, M. G. *et al.* Long-term gene expression and phenotypic correction using adeno-associated virus vectors in the mammalian brain. *Nat. Genet.* **8,** 148–154 (1994).

44. Heintz, N. Bac to the future: The use of bac transgenic mice for neuroscience research. *Nat. Rev. Neurosci.* **2,** 861–870 (2001).

45. Soriano, P. Generalized lacZ expression with the ROSA26 Cre reporter strain. *Nat. Genet.* **21,** 70–71 (1999).

46. Lin, M. Z. & Schnitzer, M. J. Genetically encoded indicators of neuronal activity. *Nat. Neurosci.* **19,** 1142–53 (2016).

47. Shimomura, O., Johnson, F. H. & Saiga, Y. Extraction, Purification and Properties of Aequorin, a Bioluminescent Protein from the Luminous Hydromedusan,Aequorea. *J. Cell. Comp. Physiol.* **59,** 223–239 (1962).

48. Hastings, J. W., Mitchell, G., Mattingly, P. H., Blinks, J. R. & Van Leeuwen, M. Response of aequorin bioluminescence to rapid changes in calcium concentration. *Nature* **222,** 1047–1050 (1969).

49. Moisescu, D. G., Ashley, C. C. & Campbell, A. K. Comparative aspects of the calcium-sensitive photoproteins aequorin and obelin. *Biochim. Biophys. Acta - Bioenerg.* **396,** 133–140 (1975).

50. Blinks, J. R., Prendergast, F. G. & Allen, D. G. Photoproteins as biological calcium indicators. *Pharmacol. Rev.* **28,** 1–93 (1976).

51. Miyawaki, A. *et al.* Fluorescent indicators for Ca2+based on green fluorescent proteins and calmodulin. *Nature* **388,** 882–887 (1997).

52. Baird, G. S., Zacharias, D. A. & Tsien, R. Y. Circular permutation and receptor insertion within green fluorescent proteins. *Proc. Natl. Acad. Sci. U. S. A.* **96,** 11241–6

(1999).

53. Chen, T.-W. *et al.* Ultrasensitive fluorescent proteins for imaging neuronal activity. *Nature* **499,** 295–300 (2013).

54. Ataka, K. & Pieribone, V. A. A Genetically Targetable Fluorescent Probe of Channel Gating with Rapid Kinetics. *Biophys. J.* **82,** 509–516 (2002).

55. Siegel, M. S. & Isacoff, E. Y. A Genetically Encoded Optical Probe of Membrane Voltage. *Neuron* **19,** 735–741 (1997).

56. Baker, B. J. *et al.* Three fluorescent protein voltage sensors exhibit low plasma membrane expression in mammalian cells. *J. Neurosci. Methods* **161,** 32–38 (2007).

57. Sakai, R., Repunte-Canonigo, V., Raj, C. D. & Knöpfel, T. Design and characterization of a DNA-encoded, voltage-sensitive fluorescent protein. *Eur. J. Neurosci.* **13,** 2314–2318 (2001).

58. Dimitrov, D. *et al.* Engineering and Characterization of an Enhanced Fluorescent Protein Voltage Sensor. *PLoS One* **2,** e440 (2007).

59. Mutoh, H. *et al.* Spectrally-Resolved Response Properties of the Three Most Advanced FRET Based Fluorescent Protein Voltage Probes. *PLoS One* **4,** e4555 (2009).

60. Lundby, A., Mutoh, H., Dimitrov, D., Akemann, W. & Knöpfel, T. Engineering of a Genetically Encodable Fluorescent Voltage Sensor Exploiting Fast Ci-VSP Voltage-Sensing Movements. *PLoS One* **3,** e2514 (2008).

61. Peron, S. P., Freeman, J., Iyer, V., Guo, C. & Svoboda, K. A Cellular Resolution Map of Barrel Cortex Activity during Tactile Behavior. *Neuron* **86,** 783–799 (2015).

62. Lam, A. J. *et al.* Improving FRET dynamic range with bright green and red fluorescent proteins. *Nat. Methods* **9,** 1005–1012 (2012).

63. Gautam, S. G., Perron, A., Mutoh, H. & Knopfel, T. Exploration of fluorescent protein voltage probes based on circularly permuted fluorescent proteins. *Front. Neuroeng.* **2,** 14 (2009).

64. Barnett, L., Platisa, J., Popovic, M., Pieribone, V. A. & Hughes, T. A fluorescent, genetically-encoded voltage probe capable of resolving action potentials. *PLoS One* **7,** e43454 (2012).

65. Tsutsui, H. *et al.* Improved detection of electrical activity with a voltage probe based on a voltage-sensing phosphatase. *J. Physiol.* **591,** 4427–4437 (2013).

66. Tsutsui, H., Karasawa, S., Okamura, Y. & Miyawaki, A. Improving membrane voltage measurements using FRET with new fluorescent proteins. *Nat. Methods* **5,** 683–685 (2008).

67. Akemann, W. *et al.* Imaging neural circuit dynamics with a voltage-sensitive fluorescent protein. *J. Neurophysiol.* **108,** 2323–2337 (2012).

68. Sung, U. *et al.* Developing Fast Fluorescent Protein Voltage Sensors by Optimizing FRET Interactions. *PLoS One* **10,** e0141585 (2015).

69. Akemann, W., Mutoh, H., Perron, A., Rossier, J. & Knöpfel, T. Imaging brain electric signals with genetically targeted voltage-sensitive fluorescent proteins. *Nat. Methods* **7,** 643–649 (2010).

70. Kralj, J. M., Hochbaum, D. R., Douglass, A. D. & Cohen, A. E. Electrical spiking in Escherichia coli probed with a fluorescent voltage-indicating protein. *Science* **333,** 345–8 (2011).

71. Kralj, J. M., Douglass, A. D., Hochbaum, D. R., Maclaurin, D. & Cohen, A. E. Optical recording of action potentials in mammalian neurons using a microbial rhodopsin. *Nat Methods* **9,** 90–95 (2012).

72. Jin, L. *et al.* Single Action Potentials and Subthreshold Electrical Events Imaged in Neurons with a Fluorescent Protein Voltage Probe. *Neuron* **75,** 779–785 (2012).

73. Ellis-Davies, G. C. R. Caged compounds: photorelease technology for control of cellular chemistry and physiology. *Nat. Methods* **4,** 619–28 (2007).

74. Shepherd, G. M. G. Circuit mapping by ultraviolet uncaging of glutamate. *Cold Spring Harb. Protoc.* **2012,** 998–1004 (2012).

75. Banghart, M., Borges, K., Isacoff, E., Trauner, D. & Kramer, R. H. Light-activated ion channels for remote control of neuronal firing. *Nat. Neurosci.* **7,** 1381–1386 (2004).

76. Boyden, E. S., Zhang, F., Bamberg, E., Nagel, G. & Deisseroth, K. Millisecond-timescale, genetically targeted optical control of neural activity. *Nat. Neurosci.* **8,** 1263–1268 (2005).

77. Zemelman, B. V. B. V. *et al.* Selective Photostimulation of Genetically ChARGed Neurons. *Neuron* **33,** 15–22 (2002).

78. Berndt, A. *et al.* High-efficiency channelrhodopsins for fast neuronal stimulation at low light levels. *Proc. Natl. Acad. Sci.* **108,** 7595–7600 (2011).

79. Kleinlogel, S. *et al.* Ultra light-sensitive and fast neuronal activation with the Ca2+-permeable channelrhodopsin CatCh. *Nat. Neurosci.* **14,** 513–518 (2011).

80. Nagel, G. *et al.* Light Activation of Channelrhodopsin-2 in Excitable Cells of Caenorhabditis elegans Triggers Rapid Behavioral Responses. *Curr. Biol.* **15,** 2279–2284 (2005).

81. Gunaydin, L. A. *et al.* Ultrafast optogenetic control. *Nat. Neurosci.* **13,** 387–392 (2010).

82. Lin, J. Y., Lin, M. Z., Steinbach, P. & Tsien, R. Y. Characterization of Engineered Channelrhodopsin Variants with Improved Properties and Kinetics. *Biophys. J.* **96,** 1803–1814 (2009).

83. Wang, H. *et al.* Molecular Determinants Differentiating Photocurrent Properties of Two Channelrhodopsins from *Chlamydomonas*. *J. Biol. Chem.* **284,** 5685–5696 (2009).

84. Yizhar, O. *et al.* Neocortical excitation/inhibition balance in information processing and social dysfunction. *Nature* **477,** 171–178 (2011).

85. Lin, J. Y., Knutsen, P. M., Muller, A., Kleinfeld, D. & Tsien, R. Y. ReaChR: a red-shifted variant of channelrhodopsin enables deep transcranial optogenetic excitation. *Nat. Neurosci.* **16,** 1499–1508 (2013).

86. Klapoetke, N. C. *et al.* Independent optical excitation of distinct neural populations. *Nat. Methods* **11,** 338–46 (2014).

87. Zhang, F. *et al.* Red-shifted optogenetic excitation: a tool for fast neural control derived from Volvox carteri. *Nat. Neurosci.* **11,** 631–3 (2008).

88. Chow, B. Y. *et al.* High-performance genetically targetable optical neural silencing by light-driven proton pumps. *Nature* **463,** 98–102 (2010).

89. Han, X. & Boyden, E. S. Multiple-Color Optical Activation, Silencing, and Desynchronization of Neural Activity, with Single-Spike Temporal Resolution. *PLoS One* **2,** e299 (2007).

90. Zhang, F. *et al.* Multimodal fast optical interrogation of neural circuitry. *Nature* **446,** 633–639 (2007).

91. Chuong, A. S. *et al.* Noninvasive optical inhibition with a red-shifted microbial rhodopsin. *Nat. Neurosci.* **17,** 1123–1129 (2014).

92. Wietek, J. *et al.* Conversion of Channelrhodopsin into a Light-Gated Chloride Channel. *Science (80-.).* **344,** 409–412 (2014).

93. Wietek, J. *et al.* An improved chloride-conducting channelrhodopsin for light-induced inhibition of neuronal activity in vivo. *Sci. Rep.* **5,** 14807 (2015).

94. Govorunova, E. G., Sineshchekov, O. A., Janz, R., Liu, X. & Spudich, J. L. Natural light-gated anion channels: A family of microbial rhodopsins for advanced optogenetics. *Science (80-.).* **349,** 647–650 (2015).

95. Govorunova, E. G., Sineshchekov, O. A. & Spudich, J. L. *Proteomonas sulcata* ACR1: A Fast Anion Channelrhodopsin. *Photochem. Photobiol.* **92,** 257–263 (2016).

96. Govorunova, E. G. *et al.* The Expanding Family of Natural Anion Channelrhodopsins Reveals Large Variations in Kinetics, Conductance, and Spectral Sensitivity. *Sci. Rep.* **7,** 43358 (2017).

97. Cosentino, C. *et al.* Engineering of a light-gated potassium channel. *Science (80-.).* **348,** 707–710 (2015).

98. Kim, C. K., Adhikari, A. & Deisseroth, K. Integration of optogenetics with complementary methodologies in systems neuroscience. *Nat. Rev. Neurosci.* **18,** 222–235 (2017).

99. Deisseroth, K. Optogenetics: 10 years of microbial opsins in neuroscience. *Nat. Neurosci.* **18,** 1213–1225 (2015).

100. Pettit, D. L., Wang, S. S.-H., Gee, K. R. & Augustine, G. J. Chemical Two-Photon Uncaging: a Novel Approach to Mapping Glutamate Receptors. *Neuron* **19,** 465–471 (1997).

101. Jaafari, N. *et al.* Combining Membrane Potential Imaging with Other Optical Techniques. in 103–125 (Springer, Cham, 2015). doi:10.1007/978-3-319-17641-3_4

102. Bloodgood, B. L. & Sabatini, B. L. Nonlinear regulation of unitary synaptic signals by CaV(2.3) voltage-sensitive calcium channels located in dendritic spines. *Neuron* **53,** 249–60 (2007).

103. Nikolenko, V., Poskanzer, K. E. & Yuste, R. Two-photon photostimulation and imaging of neural circuits. *Nat. Methods* **4,** 943–950 (2007).

104. Crocini, C., Ferrantini, C., Pavone, F. S. & Sacconi, L. Optogenetics gets to the heart: A guiding light beyond defibrillation. *Prog. Biophys. Mol. Biol.* **130,** 132–139 (2017).

105. Airan, R. D. *et al.* High-Speed Imaging Reveals Neurophysiological links to Behavior

in an Animal Model of Depression. *Science (80-.).* **317,** 819–823 (2007).

106. Lim, D. H. *et al.* In vivo Large-Scale Cortical Mapping Using Channelrhodopsin-2 Stimulation in Transgenic Mice Reveals Asymmetric and Reciprocal Relationships between Cortical Areas. *Front. Neural Circuits* **6,** 11 (2012).

107. Shipley, F. B., Clark, C. M., Alkema, M. J. & Leifer, A. M. Simultaneous optogenetic manipulation and calcium imaging in freely moving C. elegans. *Front. Neural Circuits* **8,** 28 (2014).

108. Petreanu, L., Mao, T., Sternson, S. M. & Svoboda, K. The subcellular organization of neocortical excitatory connections. *Nature* **457,** 1142–5 (2009).

109. Peron, S. & Svoboda, K. From cudgel to scalpel: toward precise neural control with optogenetics. *Nat. Methods* **8,** 30–34 (2011).

110. Scanziani, M. & Häusser, M. Electrophysiology in the age of light. *Nature* **461,** 930–939 (2009).

111. Boulting, G. L. *et al.* A functionally characterized test set of human induced pluripotent stem cells. *Nat. Biotechnol.* **29,** 279–286 (2011).

112. Maclaurin, D., Venkatachalam, V., Lee, H. & Cohen, A. E. Mechanism of voltage-sensitive fluorescence in a microbial rhodopsin. *Proc. Natl. Acad. Sci.* **110,** 5939–5944 (2013).

113. Gong, Y., Li, J. Z. & Schnitzer, M. J. Enhanced Archaerhodopsin Fluorescent Protein Voltage Indicators. *PLoS One* **8,** e66959 (2013).

114. Mattis, J. *et al.* Principles for applying optogenetic tools derived from direct comparative analysis of microbial opsins. *Nat. Methods* **9,** 159–72 (2012).

115. Bean, B. P. The action potential in mammalian central neurons. *Nat. Rev. Neurosci.* **8,** 451–65 (2007).

116. Schoenenberger, P., Grunditz, Å., Rose, T. & Oertner, T. G. Optimizing the spatial resolution of Channelrhodopsin-2 activation. *Brain Cell Biol.* **36,** 119–127 (2008).

117. Johnson, M. T. J. *et al.* Evaluating Methods for Isolating Total RNA and Predicting the Success of Sequencing Phylogenetically Diverse Plant Transcriptomes. *PLoS One* **7,** e50226 (2012).

118. Melkonian, M. & Preisig, H. R. A light and electron microscopic study of Scherffelia dubia, a new member of the scaly green flagellates (Prasinophyceae). *Nord. J. Bot.* **6,** 235–256 (1986).

119. Lin, J. Y., Lin, M. Z., Steinbach, P. & Tsien, R. Y. Characterization of Engineered Channelrhodopsin Variants with Improved Properties and Kinetics. *Biophys. J.* **96,** 1803–1814 (2009).

120. Takahashi, H. *et al.* Light-addressed single-neuron stimulation in dissociated neuronal cultures with sparse expression of ChR2. *Biosystems* **107,** 106–112 (2012).

121. Fitzsimonds, R. M., Song, H. & Poo, M. Propagation of activity-dependent synaptic depression in simple neural networks. *Nature* **388,** 439–448 (1997).

122. Foust, A., Popovic, M., Zecevic, D. & McCormick, D. A. Action Potentials Initiate in the Axon Initial Segment and Propagate through Axon Collaterals Reliably in

Cerebellar Purkinje Neurons. *J. Neurosci.* **30,** 6891–6902 (2010).

123. Popovic, M. A., Foust, A. J., McCormick, D. A. & Zecevic, D. The spatio-temporal characteristics of action potential initiation in layer 5 pyramidal neurons: a voltage imaging study. *J. Physiol.* **589,** 4167–4187 (2011).

124. Kole, M. H. P. & Stuart, G. J. Signal Processing in the Axon Initial Segment. *Neuron* **73,** 235–247 (2012).

125. Turrigiano, G., Abbott, L. F. & Marder, E. Activity-dependent changes in the intrinsic properties of cultured neurons. *Science* **264,** 974–7 (1994).

126. Desai, N. S., Rutherford, L. C. & Turrigiano, G. G. Plasticity in the intrinsic excitability of cortical pyramidal neurons. *Nat. Neurosci.* **2,** 515–520 (1999).

127. Grubb, M. S. & Burrone, J. Activity-dependent relocation of the axon initial segment fine-tunes neuronal excitability. *Nature* **465,** 1070–1074 (2010).

128. Lambo, M. E. & Turrigiano, G. G. Synaptic and Intrinsic Homeostatic Mechanisms Cooperate to Increase L2/3 Pyramidal Neuron Excitability during a Late Phase of Critical Period Plasticity. *J. Neurosci.* **33,** 8810–8819 (2013).

129. Trounson, A., Shepard, K. A. & DeWitt, N. D. Human disease modeling with induced pluripotent stem cells. *Curr. Opin. Genet. Dev.* **22,** 509–516 (2012).

130. Shcheglovitov, A. *et al.* SHANK3 and IGF1 restore synaptic deficits in neurons from 22q13 deletion syndrome patients. *Nature* **503,** 267–271 (2013).

131. Cao, G. *et al.* Genetically Targeted Optical Electrophysiology in Intact Neural Circuits. *Cell* **154,** 904–913 (2013).

132. Huys, Q. J. M., Ahrens, M. B. & Paninski, L. Efficient Estimation of Detailed Single-Neuron Models. *J. Neurophysiol.* **96,** 872–890 (2006).

133. Williams, J. C. *et al.* Computational Optogenetics: Empirically-Derived Voltage- and Light-Sensitive Channelrhodopsin-2 Model. *PLoS Comput. Biol.* **9,** e1003220 (2013).

134. Hou, J. H., Venkatachalam, V. & Cohen, A. E. Temporal Dynamics of Microbial Rhodopsin Fluorescence Reports Absolute Membrane Voltage. *Biophys. J.* **106,** 639–648 (2014).

135. Wainger, B. J. *et al.* Intrinsic Membrane Hyperexcitability of Amyotrophic Lateral Sclerosis Patient-Derived Motor Neurons. *Cell Rep.* **7,** 1–11 (2014).

136. Higurashi, N. *et al.* A human Dravet syndrome model from patient induced pluripotent stem cells. *Mol. Brain* **6,** 19 (2013).

137. Badger, J. L., Cordero-Llana, O., Hartfield, E. M. & Wade-Martins, R. Parkinson's disease in a dish – Using stem cells as a molecular tool. *Neuropharmacology* **76,** 88–96 (2014).

138. Marchetto, M. C. N. *et al.* A Model for Neural Development and Treatment of Rett Syndrome Using Human Induced Pluripotent Stem Cells. *Cell* **143,** 527–539 (2010).

139. Auerbach, B. D., Osterweil, E. K. & Bear, M. F. Mutations causing syndromic autism define an axis of synaptic pathophysiology. *Nature* **480,** 63–68 (2011).

140. Zhao, H., Giver, L., Shao, Z., Affholter, J. A. & Arnold, F. H. Molecular evolution by

staggered extension process (StEP) in vitro recombination. *Nat. Biotechnol.* **16,** 258–261 (1998).

141. Zhao, Y. *et al.* An expanded palette of genetically encoded Ca^{2+} indicators. *Science* **333,** 1888–91 (2011).

142. Lanyi, J. K. Proton translocation mechanism and energetics in the light-driven pump bacteriorhodopsin. *Biochim. Biophys. Acta* **1183,** 241–61 (1993).

143. Lanyi, J. K. Bacteriorhodopsin. *Annu. Rev. Physiol.* **66,** 665–688 (2004).

144. Kolodner, P., Lukashev, E. P., Ching, Y. C. & Rousseau, D. L. Electric-field-induced Schiff-base deprotonation in D85N mutant bacteriorhodopsin. *Proc. Natl. Acad. Sci. U. S. A.* **93,** 11618–21 (1996).

145. Ma, D. *et al.* Role of ER Export Signals in Controlling Surface Potassium Channel Numbers. *Science (80-.).* **291,** 316–319 (2001).

146. Gradinaru, V. *et al.* Molecular and Cellular Approaches for Diversifying and Extending Optogenetics. *Cell* **141,** 154–165 (2010).

147. Kirkton, R. D. & Bursac, N. Engineering biosynthetic excitable tissues from unexcitable cells for electrophysiological and cell therapy studies. *Nat. Commun.* **2,** 300 (2011).

148. Park, J. *et al.* Screening Fluorescent Voltage Indicators with Spontaneously Spiking HEK Cells. *PLoS One* **8,** e85221 (2013).

149. Pucihar, G., Kotnik, T. & Miklavčič, D. Measuring the Induced Membrane Voltage with Di-8-ANEPPS. *J. Vis. Exp.* (2009). doi:10.3791/1659

150. Enami, N. *et al.* Crystal Structures of Archaerhodopsin-1 and -2: Common Structural Motif in Archaeal Light-driven Proton Pumps. *J. Mol. Biol.* **358,** 675–685 (2006).

151. Barondeau, D. P., Putnam, C. D., Kassmann, C. J., Tainer, J. A. & Getzoff, E. D. Mechanism and energetics of green fluorescent protein chromophore synthesis revealed by trapped intermediate structures. *Proc. Natl. Acad. Sci.* **100,** 12111–12116 (2003).

152. McCarthy, K. D. & de Vellis, J. Preparation of separate astroglial and oligodendroglial cell cultures from rat cerebral tissue. *J. Cell Biol.* **85,** 890–902 (1980).

153. Banker, G. & Goslin, K. *Culturing nerve cells.* (MIT Press, 1998).

154. Chen, G., Harata, N. C. & Tsien, R. W. Paired-pulse depression of unitary quantal amplitude at single hippocampal synapses. *Proc. Natl. Acad. Sci.* **101,** 1063–1068 (2004).

155. Jiang, M. & Chen, G. High Ca2+-phosphate transfection efficiency in low-density neuronal cultures. *Nat. Protoc.* **1,** 695–700 (2006).

156. Stoppini, L., Buchs, P. A. & Muller, D. A simple method for organotypic cultures of nervous tissue. *J. Neurosci. Methods* **37,** 173–82 (1991).

157. Mukamel, E. A., Nimmerjahn, A. & Schnitzer, M. J. Automated Analysis of Cellular Signals from Large-Scale Calcium Imaging Data. *Neuron* **63,** 747–760 (2009).

158. Nagai, T., Sawano, A., Park, E. S. & Miyawaki, A. Circularly permuted green fluorescent proteins engineered to sense Ca2+. *Proc. Natl. Acad. Sci. U. S. A.* **98,** 3197–

202 (2001).

159. Nakai, J., Ohkura, M. & Imoto, K. A high signal-to-noise Ca2+ probe composed of a single green fluorescent protein. *Nat. Biotechnol.* **19,** 137–141 (2001).

160. St-Pierre, F. *et al.* High-fidelity optical reporting of neuronal electrical activity with an ultrafast fluorescent voltage sensor. *Nat. Neurosci.* **17,** 884–889 (2014).

161. Shu, X. *et al.* Mammalian expression of infrared fluorescent proteins engineered from a bacterial phytochrome. *Science* **324,** 804–7 (2009).

162. Alford, S. C., Wu, J., Zhao, Y., Campbell, R. E. & Knöpfel, T. Optogenetic reporters. *Biol. Cell* **105,** 14–29 (2013).

163. Murata, Y., Iwasaki, H., Sasaki, M., Inaba, K. & Okamura, Y. Phosphoinositide phosphatase activity coupled to an intrinsic voltage sensor. *Nature* **435,** 1239–1243 (2005).

164. Govorunova, E. G., Sineshchekov, O. A., Li, H., Janz, R. & Spudich, J. L. Characterization of a highly efficient blue-shifted channelrhodopsin from the marine alga platymonas subcordiformis. *J. Biol. Chem.* **288,** 29911–29922 (2013).

165. Wu, J. *et al.* Improved Orange and Red Ca $^{2+}$ Indicators and Photophysical Considerations for Optogenetic Applications. *ACS Chem. Neurosci.* **4,** 963–972 (2013).

166. Akerboom, J. *et al.* Genetically encoded calcium indicators for multi-color neural activity imaging and combination with optogenetics. *Front. Mol. Neurosci.* **6,** 2 (2013).

167. Wu, J. *et al.* A long Stokes shift red fluorescent Ca2+ indicator protein for two-photon and ratiometric imaging. *Nat. Commun.* **5,** 5262 (2014).

168. Wang, Q., Shui, B., Kotlikoff, M. I. & Sondermann, H. Structural Basis for Calcium Sensing by GCaMP2. *Structure* **16,** 1817–1827 (2008).

169. Cheng, Z. & Campbell, R. E. Assessing the Structural Stability of Designed β-Hairpin Peptides in the Cytoplasm of Live Cells. *ChemBioChem* **7,** 1147–1150 (2006).

170. Hochbaum, D. R. *et al.* All-optical electrophysiology in mammalian neurons using engineered microbial rhodopsins. *Nat. Methods* **11,** 825–33 (2014).

171. Zou, P. *et al.* Bright and fast multicoloured voltage reporters via electrochromic FRET. *Nat. Commun.* **5,** 4625 (2014).

172. Li, Q. *et al.* Structural mechanism of voltage-dependent gating in an isolated voltage-sensing domain. *Nat. Struct. Mol. Biol.* **21,** 244–252 (2014).

173. Han, Z. *et al.* Fluorescent Protein Voltage Probes Derived from ArcLight that Respond to Membrane Voltage Changes with Fast Kinetics. *PLoS One* **8,** e81295 (2013).

174. Brinks, D., Klein, A. J. & Cohen, A. E. Two-Photon Lifetime Imaging of Voltage Indicating Proteins as a Probe of Absolute Membrane Voltage. *Biophys. J.* **109,** 914–921 (2015).

175. De Simoni, A., Griesinger, C. B. & Edwards, F. A. Development of Rat CA1 Neurones in Acute *Versus* Organotypic Slices: Role of Experience in Synaptic Morphology and Activity. *J. Physiol.* **550,** 135–147 (2003).

176. Panaitescu, B. *et al.* Methylxanthines do not affect rhythmogenic preBötC inspiratory

network activity but impair bursting of preBötC-driven motoneurons. *Neuroscience* **255,** 158–176 (2013).

177. Cai, D., Cohen, K. B., Luo, T., Lichtman, J. W. & Sanes, J. R. Improved tools for the Brainbow toolbox. *Nat. Methods* **10,** 540–547 (2013).

178. Lewin, A., Mayer, M., Chusainow, J., Jacob, D. & Appel, B. Viral promoters can initiate expression of toxin genes introduced into Escherichia coli. *BMC Biotechnol.* **5,** 19 (2005).

179. Mullinax, R. L., Wong, D. T., Davis, H. A., Padgett, K. A. & Sorge, J. A. Dual-Expression Vectors for Efficient Protein Expression in Both E. coli and Mammalian Cells. in *E. coli Gene Expression Protocols* 19–30 (Humana Press, 2003). doi:10.1385/1-59259-301-1:19

180. Katayama, H., Yamamoto, A., Mizushima, N., Yoshimori, T. & Miyawaki, A. GFP-like Proteins Stably Accumulate in Lysosomes. *Cell Struct. Funct.* **33,** 1–12 (2008).

181. Emiliani, V., Cohen, A. E., Deisseroth, K. & Hausser, M. All-Optical Interrogation of Neural Circuits. *J. Neurosci.* **35,** 13917–13926 (2015).

182. Ronzitti, E. *et al.* Recent advances in patterned photostimulation for optogenetics. *J. Opt.* **19,** 113001 (2017).

183. Ahrens, M., Orger, M., Robson, D., Li, J. & Keller, P. Whole-brain functional imaging at cellular resolution using light-sheet microscopy. *Nat. Methods* (2013). doi:10.1038/NMETH.2434

184. Bouchard, M. B. *et al.* Swept confocally-aligned planar excitation (SCAPE) microscopy for high-speed volumetric imaging of behaving organisms. *Nat. Photonics* **9,** 113–119 (2015).

185. Prevedel, R. *et al.* Simultaneous whole-animal 3D imaging of neuronal activity using light-field microscopy. *Nat. Methods* **11,** 727–730 (2014).

186. Nadella, K. M. N. S. *et al.* Random access scanning microscopy for 3D imaging in awake behaving animals. *Nat. Methods* (2016). doi:10.1038/nMeth.4033

187. Szalay, G. *et al.* Fast 3D Imaging of Spine, Dendritic, and Neuronal Assemblies in Behaving Animals. *Neuron* **92,** 723–738 (2016).

188. Mertz, J. Optical sectioning microscopy with planar or structured illumination. *Nat. Methods* **8,** 811–819 (2011).

189. Neil, M. a, Juskaitis, R. & Wilson, T. Method of obtaining optical sectioning by using structured light in a conventional microscope. *Opt. Lett.* **22,** 1905–1907 (1997).

190. Thomas, B., Wolstenholme, A., Chaudhari, S. N., Kipreos, E. T. & Kner, P. Enhanced resolution through thick tissue with structured illumination and adaptive optics. *J. Biomed. Opt.* **20,** 26006 (2015).

191. Lim, D., Ford, T. N., Chu, K. K. & Mertz, J. Optically sectioned in vivo imaging with speckle illumination HiLo microscopy. *J. Biomed. Opt.* **16,** 16014 (2011).

192. Jost, A. *et al.* Optical Sectioning and High Resolution in Single-Slice Structured Illumination Microscopy by Thick Slice Blind-SIM Reconstruction. *PLoS One* **10,** e0132174 (2015).

193. Packer, A. M., Russell, L. E., Dalgleish, H. W. P. & Häusser, M. Simultaneous all-optical manipulation and recording of neural circuit activity with cellular resolution in vivo. *Nat. Methods* **12,** 140–6 (2015).

194. Rickgauer, J. P., Deisseroth, K. & Tank, D. W. Simultaneous cellular-resolution optical perturbation and imaging of place cell firing fields. *Nat. Neurosci.* **17,** 1816–24 (2014).

195. Carrillo-Reid, L., Yang, W., Bando, Y., Peterka, D. S. & Yuste, R. Imprinting Cortical Ensembles. *Science (80-.).* **353,** 691–4 (2016).

196. Inoue, M. *et al.* Rational design of a high-affinity, fast, red calcium indicator R-CaMP2. *Nat. Methods* **12,** 64–70 (2014).

197. Dana, H. *et al.* Sensitive red protein calcium indicators for imaging neural activity. *BioRxiv* **5,** 1–24 (2016).

198. Dunn, T. W. *et al.* Brain-wide mapping of neural activity controlling zebrafish exploratory locomotion. *Elife* **5,** e12741 (2016).

199. Freeman, J. *et al.* Mapping brain activity at scale with cluster computing. *Nat. Methods* **11,** 941–950 (2014).

200. Chhetri, R. K. *et al.* Whole-animal functional and developmental imaging with isotropic spatial resolution. *Nat. Methods* **12,** 1171–1178 (2015).

201. Bengtson, C. P., Freitag, H. E., Weislogel, J.-M. & Bading, H. Nuclear Calcium Sensors Reveal that Repetition of Trains of Synaptic Stimuli Boosts Nuclear Calcium Signaling in CA1 Pyramidal Neurons. *Biophys. J.* **99,** 4066–4077 (2010).

202. Eder, A. & Bading, H. Calcium signals can freely cross the nuclear envelope in hippocampal neurons: somatic calcium increases generate nuclear calcium transients. *BMC Neurosci.* **8,** 57 (2007).

203. Gunthorpe, M. J., Large, C. H. & Sankar, R. The mechanism of action of retigabine (ezogabine), a first-in-class K+ channel opener for the treatment of epilepsy. *Epilepsia* **53,** 412–424 (2012).

204. Saganich, M. J., Machado, E. & Rudy, B. Differential expression of genes encoding subthreshold-operating voltage-gated K+ channels in brain. *J. Neurosci.* **21,** 4609–24 (2001).

205. Petreanu, L., Huber, D., Sobczyk, A. & Svoboda, K. Channelrhodopsin-2-assisted circuit mapping of long-range callosal projections. *Nat. Neurosci.* **10,** 663–8 (2007).

206. Wu, Y.-W. *et al.* Input- and Cell-Type-Specific Endocannabinoid-Dependent LTD in the Striatum. *Cell Rep.* **10,** 75–87 (2015).

207. Ibrahim, L. A. *et al.* Cross-Modality Sharpening of Visual Cortical Processing through Layer-1-Mediated Inhibition and Disinhibition. *Neuron* **89,** 1031–1045 (2016).

208. Saunders, A., Johnson, C. & Sabatini, B. Novel recombinant adeno-associated viruses for Cre activated and inactivated transgene expression in neurons. *Front. Neural Circuits* **6,** 1–10 (2012).

209. Znamenskiy, P. & Zador, A. M. Corticostriatal neurons in auditory cortex drive decisions during auditory discrimination. *Nature* **497,** 482–485 (2013).

210. Tantama, M., Hung, Y. P. & Yellen, G. Optogenetic reporters. in *Progress in brain research*

196, 235–263 (2012).

211. Rust, M. J., Bates, M. & Zhuang, X. Sub-diffraction-limit imaging by stochastic optical reconstruction microscopy (STORM). *Nat. Methods* **3,** 793–796 (2006).

212. Dertinger, T., Colyer, R., Iyer, G., Weiss, S. & Enderlein, J. Fast, background-free, 3D super-resolution optical fluctuation imaging (SOFI). *Proc. Natl. Acad. Sci.* **106,** 22287–22292 (2009).

213. Sofroniew, N.J., Flickinger, D., King, J., Svoboda, K., Sofroniew, N. J., Flickinger, D., King, J. & Svoboda, K. A large field of view two-photon mesoscope with subcellular resolution for in vivo imaging. *Elife* **5,** 1–20 (2016).

214. Chan, K. Y. *et al.* Engineered AAVs for efficient noninvasive gene delivery to the central and peripheral nervous systems. *Nat. Neurosci.* **20,** 1172–1179 (2017).

215. Klein, S., Staring, M., Murphy, K., Viergever, M. A. & Pluim, J. elastix: A Toolbox for Intensity-Based Medical Image Registration. *IEEE Trans. Med. Imaging* **29,** 196–205 (2010).

216. Kralj, J., Hochbaum, D., Douglass, A. & Cohen, A. Electrical Spiking in Escherichia coli. *Science (80-.).* **333,** 345–348 (2011).

217. Flytzanis, N. C. *et al.* Archaerhodopsin variants with enhanced voltage-sensitive fluorescence in mammalian and Caenorhabditis elegans neurons. *Nat. Commun.* **5,** 4894 (2014).

218. Mcisaac, R. S. *et al.* Directed evolution of a far-red fluorescent rhodopsin. *Proc. Natl. Acad. Sci.* **111,** 13034–13039 (2014).

219. Adam, Y. *et al.* All-optical electrophysiology reveals brain-state dependent changes in hippocampal subthreshold dynamics and excitability. *bioRxiv* 281618 (2018). doi:10.1101/281618

220. Piatkevich, K. D. *et al.* A robotic multidimensional directed evolution approach applied to fluorescent voltage reporters. *Nat. Chem. Biol.* 1 (2018). doi:10.1038/s41589-018-0004-9

221. Lou, S. *et al.* Genetically Targeted All-Optical Electrophysiology with a Transgenic Cre-Dependent Optopatch Mouse. *J. Neurosci.* **36,** 11059–11073 (2016).

222. Chien, M.-P. *et al.* Two-photon photoactivated voltage imaging in tissue with an Archaerhodopsin-derived reporter. *bioRxiv* 211946 (2017). doi:10.1101/211946

223. Gong, Y., Wagner, M. J., Zhong Li, J. & Schnitzer, M. J. Imaging neural spiking in brain tissue using FRET-opsin protein voltage sensors. *Nat. Commun.* **5,** 3674 (2014).

224. Gong, Y. *et al.* High-speed recording of neural spikes in awake mice and flies with a fluorescent voltage sensor. *Science* **350,** 1361–6 (2015).

225. Piao, H. H., Rajakumar, D., Kang, B. E., Kim, E. H. & Baker, B. J. Combinatorial mutagenesis of the voltage-sensing domain enables the optical resolution of action potentials firing at 60 Hz by a genetically encoded fluorescent sensor of membrane potential. *J. Neurosci.* **35,** 372–85 (2015).

226. Lee, S. *et al.* Improving a genetically encoded voltage indicator by modifying the cytoplasmic charge composition. *Sci. Rep.* **7,** 8286 (2017).

227. Baker, B. J. *et al.* Genetically encoded fluorescent voltage sensors using the voltage-sensing domain of Nematostella and Danio phosphatases exhibit fast kinetics. *J. Neurosci. Methods* **208,** 190–196 (2012).

228. Yang, H. H. *et al.* Subcellular Imaging of Voltage and Calcium Signals Reveals Neural Processing In Vivo. *Cell* **166,** 1–13 (2016).

229. Chamberland, S. *et al.* Fast two-photon imaging of subcellular voltage dynamics in neuronal tissue with genetically encoded indicators. *Elife* **6,** e25690 (2017).

230. Abdelfattah, A. S., Rancic, V., Rawal, B., Ballanyi, K. & Campbell, R. E. Ratiometric and photoconvertible fluorescent protein-based voltage indicator prototypes. *Chem. Commun.* **52,** 14153–14156 (2016).

231. Kost, L. A. *et al.* Insertion of the voltage-sensitive domain into circularly permuted red fluorescent protein as a design for genetically encoded voltage sensor. *PLoS One* **12,** e0184225 (2017).

232. Willadt, S., Canepari, M., Yan, P., Loew, L. M. & Vogt, K. E. Combined optogenetics and voltage sensitive dye imaging at single cell resolution. *Front. Cell. Neurosci.* **8,** 311 (2014).

233. Popovic, M. a, Gao, X., Carnevale, N. T. & Zecevic, D. Cortical dendritic spine heads are not electrically isolated by the spine neck from membrane potential signals in parent dendrites. *Cereb. Cortex* **24,** 385–95 (2014).

234. Acker, C. D., Hoyos, E. & Loew, L. M. EPSPs Measured in Proximal Dendritic Spines of Cortical Pyramidal Neurons. *eNeuro* **3,** ENEURO.0050-15.2016 (2016).

235. Lo, S. Q., Koh, D. X. P., Sng, J. C. G. & Augustine, G. J. All-optical mapping of barrel cortex circuits based on simultaneous voltage-sensitive dye imaging and channelrhodopsin-mediated photostimulation. *Neurophotonics* **2,** 21013 (2015).

236. Lim, D. H., LeDue, J. M., Mohajerani, M. H. & Murphy, T. H. Optogenetic mapping after stroke reveals network-wide scaling of functional connections and heterogeneous recovery of the peri-infarct. *J. Neurosci.* **34,** 16455–66 (2014).

237. Gonzalez, J. E. & Tsien, R. Y. Voltage Sensing by Fluorescence Resonance Energy Transfer in Single Cells. *Biophys. J.* **69,** 1272–1280 (1995).

238. Chanda, B. *et al.* A hybrid approach to measuring electrical activity in genetically specified neurons. *Nat. Neurosci.* **8,** 1619–1626 (2005).

239. Wang, D., Zhang, Z., Chanda, B. & Jackson, M. B. Improved probes for hybrid voltage sensor imaging. *Biophys. J.* **99,** 2355–65 (2010).

240. Xu, Y. *et al.* Hybrid Indicators for Fast and Sensitive Voltage Imaging. *Angew. Chemie Int. Ed.* (2018). doi:10.1002/anie.201712614

241. Ng, D. N. & Fromherz, P. Genetic Targeting of a Voltage-Sensitive Dye by Enzymatic Activation of Phosphonooxymethyl-ammonium Derivative. *ACS Chem. Biol.* **6,** 444–451 (2011).

242. Liu, P., Grenier, V., Hong, W., Muller, V. R. & Miller, E. W. Fluorogenic Targeting of Voltage-Sensitive Dyes to Neurons. *J. Am. Chem. Soc.* **139,** 17334–17340 (2017).

243. Inagaki, S. *et al.* Genetically encoded bioluminescent voltage indicator for multi-purpose use in wide range of bioimaging. *Sci. Rep.* **7,** 42398 (2017).

244. Nagel, G. *et al.* Channelrhodopsin-2, a directly light-gated cation-selective membrane channel. *Proc. Natl. Acad. Sci. U. S. A.* **100,** 13940–5 (2003).

245. Guo, Z. V, Hart, A. C. & Ramanathan, S. Optical interrogation of neural circuits in Caenorhabditis elegans. *Nat. Methods* **6,** 891–896 (2009).

246. Szabo, V., Ventalon, C., De Sars, V., Bradley, J. & Emiliani, V. Spatially selective holographic photoactivation and functional fluorescence imaging in freely behaving mice with a fiberscope. *Neuron* **84,** 1157–69 (2014).

247. Grosenick, L., Marshel, J. H. & Deisseroth, K. Closed-loop and activity-guided optogenetic control. *Neuron* **86,** 106–39 (2015).

248. Kim, C. K. *et al.* Simultaneous fast measurement of circuit dynamics at multiple sites across the mammalian brain. *Nat. Methods* **13,** 325–328 (2016).

249. Chang, Y.-F., Arai, Y. & Nagai, T. Optogenetic activation during detector 'dead time' enables compatible real-time fluorescence imaging. *Neurosci. Res.* **73,** 341–347 (2012).

250. Ohkura, M., Sasaki, T., Kobayashi, C., Ikegaya, Y. & Nakai, J. An Improved Genetically Encoded Red Fluorescent Ca2+ Indicator for Detecting Optically Evoked Action Potentials. *PLoS One* **7,** e39933 (2012).

251. Shen, Y. *et al.* A genetically encoded Ca2+ indicator based on circularly permutated sea anemone red fluorescent protein eqFP578. *BMC Biol.* **16,** 9 (2018).

252. Venkatachalam, V. & Cohen, A. E. Imaging GFP-based reporters in neurons with multiwavelength optogenetic control. *Biophys. J.* **107,** 1554–63 (2014).

253. Fosque, B. F. *et al.* Labeling of active neural circuits in vivo with designed calcium integrators. *Science (80-.).* **347,** 755–760 (2015).

254. Zolnik, T. A. *et al.* All-optical functional synaptic connectivity mapping in acute brain slices using CaMPARI. *J. Physiol.* 1–37 (2016). doi:10.1113/JP273116.This

255. Wang, W. *et al.* A light- and calcium-gated transcription factor for imaging and manipulating activated neurons. *Nat. Biotechnol.* **35,** 864–871 (2017).

256. Rickgauer, J. P. & Tank, D. W. Two-photon excitation of channelrhodopsin-2 at saturation. *Proc. Natl. Acad. Sci. U. S. A.* **106,** 15025–30 (2009).

257. Wilson, N. R., Runyan, C. A., Wang, F. L. & Sur, M. Division and subtraction by distinct cortical inhibitory networks in vivo. *Nature* **488,** 343–348 (2012).

258. Wilson, N. R. *et al.* Two-way communication with neural networks in vivo using focused light. *Nat. Protoc.* **8,** 1184–1203 (2013).

259. Ju, N., Jiang, R., Macknik, S. L., Martinez-Conde, S. & Tang, S. Long-term all-optical interrogation of cortical neurons in awake-behaving non-human primates. *bio*R*xiv* 274308 (2018). doi:10.1101/274308

260. Prakash, R. *et al.* Two-photon optogenetic toolbox for fast inhibition, excitation and bistable modulation. *Nat. Methods* **9,** 1171–9 (2012).

261. Zhu, G., van Howe, J., Durst, M., Zipfel, W. & Xu, C. Simultaneous spatial and temporal focusing of femtosecond pulses. *Opt. Express* **13,** 2153 (2005).

262. Papagiakoumou, E. *et al.* Scanless two-photon excitation of channelrhodopsin-2. *Nat.*

Methods **7,** 848–854 (2010).

263. Chen, I.-W. *et al.* Parallel holographic illumination enables sub-millisecond two-photon optogenetic activation in mouse visual cortex in vivo. *bioRxiv* 250795 (2018). doi:10.1101/250795

264. Dal Maschio, M., Donovan, J. C., Helmbrecht, T. O. & Baier, H. Linking Neurons to Network Function and Behavior by Two-Photon Holographic Optogenetics and Volumetric Imaging. *Neuron* **94,** 774–789.e5 (2017).

265. Hernandez, O. *et al.* Three-dimensional spatiotemporal focusing of holographic patterns. *Nat. Commun.* **7,** 11928 (2016).

266. Pégard, N. C. *et al.* Three-dimensional scanless holographic optogenetics with temporal focusing (3D-SHOT). *Nat. Commun.* **8,** 1228 (2017).

267. Mardinly, A. R. *et al.* 3D All-optical Control of Functionally Defined Neurons With Cellular Resolution and Sub-millisecond Precision. in *Optics in the Life Sciences Congress* BrM3B.4 (OSA, 2017). doi:10.1364/BRAIN.2017.BrM3B.4

268. Yang, W., Carrillo-Reid, L., Bando, Y., Peterka, D. S. & Yuste, R. Simultaneous two-photon imaging and two-photon optogenetics of cortical circuits in three dimensions. *Elife* **7,** e32671 (2018).

269. Förster, D., Dal Maschio, M., Laurell, E. & Baier, H. An optogenetic toolbox for unbiased discovery of functionally connected cells in neural circuits. *Nat. Commun.* **8,** 116 (2017).

270. Baker, C. A., Elyada, Y. M., Parra, A., Bolton, M. M. & Chrisopher Baker; Yishai Elyada; Parra, Andres; Bolton, M. M. Cellular resolution circuit mapping with temporal-focused excitation of soma-targeted channelrhodopsin. *Elife* **1,** e14193 (2016).

271. Shemesh, O. A. *et al.* Temporally precise single-cell-resolution optogenetics. *Nat. Neurosci.* **20,** 1796–1806 (2017).

272. Forli, A. *et al.* Two-Photon Bidirectional Control and Imaging of Neuronal Excitability with High Spatial Resolution In Vivo. *Cell Rep.* **22,** 3087–3098 (2018).

273. Bovetti, S. *et al.* Simultaneous high-speed imaging and optogenetic inhibition in the intact mouse brain. *Sci. Rep.* **7,** 40041 (2017).

274. Molina, R. S. *et al.* Blue-Shifted Green Fluorescent Protein Homologues Are Brighter than Enhanced Green Fluorescent Protein under Two-Photon Excitation. *J. Phys. Chem. Lett.* **8,** 2548–2554 (2017).

275. Shcherbakova, D. M. *et al.* Bright monomeric near-infrared fluorescent proteins as tags and biosensors for multiscale imaging. *Nat. Commun.* **7,** 12405 (2016).

276. Shcherbakova, D. M. & Verkhusha, V. V. Near-infrared fluorescent proteins for multicolor in vivo imaging. *Nat. Methods* **10,** 751–4 (2013).

277. Kang, B. E. & Baker, B. J. Pado, a fluorescent protein with proton channel activity can optically monitor membrane potential, intracellular pH, and map gap junctions. *Sci. Rep.* **6,** 23865 (2016).

278. Kato, H. E. *et al.* Atomistic design of microbial opsin-based blue-shifted optogenetics tools. *Nat. Commun.* **6,** 7177 (2015).

279. Wang, K. *et al.* Direct wavefront sensing for high-resolution in vivo imaging in scattering tissue. *Nat. Commun.* **6,** 7276 (2015).

280. Yang, W. & Yuste, R. In vivo imaging of neural activity. *Nat. Methods* **14,** 349–359 (2017).

281. Silva, A. J. Miniaturized two-photon microscope: seeing clearer and deeper into the brain. *Light Sci. Appl.* **6,** e17104 (2017).

282. Marshall, J. D. *et al.* Cell-Type-Specific Optical Recording of Membrane Voltage Dynamics in Freely Moving Mice. *Cell* **167,** 1650–1662.e15 (2016).

283. Power, R. M. & Huisken, J. A guide to light-sheet fluorescence microscopy for multiscale imaging. *Nat. Methods* **14,** 360–373 (2017).

284. Rosenegger, D. G., Tran, C. H. T., LeDue, J., Zhou, N. & Gordon, G. R. A High Performance, Cost-Effective, Open-Source Microscope for Scanning Two-Photon Microscopy that Is Modular and Readily Adaptable. *PLoS One* **9,** e110475 (2014).

285. Perillo, E. P. *et al.* Deep in vivo two-photon microscopy with a low cost custom built mode-locked 1060 nm fiber laser. *Biomed. Opt. Express* **7,** 324 (2016).

286. Maia Chagas, A., Prieto-Godino, L. L., Arrenberg, A. B. & Baden, T. The €100 lab: A 3D-printable open-source platform for fluorescence microscopy, optogenetics, and accurate temperature control during behaviour of zebrafish, Drosophila, and Caenorhabditis elegans. *PLOS Biol.* **15,** e2002702 (2017).

287. Zhang, H., Reichert, E. & Cohen, A. E. Optical electrophysiology for probing function and pharmacology of voltage-gated ion channels. *Elife* **5,** e15202 (2016).

288. Zhang, H. & Cohen, A. E. Optogenetic Approaches to Drug Discovery in Neuroscience and Beyond. *Trends Biotechnol.* **35,** 625–639 (2017).

289. Werley, C. A. *et al.* All-Optical Electrophysiology for Disease Modeling and Pharmacological Characterization of Neurons. in *Current Protocols in Pharmacology* **78,** 11.20.1-11.20.24 (John Wiley & Sons, Inc., 2017).

290. Hempel, C. M., Werley, C. A., Dempsey, G. T. & Gerber, D. J. Targeting neuronal function for CNS drug discovery. *Drug Discov. Today Technol.* **23,** 17–25 (2017).

291. Klimas, A. *et al.* OptoDyCE as an automated system for high-throughput all-optical dynamic cardiac electrophysiology. *Nat. Commun.* **7,** 11542 (2016).

292. Dempsey, G. T. *et al.* Cardiotoxicity screening with simultaneous optogenetic pacing, voltage imaging and calcium imaging. *J. Pharmacol. Toxicol. Methods* **81,** 240–250 (2016).

293. Dempsey, G. T. & Werley, C. A. Optogenetic Approach to Cardiotoxicity Screening: Simultaneous Voltage and Calcium Imaging Under Paced Conditions. in 109–134 (Humana Press, New York, NY, 2017). doi:10.1007/978-1-4939-6661-5_6

294. Streit, J. & Kleinlogel, S. Dynamic all-optical drug screening on cardiac voltage-gated ion channels. *Sci. Rep.* **8,** 1153 (2018).

295. Kiskinis, E. *et al.* All-optical electrophysiology for high-throughput functional characterization of human iPSC-derived motor neuron model of ALS. *bioRxiv* 289959 (2018). doi:10.1101/289959

296. Lee, J. H. *et al.* Fluorescent in situ sequencing (FISSEQ) of RNA for gene expression

profiling in intact cells and tissues. *Nat. Protoc.* **10,** 442–458 (2015).

297. Kebschull, J. M. *et al.* High-Throughput Mapping of Single-Neuron Projections by Sequencing of Barcoded RNA. *Neuron* **91,** 975–987 (2016).

298. Ryan, T. J., Roy, D. S., Pignatelli, M., Arons, a. & Tonegawa, S. Engram cells retain memory under retrograde amnesia. *Science (80-.).* **348,** 1007–1013 (2015).

299. Tasic, B. *et al.* Shared and distinct transcriptomic cell types across neocortical areas. *bioRxiv* 229542 (2017). doi:10.1101/229542

300. Habib, N. *et al.* Massively parallel single-nucleus RNA-seq with DroNc-seq. *Nat. Methods* **14,** 955–958 (2017).

301. Olsen, S. R. & Wilson, R. I. Cracking neural circuits in a tiny brain: new approaches for understanding the neural circuitry of Drosophila. *Trends Neurosci.* **31,** 512–20 (2008).

302. Ford, K. J. & Davis, G. W. Archaerhodopsin voltage imaging: synaptic calcium and BK channels stabilize action potential repolarization at the Drosophila neuromuscular junction. *J. Neurosci.* **34,** 14517–25 (2014).

303. Pfeiffer, B. D. *et al.* Refinement of tools for targeted gene expression in Drosophila. *Genetics* **186,** 735–55 (2010).

304. Stocker, R. F., Heimbeck, G., Gendre, N. & de Belle, J. S. Neuroblast ablation in Drosophila P[GAL4] lines reveals origins of olfactory interneurons. *J. Neurobiol.* **32,** 443–56 (1997).

305. Fişek, M. & Wilson, R. I. Stereotyped connectivity and computations in higher-order olfactory neurons. *Nat. Neurosci.* **17,** 280–8 (2014).

306. Drews, G., Krippeit-Drews, P. & Düfer, M. Electrophysiology of Islet Cells. in 115–163 (Springer, Dordrecht, 2010). doi:10.1007/978-90-481-3271-3_7

307. Stojilkovic, S. S., Tabak, J. & Bertram, R. Ion Channels and Signaling in the Pituitary Gland. *Endocr. Rev.* **31,** 845–915 (2010).

308. Yamamura, H., Nishimura, K., Hagihara, Y., Suzuki, Y. & Imaizumi, Y. TMEM16A and TMEM16B channel proteins generate Ca2+-activated Cl-current and regulate melatonin secretion in rat pineal glands. *J. Biol. Chem.* **293,** 995–1006 (2018).

309. Roepke, T. K. *et al.* Kcne2 deletion uncovers its crucial role in thyroid hormone biosynthesis. *Nat. Med.* **15,** 1186–1194 (2009).

310. Aronova, A., Iii, T. J. F. & Zarnegar, R. Management of hypertension in primary aldosteronism. *World J. Cardiol.* **6,** 227–33 (2014).

311. Barrett, P. Q. *et al.* Role of voltage-gated calcium channels in the regulation of aldosterone production from zona glomerulosa cells of the adrenal cortex. *J. Physiol.* **594,** 5851–5860 (2016).

312. Freedman, B. D. *et al.* Adrenocortical zonation results from lineage conversion of differentiated zona glomerulosa cells. *Dev. Cell* **26,** 666–673 (2013).

313. Kaczorowski, G. J., McManus, O. B., Priest, B. T. & Garcia, M. L. Ion channels as drug targets: the next GPCRs. *J. Gen. Physiol.* **131,** 399–405 (2008).

314. Shaner, N. C. *et al.* Improving the photostability of bright monomeric orange and red

fluorescent proteins. *Nat. Methods* **5,** 545–551 (2008).

315. Zhou, X. X. & Lin, M. Z. Photoswitchable fluorescent proteins: ten years of colorful chemistry and exciting applications. *Curr. Opin. Chem. Biol.* **17,** 682–90 (2013).

316. Stiel, A. C. *et al.* 1.8 Å bright-state structure of the reversibly switchable fluorescent protein Dronpa guides the generation of fast switching variants. *Biochem. J.* **402,** 35–42 (2007).